PHENOTYPIC DISCRIMINATION OF MYCOBACTERIUM TUBERCULOSIS BY RAMAN SPECTROSCOPY

Vincent Baron

A Thesis Submitted for the Degree of PhD
at the
University of St Andrews

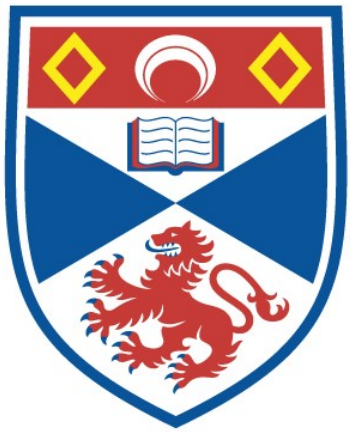

2018

Phenotypic Discrimination of *Mycobacterium tuberculosis* by Raman Spectroscopy

Vincent Baron

University of
St Andrews

This thesis is submitted in partial fulfilment for the degree of

Doctor of Philosophy (PhD)

at the University of St Andrews

February 2018

Thesis declaration

Candidate's declaration

I, Vincent Baron, do hereby certify that this thesis, submitted for the degree of PhD, which is approximately 47,457 words in length, has been written by me, and that it is the record of work carried out by me, or principally by myself in collaboration with others as acknowledged, and that it has not been submitted in any previous application for any degree.

I was admitted as a research student at the University of St Andrews in September 2013.

I received funding from an organisation or institution and have acknowledged the funder(s) in the full text of my thesis.

Date Signature of candidate

Supervisor's declaration

I hereby certify that the candidate has fulfilled the conditions of the Resolution and Regulations appropriate for the degree of PhD in the University of St Andrews and that the candidate is qualified to submit this thesis in application for that degree.

Date Signature of supervisor

Permission for publication

In submitting this thesis to the University of St Andrews we understand that we are giving permission for it to be made available for use in accordance with the regulations of the University Library for the time being in force, subject to any copyright vested in the work not being affected thereby. We also understand, unless exempt by an award of an embargo as requested below, that the title and the abstract will be published, and that a copy of the work may be made and supplied to any bona fide library or research worker, that this thesis will be electronically accessible for personal or research use and that the library has the right to migrate this thesis into new electronic forms as required to ensure continued access to the thesis.

I, Vincent Baron, confirm that my thesis does not contain any third-party material that requires copyright clearance.

The following is an agreed request by candidate and supervisor regarding the publication of this thesis:

Printed copy

No embargo on print copy.

Electronic copy

No embargo on electronic copy.

Date Signature of candidate

Date Signature of supervisor

Underpinning Research Data or Digital Outputs

Candidate's declaration

I, Vincent Baron, hereby certify that no requirements to deposit original research data or digital outputs apply to this thesis and that, where appropriate, secondary data used have been referenced in the full text of my thesis.

Date Signature of candidate

Thesis abstract

TB remains a major health issue worldwide causing around 1.5 deaths each year. The recent phase III clinical trials of shortened TB treatment failed to show superiority compared to the current regimen and this mainly because of relapse. Relapse is thought to be caused by dormant bacteria. Dormancy in *Mycobacterium* species has been shown to be associated with the accumulation of intracellular lipids, defining two phenotypes: the lipid rich (LR) cells (associated with dormancy) and the lipid poor (LP) cells (non-dormant). LR cells were shown to have a higher phenotypic antibiotic resistance compared to LP cells. Studying these two phenotypes is therefore central in tuberculosis research to understand better the disease and also potentially start to reveal the bacteriology of relapse.

We investigated the power of Raman spectroscopy, a label-free and non-destructive technique, to discriminate LR and LP bacteria both *in-vitro* and *ex-vivo.* This represents the first Raman spectroscopy study that tries to discriminate the phenotypes of *M. tuberculosis* and investigate them directly at the site of the disease.

Using total lipid extract of *M. tuberculosis,* we showed the location of the main lipid bands in the Raman spectrum. The two major lipid peaks were located around 1300 cm^{-1} and 1450 cm^{-1}.

Raman spectroscopy can discriminate LR and LP cells with high sensitivity and specificity. The main differences between the two groups are located in the two major Raman lipid peaks, the lipid band A (1300 cm^{-1}) and lipid band B (1440 to 1450 cm^{-1}). The two phenotypes were successfully discriminated in TB infected guinea pig lung tissue sections also from *in-vitro* culture using wavelength modulated Raman (WMR) spectroscopy combined with fluorescence imaging. We developed a protocol

to perform both Raman spectroscopy and immunohistochemistry on the same tissue sample.

We studied the evolution of LR and LP proportion in mycobacterial population as the growth conditions changed and showed that LR cells could rapidly convert to LP cells as they face favourable growth conditions.

The results presented in this thesis showed that LR *M. tuberculosis* cells could be predominant at the site of infection. This would suggest that drug sensitivity testing should be performed on culture presenting both LR and LP cells in high proportion.

Acknowledgments

I'm very thankful to my supervisor Prof Stephen Gillespie for giving me the chance to do a PhD in his group, for the help, support and the discussions he provided throughout my PhD.

I would like to thank Prof Kishan Dholakia for his guidance regarding the physics part of my thesis project and for giving me the opportunity to follow a course on the principle of optics.

I'm very grateful to Dr Mingzhou Chen for being someone I have enjoyed so much working with, for all the discussions about the results, the experiments…Without his help, this thesis would not have been the same.

Thanks to Dr Robert Hammond for his help in the lab, the discussions about experiments and for being such a nice person to chat and work with.

A special thank to Dr John Kennedy for all the chats about everything, all the discussions, ideas and his friendship. Having him around made my PhD a lot more enjoyable.

I'm very thankful to Dr Melissa Andrews for her support, all the chats and her friendship.

I thank all the members of the infection research group for their help and support during my PhD. I also want to thank the PhD students from the other research groups.

I would like to thank Dr Simon Clark and Dr Ann Rawkins for providing me tissue material for my project.

I thank Dr Simon Young for his help with the lipidomic project.

I thank Souad for all the discussions and her friendship.

This work was supported by the PreDiCT-TB consortium [IMI Joint undertaking grant agreement number 115337, resources of which are composed of financial contribution from the European Union's Seventh Framework Programme (FP7/2007–2013) and EFPIA companies' in kind contribution (www.imi.europa.eu)].

I would like to thank all my friends from France for all their support during this long process.

I'm more than grateful to my family and especially to my parents for supporting me and listening to me through this entire journey. Thank you so much!

Awa, I will never thank you enough, you have always been here to help me, support me, there are simply no words to express how grateful I am that you are part of my life.

Table of contents

List of figures

List of tables

List of abbreviations

ATP: Adenosine triphosphate

ADC: Albumin-dextrose-catalase

BCG: bacillus Calmette-Guérin.

CCD: charged couple devices

CFU: colony forming units

DMSO: dimethyl-sulfoxide

DNA: deoxyribonucleic acid

DST: drug sensitivity testing

EF: edge filter

EMB: ethambutol

FM: flip mirror

HIV: human immunodeficiency virus

ICL: isocitrate lyase

IFN: interferon

IHC: immunohistochemistry

IMS: industrial methylated spirits

INH: isoniazid

IR: infrared

LC/MS: liquid chromatography and mass-spectrometry

LOOCV: leave one out cross validation

LP: lipid poor

LR: lipid rich

LTBI: latent TB infection

M. africanum: Mycobacterium africanum

MBC: minimum bactericidal concentration

M. bovis: Mycobacterium bovis

Mbp: million base pair

MDR-TB: multi drug-resistant TB

mg: milligram

MGIT: mycobacteria growth indicator tubes

MIC: minimum inhibitory concentration

mL: milliliter

M. leprae: Mycobacterium leprae

MODS: microscopic observation drug susceptibility

MPER1: mycobacterial perilipin-1 protein

mper1: mycobacterial perilipin-1 gene

M. smegmatis: Mycobacterium smegmatis

M. tuberculosis: *Mycobacterium tuberculosis*

M. tb: Mycobacterium tuberculosis

mW: milliwatts

NBF: Neutral buffered formalin

NCTC: National Collection of Type Cultures

NF: notch filter

nm: nanometre

NRP: non-replicating persistence

OCT: Optimal cutting temperature

PBS: phosphate buffered saline

PCA: principal component analysis

PCs: principal components

PDIM: phthiocerol dimycocerosates

pH: potential of hydrogen

PHE: Public Health England

PTB: pulmonary TB

PZA: pyrazinamide

RIF: rifampicin

RNA: ribonucleic acid

Rpfs: resuscitation promoting factors

rpm: rotation per minute

TAGs: triacylglycerols

TB: Tuberculosis

Ti:SA laser: titanium sapphire laser

TLR: toll like receptor

UV: ultraviolet

W: Watt

WHO: world health organisation

WMR: wavelength modulated Raman

XDR-TB: extensively drug-resistant TB

°C: degree Celsius

μg: micrograms

μL: microliter

Chapter 1 Introduction

1.1 General background

1.1.1 Tuberculosis and humans

Tuberculosis (TB) has long been part of human history; signs of TB infection have been found in a 9,000 year old human skeleton (Hershkovitz *et al.*, 2008). Moreover, evidence of TB infection has also been observed in Egyptian mummies dating from 3000 BC (Zink *et al.*, 2001). In Greek antiquity, in describing TB, Hippocrates wrote about the symptoms and explained that the disease was usually fatal (Daniel and Iversen, 2015). Robert Koch, in 1882, was the first to describe *Mycobacterium tuberculosis* (*M. tuberculosis*), the causal agent of TB (Koch, 1882, Daniel, 2005b, Daniel, 2006). In the early 1900s, Albert Calmette and Camille Guérin developed a vaccine from attenuated *Mycobacterium bovis*; they called it "BCG" for Bacillus of Calmette and Guerin. After the First World War, the BCG vaccine was commonly used to prevent TB (Daniel, 2005a, Daniel, 2006). It wasn't until after the Second World War that antibiotics, showing activity against *M. tuberculosis,* were discovered. In 1946, the use of streptomycin was found to be an effective treatment for TB and later in 1952 isoniazid was found to also be effective in treating TB (Schatz *et al.*, 1944, Marshall *et al.*, 1948, Daniel, 2006). Rapidly, resistance to antibiotics appeared (Singh and Mitchison, 1955) however, the development of new drug combinations led to reduction in mortality due to TB (Fox *et al.*, 1999). The emergence of human immunodeficiency virus (HIV) and the reduction of expenses spent on controlling TB led to the resurgence of TB. The funding reduction in TB control lead to a resurgence of TB, this phenomenon was called the: "The U-shaped

curve of concern" (Reichman, 1991). During the global health emergency declaration given by the WHO in 1993 (Reichman, 1991, Glaziou *et al.*, 2011), it was declared that HIV co-infection and the existence of drug-resistant TB strains participate to the global TB burden (WHO, 2016). By 2030 the WHO plans, as part of WHO's End TB Strategy, to reduce the number of deaths due to TB by 90% compared to 2015 (WHO, 2016).

1.1.2 *Mycobacterium tuberculosis*

Mycobacterium tuberculosis is the causal agent of tuberculosis (TB) in humans. TB is a major health threat and was responsible for the deaths of about 1.4 million people around the globe in 2015 (WHO, 2016). The bacillus causing TB is part of the genus *Mycobacterium* that includes several other human pathogens. For example:

- *Mycobacterium leprae,* the causal agent of leprosy.
- *Mycobacterium africanum,* causes similar symptoms as TB but the pathogenicity is less severe.
- *Mycobacterium bovis,* the causative agent of bovine TB.

Mycobacterium smegmatis is a non-pathogenic, fast-growing *Mycobacterium* species and therefore commonly used in *M. tuberculosis* research as a surrogate organism. By opposition, *M. tuberculosis* is a slow-growing bacterium with a generation of 16 h under optimal culture conditions (Beste *et al.*, 2009). *M. tuberculosis* is an acid-fast bacterium meaning that once the organism is stained the dye used can resist the acid-alcohol wash (decolourisation step). The high stain retention is due to the high lipid content of *M. tuberculosis* cell wall. Ziehl-Neelsen, Kinyoun or Auramine stains are usually used to stain *M. tuberculosis*. This microorganism possesses a large-sized

genome among bacteria of 4.4 Mbp which encodes for approximately 4000 predicted proteins. It is an aerobic organism that can produce adenosine triphosphate (ATP) by respiration in the presence of oxygen. Aerobic respiration in bacteria is composed of three main steps: glycolysis, the Krebs cycle and electron transport chain. All together these three steps lead to the production of 38 ATPs for each molecule of glucose used. *M. tuberculosis* can also survive in low oxygen environments as a facultative anaerobe.

1.1.3 Tuberculosis

TB is an infectious disease that primarily affects the lungs and causes pulmonary TB (PTB). Many types of tissue, other than lung, can be infected by *M. tuberculosis* causing extrapulmonary TB (Noertjojo *et al.*, 2002). Active TB is usually chronic with a persistent cough, intermittent fever, loss of appetite, weight loss and chest pain. Patients with active PTB can spread the disease to other people through the air when coughing, spitting or sneezing.

TB patients can present active TB or latent TB. Latent TB infection (LTBI) occurs when the primary infection is controlled, and no clinical signs of illness can be observed (Lipworth *et al.*, 2016). Previous studies suggest that about 5 to 10 % of patients with controlled LTBI could develop an active infection during their life. The risk of active disease is strongly increased in patients co-infected with HIV (Harries and Dye, 2006). Reactivation from LTBI to active TB represents the majority of new TB cases (WHO, 2016).

1.1.4 Tuberculosis global burden

TB is still one of the leading causes of infectious death in the world. Every year around 1.5 million people die from the disease (WHO, 2016). In 2015, around 10.5 million new TB cases occurred around the globe with around 10% of new cases being co-infected with HIV. Approximately 60% of new cases are found in India, China, Pakistan, South-Africa, Nigeria and Indonesia. In TB, examples of both multiple drug-resistant TB (MDR-TB) and extensively drug-resistant TB (XDR-TB) can be observed. MDR-TB is caused by organisms resistant to at least isoniazid and rifampicin. XDR-TB is defined by resistance to rifampicin and isoniazid (first line drugs) plus resistance to at least one fluoroquinolone and also resistance to one or more second line drug. According to the WHO, around 580,000 patients with multi-drug resistant TB (MDR-TB) were counted in 2015 mostly in China, India, Russia (WHO, 2016).

1.2 Overview of TB diagnosis and treatment

1.2.1 BCG and prevention

Bacillus Calmette–Guérin (BCG) vaccine continues to be administered to infants in many countries, based on the TB epidemiology of the country. In 2015, over 160 nations were providing BCG vaccine as standard, and over 100 countries showed high coverage (superior to 90% of the population) (WHO, 2016). This vaccine is effective at preventing the severe form of TB in children but for adult PTB the efficacy is limited (WHO, 2016). Moreover, this vaccine is less effective if patients have already

been in contact with environmental mycobacteria species, which share similar antigens with *M. tuberculosis* (Andersen and Doherty, 2005).

1.2.2 A diagnostic overview

TB diagnosis is complex and can require several laboratory tests. The diagnosis should define if patients have active or latent TB and determine whether drug-resistant bacteria are present. Populations presenting a high risk of latent infection such as people born in regions where TB is endemic and people showing a risk of reactivation (HIV positive patients) should be screened for latent TB (Horsburgh and Rubin, 2011, Zumla *et al.*, 2013). To diagnose latent TB infection, the tuberculin skin test or the interferon-gamma release assay can be used (ECDC, 2011). The tuberculin skin test is less expensive than the interferon-gamma release assay showing the same sensitivity but less specificity (McNerney *et al.*, 2012).

To diagnose active TB, the use of sputum microscopy, culture in broth and antibiotic susceptibility tests are the standard methods (Zumla *et al.*, 2013). These methods could be facilitated by molecular tests, imaging and investigation of biopsied tissue. Both the tuberculin test and interferon-gamma release assay are not used to diagnose active TB. Xpert MTB/RIF (Cepheid) is a molecular diagnostic tool that can detect *M. tuberculosis* in as little as two hours with high sensitivity (Boehme *et al.*, 2010). The Xpert MTB/RIF test is using a PCR-based amplification of a specific region of *M. tuberculosis* involved in drug resistance.

To diagnose drug-resistant TB, the WHO recommend performing the Xpert MTB/RIF at the same time as the drug susceptibility tests in liquid culture (WHO, 2011a). These combined tests can confirm the resistance to rifampicin and the susceptibility or

resistance to other drugs. The resistance to rifampicin is usually accompanied by isoniazid resistance. Other tests can be conducted to diagnose drug-resistant TB such as microscopic observation drug susceptibility (MODS), nitrate reductase assay and colorimetric reductase methods (Zumla *et al.*, 2013). The diagnosis of multidrug resistance remains difficult; it is estimated that only 10% of multidrug-resistant TB cases are currently diagnosed worldwide, and only half of those cases receive appropriate treatment (Zignol *et al.*, 2012, WHO, 2011b).

1.2.3 Treatment overview

TB treatment depends on diagnosis as a drug-sensitive active TB, a latent infection a multidrug resistant or an HIV co-infection can all be detected and would be treated differently. The WHO determined the different aims for TB treatment as:

- *"to cure the patient and restore quality of life and productivity*
- *to prevent death from active TB or its late effects*
- *to prevent relapse of TB*
- *to reduce transmission of TB to others*
- *to prevent the development and transmission of drug resistance."* (WHO, 2010).

Treatment for drug-sensitive active TB is based on rifampicin (RIF), isoniazid (INH), ethambutol (EMB), and pyrazinamide (PZA) (Combs *et al.*, 1990). This standard treatment takes at least six months and is divided into two steps: the first two months includes administration of all four drugs followed by four months of isoniazid and rifampicin. The therapy can be extended up to 9 months if the patient presents risks of

relapse such as positive sputum culture after eight weeks, immunosuppression, extensive disease or cavitation (Zumla *et al.*, 2013).

In the case of latent TB, patients receive a preventive treatment (WHO, 2012). This treatment is isoniazid daily for 6 to 9 months (Zumla *et al.*, 2013).

To treat MDR-TB, a regimen combining several anti-TB drugs has to be designed. These drugs are chosen from the first-line and second-line anti-TB drugs. Regimens designed to treat MDR-TB are associated with high toxicity (Falzon *et al.*, 2011).

Treatment for drugs-resistant TB is given for 20 months in patients who have never been treated for TB and is extended to 30 months in patients that have previously been treated for TB (Zumla *et al.*, 2013).

For patients co-infected with HIV, TB treatment is combined with antiretroviral therapy. The antiretroviral therapy starts within the first eight weeks of TB treatment (Zumla *et al.*, 2013). For patients with active TB, the antiretroviral treatment is based on efavirenz (Swaminathan *et al.*, 2011).

1.3 Pathogenesis of Tuberculosis

1.3.1 Overview of the TB cycle

TB infection usually begins with the inhalation of droplets containing *M. tuberculosis.* While coughing, TB infected patients release these droplets that can remain in the air for hours, and a single bacterium is enough to infect someone (Russell, 2007). Once the bacterium is inhaled, it arrives in the lung where the bacillus is phagocytosed by an alveolar macrophage. The phagocytosis initiates a pro-inflammatory response allowing recruitment of mononuclear cells from nearby blood vessels (Russell, 2007).

Immune cells arrive at the infection site and begin to form a granuloma or tubercle; the presence of a granuloma is characteristic of TB. The granuloma is a complex structure composed of a core of infected macrophages that have phagocytosed *M. tuberculosis*. Foamy macrophages and mononuclear phagocytes surround the centre, and then an outer layer of lymphocytes associated with the extracellular matrix (collagen and other components) complete the structure (Russell, 2007, Guirado and Schlesinger, 2013). As long as *M. tuberculosis* is contained inside a granuloma, the host cannot infect others. The granuloma however can rupture and release *M. tuberculosis* in the lung. This rupture can be due to a decrease in the immune status of the host that can happen in elderly people, immunocompromised patients or someone with malnutrition and/or other adverse health conditions (Russell, 2007). Once the granuloma caseates (decays into cellular debris) it releases many infectious bacilli into the sputum and induces a cough. Coughing leads to expulsion of pathogens into the air.

1.3.2 Alveolar macrophages

Macrophages represent the first line of defence against pathogens (Nathan and Shiloh, 2000, Liu and Modlin, 2008). Once *M. tuberculosis* arrives in the lung, macrophages phagocytose the bacteria leading to the creation of a phagosome (Aderem and Underhill, 1999). Macrophages present numerous receptors that can be involved in binding to *M. tuberculosis* leading to the internalisation of the bacilli (Ernst, 1998). Once the bacillus is within the phagosome, the host defence system targets the pathogen, the pH inside the phagosome decreases and enzymes that attack bacterial lipids and proteins are produced (Huynh and Grinstein, 2007).

1.3.3 *M. tuberculosis* strategies to survive inside the macrophage

In the lung, bacilli are phagocytosed by alveolar macrophages in a process, which should kill the pathogens. *M. tuberculosis* succeeds in escaping this process and survives in the macrophage (Russell, 2001). Phagosomes containing *M. tuberculosis* cells usually show little acidification and do not have lysosomal hydrolyses as *M. tuberculosis* is able prevent maturation of the phagosome (Huynh and Grinstein, 2007, Katti *et al.*, 2008, Russell *et al.*, 2009). The acidification inside the phagosome is mediated by proton pumps, which reduce the neutral pH to an acidic pH of 5.0 (Yates *et al.*, 2005). *M. tuberculosis* can prevent the pH dropping below 6.4, which is a lot higher than the phagolysosome normal pH (pH 4.5–5.0) (Yates *et al.*, 2005, MacMicking *et al.*, 2003). The phagosome environment is nitrosative, oxidative, shows low oxygen level, and low concentration of carbohydrates (Schnappinger *et al.*, 2003). Once *M. tuberculosis* is phagocytosed by human macrophages, the bacillus metabolism change to adapt and survive to the phagosomal environment. *M. tuberculosis* can access fatty acids while being in the phagosome but there are few carbohydrates available. In order to adapt to those conditions the pathogen induces fatty acid degradation enzymes (Schnappinger *et al.*, 2003). The extreme phagosomal environment inhibits the aerobic respiration and in this environment the main carbon source may be derived from fatty acids and their β-oxidation (Schnappinger *et al.*, 2003). By means of β-oxydation, fatty acids are broken down in smaller molecules such as Acetyl-CoA or Propionyl-CoA. The author suggested that such newly synthesised products can enter the glyoxylate cycle and the citric acid cycle as *icl*, *gltA1* and Rv1130 are induced. The *icl* gene encodes for the isocitrate lyase (ICL), this enzyme is needed for the glyoxylate shunt (Schnappinger *et al.*, 2003).

Moreover, it has been shown that ICL is essential for *M. tuberculosis* persistence inside macrophages during the infection (McKinney *et al.*, 2000). When *M. tuberculosis* is deficient in cholesterol transporter Mce4 or ICL, the virulence of the bacillus decreases (McKinney *et al.*, 2000, Mohn *et al.*, 2008). Other studies showed that *M. tuberculosis* could utilise the cholesterol from the host cell membrane as a carbon source (Pandey and Sassetti, 2008, Chang *et al.*, 2009, Nesbitt *et al.*, 2010). *M. tuberculosis* is able to survive in the hostile phagosomal environment by being resistant to the adverse conditions of the phagolysosome compartment of macrophages, conditions that are lethal for most microbial pathogens (Huynh and Grinstein, 2007). Furthermore, the pathogen is able to survive inside granuloma structures (Reece and Kaufmann, 2012). Macrophages containing *M. tuberculosis* that are located in the hypoxic environment of the granuloma are likely to be found in a lipid-loaded state. Inside those macrophages, around half of the pathogens become tolerant to isoniazid and accumulate intracellular lipid inclusions (Daniel *et al.*, 2011). Inside the macrophage *M. tuberculosis* can import host cell fatty acids, derived from triacylglycerols (TAGs), and incorporate them directly. *M. tuberculosis* can also use the host cell fatty acids for its own lipid metabolism. Several genes were found to be up regulated, in *M. tuberculosis* located in macrophages, such as *icl, lipY, tgs1, hspX and dosR*. These genes are known to be involved in lipid metabolism or in dormancy in *M. tuberculosis* (Daniel *et al.*, 2011). The induction if *icl* is central to be able to use the host fatty acids. This induction also suggests that the pathogen uses host fatty acids as central energy source while being inside macrophages (Daniel *et al.*, 2011). The isocitrate lyase is a critical enzyme in the glyoxylate shunt, which is a short cut in the tricarboxylic cycle. This shunt prevents the loss of carbons that occur when CO_2 is formed. The glyoxylate cycle occurs in organisms that use fatty acids as energy

source (Gengenbacher and Kaufmann, 2012). Metabolic pathways occurring in *M. tuberculosis* during the infection such as the glyoxylate cycle are shown in **Fig. 1.1**.

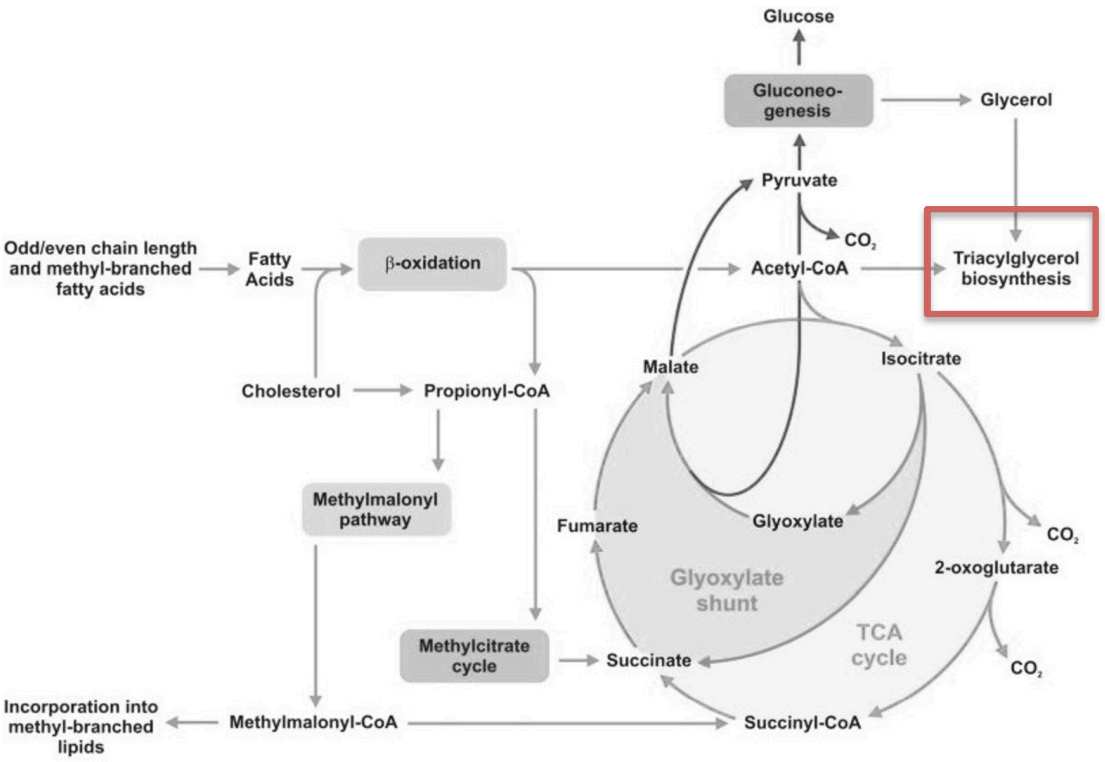

Figure 1.1 *Glyoxylate shunt pathway of M. tuberculosis in the macrophage.*

Acetyl-CoA and propionyl-CoA, produced from fatty acids or cholesterol, enter the tricarboxylic acid cycle leading to the production of pyruvate. The glyoxylate shunt avoids CO_2 loss by the bacteria. The pyruvate produced can be used for the gluconeogenesis. Acetyl-CoA and C3 molecules coming from the gluconeogenesis or glycolysis such as glycerol are needed to produce TAGs. The production of TAGs can lead to the accumulation of lipid bodies, in dormant bacteria for example. Figure modified from (Gengenbacher and Kaufmann, 2012).

1.3.4 Formation of the granuloma

Granulomas are the hallmark of TB. A TB granuloma is an organised structure of immune cells composed of infected macrophages, uninfected macrophages, epithelioid cells, multinucleated giant cells and T-cells. It is characterised by a core of infected macrophages surrounded by foamy macrophages and lymphocytes (**Fig. 1.2**.). The structure is surrounded by fibrous material (Guirado and Schlesinger, 2013, Griffiths *et al.*, 2010). The role of a granuloma is to contain *M. tuberculosis* infection leading to a localised immune response. However, *M. tuberculosis* can survive this process and reactivate later under certain conditions. Therefore, granulomatous structures are a central and important phenomenon to study. Human macrophages produce a strong pro-inflammatory response during TB infection. On the surface of host cells, there are Toll-like receptors (TLR), which recognise and bind to the bacterial surface. Once alveolar macrophages have phagocytosed *M. tuberculosis,* the innate immune response begins with production by macrophages of cytokines and chemokines. This leads to the recruitment of other host immune cells to the site of infection such as more macrophages, dendritic cells and lymphocytes (Ulrichs and Kaufmann, 2006, Algood *et al.*, 2005, Miranda *et al.*, 2012). The newly recruited immune cells also produce chemokines and cytokines to continue the cellular recruitment (Algood *et al.*, 2003). The inflammatory response is regulated by the production of interferon (IFN)-γ. For example, IFN-γ-deficient mice are unable to stop the pro-inflammatory response, leading to severe lung pathology (Cooper *et al.*, 1993). TB infection can be contained in a granuloma with the bacilli able to survive for decades inside this structure (Miranda *et al.*, 2012).

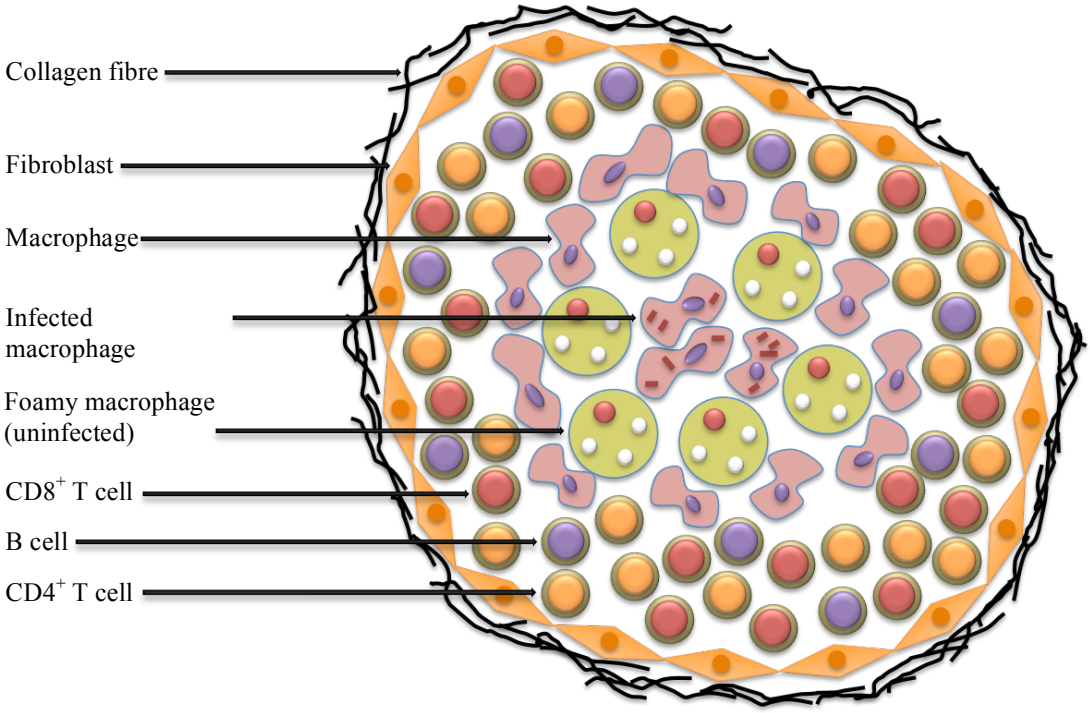

Figure 1.2 *Structure of TB Granuloma.*

The granuloma is the hallmark of TB. Infected macrophages are located in the centre of the structure surrounded by uninfected macrophages and foamy macrophages. T-cells (CD4$^+$ and CD8$^+$) and B-cells form a second layer in the granuloma structure. Finally, the granuloma is encircled by fibroblasts and collagen. At this stage, TB infection is contained.

1.3.5 *M. tuberculosis* inside the granuloma

M. tuberculosis-infected macrophages migrate to the pulmonary epithelium where an inflammatory response is induced and immune cells recruited. A granuloma structure then appears surrounding the infected macrophages. Three granuloma stages can be distinguished including, solid granulomas, necrotic granulomas and caseous granulomas (Gengenbacher and Kaufmann, 2012). The solid granuloma is formed within a fibrotic wall that separates the tubercle from the surrounding tissue. The solid granuloma corresponds to latent TB. At this stage, *M. tuberculosis* is contained in the granuloma. The necrotic granuloma remains structured overall; however the centre is necrotic and mainly composed of cell detritus. When the tubercle starts to become necrotic *M. tuberculosis* can resuscitate, become metabolically active and start to replicate. In caseous granulomas the centre starts to liquefy creating cavitation. The size of the caseous granulomas is reduced compared to the other two types of granulomas. The now open cavity allows oxygen to enter the cavity. The presence of oxygen and nutrients (caseous material) leads to an important replicating phase. At that moment, if the patient coughs there is a possibility of transmission of bacilli to other individuals. Finally, *M. tuberculosis* can access blood vessels and potentially start to spread to other organs (Gengenbacher and Kaufmann, 2012).

1.3.6 Models of the TB granuloma

As mentioned previously, the granuloma is the hallmark of TB; its role is to contain the infection. However, as previously shown *M. tuberculosis* can survive in this structure and potentially escape and induce active TB. A general granuloma formation

process and an overall granuloma structure have been proposed; however, many questions and uncertainties remain. For example, the role of *M. tuberculosis* itself in the granuloma formation is not well understood. For a long time granuloma formation has been seen as a host driven process, but more recent studies have shown that the bacilli can play a major role in this process (Guirado and Schlesinger, 2013, Davis and Ramakrishnan, 2009, Ehlers and Schaible, 2013).

Models to understand granulomas are essential as access to human lung biopsies is limited and only gives information of the granuloma structure at one time point. Therefore biopsies cannot help understand the process of granuloma formation, cellular recruitment, and bacterial influence. The natural host of *M. tuberculosis* is *Homo sapiens* therefore model organisms are needed to conduct experiments. There are several granuloma models, *in-vivo, in-vitro* and *in-silico* (Guirado and Schlesinger, 2013).

Animal models can be close to human in term of conditions, but no animal models show identical pathology compared to that found in humans. Mouse models show different granulomatous structures compared to human pathology and do not present latency. The zebrafish model is interesting for observation of the early recruitment of immune cells and the initiation of granuloma formation (Davis *et al.*, 2002). However, this animal model is limited to study late granuloma or the recruitment of lymphocytes (Rubin, 2009, Guirado and Schlesinger, 2013). The guinea-pig model presents similar granulomatous structure compared to the human, however, there is no latent TB in this *in-vivo* model. Mini-pig and non-human primates are the closest models to human. In *in-vivo* models, the parameters are not all known and controlled but those models are more “realistic” (closer to human). All of these models can be

used depending on the experiment, each of them presenting advantages and disadvantages (Guirado and Schlesinger, 2013).

In-vitro models usually use blood mononuclear cells, agarose beads and collagen to create a gel. *In-vitro* models can then be directly challenged with mycobacteria or with antigen-coated beads. They provide an understanding about macrophage recruitment and differentiation and also show the formation of a granulomatous structure with T-cells surrounding the macrophages (Puissegur *et al.*, 2004). This *in-vitro* model has been found to be similar to human TB granulomas regarding cell morphology and cell differentiation (Lay *et al.*, 2007). The *in-vitro* models have greatly increased our knowledge about granuloma formation and regulation. These models are flexible and can be modulated for specific experiments to answer specific questions. However, *in-vitro* models are limited, as their growth conditions remain very different to human tissue. They are designed using only known parameters, and therefore lack the contribution or role of unknown factors. Both *in-vivo* and *in-vitro* models generate data that can be combined and used to construct simulations.

In-silico models can be used to combine data generated by other models or experiments. They can simplify very complex systems that are difficult to study only by using *in-vivo* or *in-vitro* models. *In-silico* models present important advantages including the fact they are inexpensive and all the parameters are known and can be controlled. Parameters can be added removed or changed systematically to answer very specific questions. *In-silico* models are limited by known parameters that can be used to construct a simulation. They need *in-vivo* and *in-vitro* models to generate values and parameters to be as close to reality as possible and reduce the number of hypothetical values. Combining data and parameters from different models or experiments remains a difficulty when creating *in-silico* models. Several *in-silico*

models of the *M. tuberculosis* granuloma have been constructed (Segovia-Juarez *et al.*, 2004, Gammack *et al.*, 2005, Fallahi-Sichani *et al.*, 2011, Marino *et al.*, 2011). The granuloma represents a key structure in TB and its structure is very complex with no model alone able to mimic the pathology that occurs in the human. The use of several *in-vivo*, *in-vitro* and *in-silico* models is therefore needed to be as close to reality as possible.

1.4 Bacterial dormancy

1.4.1 Bacterial dormancy in the environment

The term dormancy has been used in microbiology for a long time and in the 1920's work was conducted on dormant bacteria (Burke *et al.*, 1925). In the 1970's Stevenson hypothesised that a significant proportion of bacteria in water can be found in a dormant state (Stevenson, 1977). Later in the 1980's Xu et al., (1982) observed that a large proportion of *Escherichia coli* and *Vibrio cholerae* cells in cultures could be non-culturable, but still viable (Xu *et al.*, 1982). More recently, the study of dormancy attracted attention as it was suspected to play a role in bacterial infections such as tuberculosis, anthrax and cholera (Lennon and Jones, 2011). The term dormant could be defined as being asleep or showing reduced activity for a period of time referring to a reversible state of the organism. Lennon and Jones proposed a general definition for dormancy: "*It refers to an organism's ability to enter a reversible state of low metabolic activity when faced with unfavourable environmental conditions*" (Lennon and Jones, 2011). Many microorganisms can show no sign of viability under certain conditions, but not be dead. Up to 80% of the bacterial cells in soil samples from the environment appear to be metabolically

inactive, many of which can be resuscitated (Lennon and Jones, 2011). Microorganisms can become dormant when faced with adverse conditions such as starvation (Kaprelyants and Kell, 1993, Kaprelyants *et al.*, 1993) or reduction in oxygen concentration (Wayne and Sramek, 1994). Bacteria converting to a dormant phenotype can contain specialised structures such as cysts, conidia, spores and akinetes. Bacteria can also enter dormancy without showing any of these structures but instead have other adaptations to the environment such as reduction of cell size, modification of proteins or lipid content, storage of compounds and change in cell structure (thickened cell walls, for example) (Lennon and Jones, 2011). Usually, microorganisms exit the dormant state when environmental conditions improve (Setlow, 2003, Whitesides and Oliver, 1997, Lennon and Jones, 2011). It has been shown that resuscitation-promoting factors (Rpfs) can also induce an exit from a dormant state. Rpfs are secreted proteins, first discovered in *M. luteus* (Mukamolova *et al.*, 1998). Very low concentrations (picomolar) of Rpf can induce an increase up to a 100 times in the count of viable cells from dormant cultures of *M. luteus* (Mukamolova *et al.*, 1998). Five proteins that are homologous to *M. luteus* Rpfs have been found in *M. tuberculosis* (Tufariello *et al.*, 2004).

1.4.2 Dormancy in *M. tuberculosis*

Dormancy in mycobacteria is defined by a combination of phenomena. A definition of mycobacterial dormancy has been proposed: *"inability to grow on solid medium, the presence of low metabolic activity, alteration of gene regulation with the accumulation of triacylglycerides in intracellular lipid bodies, loss of acid-fastness, tolerance to antibiotics, and the imputation that growth rate is slow."* (Lipworth *et*

al., 2016). Previously published definitions of dormancy in mycobacteria are shown in **Tab. 1.1**.

Table 1.1 Definitions of dormancy in mycobacteria.

Authors and reference	Definitions
(Voskuil *et al.*, 2004a)	Without replication or significant metabolism.
(Shleeva *et al.*, 2010)	The dormant state is understood here as a *reversible* state of a bacterial cell, when the level of metabolic activity is decreased and the cell is able to survive for a long time without division
(Gengenbacher and Kaufmann, 2012)	Non- replicating bacilli maintaining full viability at a very low metabolic rate; organisms show minor susceptibility or phenotypic drug resistance to antibiotics targeting functions required for growth.
(Mariotti *et al.*, 2013)	Dormancy is defined as a stable but reversible non-replicating state of *Mycobacterium tuberculosis*.

Recent TB clinical trials were aimed at reducing the treatment duration to four months instead of six months for the standard regimen. In these clinical trials the bacterial clearance was rapid. However, the tested regimens were not found to be superior to the standard regimen, as high relapse rates were observed (Gillespie *et al.*, 2014,

Jindani *et al.*, 2014, Merle *et al.*, 2014). Bacteria surviving treatment can induce relapse later. These bacteria are thought to exist in a dormant state (Phillips *et al.*, 2016, Hammond *et al.*, 2015). Investigating dormancy and antibiotic resistance is absolutely key to design new TB treatments (Lipworth *et al.*, 2016).

The existence of mycobacteria in sputum that can grow in the presence of Rpfs but not on solid media has been demonstrated. These bacteria however cannot be observed by standard culture methodologies. During treatment, the Rpf-dependent population does not decrease. This suggests that this bacterial population is phenotypically resistant to antibiotics (Mukamolova *et al.*, 2010). These bacteria could correspond to dormant cells. Phenotypic antibiotic resistance is arising from the reduced or shifted metabolic activity in dormant bacteria, rather than from genetic mutations. The importance of dormancy has been reinforced by recent studies showing that there is a difference regarding bacterial count between solid and liquid media (Bowness *et al.*, 2015).

1.4.3 Terminology and proposed definitions

In TB research there is no standardised definition for dormancy, and also there is a misuse of different terms such as dormant, persistent and latent. In 2016, Lipworth *et al.,* proposed definitions for these terms in an attempt to generate common nomenclature (Lipworth *et al.*, 2016). They proposed that latency corresponds to a controlled stage of the TB infection where bacteria can survive in the host for years without causing clinical disease. Latent refers to a state of the disease, whereas dormant corresponds to a bacterial state. In other words, TB infection can be latent (LTBI) or active, and *M. tuberculosis* can be in a dormant state or active. The

dormancy state is harder to define and refers to a hypothetical cell state. There is no commonly adopted definition for dormancy, but a recent definition has already been described above (Lipworth et al., 2016). Dormancy is a reversible cell state (Lipworth *et al.*, 2016). This notion is important to differentiate between a viable but non-culturable cell and a dead cell. Another term commonly used in TB research is persisters which refers to cells that have survived an antibiotic challenge. **Fig. 1.3** presents the differences between the terms latency, dormancy and persistence. Persister bacteria can be dormant, or not, and bacteria involved in LTBI can be dormant or not.

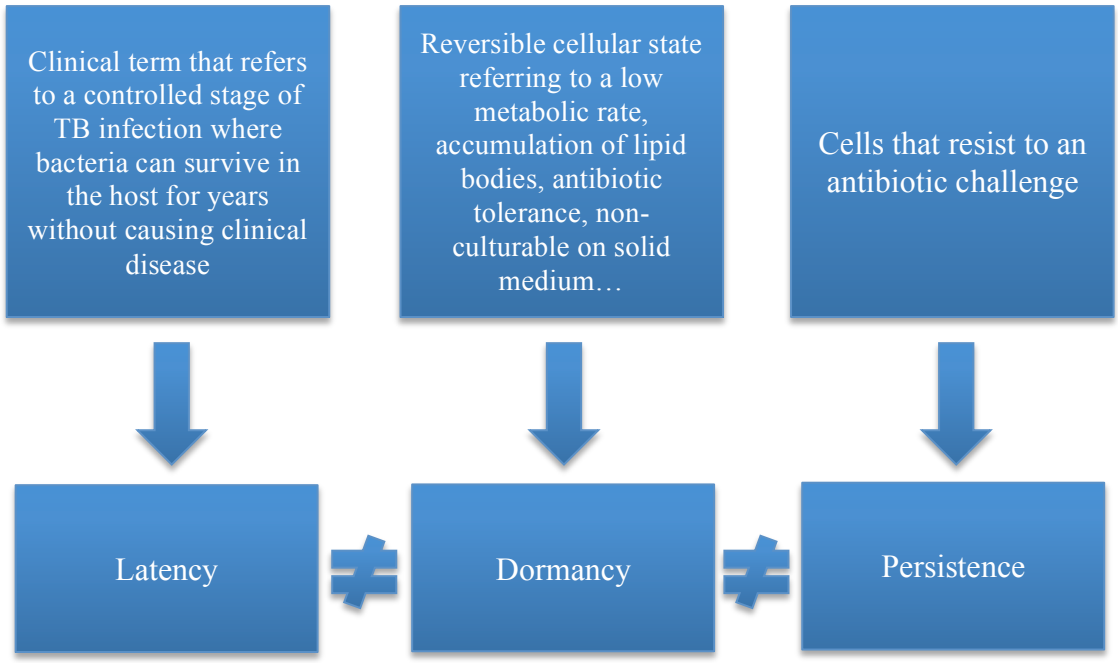

Figure 1.3 *proposed definition for the terms latency, dormancy and persistence in a TB research context.*

1.4.4 *M. tuberculosis in-vitro* dormancy models

In 1933, Loebel and colleagues observed that carbon starvation induces an important metabolic downshift in *M. tuberculosis,* and that respiration can be restored when the carbon source is reintroduced (Loebel *et al.*, 1933). The authors in this study however did not use the term dormancy. Since Loebel's work, many *in-vitro* dormancy models have been developed to try to understand this phenomenon. To generate dormant bacteria, different culture conditions to induce stress have been tested including oxygen depletion, nutrient poor medium, the presence of antibiotics, high acidity, and multiple stress models (Lipworth *et al.*, 2016). Examples of the published dormancy models have been reviewed and are listed in the **Table 1.2.**

Table 1.2 Examples of Dormancy models

Dormancy model	Description	Reference
Oxygen reduction	Long term culture in liquid medium with controlled oxygen depletion	(Wayne and Hayes, 1996)
Starvation	Bacteria starved in PBS	(Betts *et al.*, 2002)
Acidification	pH reduction down to 4.7	(Shleeva *et al.*, 2011)
Multiple stress	Culture condition: low oxygen (5%), high CO_2 (10%), nutrient poor (10% Dubos medium) and acidic (pH 5).	(Deb *et al.*, 2009)

Several models use oxygen depletion to generate dormant population (Wayne and Hayes, 1996, Dick *et al.*, 1998, Lim *et al.*, 1999). In the Wayne model, *M. tuberculosis* is cultured in liquid with low agitation, and the oxygen is depleted at a controlled rate (Wayne and Hayes, 1996). Two non-replicating persistence (NRP) stages have been described: NRP1 and NRP2. NRP1 is a microaerophilic stage and displays a high production of glycine dehydrogenase. NRP2 is an anaerobic stage, during this stage the concentration of glycine dehydrogenase decreases significantly. The authors suggest that the ability of the bacillus to survive anaerobic conditions correlates to the time it spends in a transitional stage (NRP1) (Wayne and Hayes, 1996). Previously Wayne *et al.* showed that a rapid transfer from aerobic to anaerobic culture led to cell death. However, if the oxygen depletion is gradual, the tolerance to the anaerobic conditions is higher (Wayne and Lin, 1982). To respond to hypoxia, bacteria adapt their metabolism. A shift to the glyoxylate cycle has been described in dormant cells with an increased activity of ICL and glycine dehydrogenase (Wayne and Lin, 1982). The DosR regulon is highly induced while the microorganisms are transiting to an anaerobic state (Voskuil *et al.*, 2004b).

In 1933, Loebel first observed that carbon starvation induces a significant metabolic downshift in *M. tuberculosis* (Loebel *et al.*, 1933). More recently, using the starvation model, it has been shown that *M. tuberculosis* stop their growth, have reduced respiration rate and show resistance to several drugs (rifampicin, isoniazid and metronidazole) (Betts *et al.*, 2002). To adapt to starvation, the level of expression of many genes changes. Several genes involved in surviving in the host for an extended period of time are induced while lipid biosynthesis, cell division, transcription and energy metabolism are reduced (Betts *et al.*, 2002). For starved bacilli, ICL and the

glyoxylate shunt are central to surviving in a nutrient poor environment (Gengenbacher *et al.*, 2010).

In low pH medium, *M. tuberculosis* becomes ovoid showing a thickened cell wall. These cells are resistant to heat and antibiotics. Moreover, they do not grow on solid medium, whereas the addition of Rpfs are required for successful resuscitation (Shleeva *et al.*, 2011).

The Multiple stress model has been designed to be more representative of the conditions that *M. tuberculosis* encounter *in-vivo*. Deb and colleagues designed a multiple stress model as the following: low oxygen (5%), high CO_2 (10%), nutrient poor (10% Dubos medium) and high acidity (pH 5). In this model, genes involved in the glyoxylate cycle were found to be up-regulated, bacteria stored non-polar lipids, cells were more resistant to rifampicin and isoniazid, and their buoyant density was decreased as the culture aged (Deb *et al.*, 2009).

1.4.5 *M. tuberculosis* dormancy model and drug testing

The most clinically relevant aspect of dormancy in *M. tuberculosis* and mycobacteria is their phenotypic resistance to antibiotics. **Tab. 1.3** presents examples of drug sensitivity testing on dormant cells. Many susceptibility tests have been performed in different dormancy models (MIC, MBC, % of cell survival after various drug exposure times, Alamar blue reduction…). Substantial differences have been observed regarding drug concentration for one species in different models. Looking at rifampicin in *M. tuberculosis,* in the *in-vitro* granuloma model, the MIC was found to be over $0.47\mu g.mL^{-1}$ and up to $0.94\mu g.mL^{-1}$; in the Wayne model, using rifampicin at $0.1\mu g.mL^{-1}$, 4.2% of cells survived after 192 hours (Ackart *et al.*, 2014, Wayne and

Hayes, 1996). Direct comparison between "dormancy" models and susceptibility tests is therefore difficult.

Table 1.3 Dormancy models and associated drug susceptibility.
Table modified from (Lipworth *et al.*, 2016).

Dormancy model	Methodology	Susceptibilities:				
		isoniazid	Rifampicin	Pyrazinamide	Ciprofolxacin	Metronidozole
Oxygen shift down (Wayne model) (Wayne and Hayes, 1996)	*M. tuberculosis* cell survival, CFU count	0.4 $\mu g.mL^{-1}$	0.1 $\mu g.mL^{-1}$		1 $\mu g.mL^{-1}$	12 $\mu g.mL^{-1}$ in NRP2
Oxygen depletion (BCG) (Lim *et al.*, 1999)	BCG, CFU count					BCG viable count are reduced a 1000 fold at 100$\mu g.mL^{-1}$ and 3 fold at 10 $\mu g.mL^{-1}$
Oxygen depletion (*M. smegmatis*) (Dick *et al.*, 1998)	*M. smegmatis*, percentage of survival. CFU count 24h after drug exposure					120 $\mu g.mL^{-1}$ 20± 10 percent survival for persistent culture (old culture) and 95±9 percent survival for active culture (log aerobic culture)

Long term anaerobic cultures (Filippini *et al.*, 2010)	7, 14, 21 days exposure to drugs. CFU and MGIT (negative: no growth after 100 days)		8 μg.mL^{-1}	100 μg.mL^{-1}		8 μg.mL^{-1}
Nutrient starvation (Betts *et al.*, 2002)	Cell survival after 168h of drug exposure. CFU count	10 μg.mL^{-1}	10 μg.mL^{-1}			
Multiple stress model (Deb *et al.*, 2009)	Cell survival after ≥ 96h of drug exposure. CFU count	0.8 μg.mL^{-1}	5 μg.mL^{-1}			12 μg.mL^{-1}
Human granuloma *in-vitro* model (Kapoor *et al.*, 2013, Ackart *et al.*, 2014)	*M. tuberculosis* MIC calculated using Alamar blue	MIC: 1.25–2.5 μg.mL^{-1}	MIC: 0.47–0.94 μg.mL^{-1}			

1.4.6 Dormancy theories in TB

Different theories have been proposed to explain dormancy including the Ying/Yang theory, spectrum theory and scout theory.

1.4.6.1 Yin/Yang theory

The "Yin-Yang" model describes a mixed bacterial population with growing (Yang) and non-growing (Yin) cells that are in several states and present in a continuum. During exponential and early stationary phases, there are more growing "Yang" bacteria with fewer non-growing "Yin" cells. This changes when the culture enters into a stationary phase where more non-growing bacteria appears, and the number of growing cells (Yin) decreases. The authors of this model describe the cells as a heterogeneous population, appearing as of a continuum of subpopulations exhibiting differential gene expression. The authors used this model to explain why *M. tuberculosis* after two months of intensive treatment with the four drugs (isoniazid (INH), rifampin (RIF), pyrazinamide (PZA), and ethambutol (EMB) can convert to an active form, sensitive to INH and RIF. The authors also used this model to demonstrate why isoniazid would be effective in the treatment of latent disease (Zhang *et al.*, 2012).

1.4.6.2 Spectrum theory

A theory exposed in 2002 by Shleeva and colleagues proposes a spectrum of dormancy where bacteria can be found active, in a transitional phase or dormant

(Shleeva *et al.*, 2002) (**Fig. 1.4**). The transition from actively growing to dormancy occurs through a transition phase. The more a culture ages, the less metabolically active it becomes. This model suggests that dormancy is a reversible state; bacteria can be re-grown or be resuscitated to the active state. “Wayne’s” zone refers to transition step to deep dormancy (presence of non-culturable cells). Bacteria in “Wayne’s” zone remain viable and metabolically active and those cells can be re-grown. “Cornell’s zone” corresponds to deep dormancy where cells are described as non-culturable and unable to form colonies. This state precedes cell death. These bacteria have to be resuscitated before becoming active again.

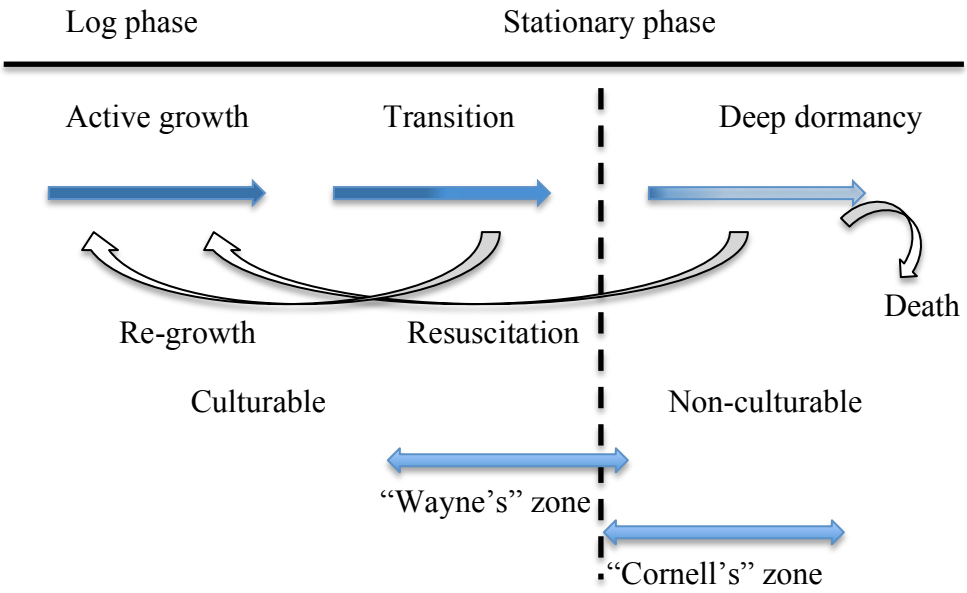

Figure 1.4 *M. tuberculosis dormancy spectrum theory.*
The metabolic activity of the cells is represented by the coloured intensity of the arrows (in blue); reducing as bacteria enter dormancy. Bacteria become dormant through a transition phase ("Wayne's zone") in which cells are still culturable; entering deep dormancy where bacteria become non-culturable ("Cornell's zone"). Dormancy is reversible, and bacteria can be re-grown or resuscitated to an active state. Figure modified from (Shleeva et al., 2002).

1.4.6.3 The scout theory

One of the proposed theories to explain resuscitation from dormancy is the "scout" theory. In this theory, a few of the *M. tuberculosis* dormant cells randomly awaken. These cells are termed the 'scouts'. These cells assess their environmental conditions and if suitable for growth they start replicating. The replicating scout cells potentially send activation signals to the dormant bacteria awakening them (Epstein, 2009, Chao and Rubin, 2010). In the opposite case if conditions are unsuitable for growth, the scout cells die, leaving the rest of the cells dormant and alive. When scouts successfully replicate and survive antibiotic treatment and the immune system, they may induce relapse (Lipworth *et al.*, 2016, Epstein, 2009).

1.4.7 Mycobacterial lipids

In 2011, Sartain *et al,* studied *M. tuberculosis* lipids using a liquid chromatography and mass-spectrometry (LC/MS) approach (Sartain *et al.*, 2011). The authors designed a lipid dataset containing about 2,500 lipid entities. The lipid profile of *M. tuberculosis* was found to be highly complex. Lipids in *M. tuberculosis* can represent up to 60% of the cellular dry weight with many lipids present *M. tuberculosis* being specific to this species or to its genus (Sartain *et al.*, 2011). The authors compared the changes in the lipid composition that occur as *M. tuberculosis* cultures age. Important differences in the abundance of TAGs and fatty acyl composition were observed. TAGs represented 35.8% of the detected molecules in logarithmic phase cultures, while they represented 77.3% in stationary phase cultures. It was shown that the concentration of TAGs and the mass of TAGs increase in stationary phase cultures

compared to logarithmic phase cultures (Sartain *et al.*, 2011). For example, TAGs, in logarithmic phase cultures, were found to be mainly esterified by C16:1 and C18:1 fatty acids (with one unsaturated bond). In stationary phase cultures, C16:0, C18:0 and C26:0 (no unsaturation) fatty acids were predominantly observed to be esterified to TAGs. In stationary phase cultures as compared to logarithmic phase cultures, there was an increase in saturated bonds in other lipid groups such as phospholipids, phosphatidylethanolamine, phosphatidylinositol and cardiolipin (Sartain *et al.*, 2011).

1.4.7.1 Mycobacterial cell envelope

Mycobacteria display a specific and very complex cellular envelope (**Fig. 1.5**). The cell wall of mycobacteria presents a thin layer of peptidoglycan surrounded by a layer of arabinoglycan and a thick layer of mycolic acids. Intercalating with the distal end of the mycolate chains are a range of complex lipids of varying polarities, to form a mycobacterial outer membrane. These complex lipids include non-polar waxes phthiocerol dimycocerosates (PDIMs) and polar glycolipids such as acyl trehaloses and sulpholipid. In addition, very long lipoarabinomannan (LAM) molecules that are anchored in the cytoplasmic membrane traverse the cell wall. Porins are found in the mycobacterial outer membrane and allow the passage of hydrophilic molecules. The cell envelope of mycobacteria is very rich in lipid content (Rajni *et al.*, 2011, Brown *et al.*, 2015, Jackson, 2014). Growth conditions can impact *M. tuberculosis* cell wall. *M. tuberculosis* cultured microaerobically and anaerobically present thickened cell wall outer layer (Cunningham and Spreadbury, 1998). In *M. tuberculosis,* there is an increased synthesis of PDIM when the bacteria are grown on odd-chain fatty acids and also during infection (Jain *et al.*, 2007).

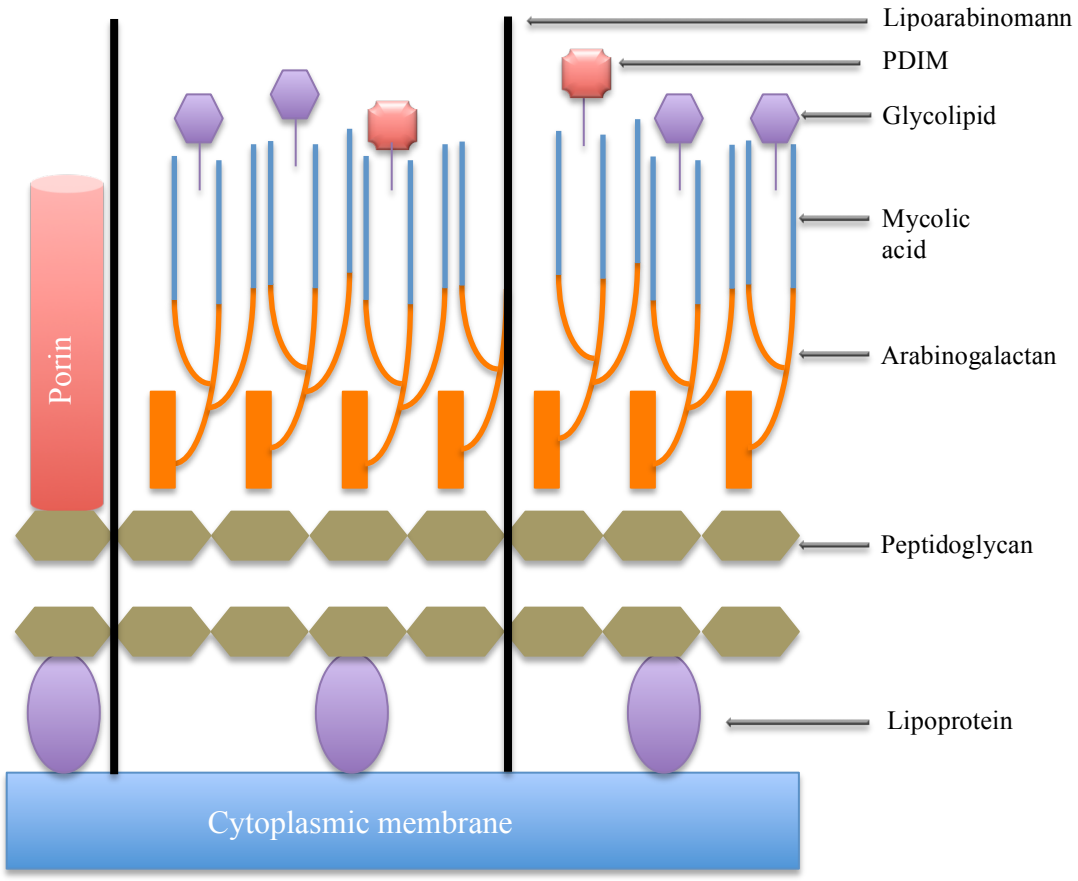

Figure 1.5 *Cellular envelope of mycobacterium species.*
A thin layer of peptidoglycan covers the cytoplasmic membrane followed by a layer of arabinoglycan and a thick layer of mycolic acids. In the cell wall several other molecules or structures can be observed such as lipoproteins, glycolipids, PDIMs very long LAM molecules and porins.

1.4.7.2 The lipid bodies in mycobacteria

Dormancy is associated with intracellular storage of lipids (lipid rich (LR) bacteria). The accumulation of intracellular lipids could be useful for the identification of dormant mycobacteria, which can then be detected by different technologies such as fluorescence microscopy. In *M. tuberculosis* and *M. smegmatis,* lipid bodies can be observed in cells (Garton *et al.*, 2002). Dormant cells from hypoxic or nutrient starvation models show a decrease in intracellular ATP levels (Rao *et al.*, 2008, Gengenbacher *et al.*, 2010). ICL knockout mycobacteria grown in nutrient poor conditions cannot reduce their ATP level and die as a result. As mentioned in **Chapter 1 Introduction section 1.3.3** above, the ICL enzyme is involved in the glyoxylate shunt which avoids CO_2 losses that would occur during the complete tricarboxylic cycle. This enzyme is essential for *M. tuberculosis* in a nutrient poor environment (Gengenbacher *et al.*, 2010). In low oxygen conditions, a shift to the glyoxylate shunt has been described in dormant cells with increased activity of ICL (Wayne and Lin, 1982). There is a global up-regulation of mycobacterial lipid metabolism genes in a low oxygen environment. This up-regulation leads to an accumulation of lipids, stored in intracellular bodies (lipid bodies) (Gengenbacher and Kaufmann, 2012). The presence of lipid bodies would be interesting to identify dormant cells.

In 1946, Burdon studied lipid bodies in several bacteria including mycobacteria. Bacteria were stained using Sudan Black and lipid bodies as “distinct fat droplets” were described. The droplets were present in many mycobacteria but not all (see **Fig. 1.6**) (Burdon, 1946a, Burdon, 1946b).

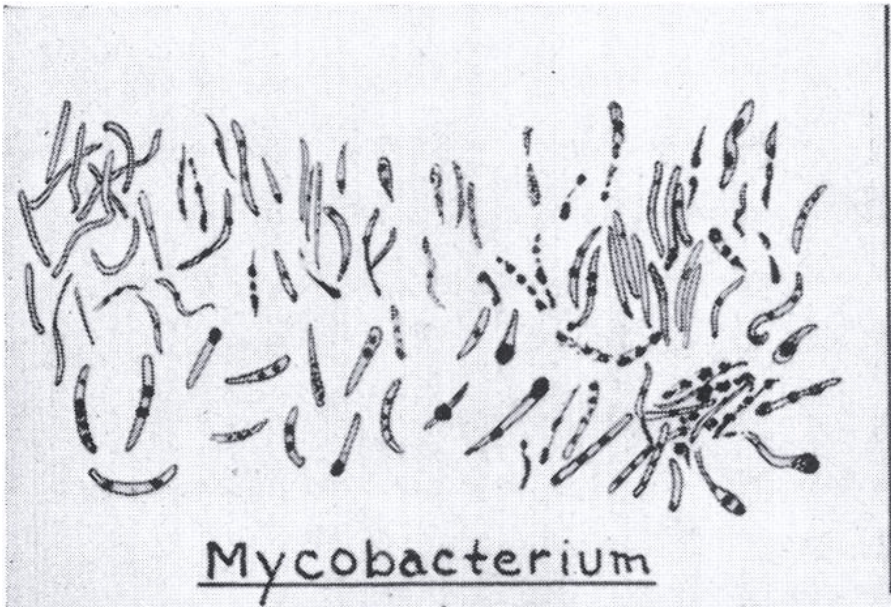

Figure 1.6 *Lipid inclusions in mycobacteria.*
This figure shows the drawing of Sudan Black stained mycobacteria. Some mycobacteria do not have any lipid droplets, while others contain one or more lipid droplets. Importantly, the size of the lipid inclusions varies from small to very large. Drawing modified from (Burdon, 1946b).

Other bacteria outside the *Mycobacterium* genus also have the capacity to store lipids in intracellular inclusions (Burdon, 1946b, Waltermann and Steinbüchel, 2005, Wang and Bakken, 1998). For example in *Rhodococcus opacus,* it was shown that PD630 fatty acids represent up to 87% of the dry weight of the bacterium (Alvarez and Steinbüchel, 2002).

More recently, in 2002 Garton and colleagues demonstrated that lipid bodies in mycobacteria could be formed using fatty acids or a simple carbon source. The authors used staining methods and microscopy to study lipid inclusions, and investigated their composition. TAGs were found to be the major component of the lipid bodies (Garton *et al.*, 2002). Using an in-vitro multiple stress model, it was shown that phenotypic antibiotic tolerance and accumulation of TAGs were highly correlated (Deb *et al.*, 2009). The mycobacterial protein perilipin-1 (MPER1), up-regulated in dormant cells, has been found to play a crucial role in the formation of lipid inclusions (containing TAGs) in *M. tuberculosis*. The *M. tuberculosis mper1* knockout strain presents a lower accumulation of lipid bodies and also a reduction in rifampicin tolerance in *in-vitro* dormancy models (Daniel *et al.*, 2016). Mycobacteria with lipid bodies can be defined as lipid rich (LR) cells as opposed to lipid poor (LP) bacteria that do not present any intracellular lipid bodies. LR mycobacteria display higher tolerance to antibiotics used in TB treatment; for example, *M.smegmatis* LR bacteria were found up to 40 times more tolerant to Rifampicin in comparison to LP bacteria (Hammond *et al.*, 2015).

Bacilli containing lipid bodies have been found to be dominant in sputum treated patients (Garton *et al.*, 2008). This could mean that the transmissible phenotypes could be lipid body positive and possibly slow-growing or dormant. This group also showed that an increase in lipid body count in *M. tuberculosis* in sputum correlated

with an increase in time to positivity of the cognate *M. tuberculosis* isolate in BACTEC system. Moreover, when they analysed the sputum transcriptome using microarray, they found a strong correlation of transcriptional signatures with slow growing mycobacteria, finding an upregulation of the DosR regulon and a downregulation of genes linked with aerobic metabolism. Ribosomal protein genes were also downregulated, which suggests that growth is reduced within this population (Garton *et al.*, 2008). This work led to a new vision for the role of dormancy in TB, revealing that lipid body positive cells can predominate in sputum of treated patients. More recently, Sloan and colleagues showed that only few patients with unfavourable outcomes were infected with bacteria with resistance-associated mutations. Moreover, in patients that had an unfavourable outcome, the authors observed a higher percentage of lipid body positive *M. tuberculosis* cells in sputum at around three and four weeks of treatment. These findings support the hypothesis that dormant bacteria are the leading cause of relapse (Sloan *et al.*, 2015).

1.5 Introduction to Raman spectroscopy

1.5.1 History of Raman spectroscopy

The inelastic scattering of light has been first suggested by Smekal in 1923 (Smekal, 1923). Five years later Sir Raman observed for the first time the phenomenon hypothesised a few years earlier by Smekal (Raman and Krishnan, 1928). In 1928 Sir Raman used sunlight as a source focused on a sample by a telescope and observed the output with his eyes. He succeeded to show the presence of light scattering with a different frequency compared to the original light; this is the principle of Raman spectroscopy. To demonstrate this, the authors used two light filters: a blue/violet one

and a yellow/green one, while examining light scattering through a liquid medium. When the two filters were placed in series in the incident light, no light would enter the observer's eyes. However, when the yellow/green filter was placed between the liquid and the experimentalist's eye, light could be observed. This proved the existence of light scattering presenting a different frequency compared to the incident light.

1.5.2 Raman spectroscopy principle

When photons reach a sample, they can go through without any interaction, or they can scattered, or be absorbed. The light scattering can be elastic or inelastic. Elastic scattering occurs when photons only interact with electrons of the molecule, the frequency of the photon is nearly unmodified and there is no shift in the energy level. This scattering event is the dominant process and is referred to as Rayleigh scattering. The inelastic scattering occurs when the photons interact with the nuclei of the molecule. In this case, there is a transfer of energy to the molecule from the photon or vice versa. The energy of the scattered photons is different compared to their initial energy level (incident photons). Those photons are Raman photons. The inelastic scattering is a rare event and only occurs in one photon every 10^6-10^8 photons. Raman spectroscopy is a technique using the inelastic scattering of monochromatic light, generated by a laser. Lasers are used in Raman spectroscopy as they produce intense monochromatic beam. This is necessary to improve the yield of the rare Raman photons. The frequencies of photons in monochromatic light can change after entering into contact with a sample in case of an inelastic scattering. In this case, photons are absorbed by the sample and re-emitted with a shifted frequency that could be shifted

up or down compared with original monochromatic frequency. This shift is measured and gives information about vibrational, rotational and other low-frequency transitions in molecules.

When photons interact with the sample they can scatter in several ways (**Fig. 1.7**) Rayleigh scattering is how most photons scatter. Scattered photons have the same energy as the incident photons and is referred to as elastic scattering. Raman scattering occurs when the energy level of the scattered photon changes compared to the incident photon, this is inelastic scattering. Examples of which include:

- Stokes scattering corresponds to a photon that excites a chemical bond that was in a non-excited state. During Stokes scattering, the photon will lose some energy that is absorbed by the atoms of the molecule.
- Alternatively, Anti-Stokes scattering corresponds to a gain of energy by the scattered photon. In this case, the atoms of a molecule are already in a vibrational state, and some energy is transferred from the molecule to the photon.

There is more Stokes scattering compared to Anti-Stokes scattering under normal conditions because at room temperature molecules are predominantly in the lowest vibrational energy level. With an increase in temperature anti-stokes events increase (Smith and Dent, 2005).

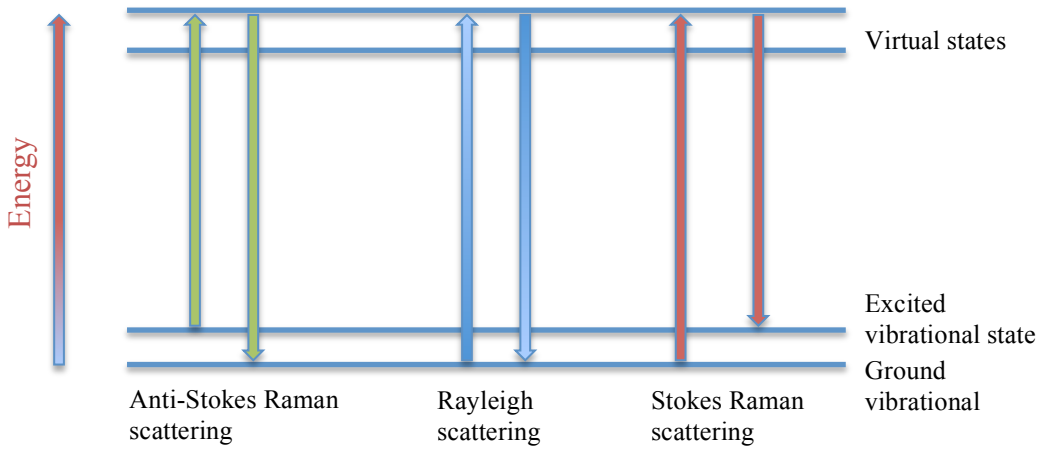

Figure 1.7 *Rayleigh and Raman scattering.*

Raman photons can either show a Stokes or an anti-Stokes scattering. Anti-Stokes scattering corresponds to a gain of energy by the scattered photon compared to the incident photon. To the contrary, Stokes scattering is the result of energy loss by the scattered photon. Rayleigh scattering corresponds to elastic scattering (no changes in the energy level between the incident photon and the scattered photon). In the figure, each type of scattering presents an arrow going up or coming back down corresponding to changes in the energy level of the scattered photon. The arrow can depart from either an excited vibrational state or a ground vibrational state. In the case of the anti-Stokes Raman scattering the arrow departs from an excited vibrational state and the scattered photons comes back to a ground vibrational state (with higher energy). The opposite is observed for the Stokes Raman scattering. And identical energy levels, between the incident photons and the emitted photons, are found in the case of Rayleigh scattering.

In Raman spectroscopy, mainly Stokes Raman scattering is used. The shift in energy level is measured by subtracting the energy of the scattered photon from the initial photon. This is the reason why Raman scattering is expressed in energy shift delta cm^{-1} or simply cm^{-1} (wavenumber, number of wave per unit of length). The wavenumber is directly related to the wavelength, the frequency and the energy of the photon. Knowing one of these parameters and using Planck's constant and the speed of light, it is easy to calculate any of the other related parameters (wavenumber, wavelength, frequency and the energy of the photon). The corresponding equations are shown below:

$$E = \frac{hc}{\lambda}$$

$$\lambda = \frac{1}{\tilde{\nu}} = \frac{c}{v}$$

Where:

h is the Planck's constant $h = 6.626 \times 10^{-34}$ *J.s (unit is Joules × seconds)*

c is the speed of light $c=3 \times 10^{8}$ $m.s^{-1}$

E is the energy in Joules

λ is the wavelengths in nm

v is the frequency in s^{-1}

$\tilde{\nu}$ *is wavenumber in* cm^{-1}

When the wavenumber is calculated from the wavelength, the wavelength needs to be in cm (10^{7} *nm).*

$$\tilde{\nu} = \frac{1}{\tilde{\lambda}} = \frac{1}{785 \times 10^{-7}} = 12738.9 cm^{-1}$$

1.5.3 Vibrational modes

There are three molecular vibration modes in Raman spectroscopy: symmetric stretch, bend and asymmetrical stretch. In **Fig. 1.8,** water (H_2O) is shown in the three different vibrational modes. A Raman spectrum corresponds to all the vibrations that occur in the sample studied; one peak corresponds to one vibration of one specific bond, and gives a unique feature for each molecule. By extension, the Raman spectrum corresponds to all the energies (frequencies) of scattered light plotted on the x-axis and the corresponding intensities are plotted on the y-axis (see **Fig. 1.10**).

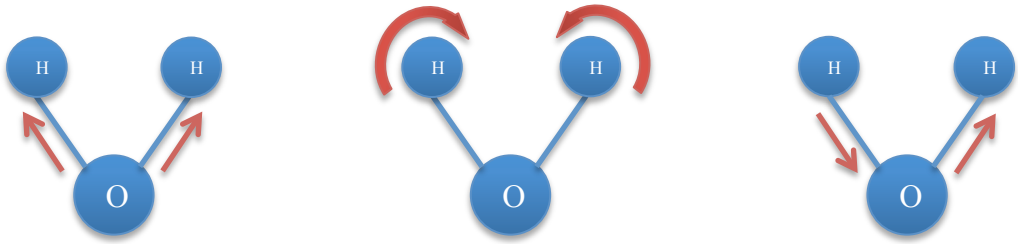

Symmetrical stretch | Bend | Asymmetrical stretch

Figure 1.8 *Vibrational modes of water.*
Any molecule can vibrate in different modes. The figure illustrates the different vibrational modes of water: symmetrical, bend and asymmetrical. The arrows indicate the movement of the atoms at one moment. To be called a vibration, this movement needs to be repeated several times. In the case of a symmetrical stretch of H_2O the two bonds are elongated then compressed at the same time. In the case of an asymmetrical stretch, one bond is compressed while the other is elongated, and vice versa. In the case of H_2O bending vibration mode, the two atoms of hydrogen are coming closer to each other and then they separate while the length of the bonds between the atoms hydrogen and the atom of oxygen do not change.

1.5.4 Raman spectroscopy methodologies

Raman scattering is a very weak process since only a small percentage of incident photons are scattered inelastically. The Raman spectra of biological samples exhibit high fluorescence background commonly due to the presence of fluorophore molecules in biological samples. There are several possible methods to reduce this fluorescence, for example, choosing the laser wavelength in the ultraviolet (UV) or infrared (IR) regions (Sengupta *et al.*, 2007). However, the UV laser generates high energy which could damage the biological samples.

1.5.4.1 Conventional Raman spectroscopy

Conventional Raman spectroscopy has been used in this study. For this type of Raman spectroscopy, first the background signal is taken (near the bacterium) then the reference signal is acquired (on the bacterium). This permits us to subtract the background mathematically. However, the auto-fluorescence coming from the biological sample (the bacterium) is not subtracted, as it is only coming from the cell. This technique can be used when the background is homogeneous, as it assumes that the background near the cell is the same as the background at the location of the cell.

1.5.4.2 Wavelength modulated Raman spectroscopy

In wavelength modulation Raman (WMR) spectroscopy, the laser wavelength is tuned during the acquisition and the Raman peaks are shifted according to the laser wavelength, while the fluorescence background is not. Several original spectra, at

different laser wavelengths, are taken during the acquisition time. This makes it possible to subtract the fluorescence background mathematically. The optimal processing algorithm to generate WMR spectra was shown to be Principal component analysis (PCA) showing high signal to noise ratio and efficient background subtraction (De Luca *et al.*, 2010, Mazilu *et al.*, 2010, Chen *et al.*, 2015). In this study, we used continuous modulation meaning that the laser was tuned continuously at a constant rate during the acquisition time.

1.5.5 Raman spectroscopy and instrumentation

Raman spectroscopy systems are composed of four main components (see **Fig. 1.9**):

- The excitation source (the laser)
- The sample illumination and the optics to collect light
- The spectrometer (the wavelength selector)
- The detector

Different lasers can be used depending on the experiment with distinct wavelengths (UV, visible light or in the infrared). The laser wavelength will have a great impact on the results as the scattering depends directly on the laser wavelength. For example, a high-frequency laser (UV) will generate higher peak intensity and therefore increase the sensitivity of Raman spectroscopy. Working in the UV wavelength also has the advantage of low levels of fluorescence compared to lower frequencies. The biggest problem encountered when working in the UV wavelength is the high energy of the photon and radiation that can be absorbed by the samples. This can lead to sample degradation and also direct burning of the sample due to increased temperature. Using

an infrared laser will allow working with a higher laser power as the photon generated presents a lower frequency. This type of laser is much less damaging for the sample compared to the UV, but the peak intensity will be lower thus requiring longer acquisition time.

The incident light usually reaches the sample through a microscope objective. The difficulty is to remove as much Rayleigh scattering as possible as Raman scattering is a rare event. The use of filters such as notch filters will remove the light with a wavelength equal to the incident laser light ± 100 cm^{-1} but the use of those filters makes it impossible to study low-frequency Raman scattering events. Raman spectrometers usually use diffraction gratings for wavelength selection. In order to detect Raman scattered light, multi-channel detectors such as charged couple devices (CCD) are used. A basic schematic of a Raman spectroscopy system is shown in **Fig. 1.9.**

In this study, two Raman spectroscopy systems have been used. The first one is presented in **Chapter 2 General methods Fig. 2.5** was used to do both standard and WMR spectroscopy. The second system is shown in **Chapter 2 General methods Fig. 2.6** and is a very similar system for the Raman spectroscopy part, however, it was designed to additionally investigate fluorescence (therefore, combining Raman spectroscopy and fluorescence imaging).

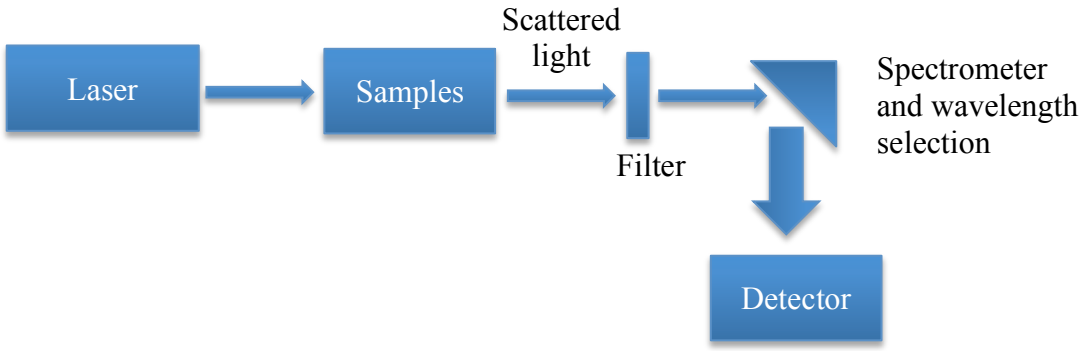

Figure 1.9 *Basic schematic of a possible Raman spectroscopy set up.*

The system is composed of a light source (laser), different optics (lenses and fibres), a sample holder, filters (to remove a maximum of Rayleigh light), a spectrometer or wavelength selector and a detector. Any system also requires the use of a computer to display and analyse the data. The arrows represent the light propagation.

1.5.6 Principal component analysis

Principal Component Analysis (PCA) is a multivariate statistical analysis used in this thesis to compare the different datasets generated by Raman spectroscopy.

PCA was also the method chosen to generate WMR spectra from the original spectra (acquired at different laser wavelengths). PCA was shown to be the optimal algorithm to generate WMR spectra presenting high signal to noise ratio and good subtraction of the fluorescence background (Mazilu *et al.*, 2010).

PCA is used to study data allowing many more parameters per sample than sample number (data with high dimensionality). This mathematical process is used to reduce the dimensionality of the dataset and retain most of the variance. The PCA determines new variables called principal components (PCs) that are linear and extracted from the previous variables; in simple terms, it corresponds to a direction. Using only several PCs, the complex dataset can be expressed by a few numbers. The first PCs correspond to the direction in which most of the variation is observed in the dataset. The second PCs are not correlated to the first one, but instead corresponds to the direction in which most of the variation is observed in the dataset after the first PCs (Ringner, 2008). The PCA determines the direction or PCs that show the highest variation in the dataset. All PCs are orthogonal to each other and listed in a decreasing order accounting for the variability in the dataset.

1.5.7 Calculation of sensitivity and specificity

To estimate the difference between two datasets the 'leave one out cross validation' (LOOCV) technique can be applied. The PCA creates a multi-dimensional space

using the datasets where one Raman spectrum is then taken out (the 'left out' spectrum), and all the other spectra from the datasets are used as training sets. The 'left out' spectrum is then placed in the multi-dimensional space and classified to either datasets. The classification is realised using the nearest neighbour algorithm. This process is then repeated for each spectrum from both datasets. Ultimately the user obtains a correct or an incorrect prediction of each spectrum, which permits the user to draw a confusion matrix and calculate the sensitivity and the specificity.

1.5.8 Raman spectroscopy in biological features

Cellular compounds and molecules (DNA, RNA, proteins, lipids, sugars) give a distinct Raman spectrum (De Gelder *et al.*, 2007a). Once the Raman spectrum is obtained, it is crucial to be able to assign the observed peaks correctly as there is a high need of database recording information about biological features. In 2007 Movasaghi and colleagues attempted to collect the assigned peaks already existing in the literature and group them in one review. This work represents a database where most of the biological features are included (Movasaghi *et al.*, 2007).

1.5.8.1 Nucleic acids

Nitrogenous bases are the components of nucleotides and nucleic acids. There are five nitrogenous bases: adenine (A), cytosine (C), guanine (G), thymine (T) and uracil (U). In DNA there is no uracil and in RNA thymine is replaced by uracil. Nitrogenous bases are complex structures composed of carbon, oxygen, hydrogen and nitrogen with single and double bonds. All of the different atoms and bonds will result in a specific Raman spectrum. Using Raman spectroscopy, it is possible to differentiate

DNA and RNA bases (De Gelder *et al.*, 2007a). In Raman spectra of nucleic acids, most Raman peaks are located between 400 and 1800 cm^{-1}. Raman peaks in DNA spectra are mainly originate from the bases. For example, the peaks located at 666, 729, 783, 1243, 1335, 1372, 1484 and 1577 cm^{-1} are related to the bases (A, T, C, G). The peak around 1060 cm^{-1} comes from the carbon-oxygen single bond vibration, at 1100 cm^{-1} it is the phosphodioxy groups (PO_2^-). The peaks around 1460 cm^{-1} are linked to CH_2 deformation, and the peak at 1664 cm^{-1} comes from C=O bond that occurs in T and G bases (Gorelik *et al.*, 2014).

1.5.8.2 Amino acids and proteins

Proteins are composed of one or several chains of amino acids. Different amino acids present distinct Raman spectra (Candeloro *et al.*, 2013). Many Raman peaks between 600 cm^{-1} and 1700 cm^{-1} correspond to the different amino acids. The most intense peak can be observed around 1450 cm^{-1} and represents the CH bond deformation. This peak becomes more intense in the Raman spectrum of proteins as the number of CH bonds increases with the number of amino acids. Around 1655 cm^{-1}, the amide I band (polypeptide backbone) can be found, which is mainly due to the C=O stretching. The amide III band, located between 1240-1280 cm^{-1}, also corresponds to the polypeptide backbone and comes from N–H bending and C–N stretching (Tuma, 2005).

1.5.8.3 Saccharides

Raman spectra of saccharides and polysaccharides show peaks related to CCH, COH and OCH deformation between 800 and 950 cm^{-1}. From 1000 to 1200 cm^{-1} the bands

observed correspond to C–C and C–O stretches; CH_2 and CH_2OH deformations are located between 1250 and 1500 cm^{-1} (De Gelder *et al.*, 2007a).

1.5.8.4 Lipids

Lipids and especially intracellular lipid inclusions could represent a possible marker to identify dormant bacteria. Knowing where the main lipid peaks are present in the Raman spectrum is therefore crucial. In 2002, Garton and colleagues studied the composition of lipid bodies and found that they mainly contain TAGs (Garton *et al.*, 2002). The positions of the major peaks for lipids are at 1296 cm^{-1} assigned for CH_2 twisting vibration, 1050-1150 cm^{-1} attributed to C–C stretching vibration, and around 1450 cm^{-1} due to CH_2 or CH_3 deformations. Raman spectra of unsaturated fatty acids show an intense and sharp peak at 1655 cm^{-1} due to C=C stretching vibrations (De Gelder *et al.*, 2007a, Wu *et al.*, 2011).

1.5.9 Raman spectroscopy on bacteria

Raman spectra of individual molecules are helpful to understand the Raman spectrum of bacteria or other cells. The Raman spectrum of a whole bacterium is very complex as many different molecules compose the cell. To extract information about the chemistry of bacteria from its spectra, it is important to have access to a reliable reference database. Most biological information in a Raman spectrum are found between 400 and 4000 cm^{-1} (nucleic acids, proteins, polysaccharides, carbohydrate and lipids) (Movasaghi *et al.*, 2007). In a complex sample such as bacteria, a Raman peak can represent several molecules. For example, the intensity of the lipid peak

around 1450 cm^{-1} is due to all the lipids present in the bacteria. It is possible to assign peaks to a group of molecules such as lipid or nucleic acid for example. In some cases, it is reasonable to assign a Raman peak to one molecule, the phenylalanine for example around 1000 cm-1 (Movasaghi *et al.*, 2007). Huang and colleagues in 2004 interrogated single bacteria (*Pseudomonas putida* NCIMB 11764) using Raman spectroscopy. They characterised the different main Raman peaks, indicated the location of the lipids, the nucleic acids, proteins, and carbohydrates (see **Fig. 1.10**) (Huang *et al.*, 2004).

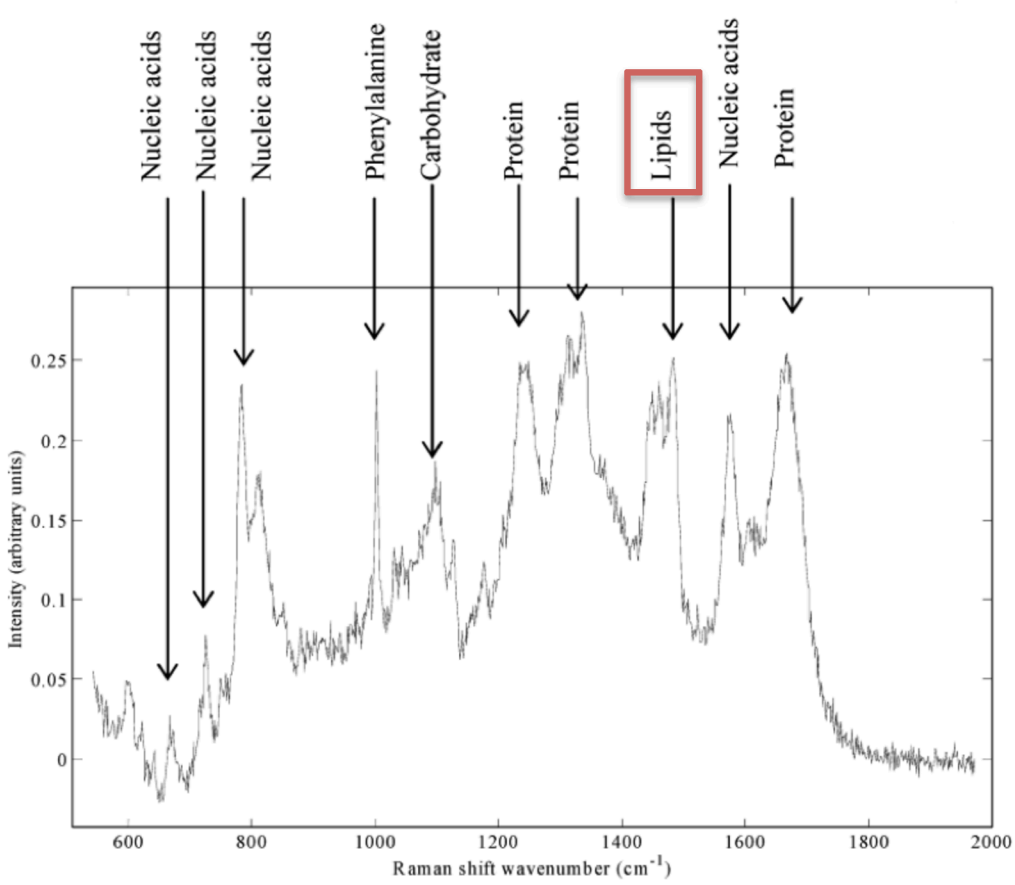

Figure 1.10 *Analysis of a single bacterium using Raman spectroscopy.*

The bacterium investigated in Huang et al., 2004 was: Pseudomonas putida NCIMB 11764. The figure shows the assignment of the major Raman peaks. The main lipid associated Raman band is present around 1450 cm^{-1}. In the Raman spectrum of a complex entity, such as a cell, information regarding specific molecules can only be obtained if there is a specific Raman peak for this molecule, such as phenylalanine (around 1000 cm^{-1}). Otherwise, the Raman spectrum provides information about large groups of molecules (lipids, proteins…etc) by giving their peak location and intensity. Figure modified from (Huang et al., 2004).

1.5.10 Table of assignment

The peak assignment is crucial for extracting information out of the Raman spectra and understanding the biological meaning of a spectral change. **Tab. 1.4** presents an overview of possible Raman peak assignment.

Table 1.4 Chemical bond assignment for Raman shifts.

Peak cm^{-1}	**Assign bond**	**Chemical association**	**Reference**
490		Glycogen	(Stone *et al.*, 2004)
666	Ring breathing G,T	Guanine, Thymine (DNA base)	(Movasaghi *et al.*, 2007, Chan *et al.*, 2006)
723-725	Ring breathing A	Adenine (DNA base)	(De Gelder *et al.*, 2007a, Movasaghi *et al.*, 2007)
780-790		DNA	(Gorelik *et al.*, 2014)
865	O—C—C—N	Phospholipid	(Wu *et al.*, 2011)
	C—C	Backbone	(Chan *et al.*, 2006)
930-935	C—C	Proline, valine protein backbone, glycogen	(Kendall *et al.*, 2011, Huang *et al.*, 2003)
1000-1005	C—C	Phenylalanine, proteins	(Kendall *et al.*, 2011, Huang *et al.*, 2003, Cheng *et al.*, 2005, Lakshmi *et al.*, 2002, Chan *et al.*, 2006)
1060-1100	C—C, COC, PO2-	Lipids, Carbohydrates, DNA/RNA	(De Gelder *et al.*, 2007b, Chiriboga *et al.*, 1998) (Gallier *et al.*, 2011, Silveira *et al.*, 2002) (Wu *et al.*, 2011, Gallier *et al.*, 2011)
1126	C—C and C—N	Lipids and proteins	(De Gelder *et al.*, 2007b, Cheng *et al.*, 2005, Lakshmi *et al.*, 2002, Chan *et al.*, 2006)
1245	Amide III	Protein (beta strand)	(Rusciano *et al.*, 2013)
1300	CH2 twist	Lipids	(Wu *et al.*, 2011, Huang *et al.*, 2003, De Gelder *et al.*, 2007b, Gallier *et al.*, 2011, Lakshmi *et al.*, 2002)
1440 to 1450	CH2, CH3 (bend)	Lipids, fatty acids, proteins	(Huang *et al.*, 2003, Wu *et al.*, 2011, Kendall *et al.*, 2011, De Gelder *et al.*, 2007b, Gallier *et al.*, 2011, Lakshmi *et al.*, 2002, Chan *et al.*, 2006)
1650-1660	C=C	Lipids	(De Gelder *et al.*, 2007b, Gallier *et al.*, 2011, Lakshmi *et al.*, 2002, Wu *et al.*, 2011)
1667	Amide I	Protein	(Rusciano *et al.*, 2013)
1740	C=O	Lipids	(Wu *et al.*, 2011)
2850-2930	C-H2, C-H3	Lipids, carbohydrate	(Wu *et al.*, 2011)
3020	=C-H	Lipid	(Wu *et al.*, 2011)

1.5.11 Raman spectroscopy studies on bacteria: a short review

In microbiology, Raman spectroscopy studies began to generate data in the 1980s, thanks to significant improvement in laser technology during the previous decade. In 1986 and 1987 Dalterio and colleagues demonstrated that Raman spectroscopy had the potential for microbiological identification as they succeeded in obtaining spectra of single bacteria (Dalterio *et al.*, 1986, Dalterio *et al.*, 1987). Since then, Raman spectroscopy has been widely used to study microorganisms in many fields including medicine and clinical applications, water quality, food quality… (Yang and Irudayaraj, 2003, Maquelin *et al.*, 2002b, Fan *et al.*, 2011, Nicolaou *et al.*, 2011). For many applications, being able to target a single bacteria and obtain information is crucial. Raman spectroscopy has the ability to target and identify bacteria at the single cell level (Huang *et al.*, 2004, Harz *et al.*, 2009, Schuster *et al.*, 2000).

In medicine, it is crucial to be able to identify the infectious agent causing a disease, where a fast diagnosis could lead to rapid and appropriate treatment. Many *in-vitro* studies using Raman spectroscopy have been carried out on medically relevant microorganisms (Ibelings *et al.*, 2005, Jarvis and Goodacre, 2004, Culha *et al.*, 2010, Buijtels *et al.*, 2008, Maquelin *et al.*, 2002a). For example, Raman spectroscopy has already been applied to mycobacteria for discrimination at a species level (Stockel *et al.*, 2016, Buijtels *et al.*, 2008). Using Raman spectroscopy it was shown that *M. smegmatis* presents an enhanced production of carotenoid when cultured on glucose compared to acetate or glycerol (Kumar *et al.*, 2015). In 2015, Stockel *et al.* showed that the Raman profile of *M.smegmatis* changes during the course of growth. In stationary phase cultures, *M. smegmatis* displays enhanced Raman lipid bands at 1081 cm^{-1}, 1305 cm^{-1}, 1446 cm^{-1} and 1748 cm^{-1} (Stockel *et al.*, 2015).

Samples obtained from TB patients and used for diagnosis and treatment management is usually sputum. Two studies investigating bacteria have been conducted using sputum samples (Rusciano *et al.*, 2013, Kloss *et al.*, 2015). Both studies showed that Raman spectroscopy could be applied to sputum samples, to identify bacteria.

The dormant phenotype in TB is associated with the presence of intracellular lipid bodies as opposed to active cells. Being able to identify both phenotypes could lead to substantial improvement in terms of understanding the disease and treatment management. Lipid content can be studied by Raman spectroscopy (van Manen *et al.*, 2005, Wu *et al.*, 2011). This technique requires minimal sample preparation, is non-destructive, label-free and can differentiate closely related single bacteria.

Thus, given the important role that dormant cells play in TB treatment, we sought to harness the discriminatory power of Raman spectroscopy to differentiate dormant (LR) from active (LP) mycobacterial cells.

1.6 Thesis aims

Dormancy in TB is a crucial area of research that could lead to a better understanding of the pathology of relapse which remains largely uncharacterised to date. Relapse is the major issue needing to be addressed to shorten TB treatment. The principal objective of this thesis project is to investigate the capacity of an all-optical, non-destructive technique, Raman spectroscopy, to differentiate dormant (LR) cells from active (LP) cells in *in-vitro* and *ex-vivo* samples. The presence (LR bacterium) or absence (LP bacterium) of intracellular lipid bodies could be used to define the two phenotypes. Up to now phenotypic discrimination has been achieved on sputum samples but never directly in TB infected lung tissue sections. This is highly

challenging, as other material could surround bacteria in tissue sections. Thus, the central aim of this thesis is to design a method and protocols using Raman spectroscopy (a non-destructive and label-free technique), to investigate and discriminate LR and LP cells, both in *in-vitro* and in *ex-vivo* samples (Chapter 4 and 5).

In Chapter 3 we will investigate lipid extracts of *M. tuberculosis* using Raman spectroscopy. The aim of this chapter is to understand the changes in lipid content that occur in *M. tuberculosis* as the population ages and between LR and LP populations (the LR proportion increases as cultures age). The objective of the chapter will include investigation of the ability of WMR spectroscopy to study lipid extraction from bacteria, and evaluation of the relationship between lipid concentration and Raman peak intensity.

In Chapter 6 we will investigate the growth dynamics of a mycobacterial population. This study will use *M. smegmatis* as a surrogate organism. The aim of this chapter is to understand the conversion from LR to LP cells when the environmental conditions are improving. Stationary phase and 24 hours old cultures will be investigated and their LR/LP proportion compared. If differences in phenotypic proportion are observed, further experiments will be conducted to try to understand the rate of conversion from LR to LP. Two methods will be used first: Nile red staining and Raman microscopy.

Chapter 2 General methods

2.1 Bacterial cultures

Three mycobacterial species were investigated in this work: *M. smegmatis* (NCTC 8159), *M. bovis* (BCG, NCTC 5692), *M. tuberculosis* (NCTC 7416; H37Rv). All mycobacteria were grown at 37°C in Middlebrook 7H9 medium (Sigma-Aldrich, UK), supplemented with two mL of glycerol (Sigma-Aldrich, UK) for 450 mL of media and with 0.05% (v/v) Tween80 (Fisher Scientific, Fisher BioReagents, UK, BP338-500). *M. bovis* and *M. tuberculosis* were grown in this medium with the addition 1 vial (50 mL; For 450 mL of medium) of Middlebrook ADC enrichment (Sigma-Aldrich, UK).

2.2 Glycerol stock

M. smegmatis and BCG bought from NCTC were cultured as described above. Then 500 µL of bacterial culture were mixed with 500 µL of 80% (v/v) glycerol solution (diluted with MiliQ water). The bacterial suspension was left at room temperature for half an hour in order to let the glycerol penetrate the cells. Then the stock tubes of *M. smegmatis* and BCG were stored at -80°C in 40% (v/v) glycerol. To start a new culture, the stock tube was taken and left to defrost at room temperature. Once defrosted, 10 µL of the bacterial suspension were plated on brain hart infusion (BHI; Oxoid, UK) agar. Then one colony was picked up, using a disposable plastic loop, to

start the new liquid culture. Every five to ten passages a new culture was started from the glycerol stock.

2.3 Deuterium separation

The bacteria were separated using a density based separation technique as described previously by Hammond et al in 2015 (Hammond *et al.*, 2015). This method was used to obtain over 90% pure fractions of LR cells and LP cells. To perform this separation, two mL of bacterial culture were heat inactivated at 80°C for 20 minutes (see **Chapter 2 General methods section 2.7** for more detail). *M. tuberculosis* has to be heat inactivated to be taken out the Cat 3 laboratory. The heat inactivation procedure does not induce a significant modification in the Raman spectra (Buijtels *et al.*, 2008). The bacteria were resuspended in a mixed solution of D_2O (Sigma-Aldrich, UK) and water at a known density. The density of pure D_2O is 1.107 $g.mL^{-1}$and the density of water is 1 $g.mL^{-1}$. The bacteria were separated over night, in a plastic cuvette covered with PARAFILM® M (Sigma-Aldrich, UK, P7793), in D_2O/H_2O solution at a known density (1.04 $g.mL^{-1}$). 100 microliters were removed from the top (LR) and the bottom (LP) of the D_2O/H_2O solution. The bacteria were spun down for three minutes at 20,000 x g and the supernatant slowly removed. The bacterial pellets were resuspended in 100 μL of PBS (Thermo Fisher Scientific, US). The two fractions were stained using Nile red (Sigma-Aldrich, UK, 19123)(see **Chapter 2 General methods Section 2.5** for more detail) and analysed by fluorescence microscopy (Leica DM5500; using an oil immersion objective x100). The fraction was used if the purity was greater than 90% (counted by eye).

2.4 Nile red stock

1 mg of Nile red (Sigma-Aldrich, UK) was weighed using a precise balance. The 1 mg of Nile red was dissolved in 4 mL of dimethyl-sulfoxide (DMSO; Sigma-Aldrich, UK) to create a 0.25 $mg.mL^{-1}$ stock solution. This solution was kept in a sealed glass vial covered with aluminium foil and tape and stored in the dark at 4°C.

2.5 Nile red staining of bacteria

From the Nile red (Sigma-Aldrich, UK) stock solution (250 $\mu g.mL^{-1}$) one µL was added to a 100 µL of bacterial suspension. The bacterial suspension was then vortexed and left at room temperature in the dark, usually covered with aluminium foil, for 10 minutes. Then the tube was centrifuged for three minutes at 20,000 x g and the supernatant discarded. The bacterial pellet was resuspended in a 100 µL of PBS (Thermo Fisher Scientific, US). These washing steps were repeated twice. Finally, the bacterial pellet was resuspended in 20 µL of PBS (Thermo Fisher Scientific, USA) and 10 µL were heat fixed on a microscopic glass slide for microscopy or on a quartz slide (SPI Supplies, PA, USA) for Raman spectroscopy.

2.6 Fluorescence microscopy

The slides with heat fixed Nile red (Sigma-Aldrich, UK) stained bacteria were covered with aluminium foil to protect them from light. The microscope used was a Leica DM5500; a 100X-magnification oil immersion objective was used (Leica). Specific Leica immersion oil (ISO8036) was added and a Leica camera DFC 3000 G

captured the images. It was shown that Nile red is an excellent stain to observe intracellular lipid droplets composed of neutral lipids such as TAGs or cholesterol esters (Greenspan *et al.*, 1985). These authors explain that the lipid droplets could be well observed using excitation ranging from 450 nm to 500 nm and observing the fluorescence emission > 528 nm. Nile red is highly fluorescent when in contact with a hydrophobic environment (Greenspan *et al.*, 1985). Nile red is soluble in organic solvent. When the polarity of the solvent decreases the excitation and emission of Nile red spectra display a shorter wavelength (Greenspan and Fowler, 1985). The fluorescent properties of Nile red change depending on whether the fluorophore is in a relative polar or non-polar lipid environment. The polarity of the lipid environment impacts the maximal wavelength of excitation and emission fluorescence of Nile red. However, the spectra of Nile red in different lipid environments do overlap (Greenspan and Fowler, 1985).

In order to observe both polar lipid environment and non-polar lipid environment, on Nile red stained samples, two filter cubes were used: L5 and TX2. In the L5 filter, the excitation light used was 480/40 nm meaning that the light going through the filter cube ranged from 460 nm to 500 nm. The emission light collected ranged from 512 nm to 542nm (527/30 nm). The L5 filter was used to detect the fluorescence of the fluorophore located in a non-polar environment. In the TX2 filter, the excitation light used was 560/40 nm meaning that the light going through the filter cube ranged from 540 nm to 580 nm. The light collected ranged from 608 nm to 683 nm (645/75 nm). The TX2 filter was used to detect the fluorescence of the fluorophore present in a polar lipid environment. The microscope's software used was LAS AF 3.bu1.0 (Leica). An example showing Nile red stained mycobacteria is presented in **Fig. 2.1**.

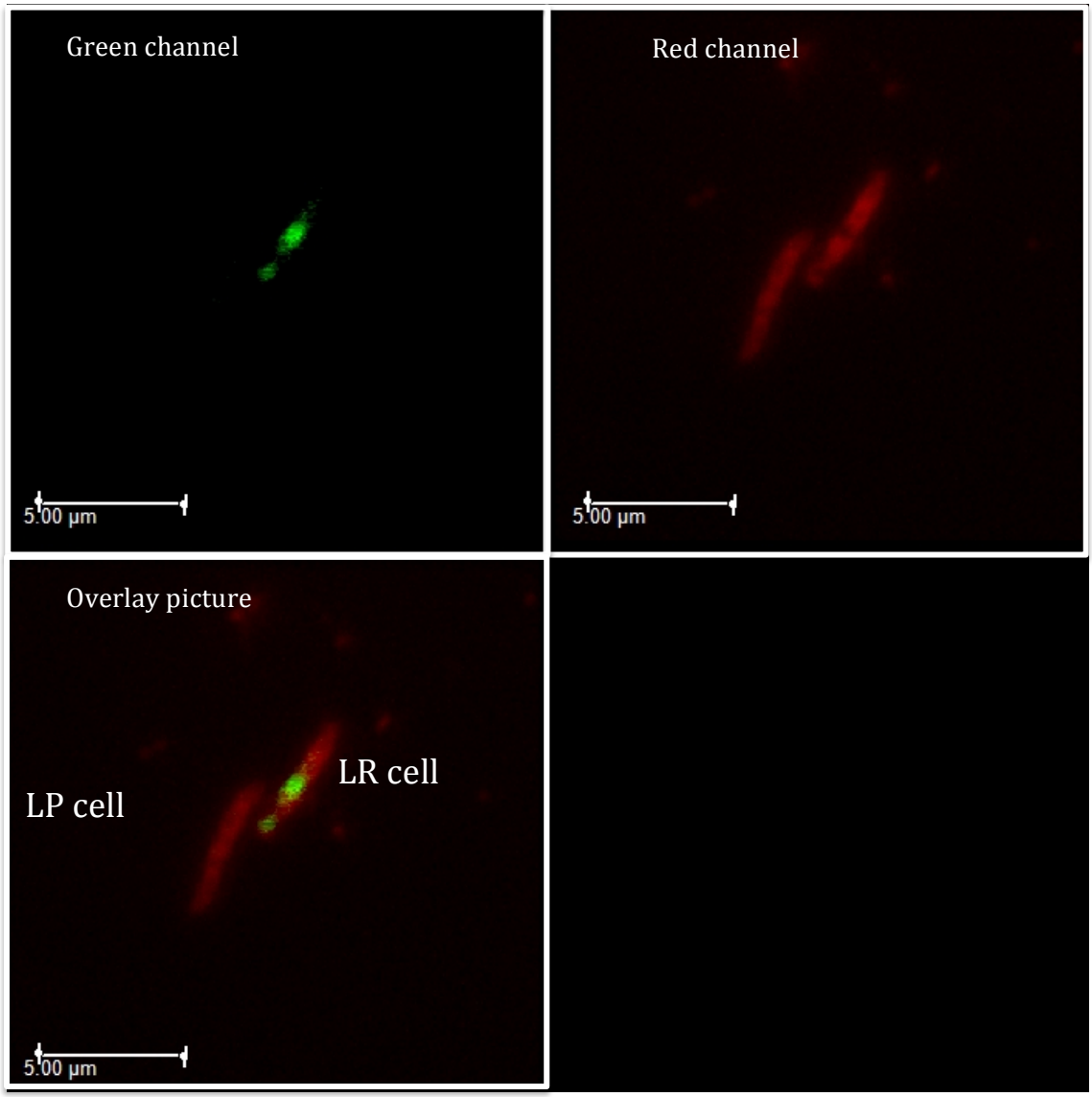

Figure 2.1 *Example of Nile red labelled M. smegmatis.*

The final concentration of Nile red used was 2.5 µg.mL^{-1}. The image showing the polar lipids (red channel) was taken using a TX2 filter cube; while the picture presenting the non-polar lipids (green channel) was taken with a L5 filter cube. The bottom left picture is the combined picture of the previous two, and one LR cell next to a LP cell can be observed. The picture was acquired using a one week old M. smegmatis culture (stationary phase). The scale bar represents 5µm.

2.7 Heat inactivation

In order to heat kill mycobacteria, one mL of cell culture was placed in a heat block for 20 minutes at 80°C. The heat killing protocol was validated (by the research group) on *M. tuberculosis*. This protocol permitted *M. tuberculosis* to be taken out of the containment level 3 (CL3) laboratory. After heat killing, the mycobacteria were plated on 7H10 (Sigma-Aldrich, UK) supplemented with 0.05% (v/v) glycerol (Sigma-Aldrich, UK) and 10% (v/v) OADC (Sigma-Aldrich, UK) and no growth was observed after four weeks. The same protocol was applied to *M. smegmatis* and BCG to work with the condition.

2.8 Standard Raman spectroscopy and WMR spectroscopy

In this work, both Standard Raman spectroscopy and WMR spectroscopy were applied to single bacteria. In the standard Raman spectroscopy, an individual spectrum was acquired over 30 seconds, the laser wavelength was fixed (784.6 nm) during the integration time. A spectrum of the background nearby the bacterium was taken and then subtracted from the spectrum of the bacterium to generate the standard spectrum. A flow chart (**Fig. 2.2**) shows how standard Raman spectra were acquired. In WMR spectroscopy a spectrum from a single bacterium was obtained using five spectra, of 30 seconds each, taken continuously (2.5 minutes in total). The laser line was tuned continuously during the acquisition; the modulation range was $\Delta\lambda$=1 nm. A WMR spectrum was generated with the five original spectra using PCA; in the process, most of the fluorescence background was removed, as it is identical in the five original spectra. PCA was explained in detail in **Chapter 1 Introduction,**

section 1.5.6. In WMR spectra the peaks are represented by the zero-crossing and the peak intensity by the peak-to-valley value. A flow chart (**Fig. 2.3**) shows how WMR Raman spectra were acquired. For each preparation 40 to 60 spectra of single cells were acquired.

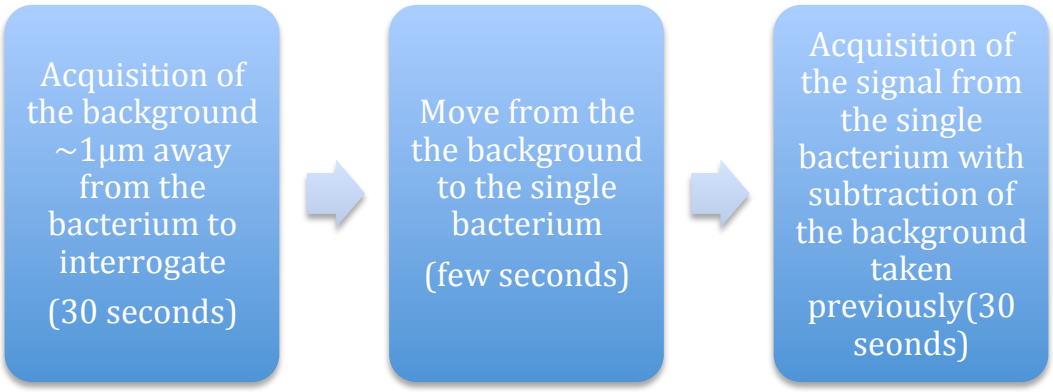

Figure 2.2 *Flow chart describing the acquisition of a standard Raman spectrum of a single bacterium. For each standard Raman spectroscopy spectrum one background and one reference were taken.*

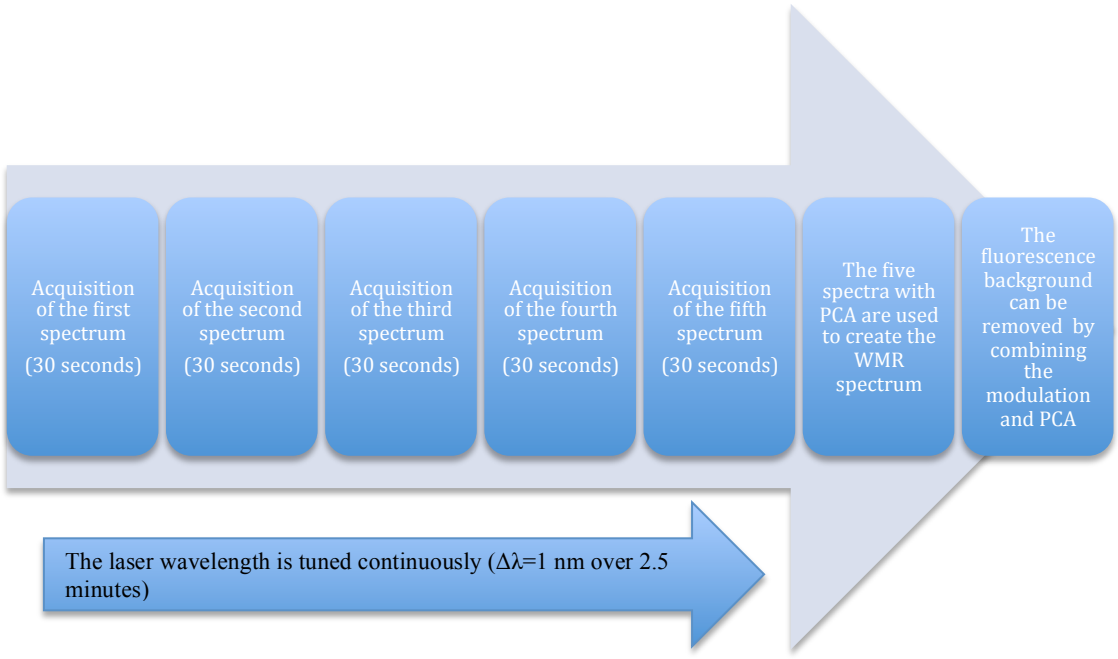

Figure 2.3 *Flow chart representing the acquisition of a WMR spectrum of a single bacterium.*

2.9 Laser Calibration using polystyrene

Polystyrene beads (1 μm in diameter) were used to calibrate the Raman spectra. The known peak position (1001.4 cm^{-1}, see **Fig. 2.4**) of a polystyrene bead was measured by our system in order to monitor drifts of the laser. Each Raman spectrum was calibrated with the nearest laser line that was calculated from the spectra of the polystyrene beads. To calculate the laser wavelength, using the known the position of the main polystyrene peak ($\Delta\omega$ = 1001.4 cm^{-1}), the following equation was used:

$$\Delta\omega(cm^{-1}) = \left(\frac{1}{\lambda_0(nm)} - \frac{1}{\lambda_1(nm)}\right) \times \frac{(10^7 nm)}{(cm)}$$

Where $\Delta\omega$ corresponds to the Raman shift, λ_0 (nm) is the laser wavelength to calculate and λ_1 (nm) the measured wavelength of the main polystyrene peak in the Raman spectrum.

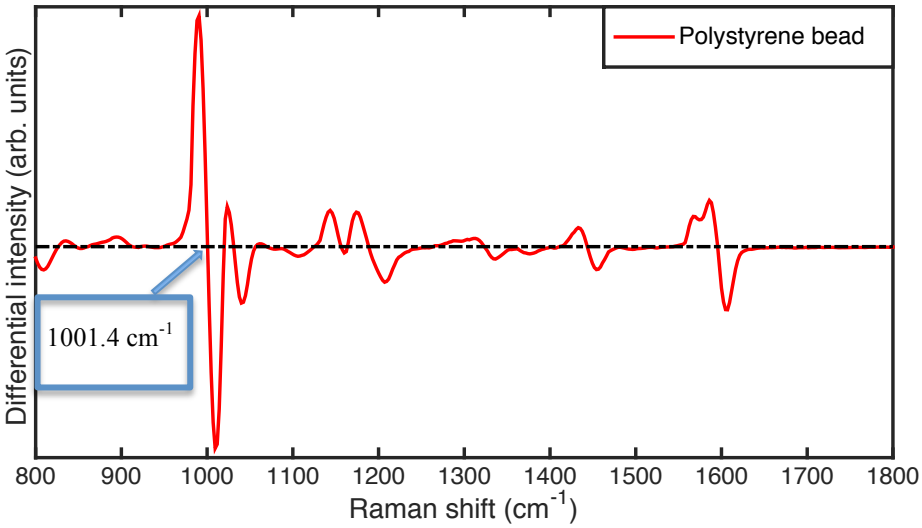

Figure 2.4 *WMR spectrum of a Polystyrene bead.*
The spectrum was acquired on a 1 µm polystyrene bead. The x-axis shows the Raman shift in cm^{-1} and the y-axis presents the differential intensity in arbitrary units. In a WMR spectrum, the peaks are located at the zero crossing; the zero is represented by the black dash dotted line. The main Raman peak of the polystyrene is visible at 1001.4 cm^{-1}. The main peak at 1001.4 4 cm^{-1} is a result of the C-C aromatic ring stretching (Winkler et al., 2003).

Each spectrum was also normalised by its total intensity (using the integration over the area covered by the spectrum) in order to avoid the influence of any fluctuation in the laser power during wavelength modulation. Raman spectra in the region of 600 cm^{-1} to 1800 cm^{-1} were taken into account for the later data analysis.

2.10 Discrimination between datasets using Principal component analysis (PCA)

PCA was explained in detail previously (see **Chapter 1 Introduction, section 1.5.6** for more detail). The PCA was run in MATLAB® (MathWorks, UK, version R2014b). Datasets (40 to 100 spectra) acquired using conventional Raman spectroscopy or WMR spectroscopy were investigated using PCA. In order to discriminate the data sets, usually LR and LP, the first seven PCs were used. The first seven PCs represented more than 70% of the variances between the datasets.

2.11 Leave one out cross validation (LOOCV)

The leave-one-out cross validation method was used to evaluate the ability to discriminate datasets. Using the LOOCV method the correct or an incorrect prediction of each spectrum were obtained and used to inform the confusion matrix and calculate the sensitivity and the specificity (see **Chapter 1 Introduction, section 1.5.7** for more detail). The LOOCV was run in MATLAB® (MathWorks, UK, version R2014b).

2.12 First Raman spectroscopy system

Raman spectra were acquired by a confocal Raman spectroscopy system shown in **Fig. 2.5**. Pumped by a green laser (Verdi V6, 532 nm, 5W), a tunable Ti:Sapphire laser (Spectra-Physics 3900s, 785 nm, 1W) was focused by a microscope objective (Nikon, 50x, oil immersion) onto a single cell. The objective numerical aperture (NA) was 0.9, the confocal diameter was 2.63 μm, and confocal depth was 2.86 μm. Excited Raman photons were then collected by a spectrometer formed with a monochromator (Andor Shamrock SR303i, 400lines/mm grating @850 nm) and a cooled CCD camera (Andor Newton). In order to get strong Raman signal from a single cell, a power of 150 mW was applied onto the sample plane. We designed an experiment to assess the impact of the laser to the bacteria. This experiment was carried out, using a stationary phase culture of *M. smegmatis,* on 3 individual bacteria (N=3). We took 10 spectra in a row on the same bacteria. This represents 1500 seconds of exposure to the laser. No spectral differences were observed between the first spectrum and the last one in the three experiments. The results for one bacterium are shown in the **Appendices section 7.** This focused laser power did not induce any damage to the cell during the acquisition of spectra.

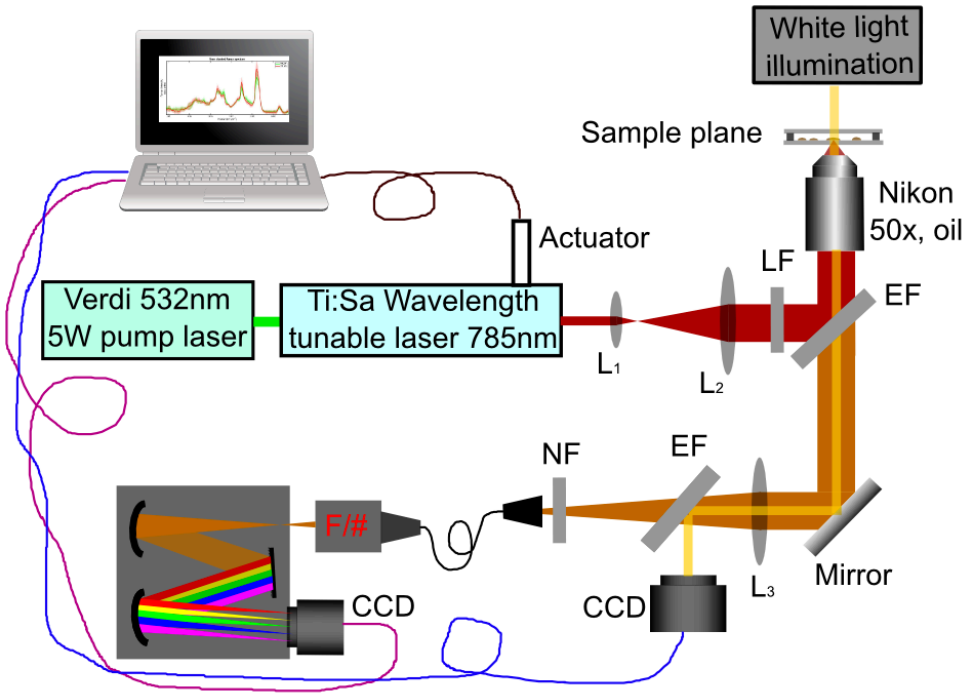

Figure 2.5 *Diagram of the initial experimental setup. First Raman system. The design used a tunable Ti:Sapphire laser (Spectra-Physics 3900s, 785 nm, 1W) that was Pumped by a green laser (Verdi V6, 532 nm, 5W). The laser used a microscope objective (Nikon, 50x, oil) to focus on the sample plane. EF stands for edge filter, NF corresponds to notch filter, L_1, L_2 and L_3 are lenses and LF stands for line filter. Finally, the spectrometer was made of a monochromator (Andor Shamrock SR303i, 400lines/mm grating @850 nm) and a cooled CCD camera (Andor Newton).*

2.13 Second Raman spectroscopy system

This combined Raman spectroscopy and fluorescence system (**Fig. 2.6**) was built up based on a Nikon microscope (Nikon TE2000-E). A tunable Ti:Sapphire laser (Solstis M squared, 1W @785 nm) was used as an excitation source which was focused by a microscope objective (Nikon Plano, 40X, oil immersion) onto a single bacteria cell. The objective NA was 1.3, the confocal diameter was 5 μm, and the confocal depth of the system was 4.68 μm. As shown in **Fig. 2.6**, excited Raman photons from the sample were dispersed by a monochromator (Andor Shamrock SR303i, 400 lines/mm grating @850 nm) and finally formed a spectrum on a cooled CCD camera (Andor Newton). A laser dosage at 150 mW at the sample plane was used in order to excite enough Raman photons. This laser dosage was tested and didn't show any damage to the cells.

The system is able to switch from Raman spectroscopy to fluorescence imaging by inserting FITC/TRITC cubes into the microscope and directing the flip mirror (FM) to CCD_1 (Hamamatsu ORCA-ER). Using a standard Nikon fluorescence white light source ($Lamp_2$) together with FITC/TRITC cubes, a green excitation light (545~565 nm) will excite red fluorescence emission (580~620 nm) from a polar lipid environment in the Nile red stained samples while a blue excitation light (475~490 nm) will excite green fluorescence emission (500~540 nm) from a non-polar lipid environment (lipid bodies).

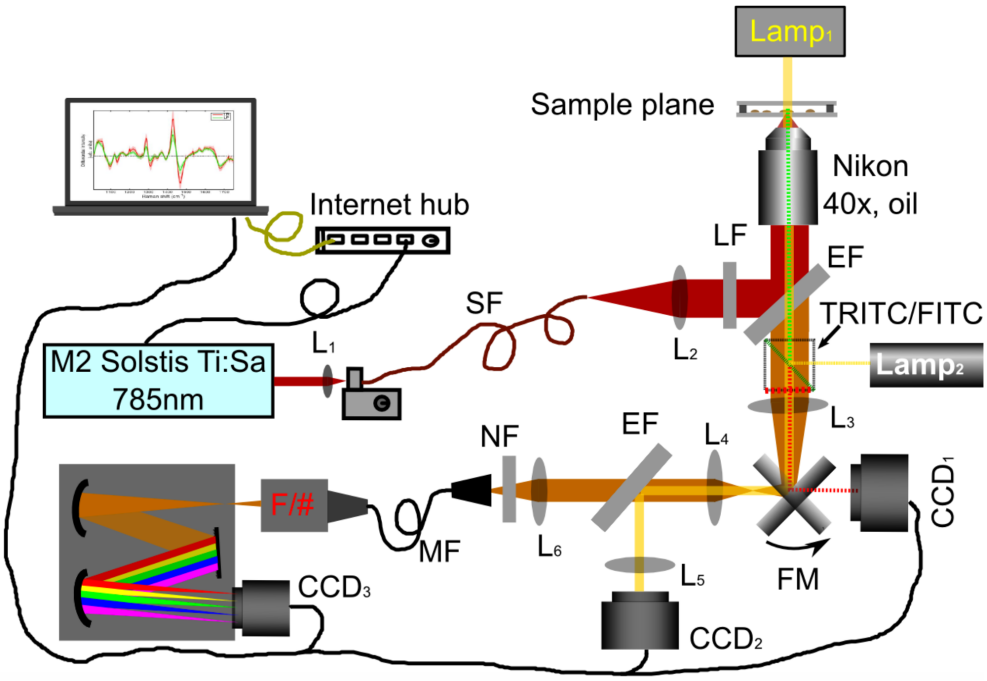

Figure 2.6 *Raman spectroscopy and fluorescence combined system. Second Raman system.*

The excitation source used is a tunable Ti:Sapphire laser (Solstis M squared, 1W @785 nm). The components used to build the system are: SF (single-mode fibre), MF (multi-mode fibre, 200um core diameter), LF (Laser line filter (Semrock LL01-785)), EF (Edge filter (Semrock LPD02-785RU)), NF (Notch filter (Semrock NF03-785E)), FM (flip mirror). For the fluorescence: TRITC/FITC: Fluorescence Filter cubes (FITC: excitation 475-490 nm/emission 500-540 nm, TRITC: excitation 545-565 nm/emission 580-620 nm). The different cameras used were: CCD_1: Hamamatsu ORCA_ER; CCD_2:Imaging Source USB camera (DFK 42AUC03); CCD_3:Andor Newton Camera (cooled at -70^{o}C); L1~L6: lenses; F/#: F number matcher.

Chapter 3 Investigation of *Mycobacterium tuberculosis* total lipid extracts using Raman spectroscopy.

3.1 Introduction

We define, based on Nile red staining and microscopic observation, the Lipid rich (LR) cells as bacteria that have one or more intracellular non-polar lipid bodies or detectable forming lipid bodies whereas lipid poor cells (LP) correspond to bacteria that have no detectable intracellular lipid bodies. The intracellular lipid bodies present in mycobacteria are mainly composed of TAGs (Garton *et al.*, 2002). The lipid composition of mycobacteria is very complex, and a lot of those lipids are unique to the *Mycobacterium* genus (Sartain *et al.*, 2011). A lipidomic study of *M. tuberculosis* has been conducted using mass spectrometry showing that the lipid content changes between a young and old culture. As the culture ages, various lipid classes contain enhanced proportion of homologues with long acyl substituents (Sartain *et al.*, 2011). This group developed a lipid database of *M. tuberculosis* using mass spectrometry ("*Mtb* LipidDB"). This lipid database presents the exact mass of over 2,500 entities.

As a mycobacterial culture ages the proportion of LR cells increases (See **Chapter 6 result section 6.3.1** for more detail). It has been demonstrated that LR cells exhibit a much higher level of tolerance to antibiotic treatment (Hammond *et al.*, 2015). Thus, the presence of intracellular lipid bodies can be seen as a potential marker of higher antibiotic tolerance and lower metabolic activity. This is clinically important as a high percentage of lipid body positive bacilli in patients at 21-28 days into treatment have

been linked to an unfavourable outcome (Sloan *et al.*, 2015). The presence or absence of lipid bodies could be used to discriminate phenotypically antibiotic tolerant from sensitive bacteria. In this study, we investigated total lipid extracts from bacteria using Raman spectroscopy. This chapter aims to: first, identify the lipid peak location in the Raman spectrum. Secondly, to evaluate the relationship between the lipid concentration and the Raman peak intensity. Finally, to investigate the changes in lipid content that occurs in LR and LP population of *M. tuberculosis* as the population ages.

3.2 Methods

3.2.1 Lipid extraction

In order to extract the total lipids, the Bligh & Dyer lipid extraction protocol was used. (Bligh and Dyer, 1959). All steps concerning the lipid extraction were performed using glass vials (Camlab, UK; 1.75 mL). All vortex steps were done at max speed for 15 to 20 seconds on a peqTWIST (Peqlab) vortex. Firstly, at room temperature, one mL of bacterial culture (≈1.10^7 bacteria per ml) was spun down at 20,000 x g for three minutes. The cell pellet was washed with 200 µL PBS three times. The bacterial suspension (200 µL) was transferred into a small glass screw cap vial, 250 µL of chloroform and 500 µL of methanol were added to the glass vial. Samples were thoroughly vortexed to ensure that bacteria were completely delipidated and lipids solubilised (up to this point, all steps were conducted at room temperature). The samples were placed in continuous agitation at 1000 rpm for at least one hour to ensure efficient extraction. This was performed at 4°C to prevent the evaporation of the solvents. Then 250 µL of chloroform were added, and the tubes were vortexed well. 250 µL of water were added, and the tubes were vortexed well again. After this step, all the procedures were conducted at room temperature. The glass vials were inserted in 15 mL Falcon tubes (CELLSTAR) that were half-filled with tissue or paper. The samples were centrifuged for 10 minutes at 3500 x g (J6-M1, Beckman Coulter centrifuge), a clear phase separation was observed with a sharp interphase (containing the cellular debris). The bottom organic phase (lipid containing) was harvested by inserting a long and thin pipette tip (Fisher Scientific, Pipettor tip SureOne, 12982571) and as much volume as possible was pipetted from

the bottom phase. The bottom phase has been placed into a new glass vial and dried in a fume cabinet. The samples were then stored at 4°C.

3.2.2 Sample preparation for Raman spectroscopy investigation

Total lipids, from the glass vial, were resuspended in chloroform (20 μL). Then a 5 μL drop was placed on a thin quartz coverslip (01015T-AB, SPI Supplies, USA; Quartz coverslip 25,4 x 25,4 mm, 0.15-0.18 mm thick) and left to air dry in the hood. The dry lipids were covered using a thick quartz slide (01016-AB, SPI Supplies, USA; Quartz microscope slide 25,4 x 25,4 mm, 1 mm thick) presenting a vinyl spacer. The mount was sealed with a transparent Nail polish; this preparation was interrogated using Raman spectroscopy.

3.2.3 Raman spectroscopy and acquisition time for extracted lipids

WMR spectroscopy acquisition was 2 seconds x5x5 (meaning that five 2 second spectra were accumulated and this was reproduced five times) 50 seconds total per WMR spectrum, for all dried total lipid extract samples. The standard Raman spectroscopy acquisition time was 10 seconds per spectrum. These results were acquired using the second Raman spectroscopy system (see **Chapter 2 General methods, section 2.13** for more details).

3.2.4 Lipid concentration and WMR spectroscopy

A commercial lipid standard (Mono-, Di-, and Triglyceride mix) (1787-1AMP, Sigma-Aldrich, UK) was diluted to the required concentration in DMSO (Sigma-Aldrich, UK). A small spacer was placed on a quartz slide and filled with 5 μL of lipids diluted in DMSO. The quartz slide was then covered with a quartz coverslip and sealed with transparent nail polish. The sample was then interrogated using WMR spectroscopy. The acquisition time was 150 seconds in total (6x5x5 seconds). These results were acquired using the first Raman spectroscopy system (see **Chapter 2 General methods, section 2.12** for more details).

3.3 Results

3.3.1 Standard Raman spectroscopy

Total lipids were extracted from *M. tuberculosis* cultures of different age: one month, three months and four months old (initial time points tested). The dried lipid extracts were investigated by Raman spectroscopy. Examples of lipid aggregates observed under the Raman spectroscopy system from the three time points are presented in **Fig. 3.1**. The standard Raman signals of the lipid extracts are shown in **Fig. 3.2.** The intensity of the Raman signal depends directly on the size of the lipid aggregate interrogated. In this study pure lipid extract were investigated. Therefore, differences in terms of absolute intensity are not relevant. However, changes in peak position or ratios between Raman peaks can be related to a change in composition.

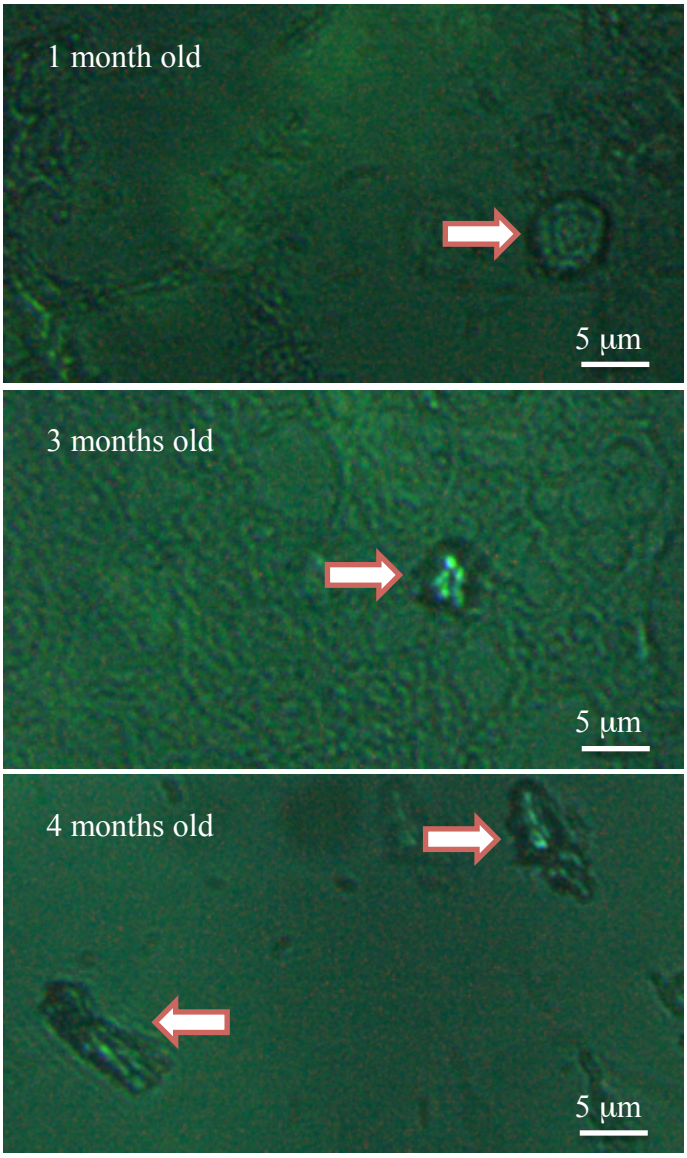

Figure 3.1 *Lipid aggregates dried out from of chloroform suspension (M. tuberculosis).*

Total lipids were extracted from one month, three months and four months old M. tuberculosis cultures. An arrow shows the lipid aggregates. The total lipid extract was left to dry on the quartz slide. Total lipid aggregates were quite rare on the slides, only several were targeted for each condition and several WMR spectra were taken on every aggregate. The scale bars correspond to 5 μm.

Five main peaks can be observed in the fingerprint region (1000-1800 cm^{-1}) and one double-headed peak in the 2800-3000 cm^{-1} region. Those seven peaks are named bands 1 to 7 from left to right (**Fig. 3.2**). For the three time points, the peak at 1449 cm^{-1} is showing a clear shoulder located at 1465 cm^{-1}.

The exact peak position for each condition is presented in **Tab. 3.1.** The peak positions of the total lipid extract do not change between the different time points.

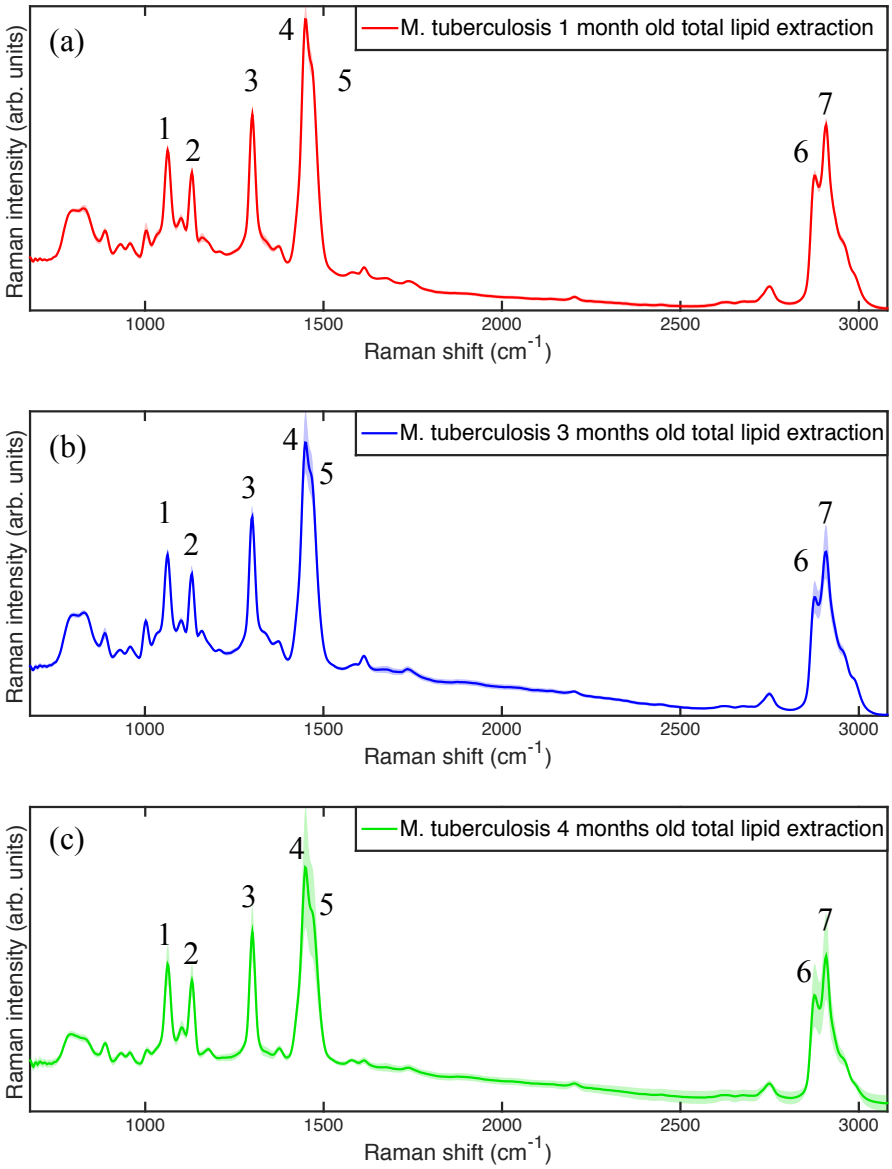

Figure 3.2 *Mean standard Raman spectra of M. tuberculosis total lipid extract of one month old (a), three month old (b) and four month old (c).*

*The colour-shaded area represents the associated single standard deviation. The x-coordinate in (**Fig. 3.2 a, b, c**) corresponds to the Raman shift (in wavenumber, cm^{-1}) and the y-coordinate corresponds to the differential Raman intensity in arbitrary units. The acquisition time is 10 seconds per spectrum in total (see **Chapter 3 section 3.2.3** for more details). Around 60 to 65 spectra were taken for each condition.*

Table 3.1 Exact position of the main Raman band present in the total lipid extract standard spectra of *M. tuberculosis*.

Main Raman bands	One month (peak position in cm^{-1}) n=1	3 months (peak position in cm^{-1}) n=1	4 months (peak position in cm^{-1}) n=1
Band 1	1063	1063	1063
Band 2	1131	1131	1131
Band 3	1300	1300	1300
Band4	1449	1449	1449
Band 5	1465	1465	1465
Band 6	2875	2875	2875
Band 7	2908	2908	2908

Using the standard Raman spectra taken from the total lipid extract of *M. tuberculosis* no changes could be found in peak positions between the three time points.

3.3.2 WMR spectroscopy

The spectra were obtained using WMR spectroscopy meaning that the laser wavelength was tuned during the acquisition. To create each WMR spectrum; five original spectra were taken while the laser wavelength was changing. In **Fig. 3.3** a clear shift in Raman peak position can be observed between the five individual spectra due to the modulation. As seen in the introduction, WMR spectroscopy can remove the fluorescence background entirely as only the position of Raman peaks changes during the modulation; the fluorescence remains unchanged. After data processing, using PCA, a modulated Raman spectrum is obtained (**Fig. 3.4**) in which

all fluorescence background has been removed and where the zero crossing corresponds to the Raman peak. PCA was previously shown to be the optimal algorithm for fluorescence subtraction in WMR spectroscopy (Mazilu *et al.*, 2010).

WMR spectra show clear and distinct peaks. For example, around 1465 cm^{-1} there is a shoulder in the standard Raman spectrum and after processing a clear peak can be observed, and its intensity measured accurately.

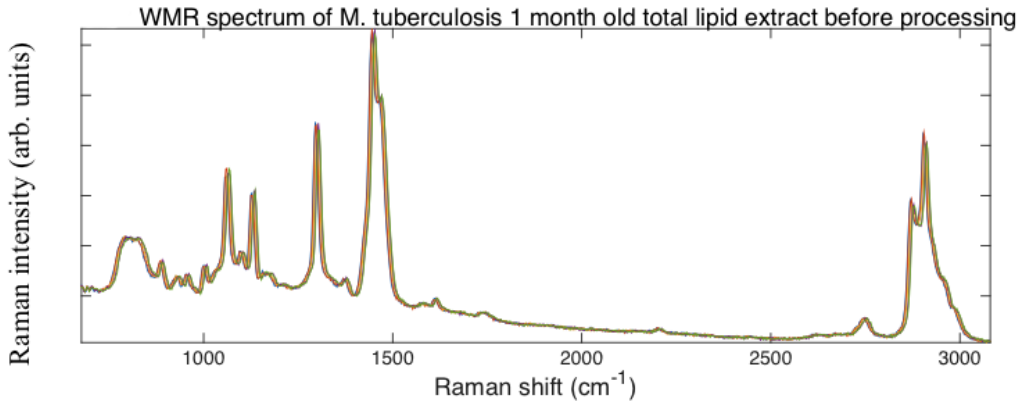

Figure 3.3 *the five initial spectra acquired during modulation.*

Each coloured line represents a different spectrum (five in total). The Raman peaks in the five spectra are shifted as the laser was tuned during the acquisition. The x-coordinate corresponds to the Raman shift (in wavenumber, cm^{-1}) and the y-coordinate corresponds to Raman intensity in counts. The acquisition time for each spectrum is 50 seconds in total ***(****see* ***Chapter 3 section 3.2.3*** *for more details).*

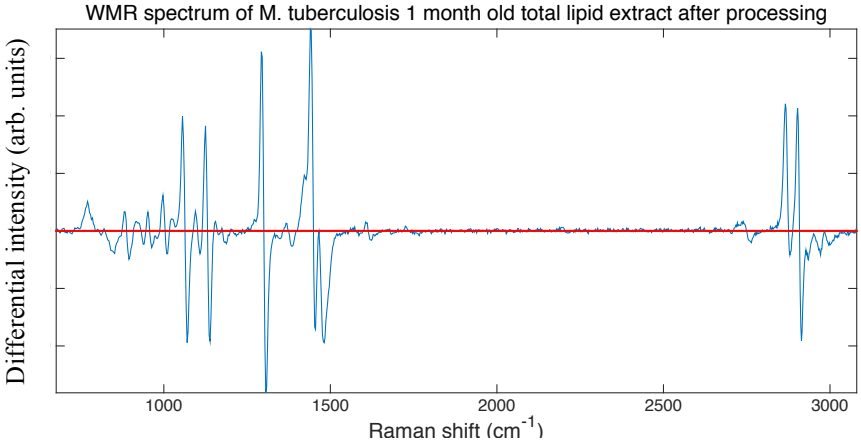

Figure 3.4 *Example of WMR spectrum after processing.*

The WMR spectrum is generated using the five original spectra presented in ***Fig. 3.3*** *and the PCA algorithm. The x-coordinate corresponds to the Raman shift (in wavenumber, cm^{-1}) and the y-coordinate corresponds to Raman intensity in counts. In a WMR spectrum, a Raman peak is located at the zero crossing point (denoted by the red line) while the Raman peak intensity is represented by the peak-to-valley value around that point. The acquisition time for each spectrum is 50 seconds in total* ***(****see* ***Chapter 3 section 3.2.3*** *for more details).*

The WMR spectra of the total lipid extract of *M. tuberculosis* are shown in **Fig 3.5.** Comparing the result from standard and modulated Raman spectroscopy, manifest differences regarding peak ratios can be observed. For example, in the standard Raman spectrum, the 1300 cm^{-1} peak is less intense compared to the 1449 cm^{-1}, and it is the opposite in the WMR spectrum. Moreover, the WMR spectrum presents more detail around 1465 cm^{-1} where a clear peak can be identified whereas this was only a shoulder in the standard Raman spectrum. The WMR spectrum allows accurate determination of the peak value and its intensity. The peak positions in all the WMR spectra are shown in **Tab. 3.2**.

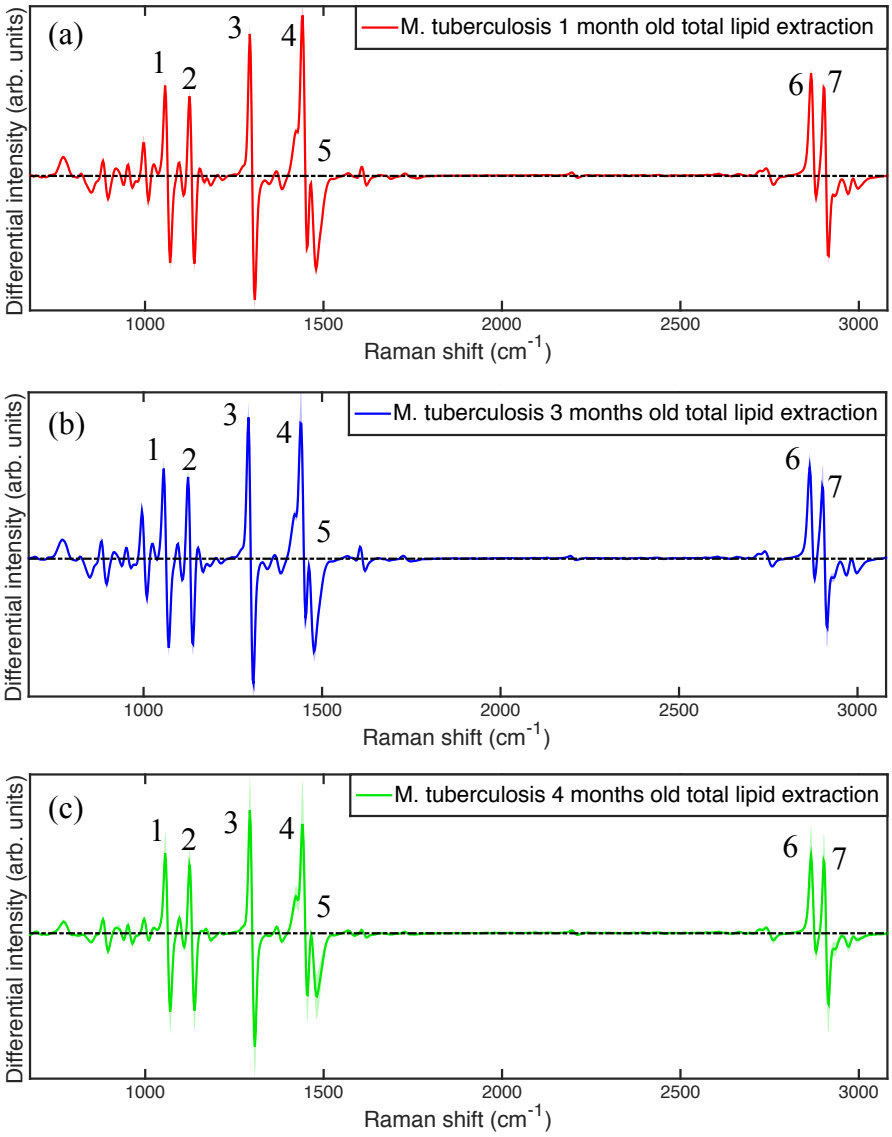

Figure 3.5 *Mean WMR spectra of M. tuberculosis total lipid extract of one month old (a), three month old (b) and four month old (c).*

*The colour-shaded area represents the associated single standard deviation. The x-coordinate in (**Fig. 3.5 a, b, c**) corresponds to the Raman shift (in wavenumber, cm^{-1}) and the y-coordinate corresponds to the differential Raman intensity in arbitrary units. In a WMR spectrum, a Raman peak is located at the zero crossing point (denoted by the dash-dotted line) while the Raman peak intensity is represented by the peak-to-valley value around that point. The acquisition time for each spectrum is 50 seconds in total (see **Chapter 3 section 3.2.3** for more details). Around 60 to 65 WMR spectra were taken for each condition.*

Table 3.2 Exact position of the main Raman band present in the WMR spectra of *M. tuberculosis* total lipid extract.

Main Raman bands	One month (peak position in cm^{-1}) n=1	3 months (peak position in cm^{-1}) n=1	4 months (peak position in cm^{-1}) n=1
Band 1	1063	1063	1063
Band 2	1131	1131	1131
Band 3	1300	1300	1300
Band4	1449	1449	1449
Band 5	1465	1465	1465
Band 6	2875	2875	2875
Band 7	2908	2908	2908

The Raman peak positions are the same before and after the data processing and fluorescence background removal. The peak-to-peak ratios between the main Raman peaks present in the fingerprint region were calculated using the WMR spectra A table showing all possible ratios, between the main bands, is shown in the **Appendices section 1.** Differences in peak-to-peak ratio can be observed between time points; however high variability among each condition is also observed. The **Tab. 3.3** displays examples of peak-to-peak ratios.

Table 3.3 Peak-to-peak ratios calculated using Raman spectra of *M. tuberculosis* lipid extracts for the different culture ages with the corresponding single standard deviation.

	1 month		3 months		4 months	
Ratios	Average	Standard deviation	Average	Standard deviation	Average	Standard deviation
1060/1131	1.06	0.02	1.07	0.10	1.08	0.03
1060/1300	0.67	0.02	0.67	0.03	0.67	0.01
1060/1449	0.76	0.04	0.95	0.16	0.96	0.12
1060/1465	1.89	0.13	1.92	0.15	2.53	0.25
1060/2876	1.43	0.09	1.64	0.20	1.72	0.26
1060/2908	1.04	0.04	1.34	0.28	1.14	0.13

Before comparing peak-to-peak ratios between time points, it is important to observe the variability among each data set. For each time point, 60 to 65 spectra were taken from several lipid aggregates of various sizes and volume. The lipid samples were homogenised. However, important variation can be observed within one dataset. This variation between items can also be observed in the 3D PCA plot where for each condition distinct groups of spectra can be observed corresponding to different lipid aggregates **Fig. 3.6**. The exact composition of lipids can change between aggregates and also the orientation of the molecules, changing the vibrational profile and therefore the peak-to-peak ratio even if the composition remains unchanged. A study showed that pure lipid could give different relative peak intensity depending on the lipid aggregate targeted (Czamara *et al.*, 2015).

Within one time point, the variability in peak-to-peak ratios can be significant. However, the variation is small in the same aggregate **Tab. 3.4**. The variability within each dataset comes from differences between lipid aggregates. For example, the ratio

1060/2908 in the first aggregate is on average 0.85, in the second aggregate it is 1.53, and it is 1 in the fourth aggregate. However, the variability among each lipid aggregate is very low as shown by the small standard deviation for all the ratios.

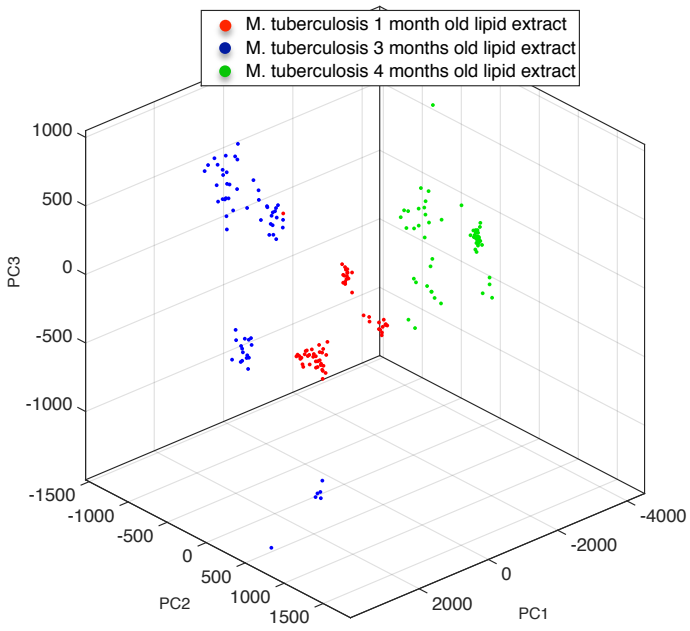

Figure 3.6 *Variability of lipid aggregates, of M. tuberculosis lipid extracts, as seen in PCA score plot.*

The one month, three months and four months old cultures, are shown in red, blue and green respectively. The first three PCs are plotted. The red, blue and green dots represent the lipid extraction of M. tuberculosis from one month old, three months old and four months old cultures respectively. Each dot corresponds to one WMR spectrum.

Table 3.4 Peak-to-peak ratios of all lipid aggregates of 3 month old *M.tuberculosis* and associated single standard deviation. For each lipid aggregate interrogated the total intensity of the seven main peaks is also shown in this table.

Aggregate	1		2		3		4		5	
Ratios	Average	Stdev	Average	Stdev	Average	Stdev	Average	Stdev	Average	Stdev
1060/1131	1.30	0.02	1.04	0.01	1.03	0.01	1.16	0.02	0.99	0.02
1060/1300	0.64	0.01	0.72	0.01	0.70	0.01	0.66	0.01	0.67	0.02
1060/1440	0.62	0.01	1.09	0.02	1.06	0.03	0.78	0.02	1.04	0.04
1060/1465	1.58	0.04	2.10	0.04	2.01	0.06	1.94	0.09	1.92	0.11
1060/2876	1.23	0.03	1.83	0.03	1.79	0.04	1.44	0.03	1.75	0.07
1060/2908	0.85	0.02	1.53	0.03	1.55	0.03	1.00	0.02	1.53	0.04
Total peak intensity	15872	910	13633	258	12863	305	18205	361	14997	412

The contribution of the major Raman peaks to the total intensity of those peaks was investigated and compared for the different conditions. The intensity of each peak and the total intensity of the seven main peaks were calculated for all the time points (**Tab. 3.5)** and plotted in **Fig. 3.7.**

No significant differences were found in relative peak intensity between time points. The great variation between lipid aggregates led to vast standard deviation values that do not permit significant statistical differences in peak contributions between time points to be obtained.

Table 3.5 Contribution of each peak to the total intensity of the seven main peaks for all time points.

time points	Raman peaks (cm^{-1})	1060	1131	1300	1440	1465	2876	2908
1 month	Percentage	14.37	13.55	21.57	18.97	7.62	10.10	13.80
	2 standard deviations (STD)	0.77	0.84	0.57	0.90	0.75	0.72	0.69
3 month	Percentage	15.61	14.73	23.12	16.79	8.14	9.57	12.04
	2 standard deviations (STD)	2.24	4.25	2.37	3.95	0.93	1.13	4.09
4 month	Percentage	15.76	14.54	23.57	16.62	6.26	9.29	13.96
	2 standard deviations (STD)	1.65	1.86	2.55	2.40	0.87	1.81	1.71

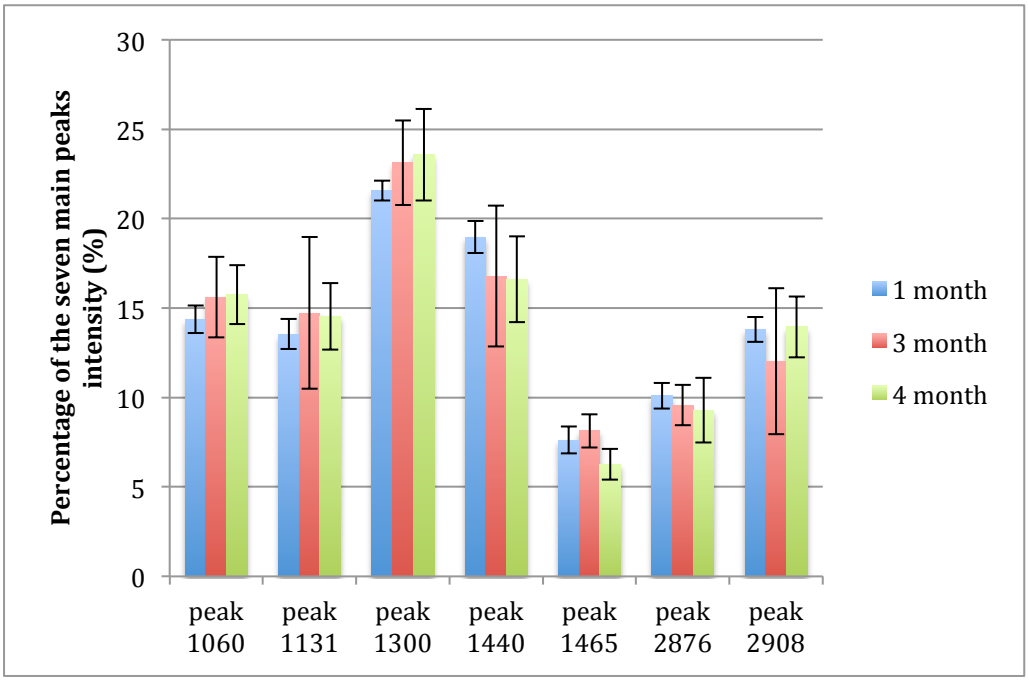

Figure 3.7 *Contribution of each peak to the total intensity of the seven main peaks for the three time points.*

The x-axis shows the seven main peaks present on the Raman spectra of 1month (blue), three months (red) and four months (green). The y-axis represents the average contribution of each peak to the sum of the seven main peaks in percentage and this for all three data sets. The error bars correspond to two standard deviations above and under the mean.

For both one month and four months old cultures, *M. tuberculosis* cells were separated using a density-based method (D_2O separation, see in **Chapter 2 General methods section 2.3** for more details) to obtain a lipid rich (LR) fraction and a lipid poor (LP) fraction. The purity of the fractions was assessed by fluorescence microscopy. The total lipids are extracted from both LR and LP fractions. The WMR spectra of one month (LR and LP) and four months (LR and LP) are shown in **Fig. 3.8** and **Fig. 3.9** respectively. Similarly, to the previous dried samples, LR and LP could not be discriminated due to important variation among each dataset (high variability between aggregates within the same sample).

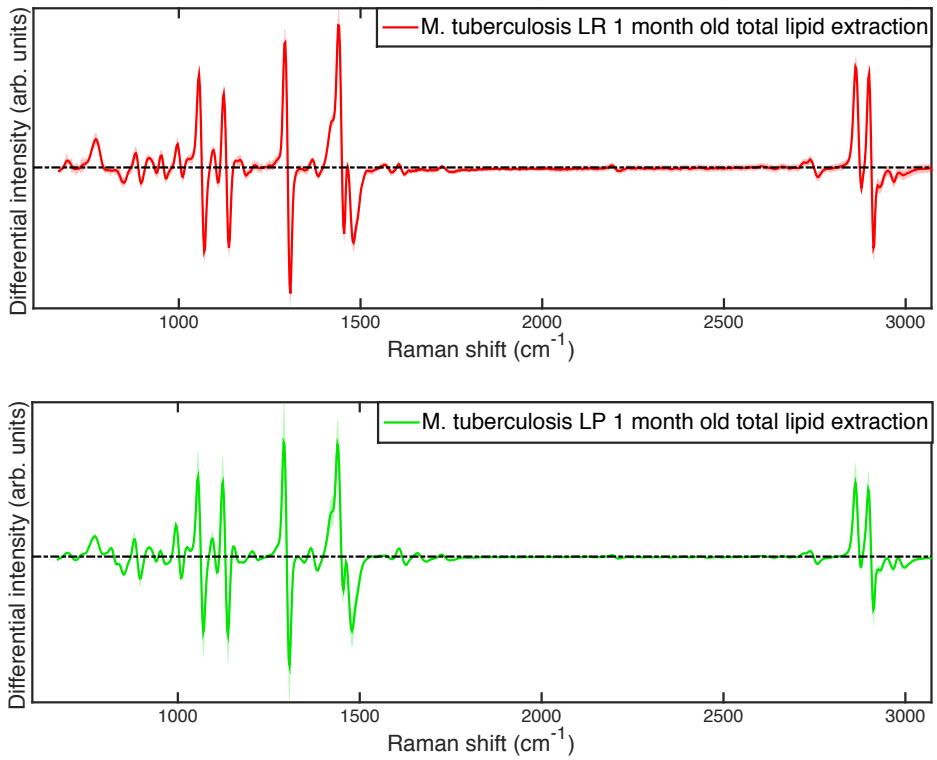

Figure 3.8 *Mean WMR spectra of M. tuberculosis lipid extract of LR (a) and LP (b) fraction of a one month old culture.*

*The colour-shaded area represents the associated single standard deviation. The x-coordinate in (**Fig. 3.8 a, b**) corresponds to the Raman shift (in wavenumber, cm^{-1}) and the y-coordinate corresponds to the differential Raman intensity in arbitrary units. In a WMR spectrum, a Raman peak is located at the zero crossing point (denoted by the dash-dotted line) while the Raman peak intensity is represented by the peak-to-valley value around that point. The acquisition time for each single spectrum is 50 seconds in total (see **Chapter 3 section 3.2.3** for more details).*

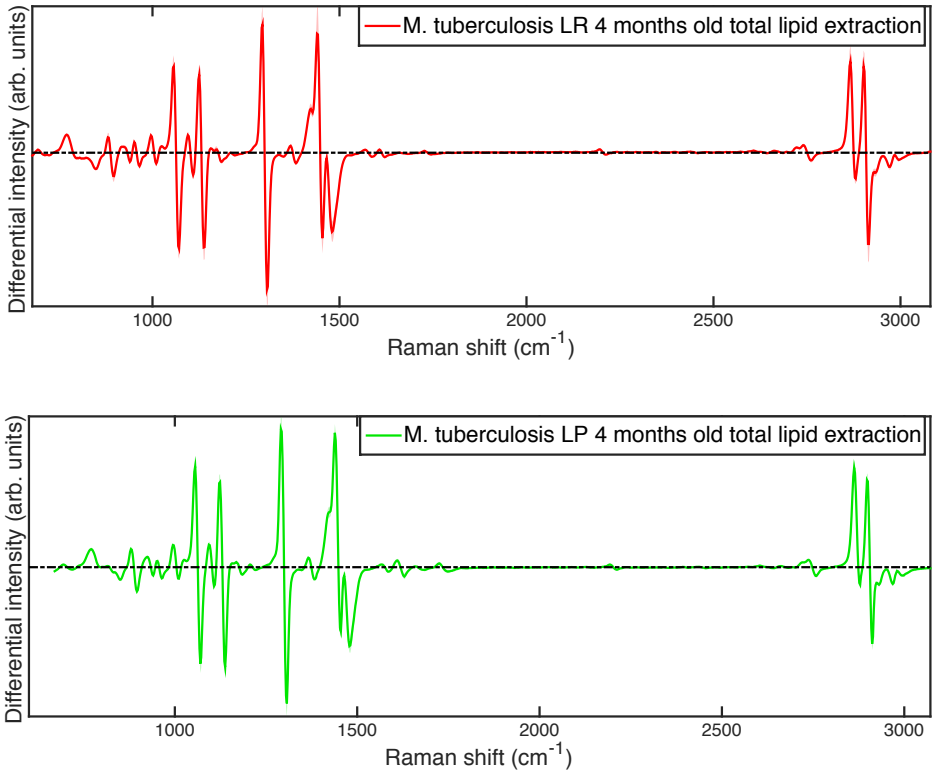

Figure 3.9 *Mean WMR spectra of M. tuberculosis lipid extract of LR (a) and LP (b) fraction of a four month old culture.*

*The colour-shaded area represents the associated single standard deviation. The x-coordinate in (**Fig. 3.9 a, b**) corresponds to the Raman shift (in wavenumber, cm^{-1}) and the y-coordinate corresponds to the differential Raman intensity in arbitrary units. In a WMR spectrum, a Raman peak is located at the zero crossing point (denoted by the dash-dotted line) while the Raman peak intensity is represented by the peak-to-valley value around that point. The acquisition time for each spectrum is 50 seconds in total (see **Chapter 3 section 3.2.3** for more details).*

Finding differences in the dried total lipid extract between the conditions using Raman spectroscopy is difficult. Investigating those samples by mass spectrometry could be an alternative. Mass spectrometry has been previously used to investigate *M. tuberculosis* lipid content (Sartain *et al.*, 2011).

3.3.3 Lipid quantification using WMR spectroscopy

To obtain the relationship between lipid concentration and Raman peak intensity we used a solvent to dissolve a known lipid mass of a commercial lipid mix (Triglyceride mix, Sigma-Aldrich). The first solvent tested was chloroform, and no signal could be acquired as it evaporates too quickly even when trapped between quartz slides. DMSO was then tested as this solvent does not evaporate fast preserving the lipid concentration while measuring. It was observed that some lipids dissolved in DMSO, but the efficacy of the dissolution was not assessed. This means that the lipid concentration of the solution was not exactly known; however, the dilution factor was known. The lipid mix was diluted in DMSO at several concentrations in order to study the relation between lipid concentration and Raman peak intensity. Pure DMSO and all the lipid dilutions were interrogated by WMR spectroscopy for 150 seconds as total acquisition time. The results are shown in **Fig. 3.10 a** and an enlarged view is presented in **Fig. 3.10 b.** Pure DMSO does not display a peak at 1730 cm^{-1} compared to the solution containing the dissolved lipids. The Raman spectrum of pure DMSO shows a peak around 1440 cm^{-1} where one of the main lipid bands is also located. We observe that the lipid band is slightly shifted compared to the DMSO peak. A shoulder that decreases with lipid intensity can be noticed at 1450 cm^{-1} **Fig. 3.10 a** and **b.**

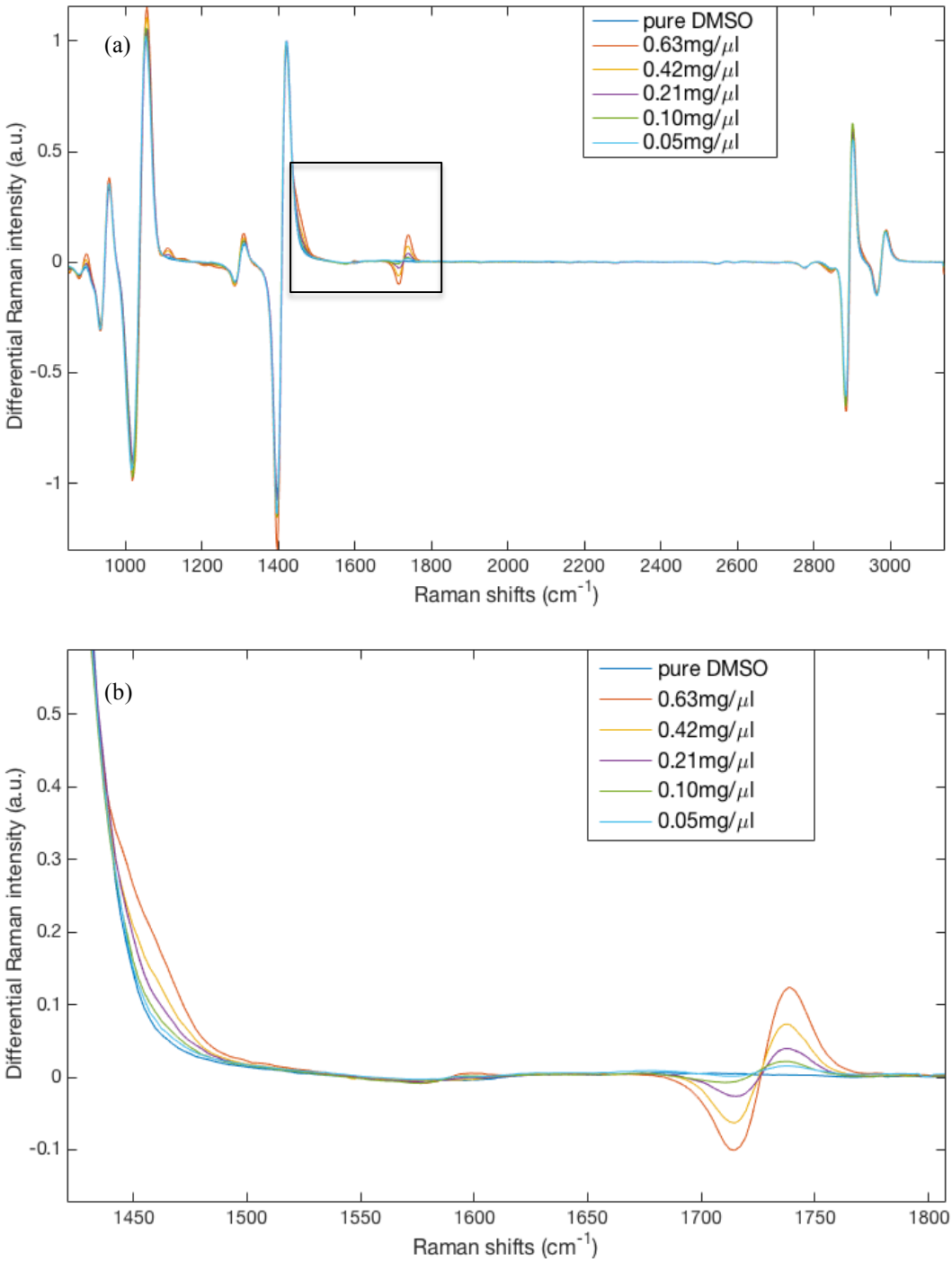

Figure 3.10 *Lipid mix dissolved in DMSO at several concentrations.*

The mean WMR spectra of each condition is calculated over 10 spectra and represented by a coloured line. The x-axis show the Raman shift in wavenumbers (cm^{-1}) and the y-axis displays the Raman intensity in arbitrary units. The ***Fig. 3.10 a*** *presents the WMR spectra of all conditions over a wide range, from 900 to 3100 cm^{-1}. The* ***Fig. 3.10 b*** *is an enlarged view of the* ***Fig. 3.10 a*** *corresponding to the black window (1440 to 1800 cm^{-1}).*

From the WMR spectra, of the diluted lipids in DMSO, the Raman peak intensity at 1730 cm^{-1} have been plotted against to the lipid concentration. The results are shown in **Fig. 3.11.** A linear relationship is found between the Raman intensity and the lipid concentration. The Raman peak intensity (in arbitrary unit) corresponds to 6132 times the lipid concentration value (in $mg.\mu L^{-1}$).

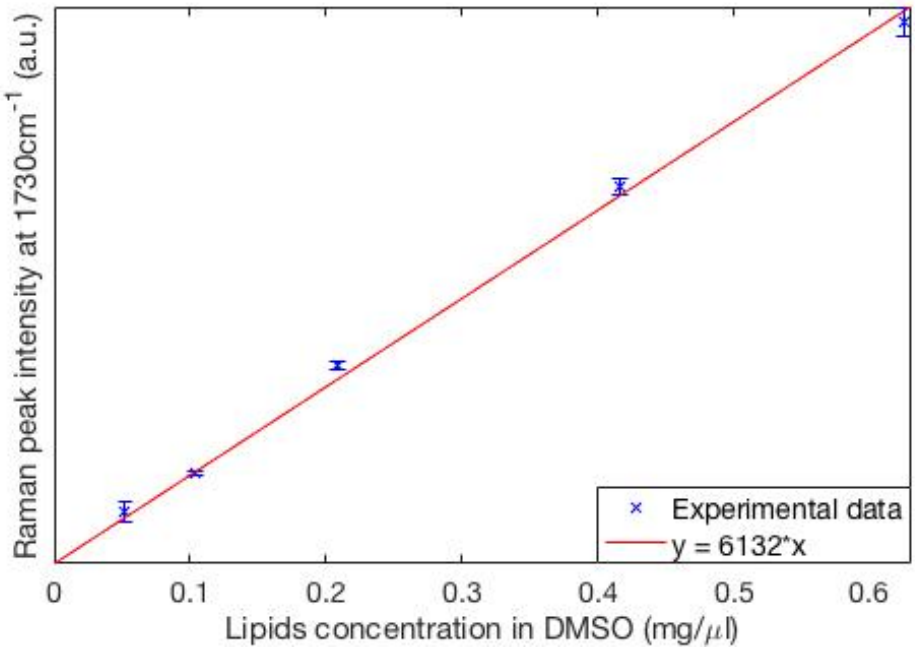

Figure 3.11 *Relation between Raman intensity and lipid concentration.*
The x-axis represents the lipid concentration in mg.μL^{-1}, the y-axis the Raman peak intensity at 1730 cm^{-1}. The dilution points are shown in blue with the corresponding standard deviation represented as error bars. The standard deviations were calculated from 10 values for each condition. A red line represents the relation between the Raman intensity and the lipid concentration.

3.4 Discussion

M. tuberculosis and other mycobacteria species were previously studied and successfully discriminated by Raman spectroscopy (Buijtels *et al.*, 2008, Stockel *et al.*, 2016). These studies provided information about the standard Raman spectrum of *M. tuberculosis*. However, as far as we know, no study has been carried out on *M. tuberculosis* extracted lipids using Raman spectroscopy. The dried total lipid extract interrogated by Raman spectroscopy showed the exact position of the main Raman lipid peaks. The lipid peaks are presented in the **Tab. 3.1** and **Tab. 3.2** are located at: 1063, 1131, 1300, 1449, 1465, 2875 and 2908 cm^{-1}. All those bands can also be associated with lipids, based on Raman database (Movasaghi *et al.*, 2007).

It is important to note that WMR spectroscopy and standard Raman spectroscopy do not produce identical spectra (**Fig. 3.3** and **Fig. 3.4**). Using WMR spectroscopy with PCA, the fluorescence background is subtracted in the WMR spectra (De Luca *et al.*, 2010, Mazilu *et al.*, 2010). In the standard Raman spectrum, the peak at 1465 cm^{-1} (**Fig. 3.3**) is visible but not clearly. The band 1449 and 1465 cm^{-1} are merged; the 1465 cm^{-1} represents a shoulder on the side of the peak. This is therefore very difficult to estimate the intensity of this peak. By comparison the WMR spectrum shows two distinct peaks and both can easily be quantified (**Fig. 3.4)**. Moreover, the ratio between peaks changes between standard Raman spectra and WMR spectra. For example, the ratio between the peak 3 and 4 is different in the standard Raman spectrum (**Fig. 3.3)** and the WMR spectrum (**Fig. 3.4)**. The peak 4 is higher compared to the peak 3 in the standard Raman spectrum; in the WMR spectrum, the opposite is observed. WMR spectroscopy produces clearer spectra, which are easier to interpret compared to standard Raman spectroscopy. The advantages of WMR spectroscopy

over standard Raman spectroscopy have been previously investigated in several studies. WMR spectroscopy presents a much higher signal to noise ratio (PCA being the optimal algorithm to generate WMR spectra) compared to standard Raman spectroscopy (Mazilu *et al.*, 2010), more easily interpreted spectra (De Luca *et al.*, 2010) and greater discrimination ability, finding higher sensitivity and specificity (Canetta *et al.*, 2011).

We observed high variability in peak-to-peak ratios from the same time point (on the same slide between lipid aggregates), as shown in **Fig. 3.6** and **Tab. 3.4**. The heterogeneity, between lipid aggregates, could be linked to a difference in composition but also be representative of the orientation of the lipids presenting different vibrational output between aggregates. This has been previously observed (Czamara *et al.*, 2015). The authors suggested that the variability in Raman spectra of solid lipids is due to differences the lipid chain orientation and differences in polarisation. They interrogated solid tripalmitin with Raman spectroscopy. From one field of view, they showed two spectra from different locations and their average spectrum. The ratio between peaks was very different. The ratio (2870 cm^{-1}/1295 cm^{-1}) from the first location was 10; it was 40 from the second spot and 24 on average over the field of view (Czamara *et al.*, 2015). The high variability among datasets of dried lipid extract led to the impossibility to discriminate between conditions. To avoid the impact of this important heterogeneity, lipid could be in the future studied in a liquid phase. The difficulty is to find a solvent that would dissolve all lipids from the sample and would not evaporate fast to preserve the sample concentration during the acquisition.

This study gave us information about *M.tuberculos*is lipid peaks, their exact position in the Raman spectrum and also where to expect high intensity peaks (around 1300 cm^{-1} and 1450 cm^{-1}). This method cannot tell us more about the specific nature of the lipid molecules that are present in the samples. Other methods could be applied, such as mass spectrometry to give accurate mass value and therefore identify specifically the molecules that are present in the sample (Sartain *et al.*, 2011). We investigated the samples shown in this study using mass spectrometry but we have not finished the study and the data analysis. Further work in this direction are required.

Raman spectroscopy is a quantitative methodology (Hanlon *et al.*, 2000), we investigated the relationship between Raman intensity and lipid concentration to demonstrate the quantitative aspect of our Raman system. A linear relationship between the lipid concentration and the Raman peak intensity is observed (**Fig. 3.11**). This means that if a lipid peak is double the size in a first item compared to another there is twice as much lipid in the first item. The efficacy of DMSO to dissolve those lipids was not assessed; therefore, it is not possible to associate an intensity value to an exact lipid concentration. The Raman spectroscopy set-up makes it possible to quantify the lipid content but the difficulty is to convert the Raman intensity (in arbitrary unit) to a concentration (in $mg.\mu L^{-1}$). It would be possible to associate the Raman intensity to a concentration if the same lipids were present in both the serial dilution and the sample and if the solvent can dissolve all those lipids. This would also be easier with a solvent that does not show Raman peaks at the same location than lipids. Further investigation in this direction could be done in future aiming at quantifying the exact lipid concentration (in $mg.\mu L^{-1}$) of a single *Mycobacterium tuberculosis* cell using WMR spectroscopy.

Direct quantification of β-carotene in lipid bodies of algae has been performed using Raman spectroscopy (Pilat *et al.*, 2012). Being able to associate Raman lipid peak intensity from a single bacterium to a lipid concentration could represent a future investigation. The use of mass spectrometry could permit investigation of the lipid content from different condition accurately; this method would provide a list of the lipid molecules present and their abundance.

In summary, this initial study provides the exact lipid Raman peak positions and confirms the quantitative aspect of the approach. This is very important to investigate single bacteria. Moreover, it presents some of the advantages of using WMR spectroscopy.

Chapter 4 Remote sensing of mycobacteria cell states (LR and LP) *in-vitro* using Raman spectroscopy

4.1 Introduction

The results of recent tuberculosis clinical trials have demonstrated that a regimen which, rendered patients culture negative more rapidly could still be associated with a high relapse rate (Gillespie *et al.*, 2014). This key result illustrates the importance of understanding mycobacterial cells that are dormant and could survive treatment in human tissue. *In-vitro* models show that "dormant" phenotype is associated with a lower metabolic rate, phenotypic resistance to antibiotics and accumulation of lipids in intracellular bodies (Baek *et al.*, 2011, Daniel *et al.*, 2004, Deb *et al.*, 2009, Wayne and Hayes, 1996). In mycobacteria, lipid inclusions have been described both *in-vitro* and in sputum samples (Garton *et al.*, 2002). An important Rpf-dependent population have been described in tuberculous sputum samples (Mukamolova *et al.*, 2010). Direct study on tuberculous sputum samples showed the presence of lipid body-positive cells and slowly replicating bacteria (Garton *et al.*, 2008). Completing the link between lipid body positive cells and the clinical outcome, it has been shown recently that these cells are up to 40 times more tolerant to key components of the treatment regimen such as rifampicin (Hammond *et al.*, 2015). Being able to identify both phenotypes (lipid rich and lipid poor) is a crucial research target to understand how to shorten TB treatment. Different methodologies have been applied to study the lipid rich and poor cells of mycobacteria species. Lipid storage was investigated using

staining methods and fluorescence microscopy. Using these techniques, it was shown that the abundance of lipid rich cells increases as the culture aged and also that the buoyant density of the cells decreases in an older culture (Deb *et al.*, 2009). This means that the buoyant density of a LR cell differs from a LP cell. The lipid bodies have also been studied directly using electron microscopy revealing a monolayer surrounding the lipid bodies (Bleck *et al.*, 2010). In this chapter we investigate the capacity of an all-optical, label-free and non-destructive method, Raman spectroscopy, to discriminate mycobacterial phenotypes (LR and LP) in cultures. Raman spectroscopy has been widely used for bacterial identification, in medically relevant organisms for example (Maquelin *et al.*, 2002b). Raman spectroscopy has been successfully applied to discriminate between mycobacterial species including *M. tuberculosis* (Buijtels *et al.*, 2008, Stockel *et al.*, 2016). The ability of Raman spectroscopy to discriminate mycobacterial phenotypes (LR and LP) at a single cell level is investigated in this study. Two techniques are compared: standard Raman spectroscopy and WMR spectroscopy to validate the best Raman method for future TB infected tissue studies.

4.2 Methods

4.2.1 Sample preparation for Raman spectroscopy

The cells were heat inactivated at 80°C for 20 minutes. They were separated using D_2O as described previously (see **Chapter 2 General methods section 2.3**). Similarly, 100 µL of both top and bottom fraction were harvested, the cells were spun down for three minutes at 20,000 x g, the supernatant was slowly removed and discarded. The cells were resuspended in 100 µL of PBS, and 20 µL was placed on a thin quartz slide left to air dry. Once the thin quartz slide was dry a thick quartz slide with a spacer was filled with 15 µL of PBS, and the thin slide was placed on the top of it upside down. In this way, the cells were captured inside the spacer and within PBS. The mount was then sealed using transparent nail polish. This sample slide was placed on a high NA microscope objective with the thin slide at the bottom and interrogated using Raman spectroscopy. In parallel, the fractions were stained with Nile red and observed under fluorescence microscopy to understand their purity (see **Chapter 2 General methods section 2.5 and 2.6**).

4.2.2 Deuterium oxide separation using centrifugation

The full protocol is presented in **Appendices Section 2.** A tube holder (**Appendices Section 2, picture 1**) was designed using the software Rhinoceros3D version 5.0 (Robert McNeel & Associates, USA) and the item was printed using an Up! Plus 3D Printer (Tiertime, USA). This tube holder was printed with polylactic acid (PLA) and acrylonitrile butadiene styrene (ABS). A 50 mL Falcon tube was filled with paper tissue at the bottom (**Appendices Section 2, picture 2**). One mL of cell culture was

harvested and washed three times using PBS. For each washing step the cells were spun down at 20,000 x g for three minutes, the supernatant discarded and 1 mL of PBS was added.

In order to get LR cells from liquid culture, the cellular pellet was resuspended in 755 µL of MiliQ H_2O, this volume was transferred into a 2 mL plastic Eppendorf tube, and 450 µL of D_2O solution were added. This achieved a final density of 1.04 $g.mL^{-1}$. The solution was mixed using a pipette. The tube was placed into a tube holder (3D-printed) the holder was inserted into a 50 mL Falcon tube see **Appendices Section 2, picture 2**. The tube was centrifuged at 500 x g (1500 rpm on the J6-M1 centrifuge) for 15 minutes. Only the top fraction (the first 100 µL) was harvested. And placed in a 1.5 mL plastic Eppendorf tube (**Appendices Section 2, picture 3**).

In order to separate the LP cells from the culture, the cellular pellet was resuspended in 280 µL of MiliQ H_2O this volume was placed in a 2 mL plastic Eppendorf tube, 830 µL of D_2O were added (1.08 $g.mL^{-1}$ final density). The 2 mL plastic Eppendorf tube was placed in a tube holder (3D-printed) the holder was then inserted into a 50 mL Falcon tube see **Appendices Section 2, picture 2**. The tube was centrifuged at 35 x g (400 rpm on the J6-M1 centrifuge) for 15 minutes. The bottom fraction was harvested (100 µL). 100 µL was harvested from the bottom fraction and care was taken not to disturb the pellet, see **Appendices Section 2, picture 4**.

The purity of the factions (LR and LP) was investigated using Nile red staining or WMR spectroscopy. If the purity was not high enough the centrifugation step was repeated. 1 mL of 1.04 $g.mL^{-1}$ (for LR) or 1.08 $g.mL^{-1}$ (for LP) solution was added to the 80 µL of remaining harvested cells and centrifuged again. The top (LR) or bottom (LP) fraction was then harvested and investigated.

4.3 Results

All the experiments in this chapter were conducted using the Raman spectroscopy system 1 (see **Chapter 2 General methods section 2.12**).

4.3.1 Conventional Raman spectroscopy

Mycobacteria from stationary phase culture were harvested and separated using D_2O separation. Both top (LR) and bottom (LP) fractions were interrogated using standard Raman spectroscopy. The experiment was performed with three mycobacteria species: *M. smegmatis*, *BCG* and *M. tuberculosis*. Conventional Raman spectra of single bacteria were taken, from more than 60 LR and LP cells *in-vitro* (randomly chosen from the slides). **Fig. 4.1 a, c, e** show the mean spectrum, of LR (red) and LP (green) averaged over all *in-vitro* conventional Raman spectra; the coloured areas are representing the associated single standard deviations. Major differences between the two cells subsets are found around 1300 cm^{-1} (lipid band A) and 1440-1450 cm^{-1} (lipid band B) in **Fig. 4.1 a, c, e**. LR cells show higher Raman peak intensity in these two bands compared to LP cells.

We applied a multivariate statistical analysis: Principal Component Analysis (PCA) (Ringner, 2008) to analyse all spectra from LR and LP data sets (for more detail see **Chapter 1 Introduction section 1.5.6** and **Chapter 2 General methods section 2.10)**. All the principal components (PCs) obtained through the PCA are orthogonal to each other. PCs are listed in a decreasing order; where the PC1 accounts for more of the variation in spectra than PC2 and so on. The first 7 PCs are used to calculate the specificity and sensitivity with the leave-one-out cross validation (LOOCV) for each

data point (for more details see **Chapter 1 Introduction section 1.5.7** and **Chapter 2 General methods section 2.11**). The first 7 PCs correspond to more than 80% of the total variance in all spectra of each data set. In the 3D space corresponding to the first three PCs clear LR and LP clusters are observed as shown in **Fig. 4.1 b, d, f**. The two phenotypes (LR and LP) are distinguished with high specificity and sensitivity, shown in **Tab. 4.1**. These results show that the LR cells can be discriminated from LP cells using standard Raman spectroscopy.

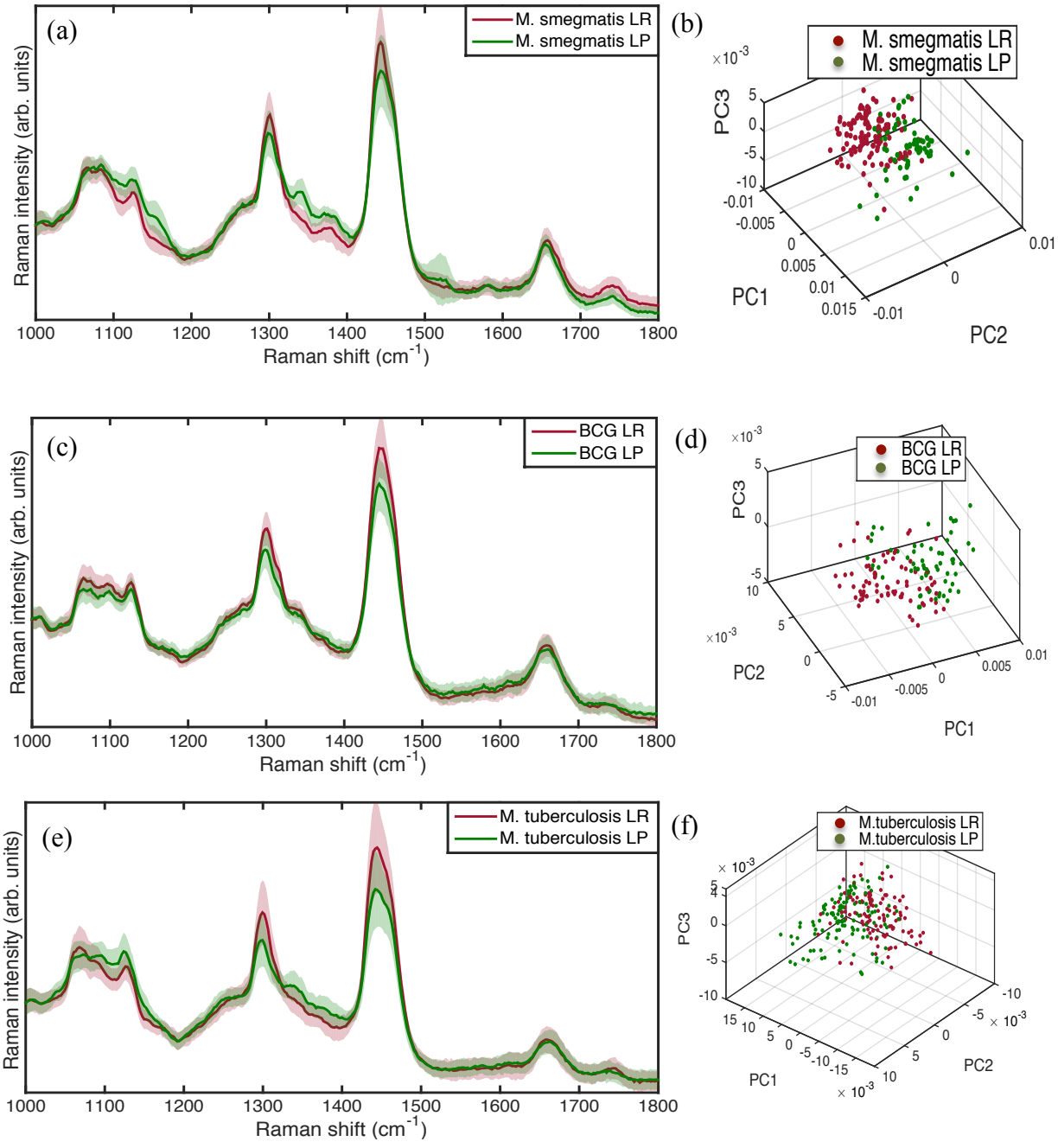
(a)
M. smegmatis LR
M. smegmatis LP
Raman intensity (arb. units)
Raman shift (cm-1)
(b)
M. smegmatis LR
M. smegmatis LP
PC1
PC2
PC3
(c)
BCG LR
BCG LP
Raman intensity (arb. units)
Raman shift (cm-1)
(d)
BCG LR
BCG LP
PC1
PC2
PC3
(e)
M. tuberculosis LR
M. tuberculosis LP
Raman intensity (arb. units)
Raman shift (cm-1)
(f)
M.tuberculosis LR
M.tuberculosis LP
PC1
PC2
PC3

Figure 4.1 *LR and LP mycobacteria compared using standard Raman spectroscopy. Three mycobacteria were interrogated: M. smegmatis, BCG and M. tuberculosis. The* ***Fig. 4.1 a, c, e*** *shows LR (red curves), and LP (green curves) mean spectra calculated from over 60 spectra, of single cells, acquired using standard Raman spectroscopy. The coloured area corresponds to the single standard deviation associated with the mean spectra. In* ***Fig. 4.1 a, c, e*** *the x-axis represents the Raman shift (in wavenumber, cm^{-1}) and the y-axis shows the Raman intensity in arbitrary units. Using principal component analysis, the spectra of both LR and LP were processed. The* ***Fig. 4.1 b, d, f*** *presents the PCA plots corresponding to the first three PCs. In this 3D space, each dot corresponds to a single bacterium. Clear LR and LP clusters can be observed. The time to acquire a Raman spectrum from a single bacterium was 30 seconds for both the background and the signal. The window chosen for the study starts at 1000 cm^{-1} and ends at 1800 cm^{-1}. This region presents several Raman peaks associated with lipids. The two main lipid peaks are the lipid band A (1300 cm^{-1}) and the lipid band B (1440-1450 cm^{-1}).*

Table 4.1 Sensitivity and specificity of LR and LP *M. tuberculosis*, BCG and *M. smegmatis* cells (calculated from conventional Raman spectra).

Species (lipid rich/lipid poor)	**Sensitivity**	**Specificity**
M. smegmatis (n=1)	95.9 %	92.4 %
BCG (n=1)	82.6 %	87.5 %
M. tuberculosis (n=1)	82.1 %	79.5 %

The calculation of sensitivity and specificity is explained in detail in **Chapter 1 Introduction section 1.5.7** and **Chapter 2 General methods section 2.11**. Both LR and LP phenotype have been discriminated using standard Raman spectroscopy with high sensitivity and specificity. However, WMR spectroscopy could potentially bring higher discriminative power by removing the auto-fluorescence background coming from the sample.

4.3.2 WMR spectroscopy

4.3.2.1 Optimisation of the acquisition time

An experiment was designed to define the optimal acquisition time to study *M. tuberculosis* phenotypes using WMR spectroscopy. The time required to obtain one WMR spectrum corresponds to the acquisition time multiplied by the number of accumulations (gives the time needed for one spectrum) times five (as five distinct spectra are taken while the laser wavelength is modulated). These five spectra are used to construct the WMR spectra. For example, 1x5x5 seconds stands for one second acquisition, 5 times accumulated to create one spectrum, and 5 spectra like this one are acquired while the laser wavelength is changing to create one WMR spectrum. So in the case of 1x5x5, the total WMR spectrum acquisition time

corresponds to 25 seconds (5 spectra of 5 seconds each). The different acquisition times tested are presented in the **Fig. 4.2**. For each condition, WMR spectra of over 30 single LR and LP cells were taken *in-vitro*. The red (LR) and the green (LP) curve in **Fig. 4.2 a, b, c and d** show the mean spectrum averaged over all *in-vitro* modulation Raman spectra, the associated standard deviations being represented by the coloured areas. The purity of the fractions, LR and LP, was assessed by fluorescence microscopy.

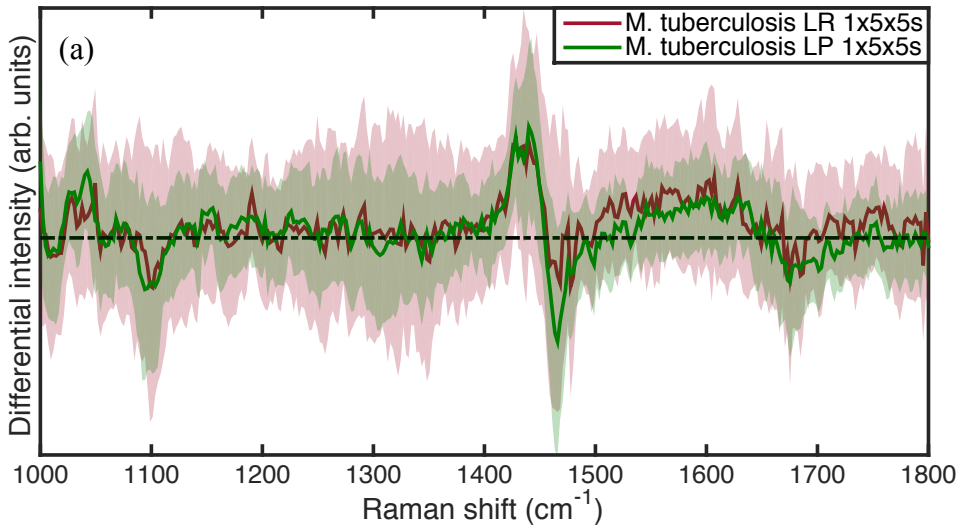
(a)
M. tuberculosis LR 1x5x5s
M. tuberculosis LP 1x5x5s
Differential intensity (arb. units)
1000
1100
1200
1300
1400
1500
1600
1700
1800
Raman shift (cm-1)

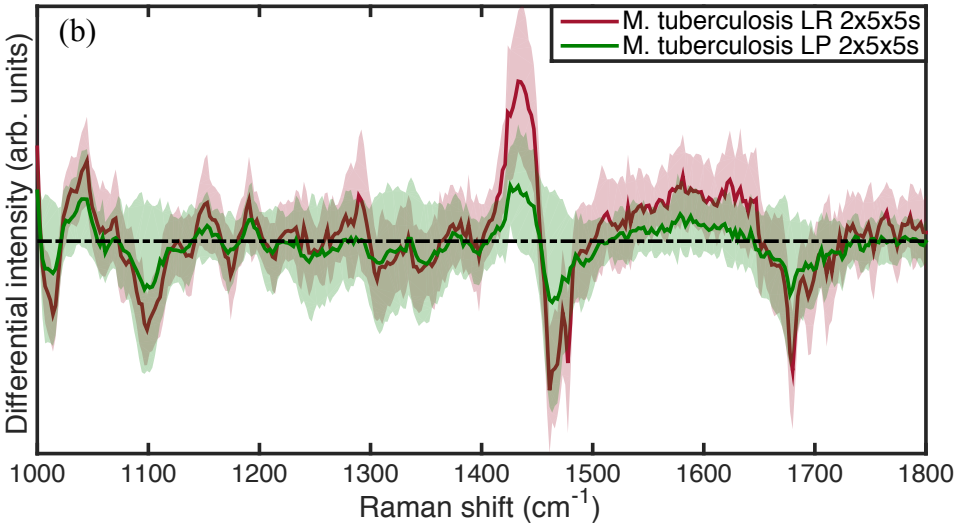
(b)
M. tuberculosis LR 2x5x5s
M. tuberculosis LP 2x5x5s
Differential intensity (arb. units)
1000
1100
1200
1300
1400
1500
1600
1700
1800
Raman shift (cm-1)

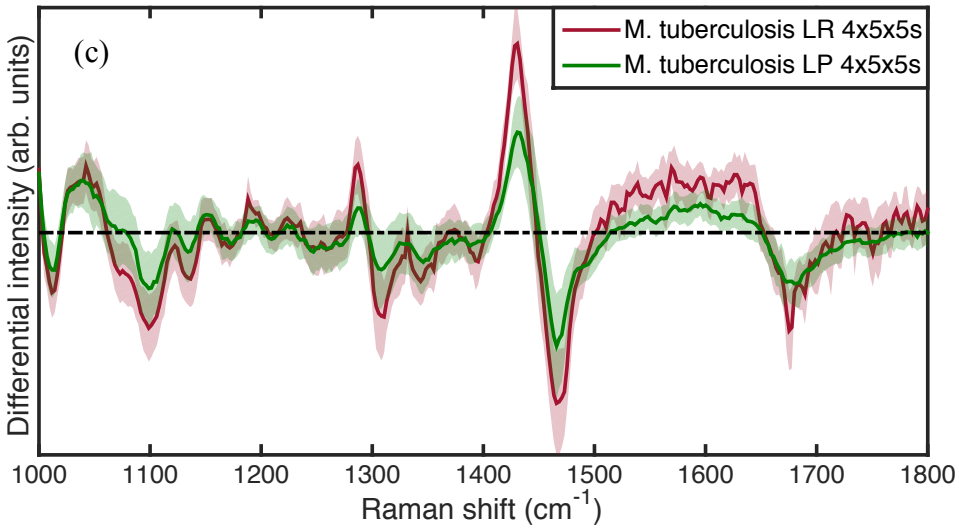
(c)
M. tuberculosis LR 4x5x5s
M. tuberculosis LP 4x5x5s
Differential intensity (arb. units)
1000
1100
1200
1300
1400
1500
1600
1700
1800
Raman shift (cm-1)

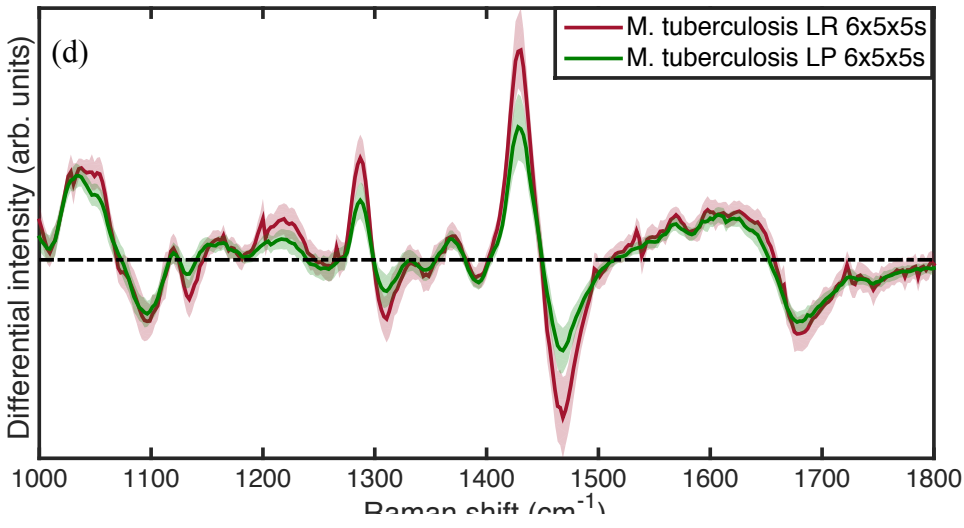
(d)
M. tuberculosis LR 6x5x5s
M. tuberculosis LP 6x5x5s
Differential intensity (arb. units)
1000
1100
1200
1300
1400
1500
1600
1700
1800

Figure 4.2 *Optimisation of acquisition time for M.tuberculosis single cell using WMR spectroscopy.*

The ***Fig. 4.2 a, b, c, d*** *shows LR (red curves) and LP (green curves) mean spectra calculated from 30 to 40 spectra, of single cells, acquired using WMR spectroscopy. The coloured area corresponds to the single standard deviation associated with the mean spectra. In* ***Fig. 4.2 a, b, c, d*** *the x-axis represents the Raman shift (in wavenumber, cm^{-1}) and the y-axis shows the differential Raman intensity in arbitrary units. In a WMR spectrum, the Raman peaks correspond to the zero crossing point (the point where the curve cross the dash-dotted line); the Raman peak intensity is the peak-to-valley value around this zero crossing. The total acquisition time for one WMR spectrum is 25 seconds (****Fig. 4.2 a****), 50 seconds (****Fig. 4.2 b****), 100 seconds (****Fig. 4.2 c****) and 150 seconds (****Fig. 4.2 d****) (see* ***Chapter 2 General methods section 2.8*** *for more details). The window chosen for the study starts at 1000 cm^{-1} and end at 1800 cm^{-1}. This region presents several Raman peaks associated with lipids. The two main lipid peaks are the lipid band A (1300 cm^{-1}) and the lipid band B (1440-1450 cm^{-1}).*

The first two acquisitions times tested (1x5x5 seconds and 2x5x5 seconds) display very low Raman intensity and a very high noise level that is visible in the **Fig. 4.2. a** and **b**. The standard deviation is very important in these two conditions. Moreover, the noise level reduces compared to the Raman intensity as the acquisition time increases. The information cannot be extracted from the spectra if the signal to noise level is too low, the differences have to come from the Raman peaks and not from noise. When total acquisition was increased to 100 seconds (4x5x5 seconds), a much better signal to noise ratio was observed compared to previously **Fig. 4.2. c**. However, the noise level and, therefore, the standard deviation remained high. For example, many little peaks due to noise could be found between 1500 and 1800 cm^{-1} **Fig. 4.2. c.** The next total acquisition time tested was 150 seconds (6x5x5 seconds), which showed a good signal to noise ratio and a low standard deviation **Fig. 4.2. d**. The acquisition time 6x5x5 seconds was chosen and used for all the future WMR spectroscopy measurements of single mycobacteria. The **Fig. 4.2. d** is also presented in **Fig. 4.3. e.**

4.3.2.2 WMR spectroscopy on *in-vitro* LR and LP cells

Mycobacteria from stationary phase culture were harvested and separated using D_2O separation. Both top and bottom fractions were stained using Nile red and observed with fluorescence microscopy. A clear enrichment in LR cells was observed in the top fraction; similarly, the bottom fraction showed mainly LP cells. The LR and LP fractions used in Raman spectroscopy were over 90% pure based on direct microscopy counts assessed by eye. The experiment was performed with three mycobacteria species: *M. smegmatis*, *BCG* and *M. tuberculosis*. WMR spectra of

single bacteria were taken, from approximately 60 LR and LP cells *in-vitro* (randomly chosen from the slides). The differences between LR and LP WMR spectra are mostly the same than observed in the standard method. LR cells display higher Raman peak intensity in both lipid bands A and lipid band B compared to LP cells **Fig. 4.3 a, c, e**. We applied the PCA to analyse all spectra of each LR and LP subsets. The first 7 PCs represent over 70% of the total variance in all WMR spectra from each phenotype set. With only the first 3 PCs distinct cluster can be identified as shown in **Fig. 4.3 b, d, f**. LR and LP phenotypes are distinguished with high specificity and sensitivity as shown in **Tab. 4.2.** In order to calculate the sensitivity and specificity, the first 7 PCs are used in the LOOCV for each cell subsets. The sensitivity and specificity are higher when using WMR spectroscopy compared to conventional Raman spectroscopy.

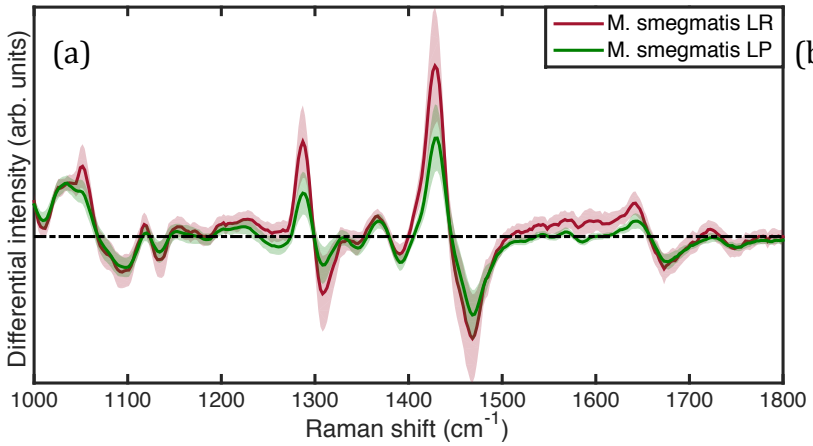
(a)
M. smegmatis LR
M. smegmatis LP
Differential intensity (arb. units)
Raman shift (cm-1)
1000
1100
1200
1300
1400
1500
1600
1700
1800

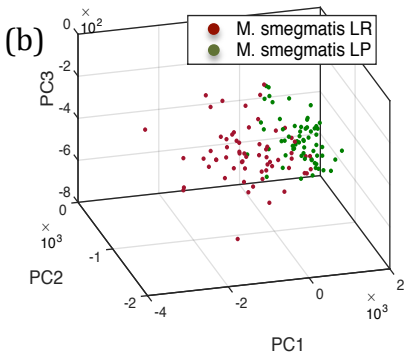
(b)
M. smegmatis LR
M. smegmatis LP
PC3
PC2
PC1

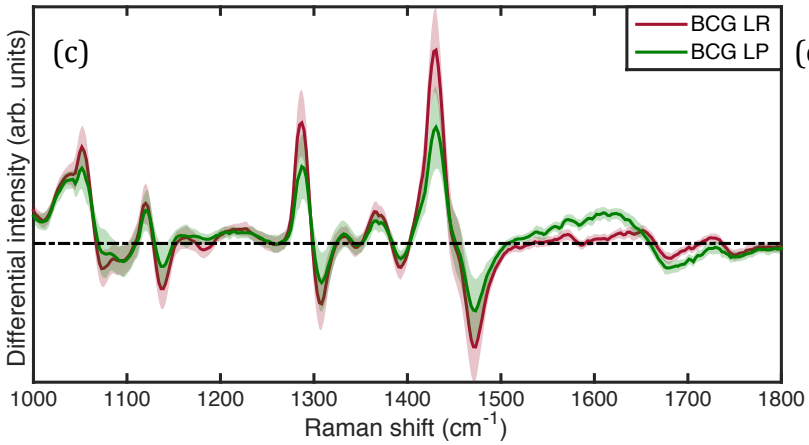
(c)
BCG LR
BCG LP
Differential intensity (arb. units)
Raman shift (cm-1)
1000
1100
1200
1300
1400
1500
1600
1700
1800

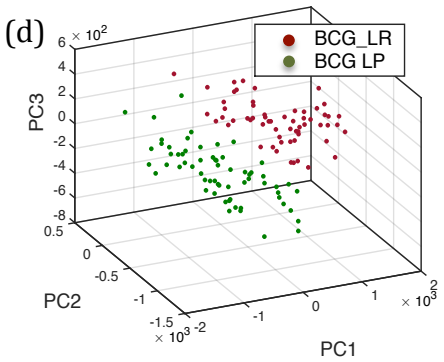
(d)
BCG_LR
BCG LP
PC3
PC2
PC1

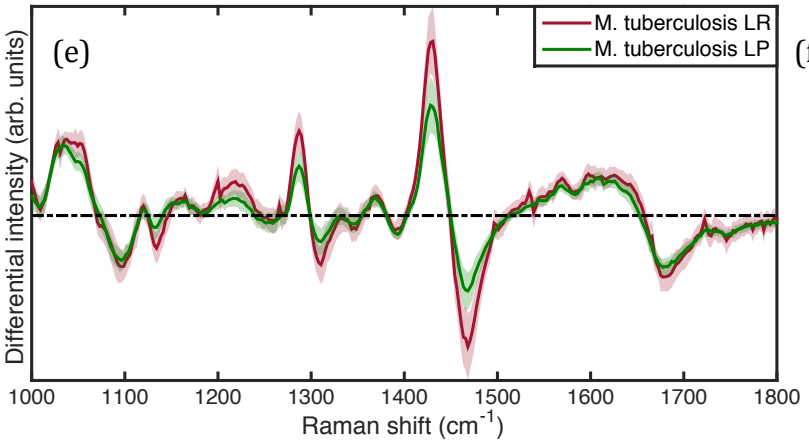
(e)
M. tuberculosis LR
M. tuberculosis LP
Differential intensity (arb. units)
Raman shift (cm-1)
1000
1100
1200
1300
1400
1500
1600
1700
1800

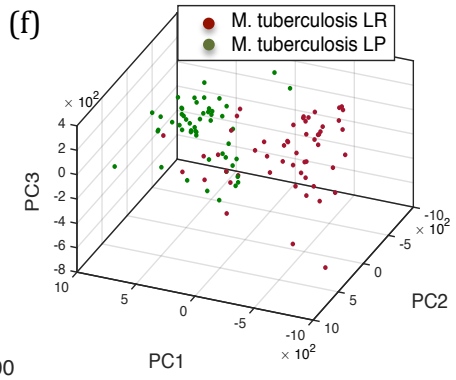
(f)
M. tuberculosis LR
M. tuberculosis LP
PC3
PC2
PC1

Figure 4.3 *WMR spectroscopy on LR and LP cells of M. smegmatis, BCG and M. tuberculosis.*

The ***Fig. 4.3 a, c, e*** *shows LR (red curves) and LP (green curves) mean spectra calculated from approximately 60 spectra, of single cells, acquired using WMR spectroscopy. The coloured area corresponds to the single standard deviation associated with the mean spectra. In* ***Fig. 4.3 a, c, e*** *the x-axis represents the Raman shift (in wavenumber, cm^{-1}) and the y-axis shows the differential Raman intensity in arbitrary units. In a WMR spectrum, the Raman peaks correspond to the zero crossing point (the point where the curve crosses the dash-doted line); the Raman peak intensity is the peak-to-valley value around this zero crossing. Using principal component analysis, the spectra of both LR and LP were processed. The* ***Fig. 4.3 b, d, f*** *presents the PCA plots corresponding to the first three PCs. In this 3D space, each dot corresponds to a single bacterium. Clear LR and LP clusters can be observed. The total acquisition time for one WMR spectrum was 150 seconds (see* ***Chapter 2 General methods section 2.8*** *for more details). The window chosen for the study starts at 1000 cm^{-1} and end at 1800 cm^{-1}. This region presents several Raman peaks associated with lipids. The two main lipid peaks are the lipid band A (1300 cm^{-1}) and the lipid band B (1440-1450 cm^{-1}).*

Table 4.2 Sensitivity and specificity of lipid poor and lipid rich *M. tuberculosis*, BCG and *M. smegmatis* cells (calculated from WMR spectra).

Cell type (lipid rich/lipid poor)	**Sensitivity**	**Specificity**
M. smegmatis (n=1)	96.8 %	93.8 %
BCG (n=1)	96.8 %	100 %
M. tuberculosis (n=1)	96.1 %	92.6 %

4.3.3 D_2O separation using centrifugation

The D_2O separation has an overnight step; to speed up this protocol and reduce the stress to the bacteria undergoing separation, a protocol of separation using centrifugation have been developed. The protocol is presented in the **Appendix Section 2**. This protocol uses two steps to obtain both LR and LP cell from one bacterial culture. Each step was optimised to get high purity of either LR (lower density solution, higher centrifugation speed and harvested the top) or LP (higher density solution, slower centrifugation speed and harvested the bottom above the pellet). Firstly, to obtain LR bacteria, cells were resuspended in a low density solution (1.04 $g.mL^{-1}$) and centrifuged at 500 x g for 15 minutes. The top fraction, enriched in LR cells, was subsequently harvested. The second step, to separate LP bacteria, used a higher density solution (1.08 $g.mL^{-1}$) and a lower centrifugation speed (35 g for 15 minutes). The bottom of the tube, enriched in LP cells, was harvested. Bacteria remain less than 20 minutes in H_2O/D_2O solution, and both LR and LP bacteria can be obtained within one hour.

Initial experiments were carried out using *M. smegmatis* to validate this protocol. First using Nile red staining to get the proportion, of LR and LP, for each set. One example of both LR and LP preparation are shown in **Fig. 4.4** and **Fig. 4.5** respectively**.** A clear enrichment was observed in both LR and LP fraction. LR fraction was found to

be 92% pure based on the count of 134 bacteria and LP fraction 90% pure based on the count of 351 bacteria.

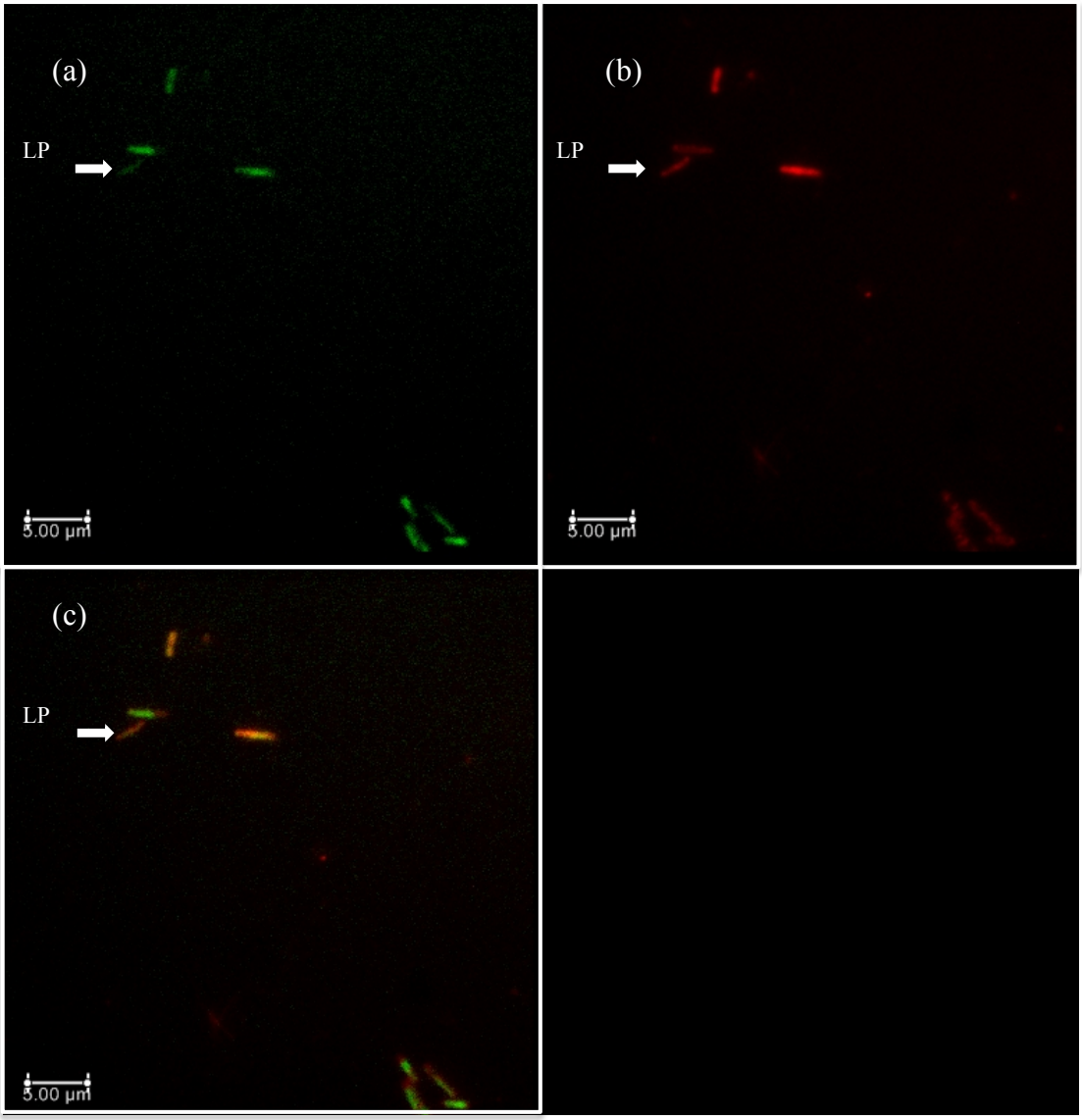

Figure 4.4 *Nile red stained M. smegmatis from the top fraction (LR) of the centrifuged D_2O separation.*

Bacteria were centrifuged in H_2O/D_2O solution (density, 1.04 $g.mL^{-1}$) at 500 g for 15 minutes. The top fraction was harvested and Nile red stained (2.5 $\mu g.mL^{-1}$) (see ***Chapter 2 General methods section 2.5*** *for more details). The fraction was observed under fluorescence microscopy (see* ***Chapter 2 General methods section 2.6*** *for more details). The figure shows: the green emission in* ***Fig. 4.4. a*** *that corresponds to intracellular non-polar lipids, the red emission in* ***Fig. 4.4.b*** *that represents the polar lipid and the combined picture in* ***Fig. 4.4. c****. In this figure, the white arrow shows a LP cell, all the other bacteria in this picture are LR. The scale bar represents 5 µm.*

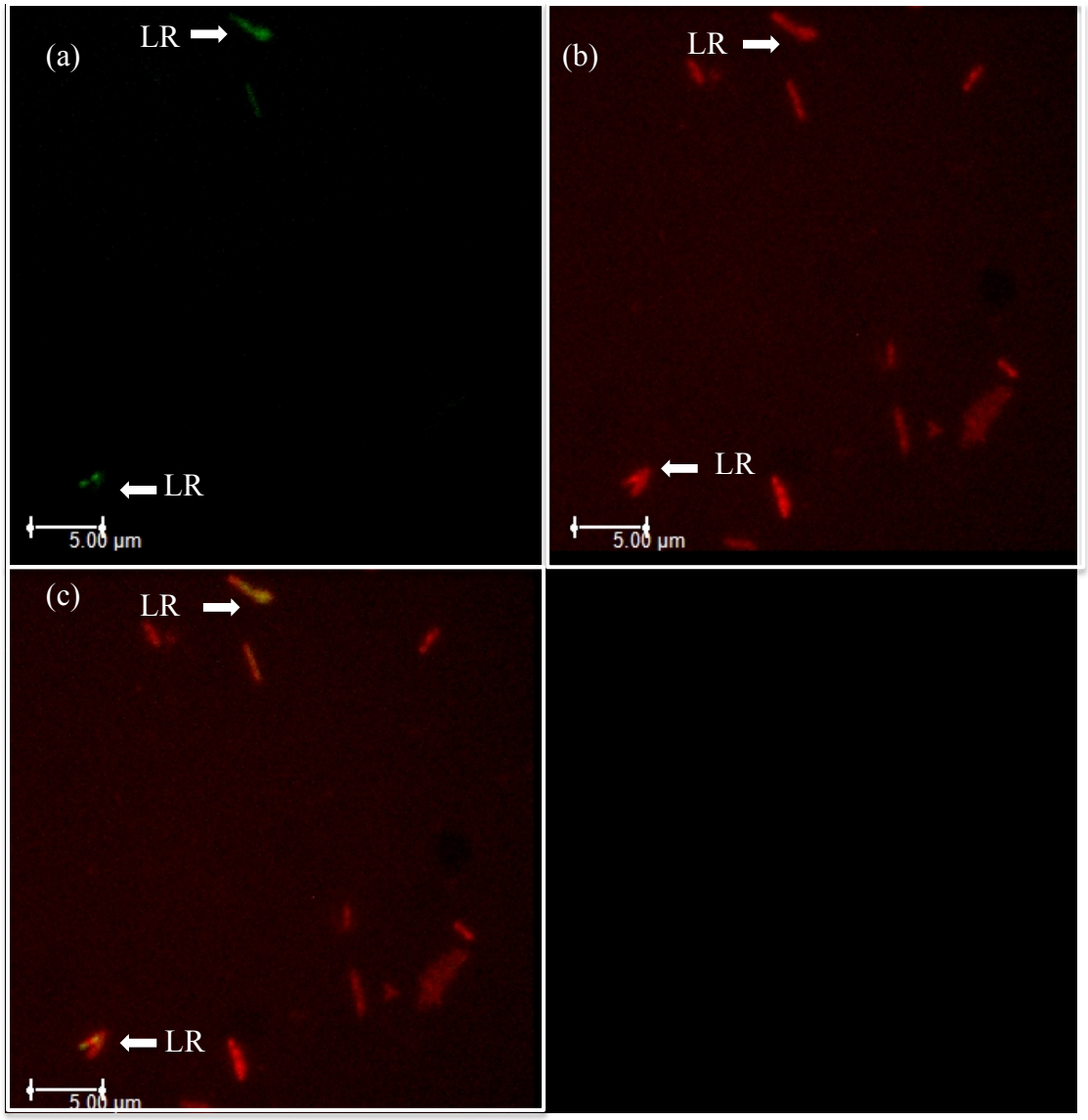

Figure 4.5 *Nile red stained M. smegmatis from the bottom fraction (LP) of the centrifuged D_2O separation.*

Bacteria were centrifuged in H_2O/D_2O solution (density, 1.08 $g.mL^{-1}$) at 35 g for 15 minutes. The bottom fraction was harvested and Nile red stained (2.5 $\mu g.mL^{-1}$, see ***Chapter 2 General methods section 2.5*** *for more details). The fraction was observed under fluorescence microscopy (see* ***Chapter 2 General methods section 2.6*** *for more details). The figure shows: the green emission in* ***Fig. 4.5. a*** *that corresponds to intracellular non-polar lipids, the red emission in* ***Fig. 4.5. b*** *that represents the polar lipid and the combined picture in* ***Fig. 4.5. c****. In this figure, the white arrow shows a LR cell, all the other bacteria in this picture are LP. The scale bar represents 5 µm.*

The centrifugation D_2O separation was tested on *M. tuberculosis* and the fractions interrogated by WMR spectroscopy. After processing the two sets (LR and LP) were successfully discriminated with both high sensitivity (0.88) and specificity (0.95) using the first 7 PCs (corresponding to 75.3% of the total variance). The average spectra of *M. tuberculosis* LR and LP cells are shown in **Fig. 4.6. a** and the corresponding PCA plot is presented in **Fig. 4.6. b.** Based on those initial experiments it seems that the centrifuged D_2O separation could be an interesting way of getting enriched fraction in LR and LP cells. More repeats should be performed to strengthen these results.

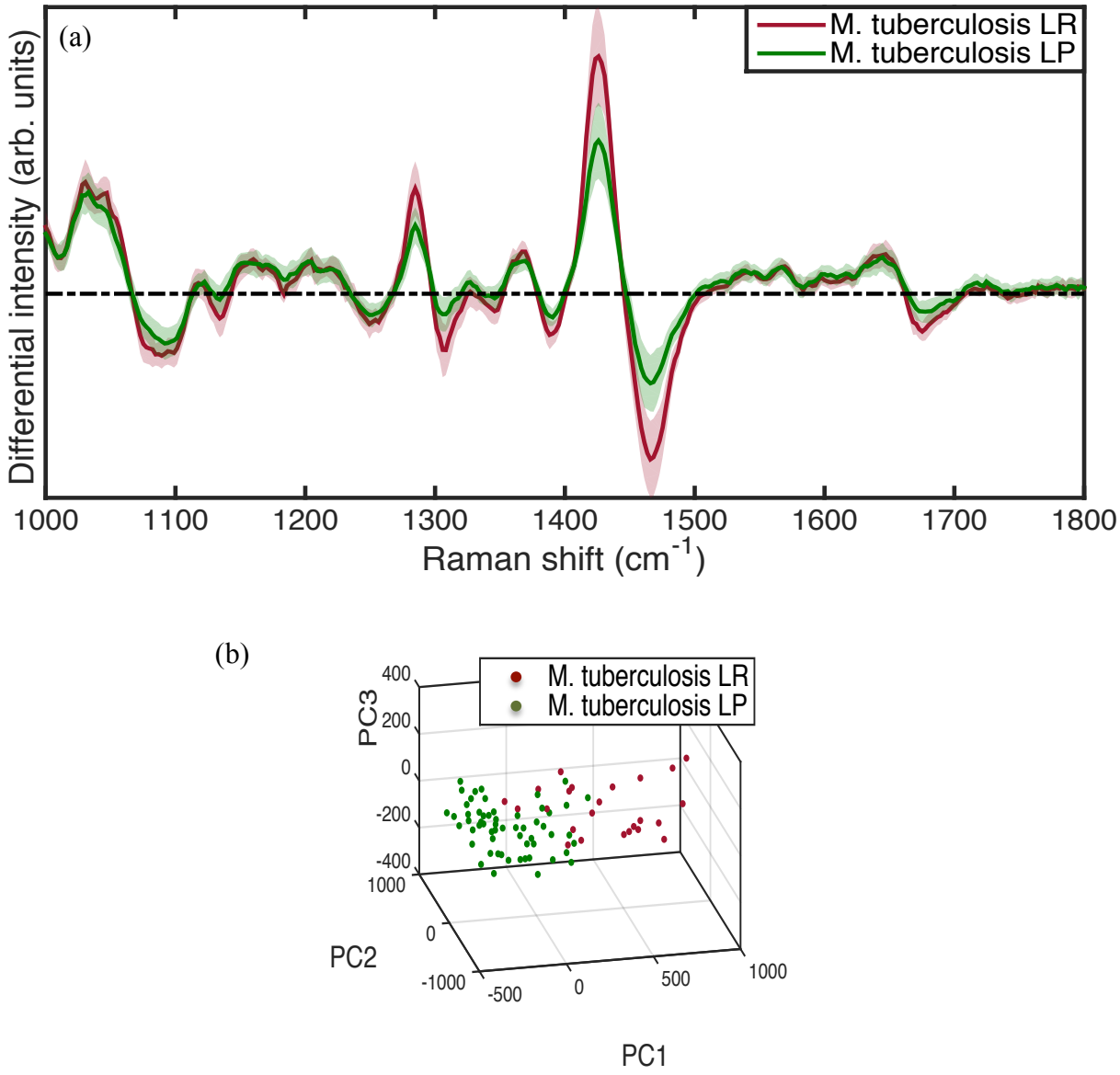

Figure 4.6 *WMR spectra of M. tuberculosis LR and LP fraction after centrifugation D_2O separation and their corresponding PCA cluster.*

*The **Fig. 4.6 a** shows LR (red curves) and LP (green curves) mean spectra calculated from approximately ~30 (LR) and ~60 (LP) spectra, of single cells, acquired using WMR spectroscopy. The coloured area corresponds to the single standard deviation associated with the mean spectra. In **Fig. 4.6 a** the x-axis represents the Raman shift (in wavenumber, cm^{-1}) and the y-axis shows the differential Raman intensity in arbitrary units. In a WMR spectrum, the Raman peaks correspond to the zero crossing point (the point where the curve crosses the dash-doted line); the Raman peak intensity is the peak-to-valley value around this zero crossing. Using principal component analysis, the spectra of both LR and LP were processed. The **Fig. 4.6 b** presents the PCA plots corresponding to the first three PCs. In this 3D space, each dot corresponds to a single bacterium. Clear LR and LP clusters can be observed. The total acquisition time for one WMR spectrum was 150 seconds (see **Chapter 2 General methods section 2.8** for more details). The window chosen for the study starts at 1000 cm^{-1} and end at 1800 cm^{-1}. This region presents several Raman peaks associated with lipids. The two main lipid peaks are the lipid band A (1300 cm^{-1}) and the lipid band B (1440-1450 cm^{-1}).*

4.4 Discussion

Raman spectroscopy provides global information, about all components of the cell, requires minimal sample preparation and can target a single bacteria (Wagner, 2009). This technology has already been used to study mycobacteria and discriminate species but not using the WMR spectroscopy technique (Buijtels *et al.*, 2008, Stockel *et al.*, 2016). More importantly, Raman spectroscopy has never been used to discriminate mycobacterial phenotypes. Our findings using Raman spectroscopy indicate that discrimination between the two phenotypes (LR and LP) can be realised with both standard and WMR spectroscopy techniques (**Fig. 4.1** and **Fig. 4.3**). These results also highlight the advantages of using WMR spectroscopy over standard Raman spectroscopy to investigate phenotypic differences among bacterial species. WMR spectroscopy brings both higher sensitivity and specificity (**Tab. 4.1** and **Tab 4.2**). In this method, the Raman excitation corresponds to a scan of laser wavelength and when combined with multivariate statistical analysis it allows a complete fluorescence background removal (De Luca *et al.*, 2010, Chen *et al.*, 2015). However, this technique needs a longer acquisition time, more mathematical processing, a laser and a system that allows the modulation (**Fig. 4.2**). The acquisition time for one spectrum with standard Raman spectroscopy is around one minute, and it is around 2.5 minutes with WMR spectroscopy.

The major differences allowing the discrimination between the two phenotypes were mainly the lipid band A and lipid band B. LR cells present higher lipid peak intensities on average compared to LP cells and there is important heterogeneity among each group. Raman intensity of LR and LP lipid peaks overlap, this shows a continuum of lipid concentration from low lipid content to a much higher. This study confirms that LR and LP cells are both present in all studied mycobacterial species.

The intracellular accumulation of non-polar lipid and specifically the storage of TAGs is common in the Actinomycetes group: in *Rhodococcus*, *Nocardia*, *Mycobacterium* and *Streptomyces* species. A *Rhodococcus opacus* strain is known to be able to store fatty acids up to 87% of the cell dry weight (Alvarez and Steinbüchel, 2002). The accumulation of those lipids is one of the factors associated with a dormancy phenotype in mycobacteria (Lipworth *et al.*, 2016). Many other bacterial species are known to store intracellular energy reserves (Wang and Bakken, 1998, Alvarez and Steinbüchel, 2002). Moreover, the capacity of a strain to store intracellular energy compounds has a positive impact on its survival in a starvation period (Wang and Bakken, 1998). Many microorganisms can show no sign of life under adverse conditions, but they are not dead. When the conditions change, they can restore and return to normal activity. Up to 80% of the microorganisms in soil samples appear to be metabolically inactive and many of these can be resuscitated (Lennon and Jones, 2011). Dormant mycobacteria present lipid accumulation, tolerance to antibiotics and display a low metabolic rate (Lipworth *et al.*, 2016). Based on this definition all dormant cells are LR, but it is difficult to say if all LR cells are dormant. However, we know that LR cells present a much higher tolerance towards key antibiotics of the regimen used to treat TB, *M.smegmatis* LR cells were found up to 40 times more resistant to rifampicin compared to LP cells (Hammond *et al.*, 2015). Therefore, study of the LR phenotype is of high medical relevance. Identifying both LR and LP phenotypes with our methodology could indicate whether the bacterium targeted is phenotypically resistant to antibiotics or not. This opens wide possibility to investigate the phenotypic antibiotic resistance of single *M.tuberculosis* cell directly in infected tissue and understand better the phenotypic antibiotic resistance *ex-vivo*. Studies targeting sputum samples have shown that the LR phenotype could be

predominant *in-vivo* (Garton *et al.*, 2008). However, sputum may not reflect exactly what happens in the lungs. Determining the proportion of phenotypically antibiotic resistant bacilli at the site of infection to understand more about the pathology of TB and potentially understand more about the bacteriology of relapse is key. Sloan et al. 2015 showed that few patients with unfavourable outcomes had bacteria with mutations associated with antibiotic resistance, supporting the notion that dormant organisms could be the main reason for relapse (Sloan *et al.*, 2015). Moreover, they observed a higher percentage of lipid body positive cells in sputum, three to four weeks into treatment, in patients that had unfavourable outcome compared to other patients.

Measuring single bacteria is a real challenge as the bacilli targeted are very small, less than a micron wide and few microns long (mycobacteria are rod shaped: 0.2-0.6 μm wide and 1-10 μm long) (McMurray, 1996). Regarding the measurement accuracy and the focusing a manual stage was used. Focusing 0.1 μm out of the cell could result in a loss of signal. Standard and WMR spectroscopy succeeded to discriminate LR and LP cells with both a high sensitivity and specificity. The two phenotypes after separation were placed on two separate quartz slides and it is possible that their background signal (debris, unwashed molecules…) were not exactly identical and could have increased the discriminative power. However, most of the variation between the two sets come from the lipid band B. If only this region 1400 to 1500 cm^{-1} is used for the analysis; both LR and LP can still be discriminated for all the data sets (**Appendices section 4 Tab. 1 and 2**).

All bacteria separated using the overnight D_2O separation were heat killed. Heat killing is known to produce no significant changes in the Raman spectra (Buijtels *et*

al., 2008). All the measurements have been taken from heat-killed bacteria. Even if this process can affect the Raman spectrum slightly both lipid rich and lipid poor cells were going through the same process as they were separated. Moreover, to be able to work on *M. tuberculosis* outside a category 3 laboratory an inactivation step is required.

The presence of lipid bodies results in a difference of buoyant density between the two fractions (Deb *et al.*, 2009). The buoyant density of *M. tuberculosis* cells is between 1.02 $g.mL^{-1}$ and 1.13 $g.mL^{-1}$ (den Hertog *et al.*, 2009). Hammond *et al.* proposed a density-based technique, making possible to obtain both lipid rich and lipid poor fractions with a high purity (Hammond *et al.*, 2015). The D_2O separation was applied in this study. The results presented in this study confirm the enrichment of the top fraction in LR cells and the bottom fraction in LP cells as LR and LP datasets were discriminated with high specificity and sensitivity. Moreover, the Raman spectra of the LR single cells display much higher Raman intensity in the lipid peaks and similar Raman intensity in the other spectral region when compared to Raman spectra of LP single cells.

In order to speed up the D_2O separation that takes several hours, a protocol using a centrifugation step has been designed in this chapter (**Appendices Section 2**). Both LR and LP samples can be obtained from the culture within one hour. Moreover, the bacteria would remain for less than 20 minutes in the H_2O/D_2O solution, limiting the stress on live bacteria. The initial separations using this protocol have been analysed using Nile red staining or WMR spectroscopy (**Fig. 4.4, Fig. 4.5** and **Fig. 4.6**). The data suggest that the protocol succeeded in enriching both top and bottom fraction in LR and LP cells respectively. More experiments are required to validate this protocol.

The LR and LP samples could be centrifuged again if the purity is not high enough from the first passage; a second centrifugation could increase the enrichment while the bacterial load would decrease.

If we are to shorten TB treatment, understanding relapse mechanism is key and therefore the link between bacterial phenotype and relapse. Relapse could be due to LR cells that resist treatment. To investigate this hypothesis we need a label-free, non-destructive technique such as WMR spectroscopy ensuring that the outcome will not be impacted by the methodology. The future experiment is to apply the method developed in this chapter to tissue samples infected by *M.tuberculosis* and test if we can obtain the phenotype of a single bacterium.

In summary, we have shown that Raman spectroscopy could be used to discriminate LR cells (associated with dormancy) from LP cells (not associated with dormancy) in mycobacterial species. Spectral regions corresponding to lipids can be used to perform this discrimination: the lipid band A (1300 cm^{-1}) and the lipid band B (1440 to 1450 cm^{-1}). We also demonstrated the interest of using WMR spectroscopy when studying bacterial phenotypes. This method provides higher sensitivity and specificity when discriminating LR and LP bacteria compared to standard Raman spectroscopy.

Chapter 5 Investigation of dormancy in TB infected tissue by Raman spectroscopy and fluorescence imaging

5.1 Introduction

Raman spectroscopy has been previously used to study medically relevant microorganisms (Maquelin *et al.*, 2000, Maquelin *et al.*, 2002a, Maquelin *et al.*, 2002b, Pahlow *et al.*, 2015). This method is showing great promise for potential medical applications such as diagnostics (Choo-Smith *et al.*, 2002, Tu and Chang, 2012). There are yet few studies on *Mycobacterium tuberculosis* using Raman spectroscopy (Buijtels *et al.*, 2008, Stockel *et al.*, 2016). To date, most studies on mycobacteria using Raman spectroscopy were conducted using *in-vitro* samples (Pahlow *et al.*, 2015). Several identification studies present results of bacteria in clinical samples such as urine blood and sputum but not on mycobacteria species (Rusciano *et al.*, 2013, Cheng *et al.*, 2013, Kloss *et al.*, 2013, Kloss *et al.*, 2015). However, studies interrogating single bacteria directly in tissue, such as lung infection, have not been reported. Studying bacteria with Raman spectroscopy in tissue is challenging as tissue itself produces Raman signal. It would be very informative to work directly on the actual causal agent of the disease in a real context. The organisms grown in an animal could present differences compared to the organisms grown *in-vitro*. Growth conditions can impact the Raman spectrum (Harz *et al.*, 2005). Animal models are used to study TB pathology and test treatment regimens. Models have been used for decades to develop anti-tuberculosis drugs and

to evaluate the efficacy of drug combinations. Gumbo et al. in 2015 defined three questions that the model should be able to answer in a TB drug development context: "*What combination(s) of drugs will be most effective? What dose(s) and schedule(s) of each drug should be administered? And What duration of treatment(s) will be efficacious?*" (Gumbo *et al.*, 2015). All TB animal models show advantages and disadvantages. There is no model that perfectly mimics Human TB. Guinea pigs are the chosen TB animal model for this study because the lesions which they develop during PTB are histologically similar to the disease seen in humans (Clark *et al.*, 2015). Moreover, there is some relationship between treatment shortening potential of certain drugs in this animal model and clinical outcome (Gumbo *et al.*, 2015).

Having the possibility to target a single bacterium directly at the site of infection and obtain information about its chemical and cellular content and use this to make an inference regarding its phenotype and its potential antibiotic tolerance could bring a greater biological understanding of the diseases and the bacteriology of relapse. Therefore, I investigated single bacteria cells in TB infected guinea pig lung tissue using Raman spectroscopy by designing a system and a methodology able to target single bacillus in tissue and assigning it to a lipid rich or lipid poor phenotype. Getting information about bacterial phenotype and population in the lung could help understanding the pathology better.

5.2 Methods

5.2.1 Animal infection

This method section was carried out in Public Health England (PHE) see **Appendices section 3** for more details. Each guinea pig was infected, using *M.tuberculosis* H37Rv, for 4 weeks. The guinea pig showing the highest bacteria load was killed, and the lungs were taken and directly fixed in formalin.

5.2.2 Paraffin sectioning of TB infected guinea pig lungs

This method section was carried out in PHE. Tissues were fixed in 10% (v/v) neutral buffered formalin (10% NBF) for 24 hours. They were then cut into small pieces and processed overnight. The tissue sat in 10% (v/v) NBF until the cycle began and then they were dehydrated through a series of alcohols (70%, 90% and 100% (v/v) IMS (Industrial Methylated Spirits) for a total of 7 hours. The tissue was then cleared with xylene; the sections went through 3 changes of this chemical over 3.5 hrs. Then finally the sections went through 4 changes of paraffin wax for a total of approximately 5 hours, the samples sat in the wax until removed from the processor. They were then embedded in paraffin wax (ultraplast wax) in moulds and attached to the cassettes for microtomy. The wax blocks were then cut to produce 3-5 microns slices that were placed onto the quartz slides.

5.2.3 Frozen section of TB infected guinea pig lungs

This method section was carried out in PHE and at Amsbio, UK. Once the guinea pig was dead, the tissue was immediately taken and fixed in 10% neutral buffered

formalin. Optimal cutting temperature (OCT) solution (30% w/v sucrose in PBS) was used to embed and freeze the tissue before cutting. The tissue was then cryosliced by the external company (Amsbio, UK). The tissue sections were 5 μm thick.

Amsbio, UK AMS Biotechnology (Europe) Limited / Registered office: 184 Park Drive, Milton Park, Abingdon OX14 4SE / Registered in England & Wales: Company number 2117791 / ISO 9001:2008 registered firm).

5.2.4 Unstained tissue mount for Raman spectroscopy

The frozen section on a thick quartz slide (SPI Supplies, 01016-AB) was directly mounted with a quartz coverslip (SPI Supplies, 01015T-AB) without any spacer and without PBS. The mount was sealed using transparent nail polish. This preparation was observed under WMR spectroscopy.

The frozen section on a quartz coverslip (SPI Supplies, 01015T-AB) was directly mounted on a thick quartz slide (SPI Supplies, 01016-AB) without any spacer and without PBS. The mount was sealed using transparent nail polish. This preparation was ready for observation under WMR spectroscopy.

5.2.5 Nile red stained bacteria, slide preparation

From Nile red stock solution at 250 $\mu g.mL^{-1}$ in DMSO (Sigma-Aldrich), 1 μL was added to 100 μL of bacterial suspension. The bacteria were then left for ten minutes at room temperature and in the dark (covered with aluminium foil). After the tubes were centrifuged for three minutes at 20,000 x g, the supernatant was discarded and the pellet resuspended in 100 μL of PBS. The bacteria were washed like this, with PBS,

twice. Finally, the pellet was resuspended in 20 μL of PBS, 10 μL were heat fixed either on a quartz coverslip for Raman spectroscopy or on a glass slide for microscopy. For Raman the fixed cells were mounted on top of a quartz slide, meaning that they end up trapped between the two quartz slides. The mount was then sealed with nail polish and observed under Raman spectroscopy (combined system, see **Chapter 2 General methods section 2.13** for more details). For fluorescence microscopy, a drop of immersion oil was directly placed on the fixed cells for direct observation (see **Chapter 2 General methods section 2.6** for more details).

5.2.6 Nile red staining of TB infected guinea pig tissue lung tissue sections

The infected guinea pig frozen lung was sliced to produce 5 μm thick sections that were attached to a quartz coverslip (SPI Supplies, 01015T-AB). The tissue was stained using Nile red at a final concentration of 25 $\mu g.mL^{-1}$ (DMSO 10% v/v final concentration). A 2 μL drop of Nile red solution was pipetted on top of the frozen tissue section, and directly a thick quartz slide (SPI Supplies, 01016-AB) was placed on top it. This mount was sealed using transparent Nail polish. The sample was studied using the Raman system or fluorescence microscopy (see **Chapter 2 General methods section 2.6 and 2.13** for more details).

5.2.7 Charging quartz slides

The quartz slides were first washed with distilled water followed by 70% (v/v) ethanol. The slides were covered by tissue to be protected from dust and left to air dry for several minutes. The coating agent used, to positively charge the quartz slides,

was 3-Aminopropyltriethoxysilane (Sigma, UK; A-3648; Silane). A 2% silane solution was prepared by adding 0.3 mL of coating agent to 15 mL of acetone. The quartz slides to charge were placed in the silane solution for approximately 30 seconds. Quickly after taking the slides out of the silane solution, the slides were washed with distilled water for only a few seconds. Then the slides were covered (typically placed in a box) and left to air dry in an incubator at 37°C overnight.

5.2.8 Frozen section of mice lymph nodes

Fresh BCG infected mice lymph node tissue was taken out of the freezer (-80°C). On dry ice, a mould was filled at 50% with OCT (Thermo-scientific), the fresh piece of tissue placed on top of it, and then the mould was filled to the top with OCT covering the tissue. On the dry ice, the OCT frost and made a block. The block was then removed from the holder, adjusted on a chuck and covered with OCT, left to freeze on dry ice. Moving on a cryostat (-20°C) the chuck was inserted in the holder, and 10 microns thick sections were serially cut. The tissue sections were attached to the positively charged glass or quartz slides.

5.2.9 Nile red staining and immunostaining of BCG infected tissue

Tissue sections attached to positively charged glass microscopy slides (Fisher Scientific, 10149870) were stained with Nile red. A 10 μL drop was added on top of the tissue sections at a final concentration of 25 $\mu g.mL^{-1}$ (DMSO 10% v/v final concentration). The tissue sections were washed with MiliQ water, left to air dry at room temperature and protected from dust for several minutes. A glass coverslip was

placed on top of the tissue sections. The tissue was then observed under Leica fluorescent microscope (see **Chapter 2 General methods section 2.6** for more details). After fluorescence microscopy, the same stained tissue section was investigated by immuno-staining.

5.2.10 Raman spectroscopy on tissue attached to positively charged slides

Quartz coverslip, quartz slides and glass microscopy slides were used for both immuno-staining and WMR spectroscopy. The tissue sections were attached to each slide types. The tissue sections on quartz coverslip (SPI Supplies, 01015T-AB), were mounted on top of a quartz slide (SPI Supplies, 01016-AB) and no spacer or PBS was used. The mount was then sealed at the corners only with transparent nail polish. The tissue sections on quartz slide (SPI Supplies, 01016-AB) were mounted with a quartz coverslip (SPI Supplies, 01015T-AB) and no spacer or PBS was used. The mount was sealed at the corners only with transparent nail polish. The tissue sections on glass microscopy slide (Fisher Scientific, 10149870) were mounted with a quartz coverslip (SPI Supplies, 01015T-AB) and no spacer or PBS was used. The mount was sealed at the corners only with transparent nail polish. Each of those preparations was then interrogated by WMR spectroscopy.

5.2.11 Immunostaining procedure

Once the tissue was investigated with either WMR spectroscopy or microscopy (for the Nile red stained slide) the mount was opened, and the slide with the tissue section placed at -20°C. All the incubation steps during the immuno-staining procedure were

realised inside a humid box (the box was humidified using a wet tissue). The immuno-staining was carried out as follows: in order to remove the OCT from the tissue sample, all the slides to study were immersed in PBST (PBS and tween 20 at 0.1% v/v) for ten minutes under permanent agitation (35 oscillation per minute). Directly on the slide and around the tissue an hydrophobic wall was created using a A Dako pen (Dako, S2002). From a 30 % (v/v) H_2O_2 stock solution (Sigma, H1009) a 3% (v/v) solution was generated using distilled water; 120 µL of this preparation was pipetted on top of the tissue, within the hydrophobic wall. The tissue was incubated ten minutes with the H_2O_2 solution. Again, the slides were immersed in PBST, for five minutes and with agitation (35 oscillation per minute). Dako serum-free protein block (Dako, X0909) was directly pipetted on top of the tissue sections, approximately two drops. The tissue was incubated with the Dako serum-free protein block (Dako, X0909) for ten minutes. During the incubation the primary antibody (Dako, A0452, CD3 antibody) solution was generated as follows: 1 in 400 dilution in Dako (S0809) solution. After the incubation with Dako serum-free protein block (Dako, X0909) the liquid was removed, and without any washing, the primary antibody was pipetted on top of the tissue sections. The incubation with the primary antibody was around 30 minutes. After the incubation, the slides were washed two times in PBST for five minutes each under continuous agitation (35 oscillation per minute). The secondary antibody (Dako, K4003; HRP conjugated) was used, two to three drops, on the tissues sections. The incubation time with the secondary antibody was also 30 minutes. Again, the tissue sections were immersed twice in PBST for five minutes each time and under permanent agitation (35 oscillation per minute). On tissue, 120 µL of tyramine-signal-amplification (TSA)-CY5 (PerkinElmer, NEL745 B001KT) was pipetted, and the slides were incubated for 10 minutes. Following this

incubation step, the slides were immersed in PBST twice, five minutes each time and under permanent agitation (35 oscillation per minute). The tissue sections were counter stained using 120 µL of Hoechst dye solution (Thermo Fisher, H3570) diluted at 1:1000 with distilled water. The incubation with the counter stain was 10 minutes. The slides were immersed in PBST, five minutes each time and under permanent agitation (35 oscillation per minute). Directly after the second wash, the slides were immersed into 80% (v/v) ethanol for approximately one minute. The slides were air dried at room temperature, protected from light. Following this step, tissues sections were mounted with a coverslip or a slide and using 30 µL of mounting medium (Life technology, P36930). The slides were air dried for several hours and stored at 4°C. For the image acquisition the slides were investigated using a HistoRX microscope station (HistoRX, PM2000) with the AQUA software. The settings through the experiments were 30 ms acquisition time for CY5 (viewed using a CY5 filter cube) and 2 ms acquisition time for Hoechst (viewed using a DAPI filter cube).

5.2.12 Raman spectroscopy acquisition time

All spectra taken in this chapter were WMR spectra and the acquisition time was 150 seconds (See **Chapter 2 General methods section 2.8** for more details).

5.3 Results

5.3.1 Tissue embedded in paraffin

Our collaborators in PHE provided TB infected guinea pig lung tissue. Two Raman spectroscopy systems were used in this chapter to acquire the WMR spectra (see **Chapter 2 General methods section 2.12** and **2.13** for more details).

First, paraffin embedded TB infected lung tissue sections were used and studied using the first Raman spectroscopy system. Single bacteria were observed on the Raman spectroscopy system (**Fig. 5.1**). A single bacillus is clearly visible and located in lung alveoli. Bacteria were identified based on their shape and size (rod shape: 0.2-0.6 μm wide and 1-10 μm long) (McMurray, 1996). The corresponding spectrum was then compared to the in-vitro data previously acquired for comparison. The tissue structure was found intact and preserved after the fixation and sectioning process.

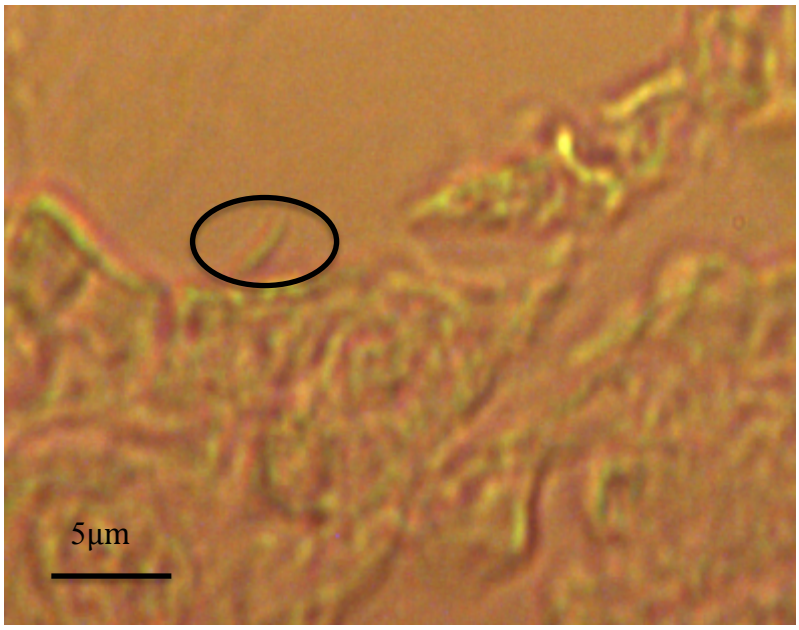

Figure 5.1 *Paraffin embedded tissue section.*

The picture is showing a single bacillus in guinea pig lung alveoli. The picture was acquired in the Raman spectroscopy system one. The single bacillus is encircled. The scale bar is 5 µm.

In this study, only single bacteria located in alveoli were targeted as the presence of surrounding tissue or material would have an impact on the spectrum. When the bacteria were interrogated, a very intense signal was observed even within a second, **Fig. 5.2**. The values of intensity observed were highly superior (more than 10 times) to the one expected according to previous single cell results or even compared to other biological features. When targeting other areas of the lung tissue section the same spectrum was observed and this intense signal was also displayed outside the tissue section (in the paraffin). The signal was mostly coming from the embedding agents, as the signal did not change even when taken outside of the tissue section. Paraffin was used to embed the tissue; the background signal was too strong to permit getting any data from the tissue or single bacteria. The spectrum displays very intense bands especially around 1000 cm^{-1} and 1440-1450 cm^{-1}; the last one being the main band (Lipid band B) used to discriminate between LR and LP.

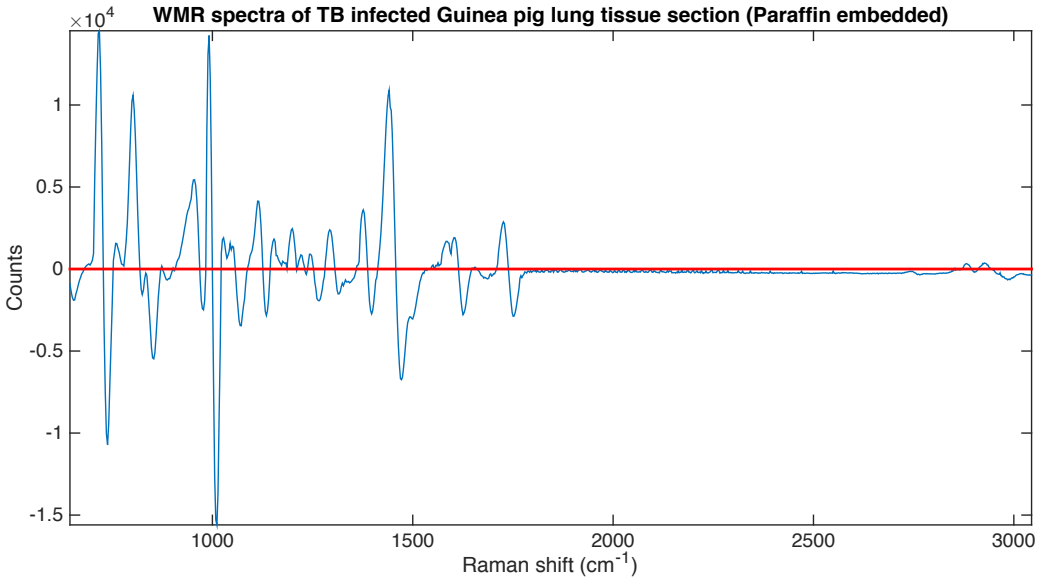

Figure 5.2 *WMR spectrum of paraffin embedded tissue section.*

The blue line represents the WMR spectrum after processing. All spectra taken across the tissue section gave the same signal, targeting single bacillus, lung tissue, alveoli or even only the paraffin. The x-axis shows the Raman shift in cm^{-1}*, the y-axis represents the counts. The zero crossing that is represented by the red line shows the Raman peak position. The intensity of the peak corresponds to the peak-to-valley around the zero crossing point. The acquisition time was 150 seconds per spectra (see* ***Chapter 2 General methods section 2.8*** *for more details).*

Observing the problem that paraffin embedding caused for the use of Raman spectroscopy, the initial idea was to de-paraffin using dewaxing agents. But reading about the dewaxing protocols and its use with Raman spectroscopy it was found that after using dewaxing agents the section still presents wax residues. Even if the major part of the wax can be removed, it cannot be in totality. Raman spectroscopy could still after dewaxing pick-up signal coming from the paraffin residues (Faolain *et al.*, 2005). Moreover, the paraffin presents a high intensity peak around 1440 cm^{-1}, which is one of the main regions of interest for the study of LR and LP in *Mycobacterium tuberculosis.* This precluded the use of Paraffin embedding for the study of single bacteria within tissue sections. Frozen sectioning was another technique available that had the advantage that fewer compounds are added during the sample preparation process.

5.3.2 First experiment using frozen tissue sections

The infected lung tissue section was attached to the thicker quartz slide, see **Fig. 5.3,** this made the working distance more important compared to the *in-vitro* work. In this case, the objective was further away from the target. This mount was the same as the one used for paraffin embedded tissue. The tissue was fixed on the most solid slide because the quartz coverslips are very thin and highly breakable.

The frozen section of the guinea pig lung showed intact tissue with clear alveoli and structures and intact single bacteria as the shown in **Fig. 5.4**.

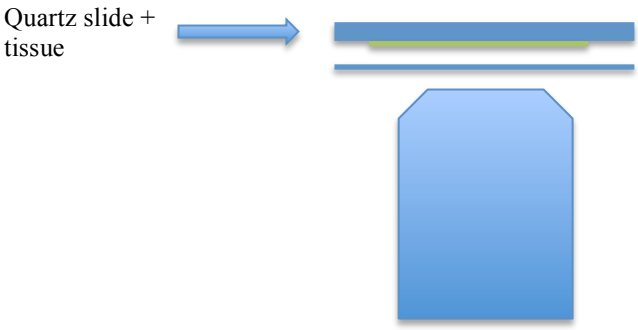

Figure 5.3 *Description of the sample preparation.*
This figure shows the tissue sample between the two quartz slides and the objective of the Raman spectroscopy system. The mount is composed of a thick quartz slide onto which the tissue was attached and a quartz coverslip that is in direct contact with the oil immersion objective. The mount is sealed using transparent nail polish at the edges.

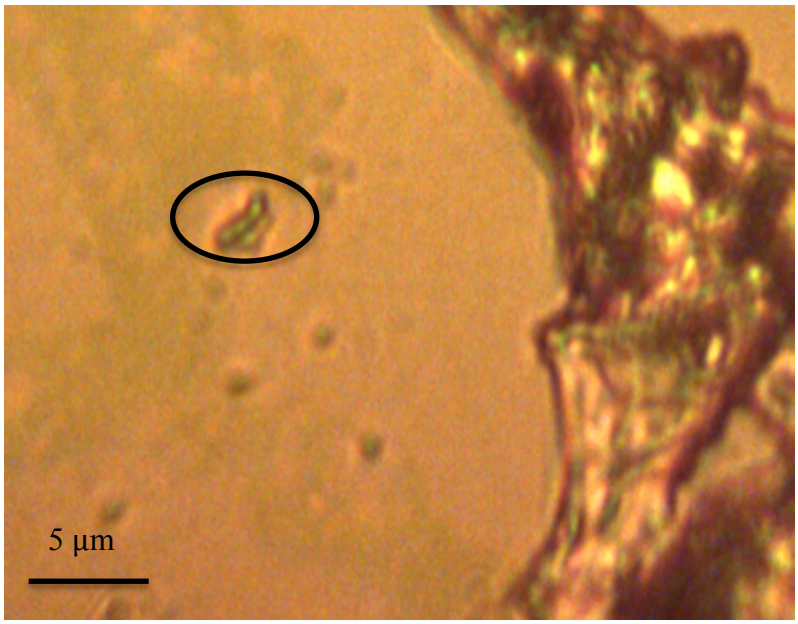

Figure 5.4 *Frozen section of TB infected guinea pig lung showing a single bacillus in alveoli. The picture shows how images were displayed on the Raman spectroscopy system. The scale bar is 5 μm.*

The background Raman signal in the alveoli was very low, and it was possible to target single bacterium and obtain a signal from a single cell. The signal coming from a single cell was stronger than the signal coming from the background only. Over a hundred single bacteria (112) were interrogated in the first experiment on frozen lung tissue section. The results are shown in **Fig. 5.5**. The intensity level was lower than for *in-vitro* spectra, between 5 to 6 times lower, the energy level could not be compared to the training sets of LR and LP *in-vitro* bacteria from the previous chapter. Moreover, the signal to noise ratio was high meaning that the noise intensity was high compared to the Raman peak intensity.

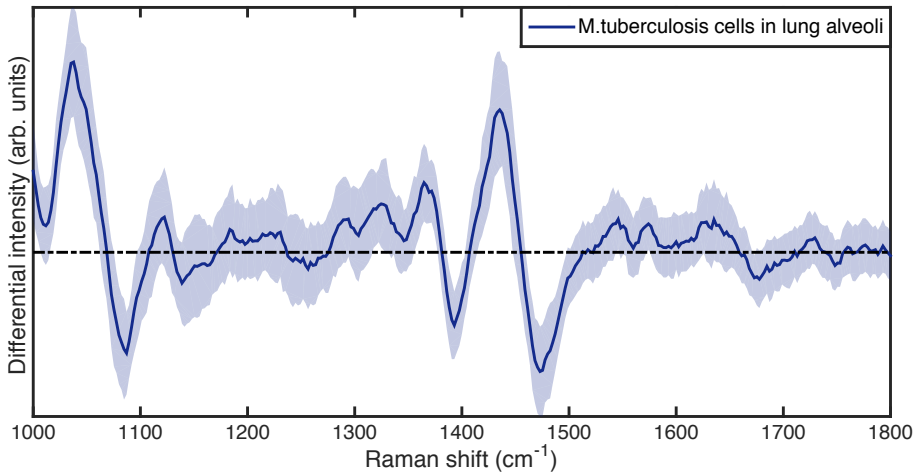

Figure 5.5 *WMR spectra of M. tuberculosis from frozen guinea pig lung tissue sections.*

The blue line represents the average WMR spectrum calculated from the spectra of 112 single bacilli. The colour shade corresponds to one standard deviation. The x-axis shows the Raman shift (cm^{-1}), the y-axis the intensity in arbitrary units. The figure displays the finger print region of the spectrum (between 1000 to 1800 cm^{-1}). The zero crossing that is represented by the dash-dotted line shows the Raman peak position. The intensity of the peak corresponds to the peak-to-valley around the zero crossing point. The acquisition time was 150 seconds per spectra (see ***Chapter 2 General methods section 2.8*** *for more details).*

The main difference between this study and the *in-vitro* study, previously showed in Chapter 4, is where the sample is located in the mount. In the previous *in-vitro* work the bacteria were dried directly on the coverslip, very close to the objective. In this experiment, the tissue was fixed on the thick slide as shown in **Fig. 5.3,** which means that the working distance was different. This could have led to signal loss. The technique using frozen tissue sections, however, showed that the tissue could be interrogated by WMR spectroscopy. We observed a high conservation of the tissue structure, clearly visible single bacteria and a very low background signal. For the next experiment, frozen tissue sections were used and were attached to the coverslip to reduce the working distance with the objective.

5.3.3 Second experiment using frozen tissue sections

For the second experiment studying, TB infected guinea pig lung tissue the same methodology as previously was used, but the tissue was fixed to the coverslip as shown in the **Fig. 5.6.** Over a hundred single bacilli present in alveoli and clearly identified were interrogated. The **Fig. 5.7** shows several examples of single bacilli in guinea pig lung alveoli. In total 107 single bacteria were interrogated by WMR spectroscopy. The average WMR spectrum and associated standard deviation are shown in **Fig. 5.8 a**. Very important variability could be observed in both lipid band A (1300 cm^{-1}) and lipid band B (1440-1450 cm^{-1}) in **Fig. 5.8 a**. Very little differences were observed between the quartz slide Raman spectrum, and the TB infected guinea pig lung alveoli background Raman spectrum **Fig 5.8 b. Fig 5.8 b and c** show that no signal from the tissue participates to the WMR spectrum of the single *M. tuberculosis* cells as the alveoli background is comparable to the quartz slide itself. In this study,

bacteria located in the tissue were not targeted as their Raman signal could be distinguished from the lung tissue signal itself. The majority of bacteria are probably located in consolidated tissue and not in alveoli.

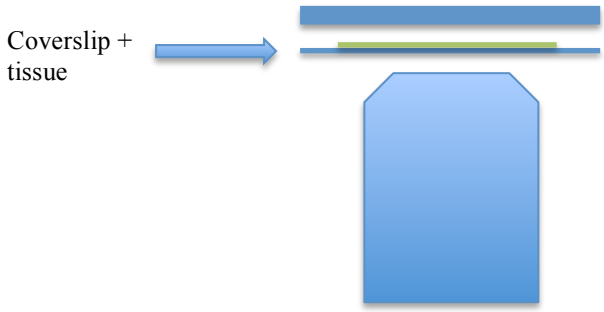

Figure 5.6 *Description of the sample preparation.*

This figure shows the tissue sample between the two quartz slides and the objective of the Raman spectroscopy system. The mount is composed of a coverslip onto which the tissue sections were attached and a quartz slide placed on top of it. The mount is sealed using transparent nail polish at the edges. The coverslip is directly in contact with the oil immersion objective of the Raman spectroscopy system.

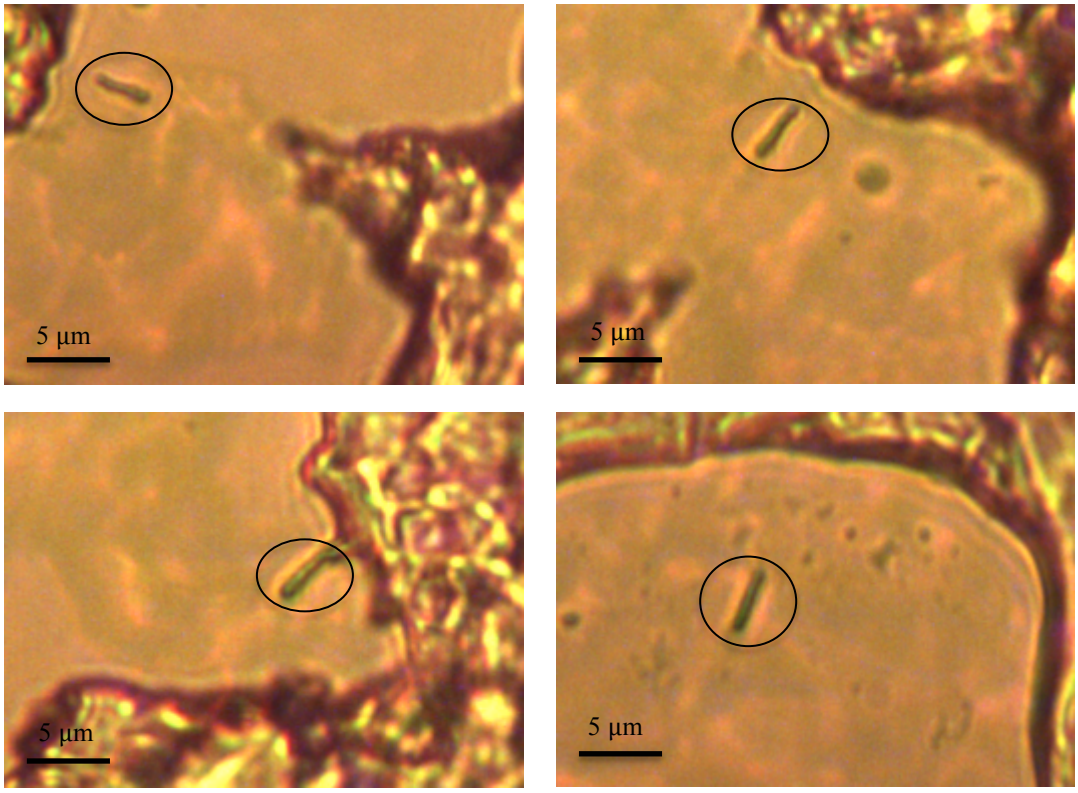

Figure 5.7 *Frozen lung tissue section with single bacteria in alveoli.*

The picture displays four fields of view, taken in the Raman spectroscopy system, with a single M.tb bacillus present in lung alveoli (encircled). The scale bar is 5 µm.

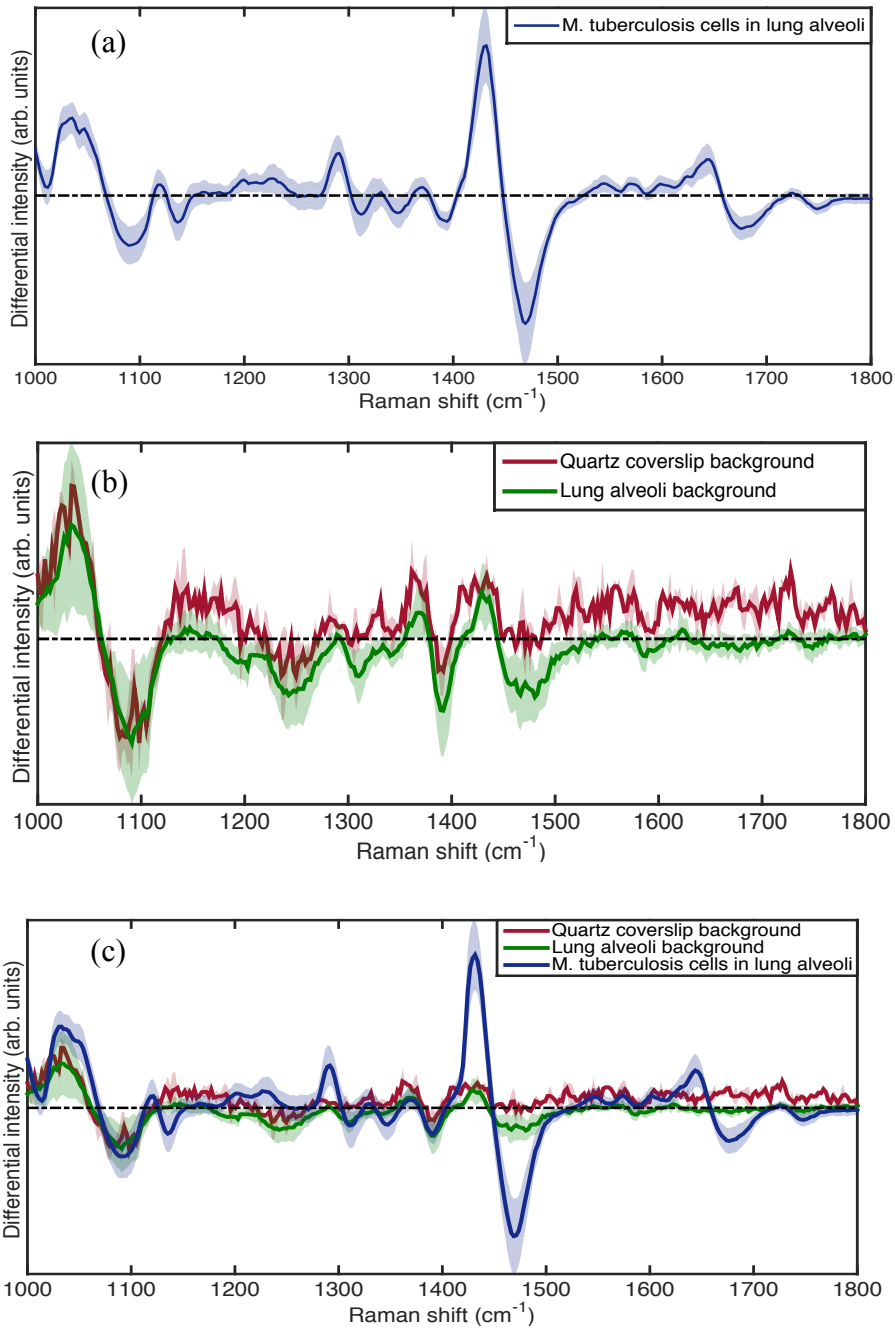

Figure 5.8 *WMR spectra of M. tuberculosis from frozen guinea pig lung tissue sections.*

Fig 5.8 a *shows the average WMR spectrum calculated from the spectra of 107 single bacilli (blue line).* ***Fig 5.8 b*** *presents the average WMR spectrum of a quartz slide (red), and the TB infected guinea pig lung alveoli background (green).* ***Fig 5.8 c*** *combines the previous two figures (**Fig 5.8 a** and **b**). The colour shade represents one standard deviation. The x-axis shows the Raman shift (cm^{-1}), the y-axis the intensity in arbitrary units. The figure displays the finger print region of the spectrum (between 1000 to 1800 cm^{-1}). The zero crossing that is represented by the dash-dotted line shows the Raman peak position. The intensity of the peak corresponds to the peak-to-valley around the zero crossing point. The lipid band A is located at 1300 cm^{-1} and the lipid band B around 1440-1450 cm^{-1}. The acquisition time was 150 seconds per spectra (see **Chapter 2 General methods section 2.8** for more details).*

It was difficult to compare the *in-vitro* and *ex-vivo* data sets directly; the lipid bands A and B were not affected equally by the fixation and freezing procedure (Buijtels *et al.*, 2008, Galli *et al.*, 2014) (**Fig. 5.9 a and b**). We observed that the lipid band A intensity was lower in tissue spectra by comparison to the *in-vitro* spectra. However, there was little change in the lipid band B intensity. This lipid band was less impacted by the sample preparation process and could be compared to the *in-vitro* data sets. In order to understand the proportion of LR and LP cells in tissue, we designed a ratio using a lipid band presenting important variability (lipid band B) and a band that does not vary much between LR and LP, a reference band. The band selected is between 1050 cm^{-1} and 1070 cm^{-1} (reference band), a region, which is conserved between LR and LP (**Fig. 5.9 a**), and this band is intense showing a good signal to noise ratio. The reference band also displayed little variability among the spectra taken from lung tissue sections. This band was the internal reference for the ratio. The peak-to-peak ratio calculated between the lipid band B and the reference band was named ($R_{\text{band B/Ref band}}$). For each WMR spectrum of both *M.tuberculosis in-vitro* (LR and LP) **(Fig. 5.9 a**) and *M.tuberculosis* in lung tissue (**Fig. 5.9 b**), the maximum peak intensity value of the two bands (lipid band B and the reference band) were used to calculate the ratio ($R_{\text{band B/Ref band}}$). The results of $R_{\text{band B/Ref band}}$ are shown in **Fig. 5.9 c**; a higher ratio value corresponds to a higher relative quantity of lipids in the bacteria. The ratio values of *in-vitro* LR and LP overlap but their respective peaks of distribution are very distinct (**Fig. 5.9 c**). Looking at *M.tuberculosis ex-vivo* $R_{\text{band B/Ref band}}$, we observed ratio values corresponding to both LP and LR. The wide distribution of the $R_{\text{band B/Ref band}}$, calculated from WMR spectra of bacteria in lung tissue confirmed that both LR and LP cells were present in the infected lung tissue. Interestingly we also observed that *ex-vivo* ratio predominantly overlap with LR ratio (**Fig. 5.9 c**).

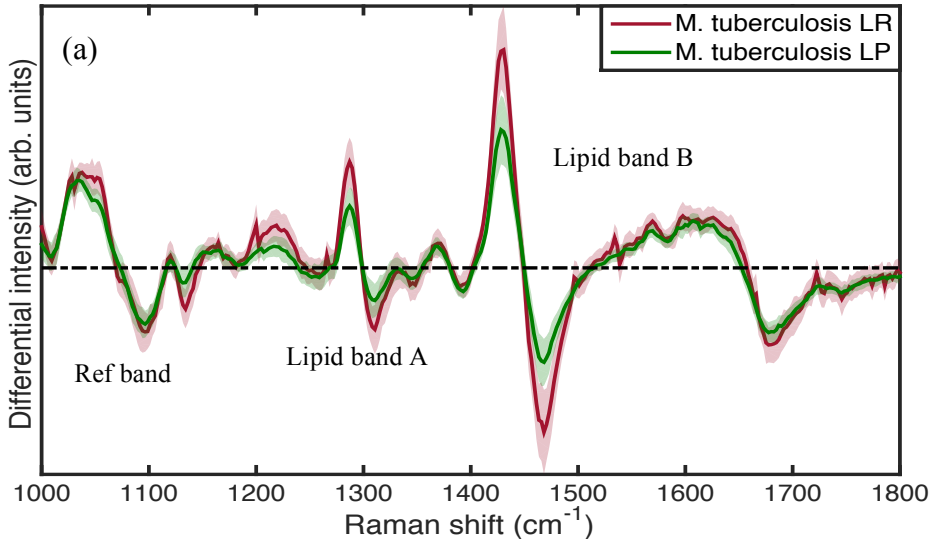
(a)
M. tuberculosis LR
M. tuberculosis LP
Lipid band B
Lipid band A
Ref band
Differential intensity (arb. units)
1000
1100
1200
1300
1400
1500
1600
1700
1800
Raman shift (cm-1)

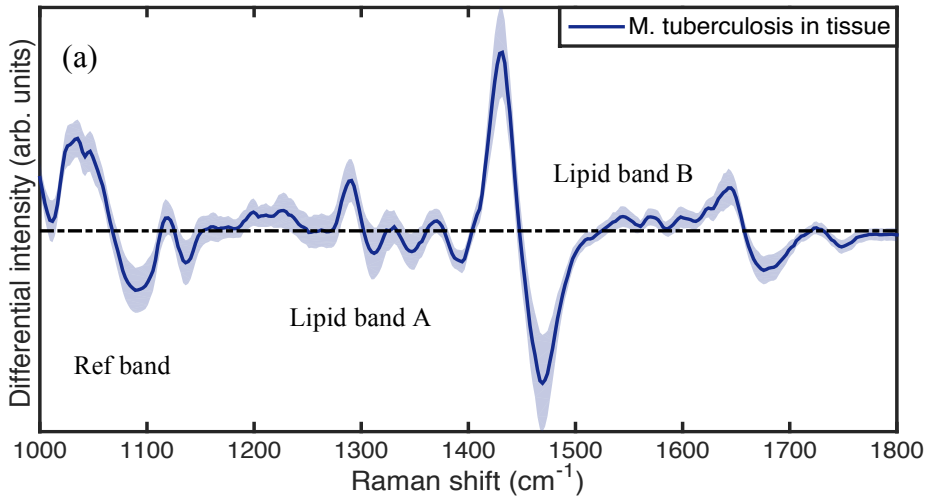
(a)
M. tuberculosis in tissue
Lipid band B
Lipid band A
Ref band
Differential intensity (arb. units)
1000
1100
1200
1300
1400
1500
1600
1700
1800
Raman shift (cm-1)

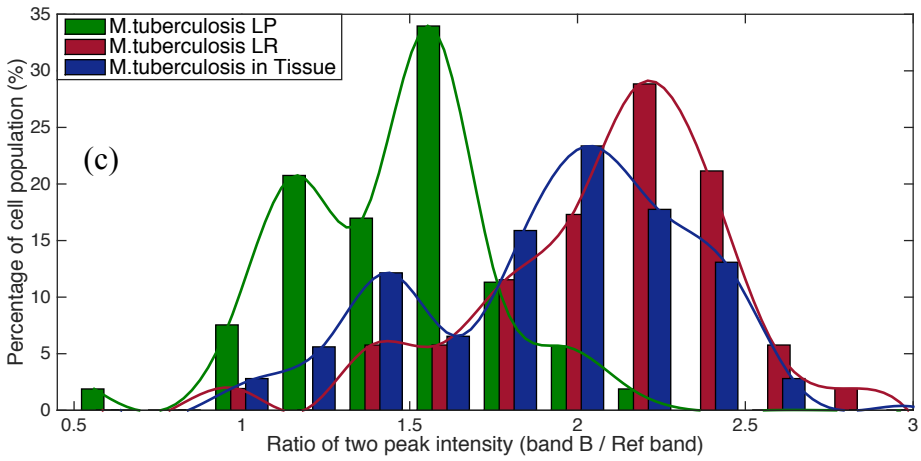
M.tuberculosis LP
M.tuberculosis LR
M.tuberculosis in Tissue
(c)
Percentage of cell population (%)
0
5
10
15
20
25
30
35
0.5
1
1.5
2
2.5
3
Ratio of two peak intensity (band B / Ref band)

Figure 5.9 *M. tuberculosis in guinea pig lung tissue, a phenotypic investigation.*
Fig. 5.9 a *shows the average WMR spectra of both LR (red line) and LP (green) cells taken in-vitro over 60 single bacteria for each set. The shaded coloured zone represents the corresponding single standard deviation. The x-axis is the Raman shift (in wavenumber, cm^{-1}) and the y-axis shows the differential Raman intensity in arbitrary units.* ***Fig. 5.9 b*** *presents the average WMR spectra of M. tuberculosis cells taken in the guinea pig lung tissue and calculated using 107 single bacterial WMR spectrum. The shaded coloured zone represents the corresponding single standard deviation. The lipid band A is located at 1300 cm^{-1} and the lipid band B around 1440-1450 cm^{-1}. For all single WMR spectrum the acquisition time is 150 seconds in total (see* ***Chapter 2 General methods section 2.8*** *for more details). Both the* ***Fig. 5.9 a*** *and* ***b*** *show the finger print region of the spectrum (between 1000 to 1800 cm^{-1}).* ***Fig. 5.9 c*** *displays the peak-to-peak ratio ($R_{band\ B/Ref\ band}$) calculated for all WMR spectrum of M. tuberculosis in-vitro LR, LP (****Fig. 5.9 a****) and ex-vivo (****Fig. 5.9 b****). In order to calculate this ratio the maximum peak value from the lipid band B is divided by the maximum peak intensity of the reference band (Ref band: 1050 cm^{-1} to 1070 cm^{-1}). The in-vitro LR $R_{band\ B/Ref\ band}$ values are represented by the red bars, the LP by the green bars and the ex-vivo ratio by the blue bars. Corresponding coloured lines have been inserted to show the shape of distribution for each set. The x-axis shows the $R_{band\ B/Ref\ band}$ values; the y-axis corresponds to the percentage of the bacterial population at each $R_{band\ B/Ref\ band}$ value. For example, 5.5% of in-vitro LR cells show an $R_{band\ B/Ref\ band}$ of 1.5, where it is 34% of in-vitro LP cells and 6.5% of M. tuberculosis in tissue.*

The lipid band A was lower in the WMR spectrum of *M. tuberculosis* cells taken in tissue than it was in WMR spectrum acquired *in-vitro*. The lipid band A in the *ex-vivo* WMR spectra was reduced to 61% of the lipid band A of the *in-vitro* WMR spectra. Applying a multiplication factor to the lipid band A of the *ex-vivo* WMR spectra we calculated ratios using the lipid band A and the same reference band used previously. This ratio was named $R_{\text{band A/Ref band}}$. Similarly to the previous ratio, this one was applied to all WMR spectra both *in-vitro* (LR and LP) and *ex-vivo.* The results of this ratio ($R_{\text{band A/Ref band}}$) are presented in **Fig. 5.10**. The *ex-vivo* $R_{\text{band A/Ref band}}$ values are widely distributed, and we can observe values that match both LR and LP $R_{\text{band A/Ref band}}$ values. The *ex-vivo* $R_{\text{band A/Ref band}}$ values are also skewed to LR phenotype similarly to what was observed previously in **Fig. 5.9**.

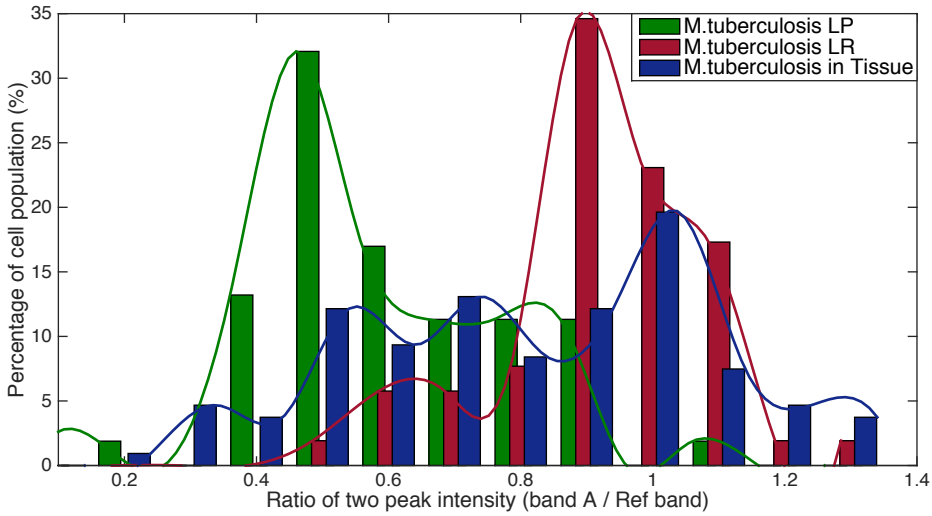

Figure 5.10 *Peak-to-peak ratio ($R_{Band\ A/Ref\ Band}$) calculated from M. tuberculosis in-vitro (LR and LP) and ex-vivo WMR spectra.*

This ratio has been calculated by dividing the maximum value in lipid band A with the maximum value from the reference band (Ref Band: 1050 cm^{-1} to 1070 cm^{-1}). The fixation and freezing process of the infected guinea pig lung tissue have impacted the lipid band A and reduced it to 61% of the lipid band A found in the in-vitro WMR spectra. In order to calculate the $R_{Band\ A/Ref\ Band}$ the lipid band A in the ex-vivo spectra have been adjusted to take the intensity reduction into account. The coloured bars represent the $R_{Band\ A/Ref\ Band}$ values of the in-vitro LR cells (in red), the in-vitro LP cells (in green) and the ex-vivo cells (in blue). Corresponding coloured lines have been inserted to show the shape of distribution for each set. The x-axis shows the $R_{Band\ A/Ref\ Band}$ values; the y-axis corresponds to the percentage of the bacterial population at each the $R_{Band\ A/Ref\ Band}$ value.

M. tuberculosis in tissue showed important variability in terms of lipid content as shown in **Fig. 5.9 c**. It is notable that ratios homologous to both LR and LP cells can be observed in tissue. As shown in **Chapter 3** the relation between Raman peak and the lipid concentration is linear. Therefore if a lipid peak in a single bacterium is twice higher compared to another cell, it would suggest that the first bacterium contains twice the quantity of lipids. This result suggests that in tissue some bacteria can present twice as much lipid than others. Further experiments are required to associate the presence of intracellular lipid bodies in *M. tuberculosis* cells and the increase in Raman lipid peaks intensity.

5.3.4 Nile red staining and fluorescence microscopy

A one-week-old culture of *M. smegmatis* was stained using 2.5 $\mu g.mL^{-1}$ of Nile red and observed using fluorescence microscopy. The results are visible in **Fig. 5.11** and **Fig. 5.12**. LR and LP cells could clearly be identified and the lipid bodies observed and counted using Nile red staining.

Bacteria present different sizes, a different number of lipid bodies and different lipid body sizes. In terms of lipid content, the bacterial population present a large spectrum between absence to presence of several large lipid bodies and all different scenarios could be found from zero to several lipid inclusions. In **Fig. 5.12** LR and LP cells can be observed, LR cells present very different lipid content up to 5 distinct lipid inclusions in **Fig. 5.12 b**. The lipid content among mycobacteria is very heterogeneous.

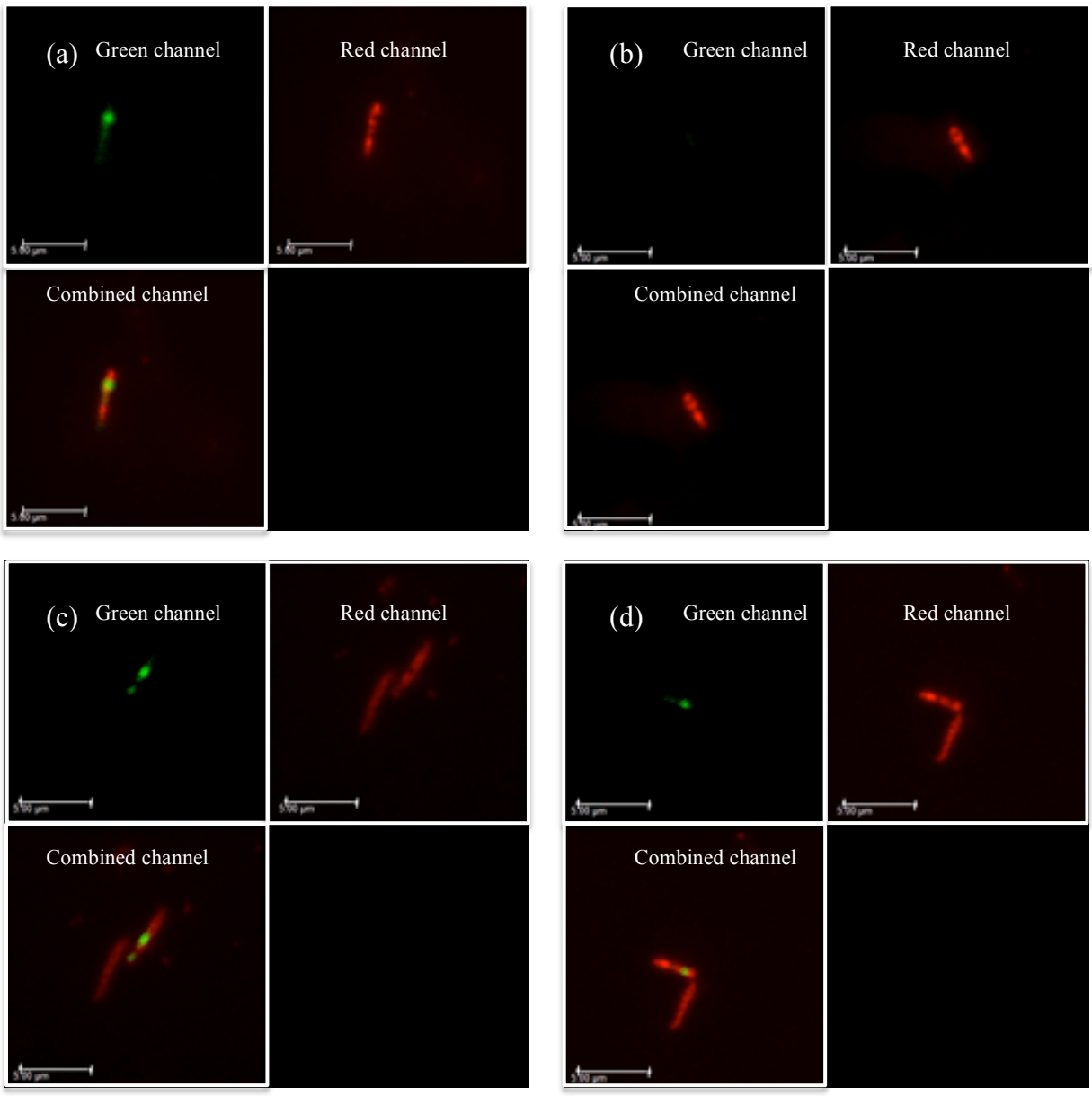

Figure 5.11 *M.smegmatis one-week-old (stationary phase) culture stained using Nile red and observed using fluorescence microscopy.*

*The figure is showing four composite images (**Fig. 5.11 a, b, c and d**). Each image is composed of three sections, on the top left the green channel, on the top right the red channel and on the bottom left the combined image of the previous two pictures. In **Fig. 5.11 a,** a LR bacteria can be observed with one clear lipid body, in **Fig. 5.11 b** a LP bacteria can be observed with no clear lipid body visible. In **Fig. 5.11 c** and **d** both a LR and a LP cell can be observed, with an LR cell showing two lipid bodies in **Fig. 5.11 c.** The scale bar represents 5 µm.*

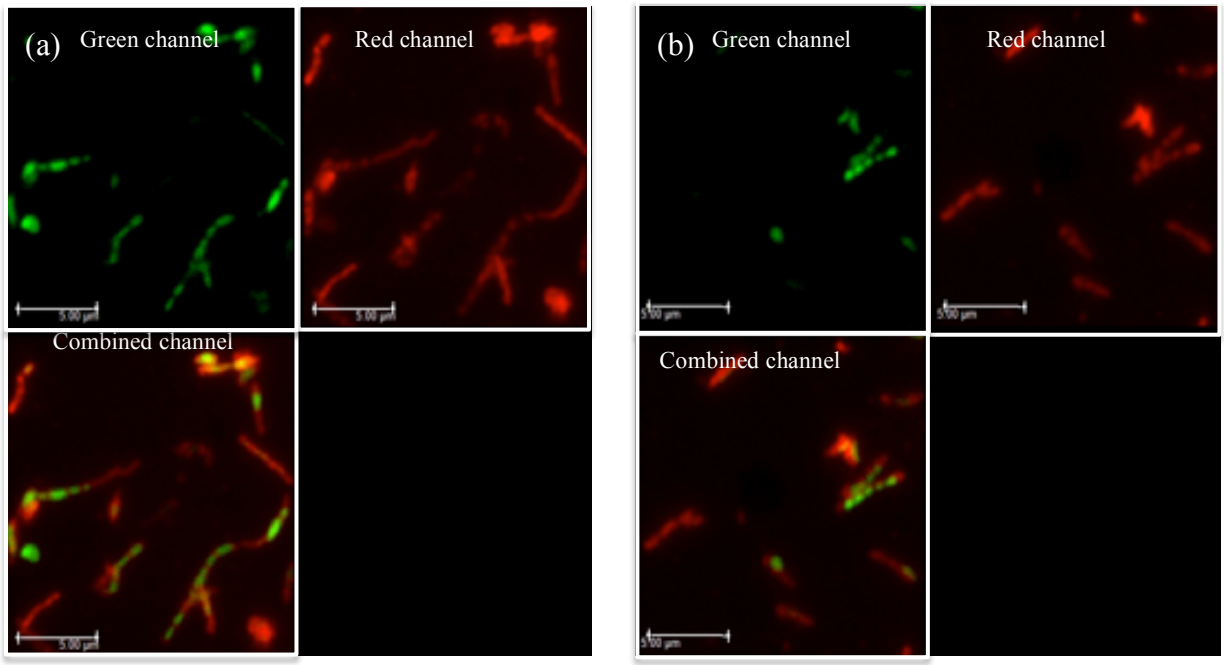

Figure 5.12 *M.smegmatis one-week-old culture stained using Nile red and observed using fluorescence microscopy.*

*The figure is showing two composite images (**Fig. 5.12 a** and **b**). Each image is composed of three sections, on the top left the green channel, on the top right the red channel and on the bottom left the combined image of the previous two pictures. LR and LP cells can be observed in both **Fig. 5.12 a** and **b.** LR cells show various number and sizes of lipid bodies. The scale bar represents 5 µm.*

5.3.5 System combining Raman spectroscopy and fluorescence imaging

A new Raman spectroscopy system was developed to be able to study stained bacteria and then take their Raman spectrum. This system was able to generate blue and green light used to excite stained bacteria similarly to the Leica fluorescence microscope (see previous images). The green excitation light gave rise to red fluorescence emission predominantly from Nile red in a polar lipid environment; the blue excitation light gave rise to the green emission associated with Nile red in a non-polar lipid environment. The fluorescence part of the combined system was designed to mimic the Leica fluorescence microscope (light source and filter cubes). For the Raman spectroscopy part this system was built to be comparable to the Raman spectroscopy system one, the same laser is powering the system. For more details about the combined system refer to the **Chapter 2 General methods section 13**.

5.3.5.1 *In-vitro* comparison between stained and unstained bacteria using WMR spectroscopy

In order to investigate the impact of Nile red on the WMR spectra of single bacteria; *M.smegmatis* culture was stained using 2.5 $\mu g.mL^{-1}$ Nile red, heat fixed on a quartz coverslip and interrogated using Raman spectroscopy. The results are shown in **Fig. 5. 13**. Nile red staining gave stronger fluorescence background than unstained samples. The stain affected the standard Raman spectra, especially the fluorescence background but the WMR approach removed the influence coming from the dye (removed the auto-fluorescence background). Nile red staining does not impact the WMR spectra significantly.

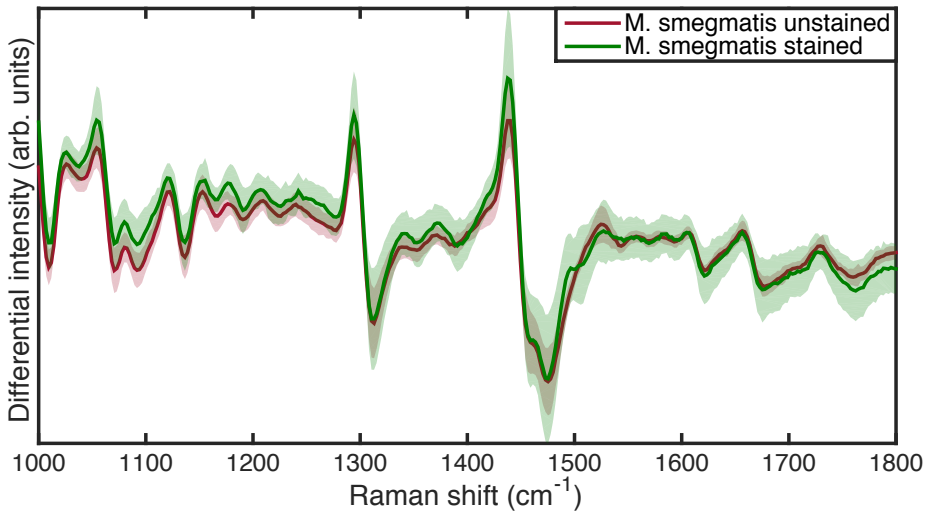

Figure 5.13 *Comparison of Nile red stained and unstained M. smegmatis single cell using WMR spectroscopy.*

The coloured lines correspond to the average spectrum of unstained (red) and stained (green), the average spectrum has been calculated using 40 single spectra for each set. The colour-shaded area surrounding the lines represents a single standard deviation. The x-axis displays the Raman shift in wavenumber (cm^{-1}), the y-axis represents the differential Raman intensity in arbitrary units. The time required to obtain one single cell spectrum is 150 seconds (see ***Chapter 2 General methods section 2.8*** *for more details).* ***Fig. 5.13*** *shows the finger print region of the spectrum (between 1000 to 1800 cm^{-1}).*

5.3.5.2 *In-vitro* experiment on Nile red stained mycobacteria

An initial *in-vitro* experiment using Nile red stained *M. smegmatis* was performed. A 100 µL of bacterial suspension was stained using 2.5 µg.mL^{-1} Nile red. The new system built was able to combine fluorescence imaging and Raman spectroscopy (see **Chapter 2 General methods section 13** for more details). Prior to taking Raman signal the preparation was studied using white light, then green excitation light (TRITC, standard Nikon fluorescence cube) leading to red emission (Nile red in polar lipid environment) and finally blue excitation light (FITC, standard Nikon fluorescence cube) generating green emission (Nile red in a non-polar lipid environment). This system mimics the fluorescence microscope used previously (**Fig. 5.11** and **Fig. 5.12**). The **Fig. 5.14** shows the white light output, single bacilli and groups of cells can be observed in this field of view. The circles show the single bacteria studied, 8 in total.

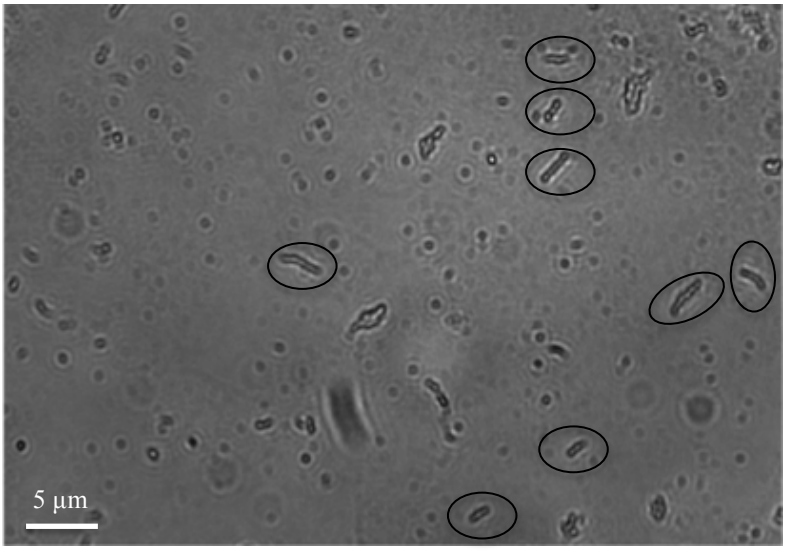

Figure 5.14 *M. smegmatis Nile red stained observed under white light.*
Field of view showing several bacilli, the bacteria encircled are studied in this experiment. The exposure time to acquire this picture, using white light, in the combined fluorescence and Raman spectroscopy system is 2 ms. The scale bar represents 5 µm.

Once the white light image was saved the green excitation light, showing the red emission, was switched on. The **Fig. 5.15 a** shows the corresponding picture. All bacteria can be clearly observed on this picture. The red emission corresponds to that of Nile red in a polar lipid environment. The image was processed in MATLAB® in order to remove uniformly the light background, see **Fig. 5.15 b.** Most bacteria are showing similar red light emission intensity level. The blue excitation light was then switched on showing the green emission, coming from Nile red in a non-polar lipid environment (lipid bodies). The results are presented in **Fig. 5.16 a** and the image processed in MATLAB® in **Fig. 5.16 b.** Important differences can be observed between bacteria in this image. A combined image, red and green light emission, is shown in **Fig. 5.17 a** and the **Fig. 5.17 b** displays the assignment of bacteria to LR or LP based on their fluorescence profile.

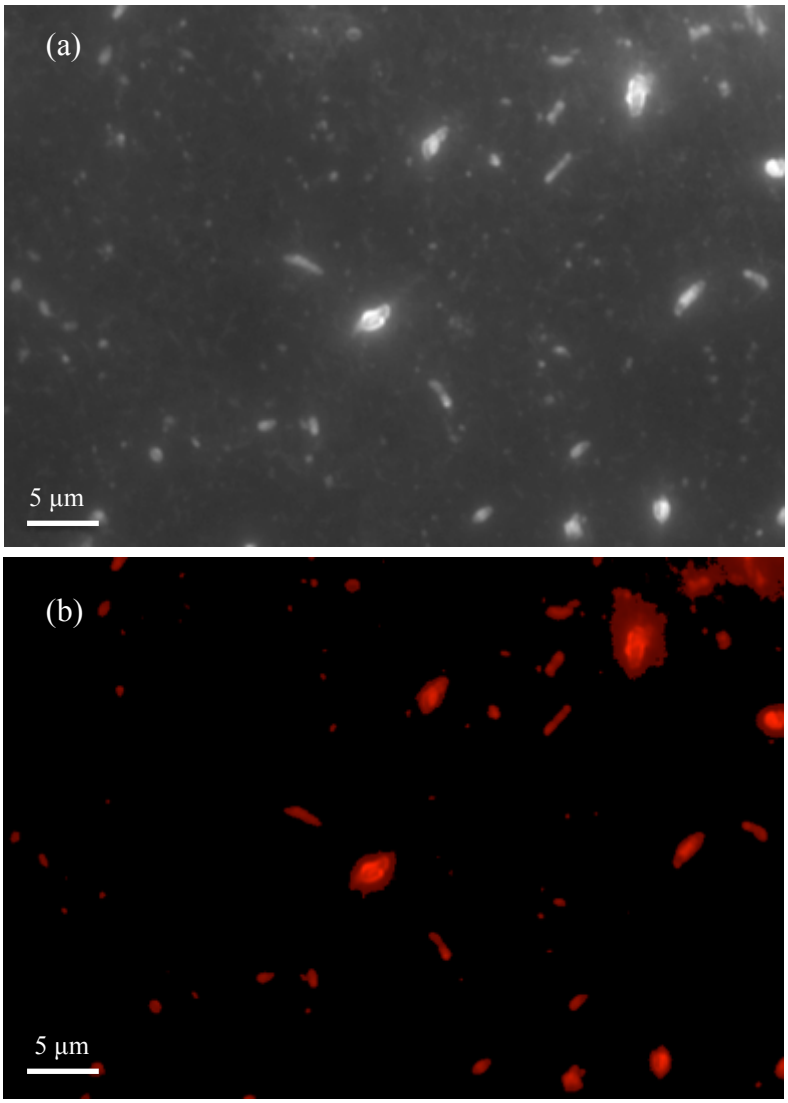

Figure 5.15 *M. smegmatis Nile red stained observed under green excitation light showing red emissions.*

The image shows the same field of view as ***Fig. 5.14*** *but shows red fluorescence. The total acquisition time is 150 ms. The* ***Fig. 5.15 a*** *displays the original image showed by the camera on the system. The camera only shows black and white; the intense white corresponds to intense red light emission (Nile red in a polar lipid environment). The* ***Fig. 5.15 b*** *shows the same image but processed in MATLAB®; this permit to remove the background light. The red light emission corresponds to Nile red in a polar lipid environment. This system is mimicking the Leica fluorescence microscope. The scale bar represents 5 µm.*

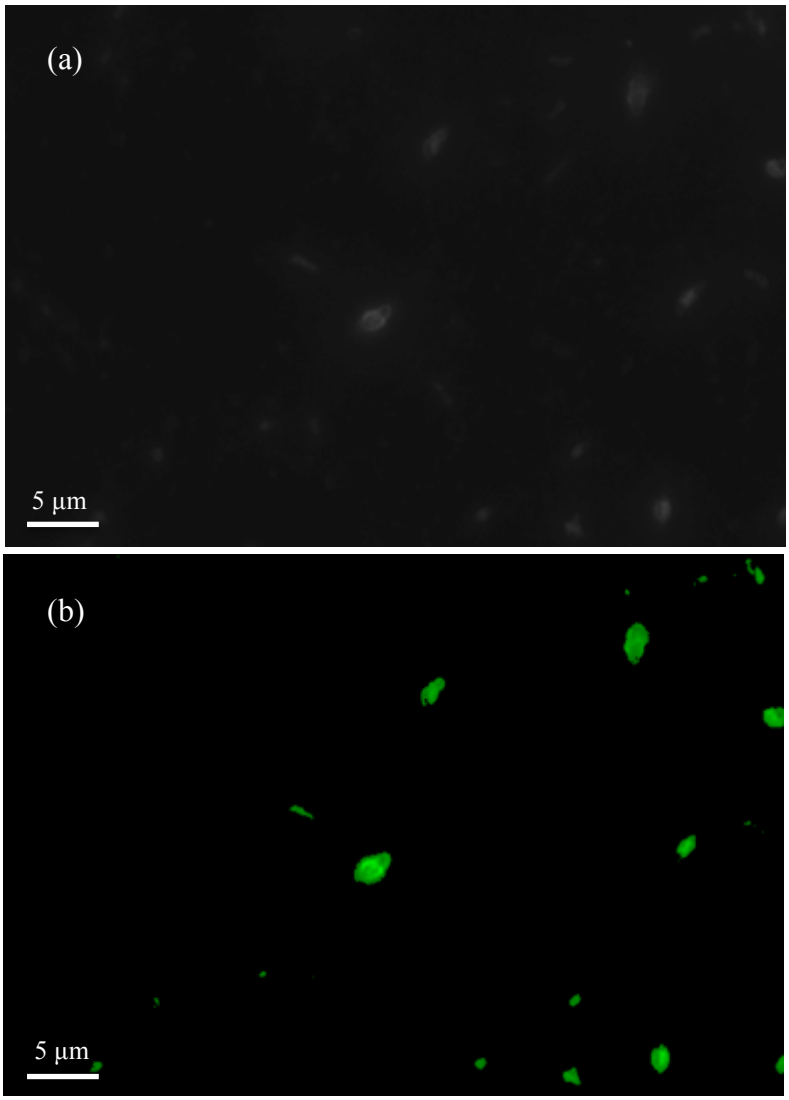

Figure 5.16 *M. smegmatis Nile red stained observed under blue excitation light showing green emissions.*

The image shows the same field of view as ***Fig. 5.14*** *with fluorescence acquired with the blue light excitation. The total acquisition time is 600 ms. The* ***Fig. 5.16 a*** *displays the original image showed by the camera on the system. The camera only shows black and white; the intense white corresponds to intense green light emission (Nile red in a non-polar lipid environment). The* ***Fig. 5.16 b*** *shows the same image but processed in MATLAB®; this permit to remove the background light. The green light emission corresponds to Nile red in a non-polar lipid environment. This system is mimicking the Leica fluorescence microscope. The scale bar represents 5 µm.*

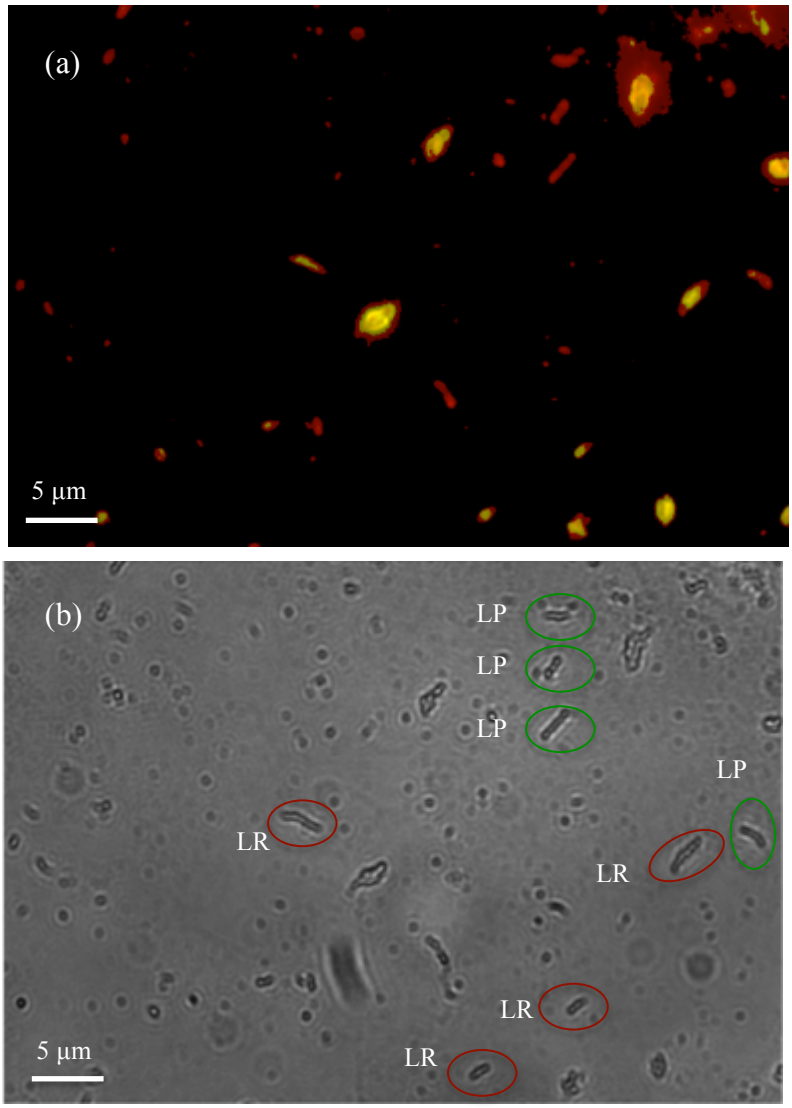

Figure 5.17 *Composite image of both green and red light emission and assignment to LR or LP.*

*The **Fig 5.17 a** present the composite image of both the red and green fluorescence emission. Among the studied bacteria, some display only red fluorescence and others show both red and green fluorescence. Based on those results the bacteria are assigned to either LR (red circle) or LP (green circle) as shown in **Fig 5.17 b.** The scale bar represents 5 µm.*

When the green fluorescence background was removed, some bacteria did not display any green fluorescence; compared to other cells that presented strong green intensity, much higher than the background level. Clear differences between LR and LP cells were observed based on the green light emission **Fig. 5.16** (presence of non-polar lipids) and also when looking at the combined picture **Fig. 5.17 a.** Based on this, single bacteria were assigned to either LR or LP **Fig. 5.17 b.** There is, especially among LR cell, high variability in green emission light intensity. This suggests that LR cells do not all carry a similar quantity of lipids.

Each single bacterium (shown in **Fig. 5.17 b)** was interrogated with Raman spectroscopy; the results are shown in **Fig. 5.18.** Only 8 spectra were taken on this initial experiment using conventional Raman spectroscopy (see **Chapter 2 General methods section 2.8** for more details). An important background signal was coming from the slide, and Nile red, removing this fluorescence entirely was difficult, and some was still visible in the reference spectra. Higher lipid peaks intensities were observed in the original spectra for each assigned LR cells compared to the assigned LP bacteria. After processing and normalisation, the two groups were not discriminated.

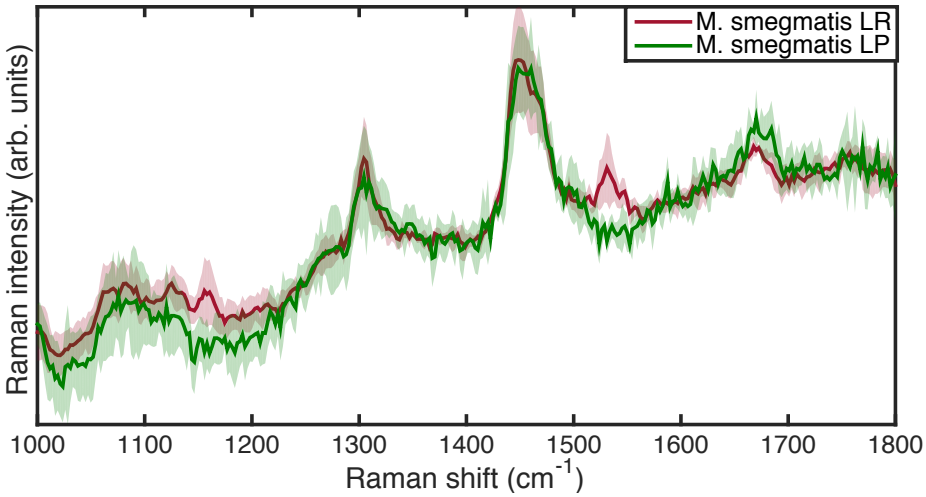

Figure 5.18 *Standard Raman spectroscopy average spectra of LR and LP cells.*

*The cells (8 in total) have been pre assigned to either LR or LP based on their fluorescence output (**Fig. 5.17 b.**). The red line represents the average standard Raman spectrum of LR cells, and the green corresponds to LP cells. The shaded coloured area shows one standard deviation. The x-axis shows the Raman shift (in wavenumber, cm^{-1}) and the y-axis displays the differential Raman intensity in arbitrary units. The acquisition time for both the background and the bacteria is 30 seconds, so around a minute per spectrum in total (see **Chapter 2 General methods section 2.8** for more details). The **Fig. 5.18** shows the finger print region of the spectrum (between 1000 to 1800 cm^{-1}).*

This short study showed interesting preliminary results and suggested that the system could perform both Raman spectroscopy and fluorescence analysis. Moreover, it was demonstrated that LR and LP cells could be described using the fluorescence and targeted by Raman spectroscopy. These initial results had to be confirmed more widely. WMR spectroscopy was used because of the high fluorescence background observed (**Fig. 5.18**).

An *in-vitro* experiment using Nile red stained and heat killed *M. tuberculosis* (4 month old culture) was carried out. A 100 µL volume of bacterial suspension was stained using 2.5 $\mu g.mL^{-1}$ Nile red (final concentration). Prior to taking Raman signal the preparation was studied using the white light, then the green excitation light (TRITC, standard Nikon fluorescence cube) and finally the blue excitation light (FITC, standard Nikon fluorescence cube). The first image **(Fig. 5.19**) shows the white light output, single bacilli and groups of cells (clumps) can be observed in the field of view. Then the green excitation light corresponding to the red fluorescence emission is shown in **Fig. 5.20 b**. All bacteria can be clearly observed on this image. Most of the bacteria showed similar red fluorescence emission intensity level. The blue excitation light resulting in green fluorescence emission, arises from Nile red in a predominantly non-polar lipid environment is shown in **Fig. 5.20 a**. Important differences can be observed between bacteria on this image. The combined image of both Red and green emission is shown in **Fig. 5.20 c**, **Fig. 5.20 d** presents a zoomed view of the combined image with an LR cell next to an LP cell**.** The assignments to LR or LP, based on the fluorescence results, are presented in **Fig. 5.21.**

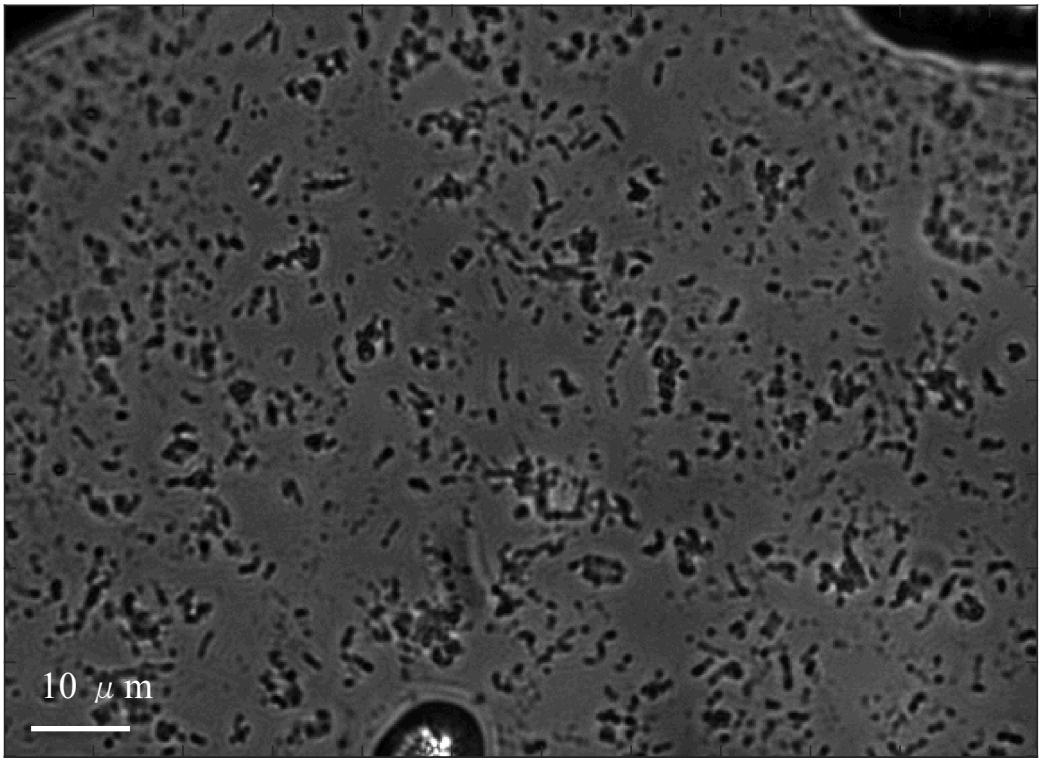

Figure 5.19 *Nile red stained M. tuberculosis observed under white light.*
This field of view is showing many bacilli, single cells and aggregated cells. The exposure time to acquire this picture, using white light, in the combined fluorescence-Raman spectroscopy system is 2 ms. The scale bar represents 10 μm.

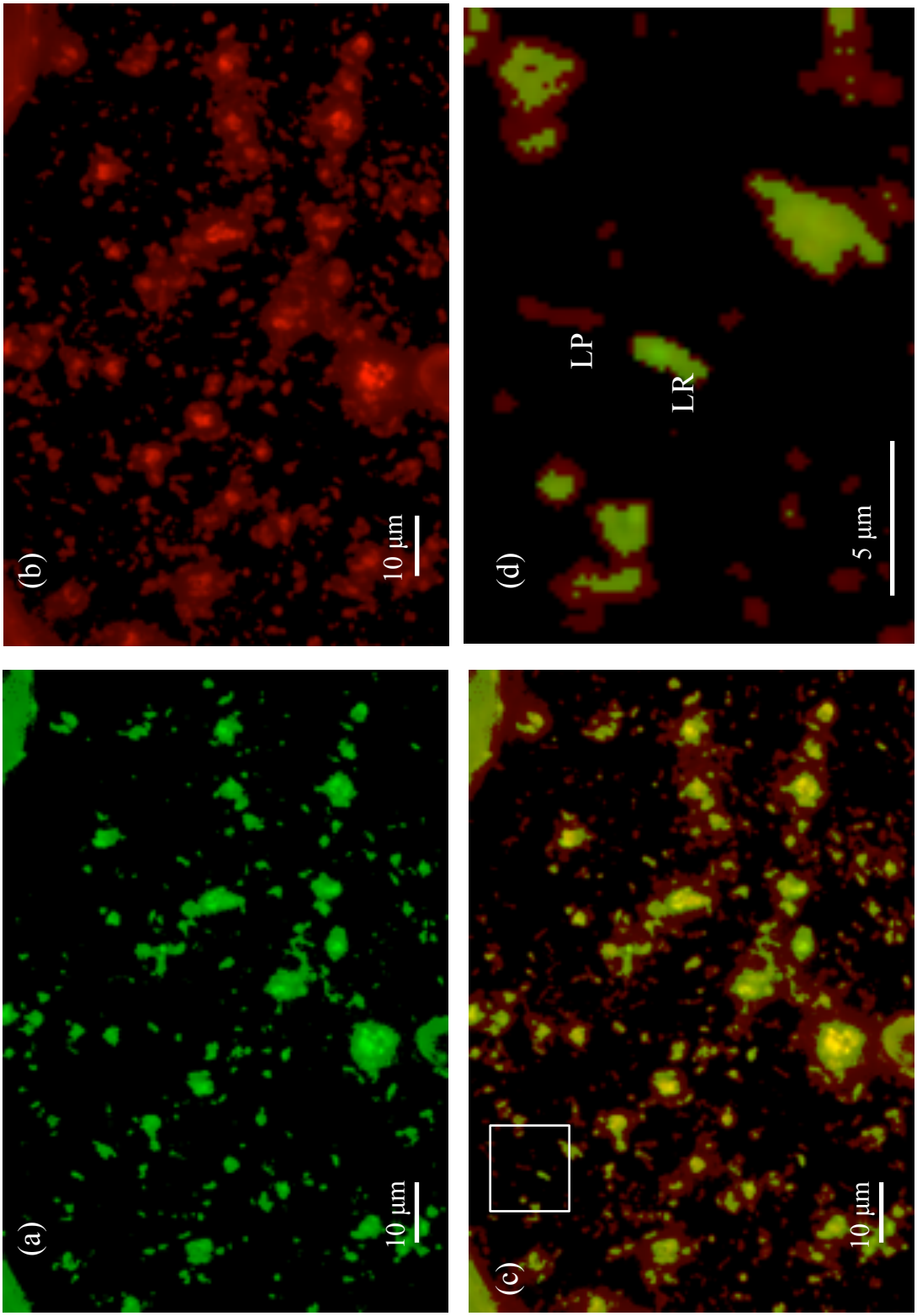

Figure 5.20 *M. tuberculosis Nile red stained observed under both green and blue excitation light.*

The green fluorescence emission (blue excitation light) output is shown in ***Fig. 5. 20 a;*** *The red fluorescence emission (green excitation light) output is shown in* ***Fig. 5. 20 b.*** *The* ***Fig. 5. 20 c*** *shows the combined image of red and green light emission.* ***Fig. 5. 20 d*** *is a zoomed area corresponding to the white rectangle in the combined picture; it shows a clear LR cell, with an intracellular lipid body and a LP cell next to it. The total acquisition time is 150ms for the red light emission and 600ms for the green light emission. The scale bar represents 5 µm. The* ***Fig. 5.20*** *shows the MATLAB® processed picture, with the background light removed.*

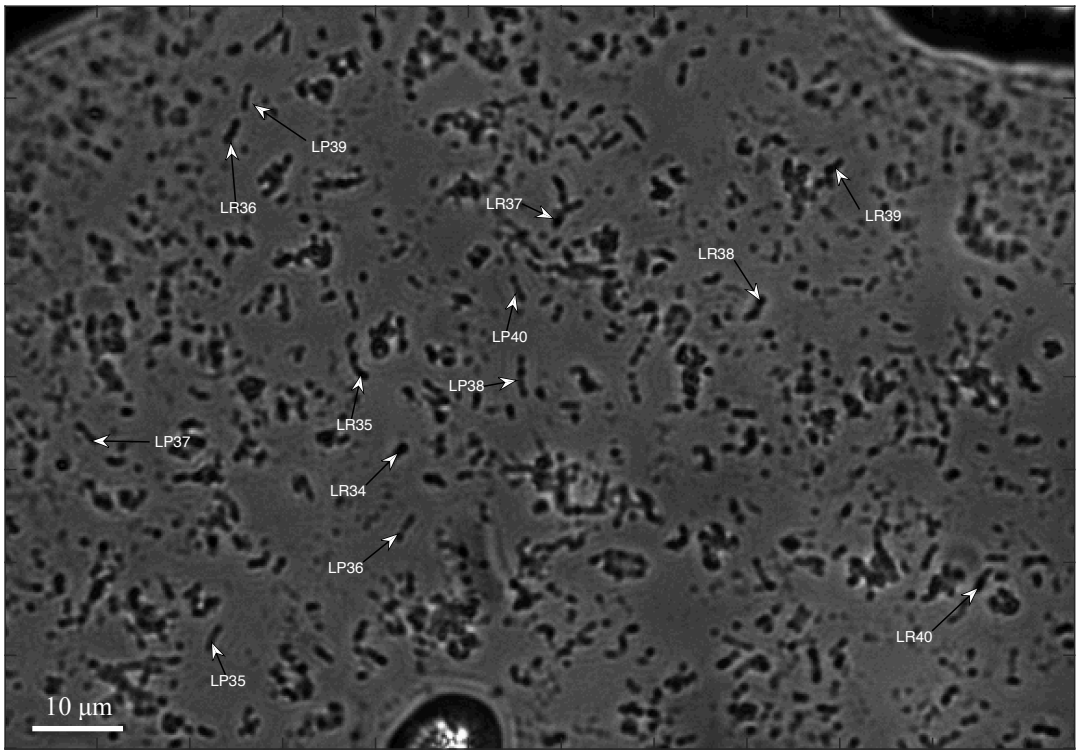

Figure 5.21 *Assignment to LR or LP based on fluorescence information. Among the studied single bacteria, some display only red and other show both red and green. Based on those results the bacteria are assigned to either LR or LP as shown in this figure. The scale bar represents 10 μm.*

In each field of view, some bacteria were presenting much higher intensity green fluorescence emission compared to the other cells. Two groups were created a LR and a LP as shown in **Fig. 5.21**. WMR spectroscopy was used on each single bacterium previously assigned by fluorescence. In total 200 spectra (100 LR and 100 LP) across 20 fields of view were acquired coming from four different slides and over six working days. The WMR spectroscopy results and associated PCA analysis are presented in **Fig. 5.22**. The *in-vitro* cell pre-assigned to LR or LP based on their fluorescence were discriminated by WMR spectroscopy with both high sensitivity (84.0%) and specificity (80.2%) (n=4) (**Fig. 5.22 a and b)**. Most of the variability among the WMR spectra is located in the lipid band A and the lipid band B. Moreover, the LR cluster in **Fig. 5.22 b** is much more dispersed than the LP cluster.

By using this combined fluorescence and Raman spectroscopy system, we demonstrated that the presence of green fluorescence emission of Nile red and therefore intracellular lipid bodies (LR cell) correlates with higher Raman intensity lipid bands (A and B) (**Fig. 5.22 a**).

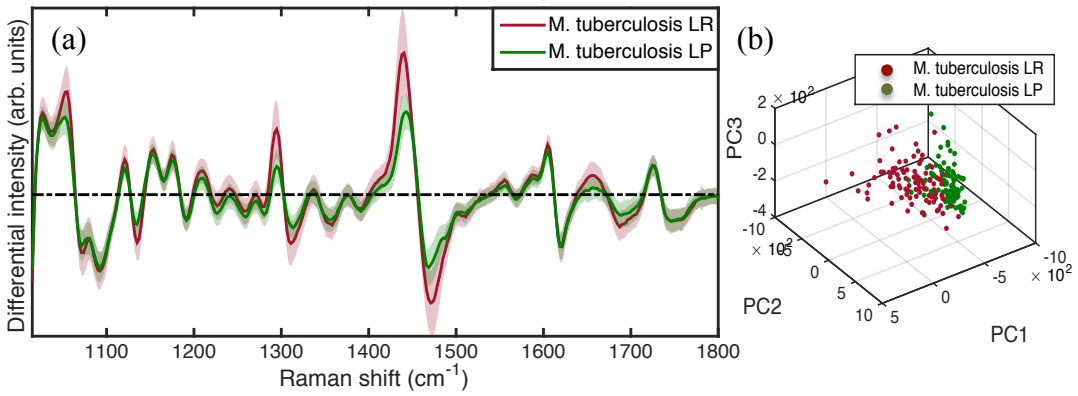

Figure 5.22 *Nile red stained in-vitro grown M. tuberculosis studied by fluorescence and WMR spectroscopy.*

Stained cells have been assigned to either LR or LP based on their fluorescence as seen in the previous figures. Then each single bacterium is interrogated by WMR spectroscopy. The ***Fig. 5.22 a*** *shows the average WMR spectrum of LR (red line) and LP (green line) cells pre-assigned by fluorescence. The average spectrum is calculated over a 100 single bacterium for both LR and LP phenotypes. The shaded coloured zone represents the corresponding single standard deviation. The x-axis is the Raman shift (in wavenumber, cm^{-1}) and the y-axis shows the differential Raman intensity in arbitrary units. The* ***Fig. 5.22 b*** *displays the corresponding PCA plot showing how the two data sets are clustering. The plot is showing the first three PCs, and each dot corresponds to a single bacterium. The lipid band A is located at 1300 cm^{-1} and the lipid band B around 1440-1450 cm^{-1}. The time required to obtain one single cell spectrum is 150 seconds (see* ***Chapter 2 General methods section 2.8*** *for more details). The figure shows the finger print region of the spectrum (between 1010 to 1800 cm^{-1}).*

5.3.6 TB infected guinea pig lung tissue stained with Nile red and interrogated by the combined system (WMR spectroscopy and fluorescence imaging)

The frozen TB infected guinea pig lung tissue sections were stained with Nile red using a final concentration of 25 μg.mL^{-1}. *M. tuberculosis* cells in the alveoli of infected lung tissue sections were interrogated by both fluorescence and WMR spectroscopy. A total of 93 single bacilli were studied, 56 assigned to LR and 37 to LP based on their fluorescence emission. An example of single LR and LP cell located in alveoli of infected lung tissue section are shown in **Fig. 5.23.** Once assigned to LR or LP the bacteria were interrogated using WMR spectroscopy; the average spectra for both phenotypes are shown in **Fig. 5.24 a**. The corresponding PCA plot, **Fig. 5.24 b**, displays two distinct clusters with LR cells showing a wider distribution as found previously in the *in-vitro* results (**Fig. 5.22 b**). Similarly to the *in-vitro* results the presence of green light emission correlates with higher intensity in lipid bands A and B. The two phenotypes were successfully discriminated with high sensitivity (92.6%) and specificity (84.6%) (n=3) (**Fig. 5.24 a** and **b**). The *in-vitro* and *ex-vivo* spectra are plotted together in **Fig. 5.24 c** with the corresponding PCA plot, shown in **Fig. 5.24 d**. The *in-vitro* and *ex-vivo* spectra of LR cells cluster together, and the same is observed for the LP cells (**Fig. 5.24 d**). The LR phenotype is predominant in the TB infected lung with 60% of the cells interrogated being LR.

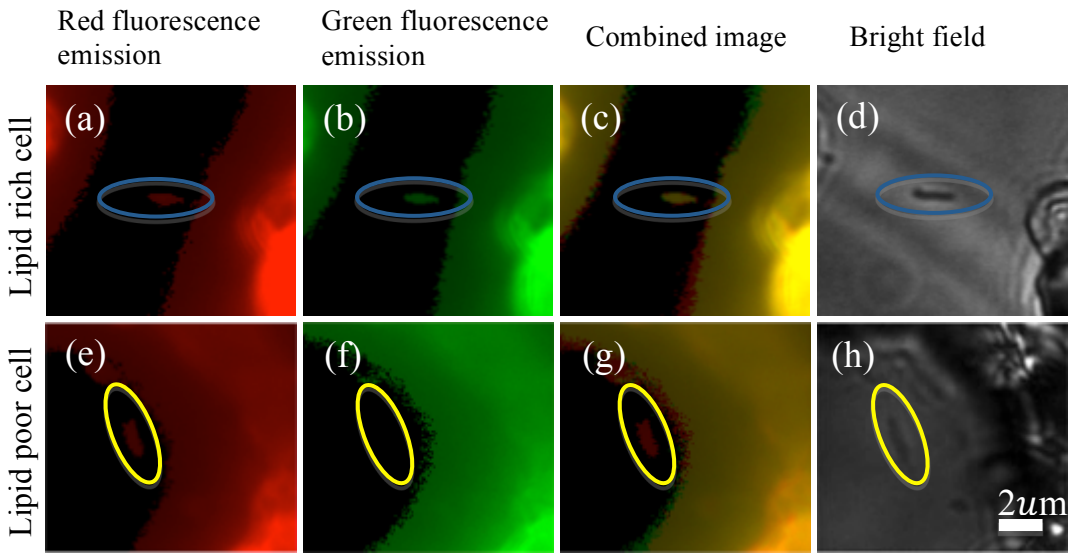

Figure 5.23 *Guinea pig TB infected lung tissue section stained with Nile red. The tissue sections are investigated using the combined fluorescence and Raman spectroscopy system. The first column (**Fig. 5.23 a** and **e**) shows the red fluorescence emission (Nile red in a polar lipid environment), the second column (**Fig. 5.23 b** and **f**) displays the green fluorescence emission (Nile red in a non-polar lipid environment). The third column (**Fig. 5.23 c** and **g**) corresponds to the combined image of the red and green fluorescence emission, and the last column (**Fig. 5.23 d** and **h**) represents the bright field image. The **Fig. 5.23 a, b, c and d** present an example of LR cell, encircled in blue, showing clear green fluorescence emission coming from intracellular non-polar lipids (**Fig. 5.23 b**). The **Fig. 5.23 e, f, g and h** present an example of LP cell, encircled in yellow, which does not shows any green fluorescence emission (**Fig. 5.23 f**). The fluorescence background is coming from the Nile red stained tissue. The scale bar represents 2 µm.*

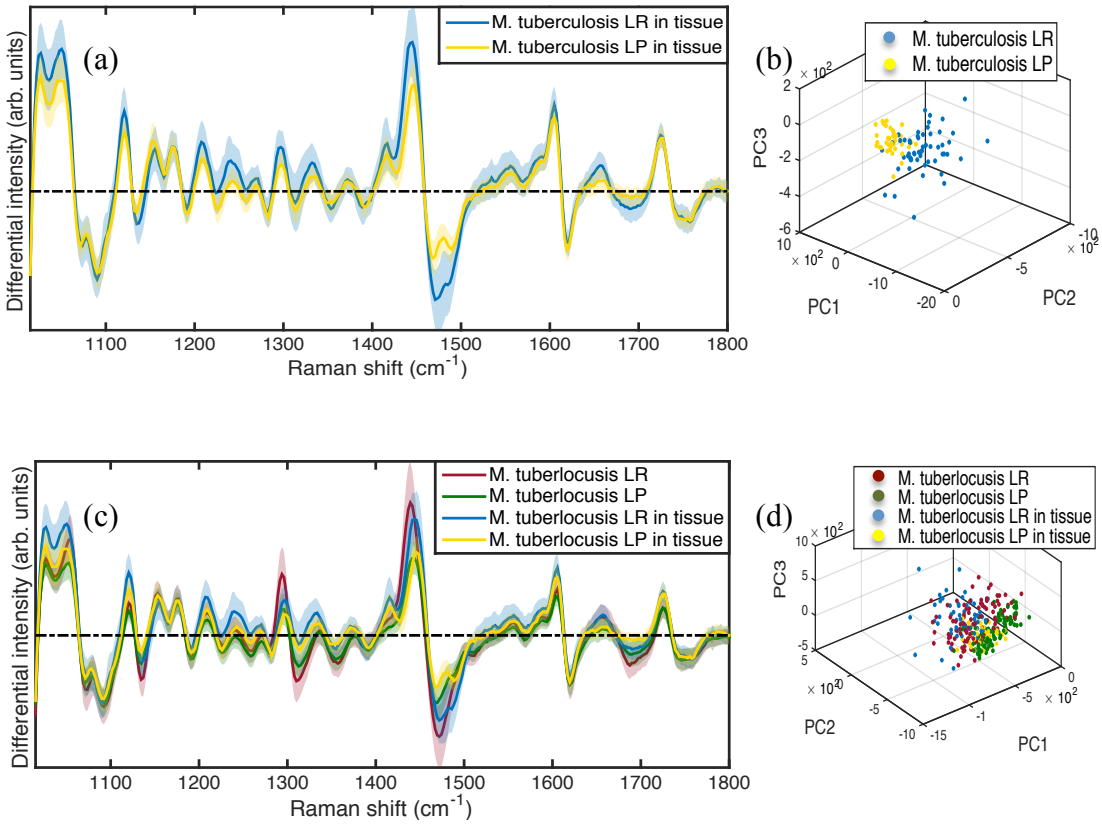

Figure 5.24 *M. tuberculosis from guinea pig lung tissue investigated by WMR spectroscopy.*

Prior to WMR spectroscopy measurements the single bacteria have been assigned to LR or LP based on their fluorescence emission. The ***Fig. 5.24 a*** *shows the average WMR spectrum of LR (red line) and LP (green line) cells pre-assigned by fluorescence. The shaded coloured zone represents the corresponding single standard deviation. The* ***Fig. 5.24 b*** *displays the corresponding PCA plot showing how the two data sets are clustering. The plot is showing the first three PCs, and each dot corresponds to a single bacterium. The* ***Fig. 5.24 c*** *and* ***d*** *show both in-vitro (****Fig. 5.22****) and ex-vivo (****Fig. 5.24 a*** *and* ***b****) data combined. The* ***Fig. 5.24 c*** *shows the average spectrum of in-vitro LR (red line), in-vitro LP (green line), ex-vivo LR (blue line) and ex-vivo LP (yellow line). The* ***Fig. 5.24 c*** *display the corresponding PCA plot showing the first three PCs. The x-axis is the Raman shift (in wavenumber, cm^{-1}) and the y-axis shows the differential Raman intensity in arbitrary units. The lipid band A is located at 1300 cm^{-1} and the lipid band B around 1440-1450 cm^{-1}. The time required to obtain one single cell spectrum is 150 seconds (see* ***Chapter 2 General methods section 2.8*** *for more details). The figure shows the finger print region of the spectrum (between 1010 to 1800 cm^{-1}).*

5.3.7 Study of Raman shift windows

All *M. tuberculosis in-vitro* and *ex-vivo* data sets have been analysed using different Raman shift windows: 700~1800 cm^{-1}, 1000~1800 cm^{-1}, 1000~1500 cm^{-1}, 1250~1500 cm^{-1} and 1400~1500 cm^{-1}. This was done in order to observe if the sensitivity and specificity would decrease when using a smaller portion of the Raman spectrum for analysis. All Raman shift windows showed similar sensitivity and specificity results in all *M.tuberculosis* data sets (*in-vivo* and *ex-vivo*); the highest standard deviation, in sensitivity or specificity, found was less than 0.045 (**Appendices Section 4 Tab. 1 to 4).** The two phenotypes can still be discriminated in all data sets, with high sensitivity and specificity, when targeting only the region 1250~1500 cm^{-1} (lipid band A and B) or 1400~1500 cm^{-1} (lipid band B) **(Appendices Section 4 Tab. 1 to 4)**. This confirms that the major difference between the two phenotypes are located in lipid bands A and lipid band B.

5.3.8 Immunostaining

In order to compare the impact of Nile red staining and WMR spectroscopy, on tissue samples, immuno-staining was performed on tissue sections after these two methods. The quartz slides and coverslips were positively charged using a silane solution. The slide surface was interrogated using WMR spectroscopy to observe if any extra peaks could be observed compared to uncharged slides. This process did not impact the Raman spectrum, as no signal from silane was observed; both charged and uncharged quartz slides showed identical background, see in **Fig. 5.25**.

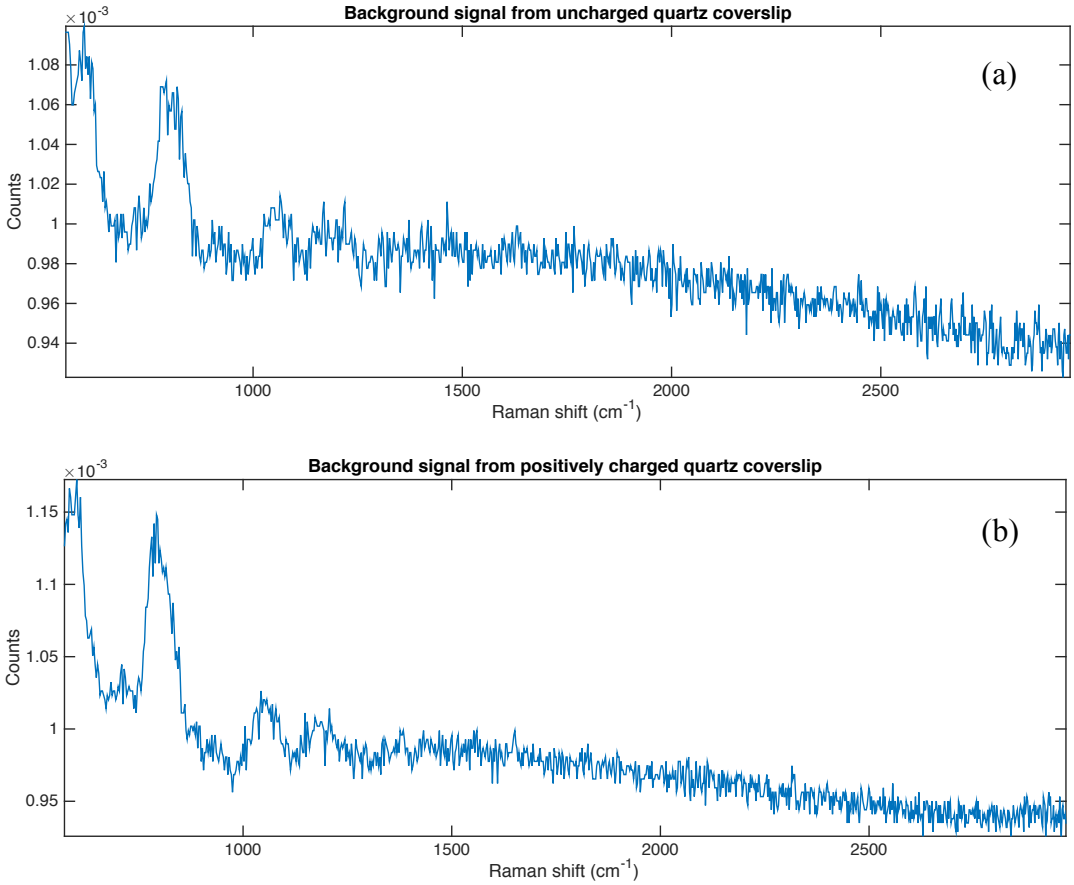

Figure 5.25 *Raman spectrum of the surface of uncharged and charged quartz coverslips.*

*The blue line represents the Raman spectrum of uncharged (**Fig. 5.25 a**) and charged (**Fig. 5.25 b**) quartz coverslip. The x-axis shows the Raman shift in cm^{-1}, the y-axis represents the counts. The acquisition time was 1 seconds per spectrum. Both charged and uncharged slides display identical signals no peak from aminopropyltriethoxysilane can be observed.*

Frozen sections of mice lymph node infected with BCG were attached to positively charged glass slides or quartz slides (both coverslip and slide). Tissue sections attached to a glass slide, quartz slide and quartz coverslip were investigated using WMR spectroscopy. The **Fig. 5.26** shows WMR spectra of mice lymph node tissue acquired from glass slide (**Fig. 5.26 a** and **b**), quartz slide (**Fig. 5.26 c** and **d**) and quartz coverslip (**Fig. 5.26 e** and **f**). The **Fig. 5.26** presents the unprocessed (**Fig. 5.26 a, c and e**) and the processed (**Fig. 5.26 b, d and f**) spectra. The unprocessed spectrum shows five spectra (five different coloured lines, in **Fig. 5.26 a, c and e**) acquired while the laser wavelength was tuned. This is why the Raman peak positions changes slightly for each of the five Raman spectra. In the unprocessed spectrum, there is still both Raman peaks and fluorescence. After processing all fluorescence is removed and only the Raman peaks, which did shift according to the laser wavelength, are kept. The Raman peaks coming from the tissue are clearly visible, in unprocessed spectra, when the tissue is attached to quartz slide (**Fig. 5.26 c**) or quartz coverslip (**Fig. 5.26 e**) but the peaks are hidden in the background signal coming from the glass in (**Fig. 5.26 a**). The Raman peaks, from tissue attached on glass, appear after data processing. This shows how the background signal from glass has been removed using WMR spectroscopy. The WMR spectrum of tissue can be observed in all preparations after data processing (**Fig. 5.26 b, d and f**). However, the processed spectrum acquired from tissue on the quartz coverslip shows much higher signal intensity and low noise level. The best WMR spectrum of tissue was acquired when the tissue section was attached to quartz coverslip.

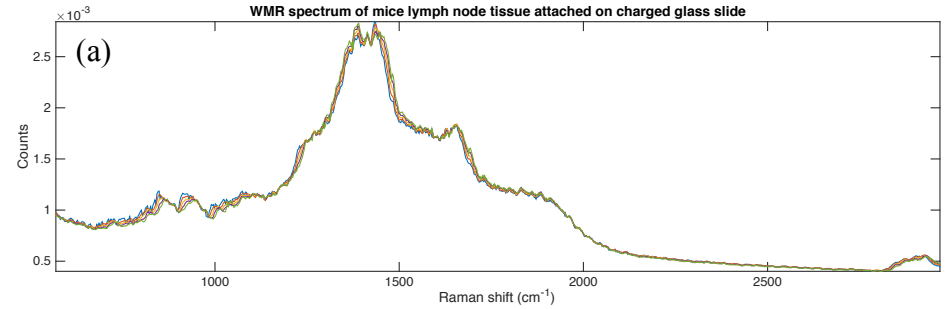
WMR spectrum of mice lymph node tissue attached on charged glass slide
(a)
×10^-3
Counts
Raman shift (cm^-1)

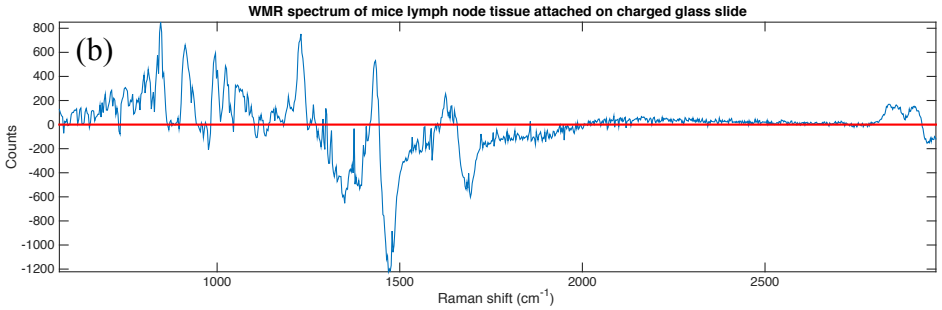
WMR spectrum of mice lymph node tissue attached on charged glass slide
(b)
Counts
Raman shift (cm^-1)

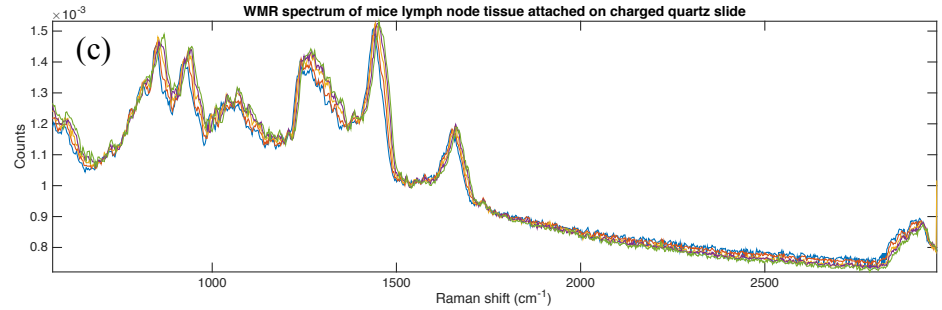
WMR spectrum of mice lymph node tissue attached on charged quartz slide
(c)
×10^-3
Counts
Raman shift (cm^-1)

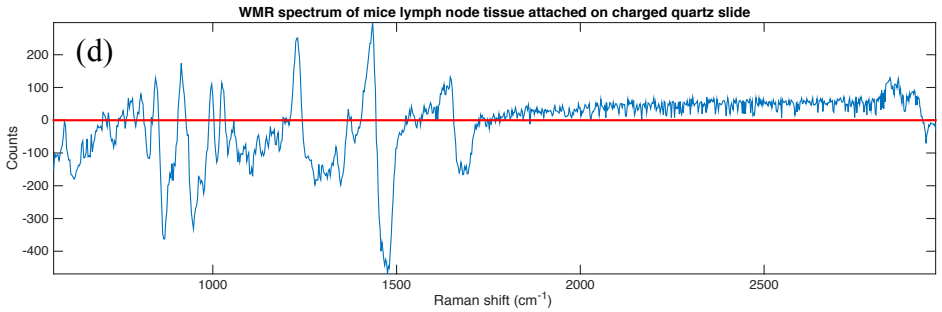
WMR spectrum of mice lymph node tissue attached on charged quartz slide
(d)
Counts
Raman shift (cm^-1)

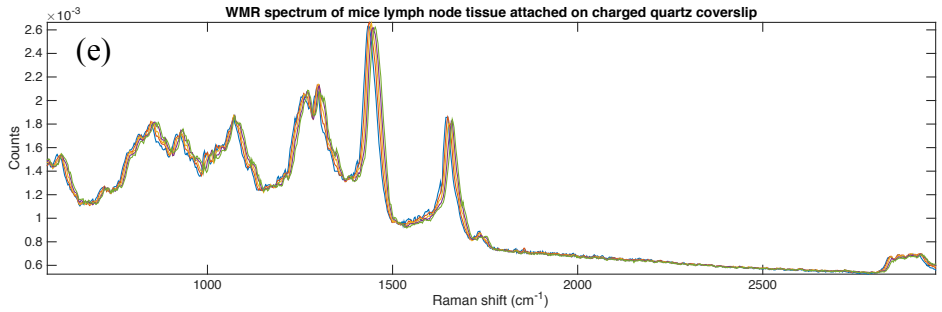
WMR spectrum of mice lymph node tissue attached on charged quartz coverslip
(e)
×10^-3
Counts
Raman shift (cm^-1)

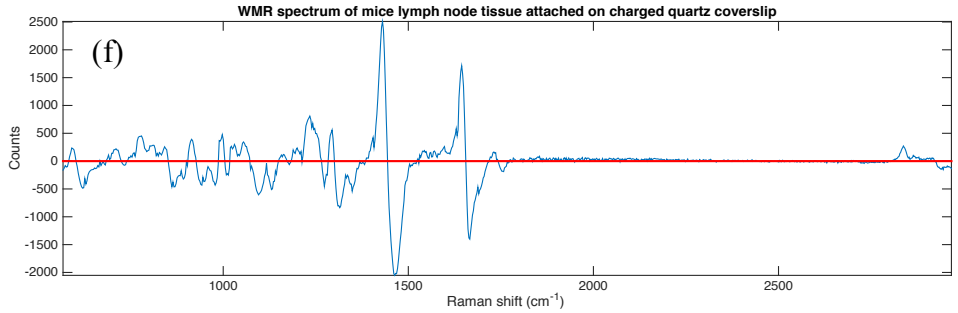
WMR spectrum of mice lymph node tissue attached on charged quartz coverslip
(f)
Counts
Raman shift (cm^-1)

Figure 5.26 *WMR spectra of BCG infected lymph node tissue sections, a comparison between preparations.*

*The mounts were made of a glass slide, quartz slide or quartz coverslip. Both unprocessed (**Fig. 5.26 a, c** and **e**) and processed (**Fig. 5.26 b, d** and **f**) WMR spectra of tissue attached to a glass slide (**Fig. 5.26 a** and **b**), quartz slide (**Fig. 5.26 c** and **d**) or attached to quartz coverslip (**Fig. 5.26 e** and **f**) are presented. For all the figures the x-axis shows the Raman shift in cm^{-1}, the y-axis represents the counts. In the unprocessed data (**Fig. 5.26 a, c** and **e**) each coloured line corresponds to one of the five Raman spectra taken during the modulation. In the processed data (**Fig. 5.26 b, d** and **f**) the blue line represents the WMR spectrum after processing. The zero crossing that is represented by the red line shows the Raman peak position. The intensity of the peak corresponds to the peak-to-valley around the zero crossing point. The acquisition time was 150 seconds per spectra (see **Chapter 2 General methods section 2.8** for more details).*

The frozen mice lymph nodes infected with BCG were stained with Nile red and studied with fluorescence microscopy.

All the tissue preparations were studied by immuno-staining and compared:

- The positive control corresponding to tissue attached to a positively charged glass slide (usually used in this method),
- Tissue attached to positively charged quartz slides both coverslip and slides.
- Nile red stained tissue attached to positively charged glass slides.
- Negative control (no primary antibody) with tissue attached to positively charged glass slide (usually used in this method).

The immuno-staining was targeting T-cell using an anti-CD3 primary antibody. A secondary anti-primary antibody was then used. The secondary antibody was HRP conjugated. Finally, tyramine-signal-amplification (TSA)-CY5 was added leading to an enzymatic reaction involving Tyramine and HRP. The two molecules form a covalent bond; the CY5 attached to the TSA can now produce fluorescence. The tissue was counter stained with Hoechst dye that stained the nucleus of all cells present in the tissue. The positive control was compared to a negative control. The negative control followed the same protocol as the positive protocol but no primary antibody was added, to verify that there was no unspecific staining. Negative control did not show any specific staining on the cells meaning that the staining observed in the positive control slide was specific to T-cells (**Fig. 5.27**).

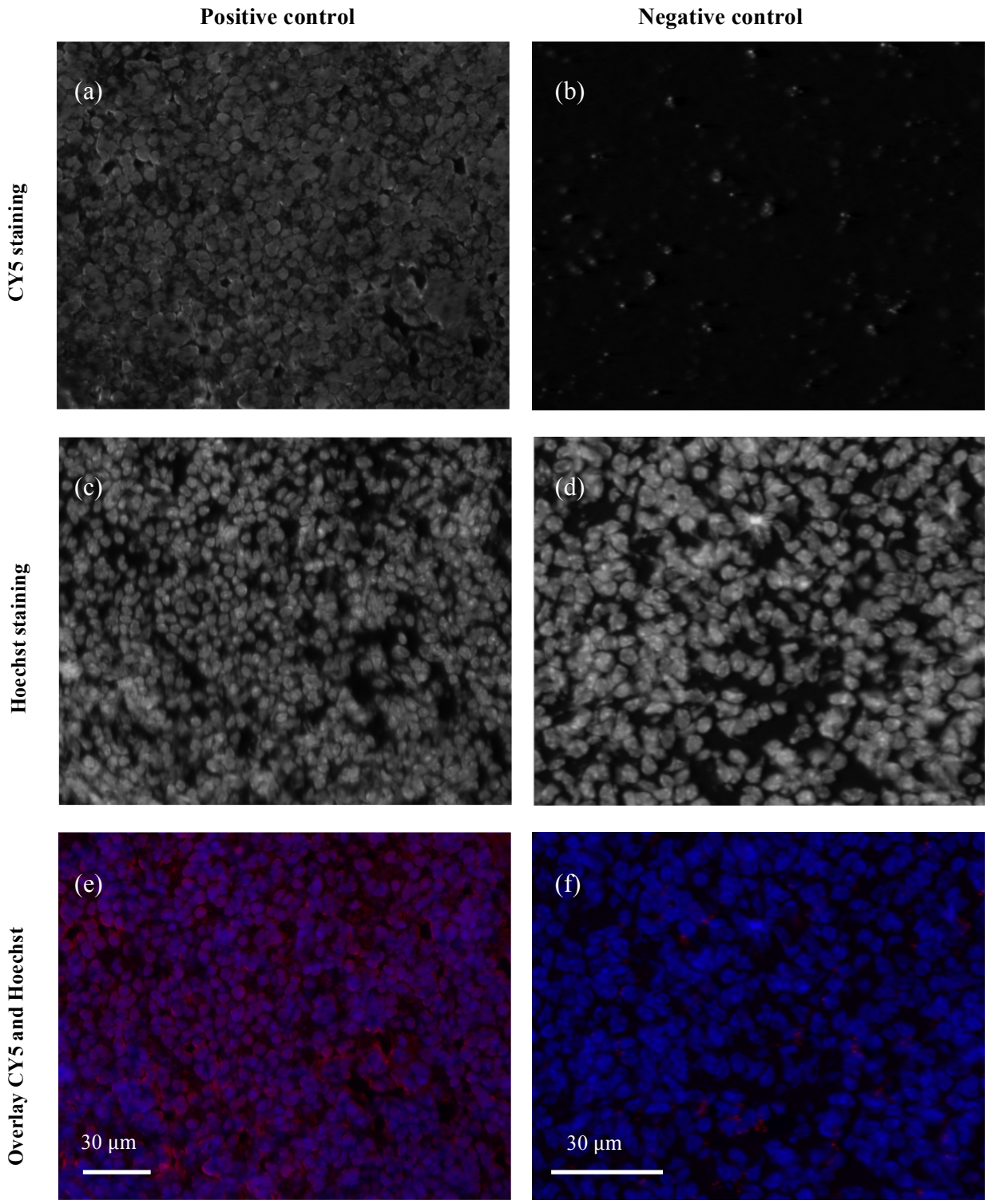
Positive control
Negative control
CY5 staining
Hoechst staining
Overlay CY5 and Hoechst
(a)
(b)
(c)
(d)
(e)
(f)
30 µm
30 µm

Figure 5.27 *Comparison between positive and negative control of immuno stained tissue sections.*

Frozen sections of BCG infected mice lymph node were used in this experiment. The sections were 10 µm thick. The tissue was stained using a CY5 dye that conjugates to a secondary antibody, which is attached to a primary antibody targeting specifically T-cells. The tissue was also stained using a counter stain called Hoechst, staining cell nuclei. The difference between the positive control and the negative control is that no primary antibody was used in the negative control. This test was realised to demonstrate that the CY5 fluorescence was specific. The positive control is shown in the first column ***Fig. 5.27 a, c*** *and* ***e*** *and the negative control in the second* ***Fig. 5.27 b, d*** *and* ***f****. The first row,* ***Fig. 5.27 a*** *and* ***b****, is a grey scale picture showing CY5 fluorescence (T-cells). The second row,* ***Fig. 5.27 c*** *and* ***d****, presents Hoechst staining (cells nuclei) in grey scale. The last row corresponds to the overlay of the previous two rows; where the CY5 fluorescence is shown in red and the Hoechst counter staining in blue. The scale bars represent 30 µm.*

Then we compared the tissue attached to a positively charged glass slide that was interrogated by WMR spectroscopy previously and the tissue attached to a positively charged glass slide that was stained by Nile red previously. The results are shown in **Fig. 5.28**. If the tissue sections were stained with Nile red first and then immuno stained the CY5 and Hoechst staining were found very poor in quality. The CY5 staining was not specific **Fig. 5.28 b** and **f** and the counter stain was not making possible an accurate localisation of cells nuclei. This made it impossible to observe T-cells specifically. In comparison the tissue previously studied by WMR spectroscopy was not damaged at all, good quality Hoechst staining was observed, showing the nuclei of cells, specific CY5 stain was clearly visible, rendering possible the specific localisation of T-cells. The comparison between the two slides (Nile red stained and WMR spectroscopy) in **Fig. 5.28** shows clearly that Nile red staining did impact and damage the tissue investigated whereas Raman spectroscopy did not.

The tissue attached to quartz (slide and coverslip) previously interrogated by WMR spectroscopy was immunostained. The results were compared to the one previously obtained when the tissue was attached to a glass slide (**Fig. 5.28 a c and e**). Similar immunostaining results were found with the charged quartz slides compared with the glass slide. High quality Hoechst counter stain is observed and specific CY5 staining. T-cells can be specifically identified **Fig. 5.29**. Immunostaining can be performed on tissue sections that have been previously interrogated by Raman spectroscopy, as this method does not damage the sample. Moreover, immunostaining performed well on any of the positively charged slides tested, glass and quartz.

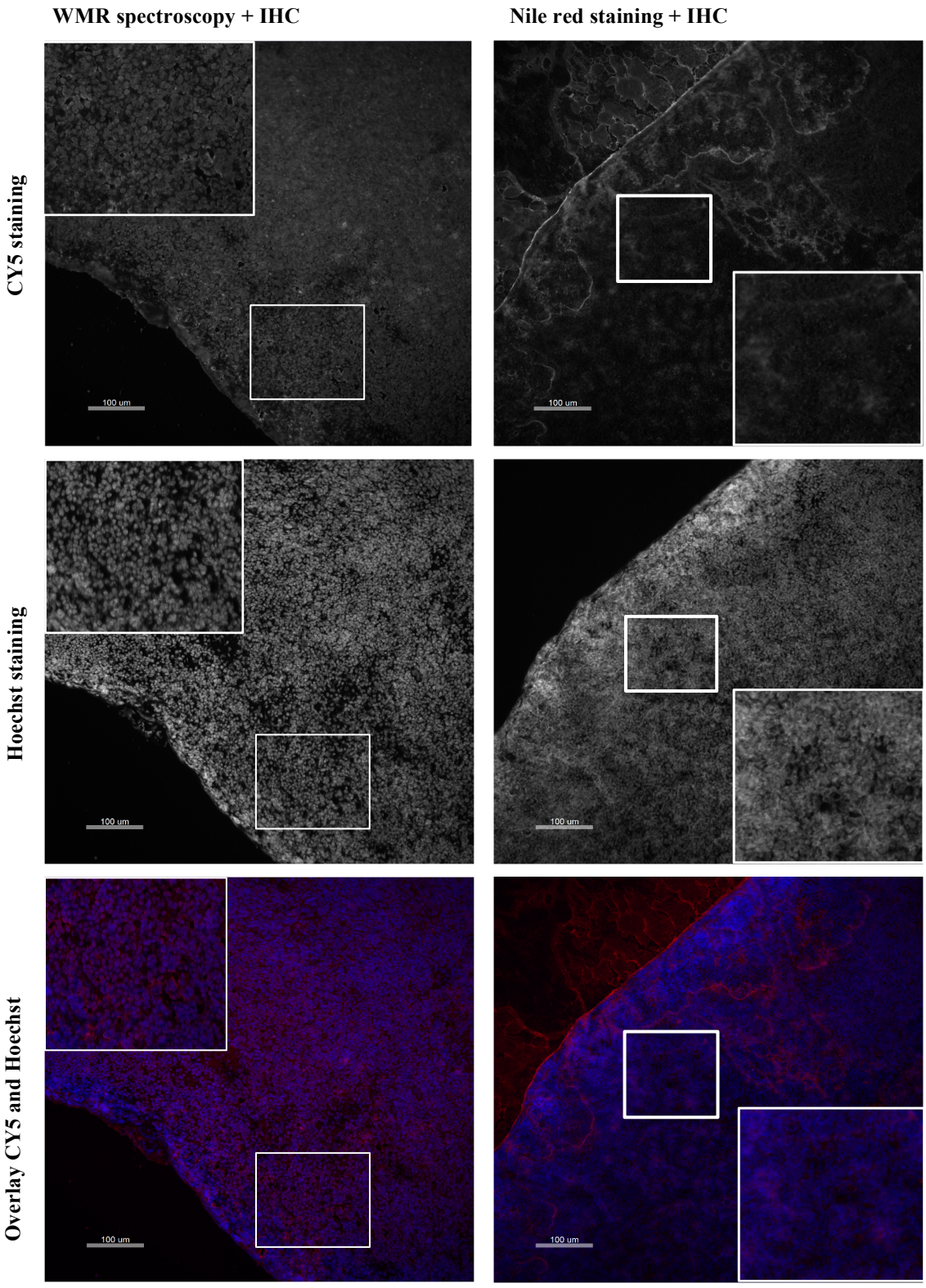
WMR spectroscopy + IHC
Nile red staining + IHC
CY5 staining
Hoechst staining
Overlay CY5 and Hoechst
100 um
100 um
100 um
100 um
100 um
100 um

Figure 5.28 *Impact of WMR spectroscopy and Nile red staining on the output of immuno-staining.*

The ***Fig. 5.28*** *shows a comparison of immuno-stained tissue sections that were previously interrogated by WMR spectroscopy (****Fig. 5.28 a, c*** *and* ***e)*** *or Nile red staining (****Fig. 5.28 b, d*** *and* ***f)****. Frozen sections of BCG infected mice lymph node were used in this experiment. The sections were 10 µm thick. The tissue was stained using a CY5 dye that conjugates to a secondary antibody, which is attached to a primary antibody targeting specifically T-cells. The tissue was also stained using a counter stain called Hoechst, staining cell nuclei. The tissue interrogated first by WMR spectroscopy is shown in the first column (****Fig. 5.28 a, c*** *and* ***e)*** *and the tissue investigated first by Nile red staining is presented in the second column* ***(Fig. 5.28 b, d*** *and* ***f)****. The first row,* ***Fig. 5.28 a*** *and* ***b****, is a grey scale picture showing CY5 fluorescence (T-cells). The second row,* ***Fig. 5.28 c*** *and* ***d****, presents Hoechst staining (cells nuclei) in grey scale. The last row corresponds to the overlay of the previous two rows; where the CY5 fluorescence is shown in red and the Hoechst counter staining in blue. The scale bars represent 100 µm. Each figure shows a zoomed area.*

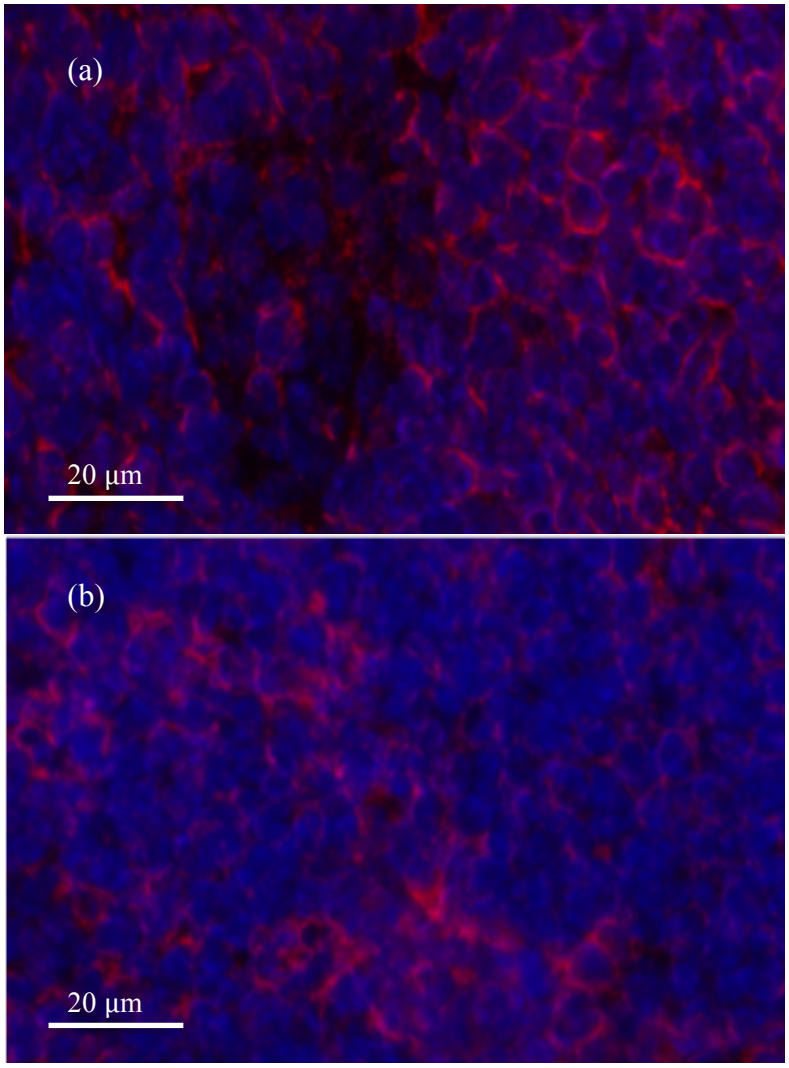

Figure 5.29 *Immuno-staining on tissue attached to quartz slides.*
The tissue sections were previously interrogated by WMR spectroscopy. Frozen sections of BCG infected mice lymph node were used in this experiment. The sections were 10 µm thick. The tissue was stained using a CY5 dye that conjugates to a secondary antibody, which is attached to a primary antibody targeting specifically T-cells. The tissue was also stained using a counter stain called Hoechst, staining cell nuclei. The ***Fig. 5.29*** *shows the immuno-staining results from tissue attached to quartz slide (****Fig. 5.29 a****) and the results from tissue attached to quartz coverslip (****Fig. 5.29 b****). The* ***Fig. 5.29 a*** *and* ***b*** *corresponds to an overlay picture showing both CY5 fluorescence in red and the Hoechst counter staining in blue. The scale bars represent 20 µm.*

5.4 Discussion

Recent clinical trials failed to shorten TB treatment to four months due to high relapse rate. The pathology of relapse remains largely unknown (Gillespie *et al.*, 2014, Phillips *et al.*, 2016). Relapse can be observed in patients that have been found sputum culture negative early in treatment (Phillips *et al.*, 2016). Relapse is a crucial area of research to shorten TB treatment. The study of *M.tuberculosis* phenotypes has been mainly focussed on sputum. However, sputum might not fully represent the bacteria present in the lung and more importantly the one responsible for relapse (Mukamolova *et al.*, 2010). This chapter proposes a method to investigate mycobacterial phenotype directly at the site of infection using lung tissue section of TB infected guinea pig. To our knowledge, this work represents the first study using Raman spectroscopy to investigate *M. tuberculosis* phenotypes *in-situ*. Guinea pigs are used in TB research as an animal model (Gumbo *et al.*, 2015). This animal model has been chosen for this study because guinea pigs develop similar lesions to humans in PTB (Clark *et al.*, 2015).

The first infected guinea pig tissue sections tested were paraffin embedded. When observed on the Raman spectroscopy system the lung structure was preserved meaning that the process did not damage the tissue. Moreover, single bacteria could be observed within alveoli (**Fig. 5.1**). Spectra of single bacillus were taken using WMR spectroscopy method and a very strong and complex spectrum signal was then noted (**Fig. 5.2**). This signal was very different from the *in-vitro M. tuberculosis* spectrum from single cells (see **Chapter 4 Fig. 4.3**), and the level of intensity was a lot higher, over 20 times more intense. This spectrum was obtained from locations all over the slide and corresponds to the paraffin used to embed the tissue. The dewaxing

procedure does not remove 100 percent of the paraffin and Raman spectroscopy can still pick up signals from the paraffin after dewaxing (Faolain *et al.*, 2005). Paraffin presents an intense band around 1450 cm^{-1} meaning it would participate in the main lipid band (lipid band B) used as a major discriminating factor between LR and LP cells. This would make the result not interpretable, and bacteria could not be assigned to any phenotype. Frozen sections are also commonly used; the main advantage of the frozen section is that fewer chemicals are used in the process compared to the paraffin embedding method. The first experiment using frozen tissue sections showed low intensity spectra as the tissue sample was located far away from the objective. The tissue was attached further away compared to previous experiment resulting in a loss of signal (**Fig. 5.3**, **Fig. 5.4** and **Fig. 5.5**). The optimal protocol and slide preparation for the study of single bacteria in a frozen tissue section by WMR spectroscopy are shown in **Fig. 5.6**, **Fig. 5.7** and **Fig. 5.8.** The spectra of single *M. tuberculosis ex-vivo,* in Guinea pig lung tissue sections, are comparable to the *in-vitro* results regarding peak intensity and position. However, a direct comparison is difficult as differences are observed between *in-vitro* and *ex-vivo* spectra. For example, the lipid band A, around 1300 cm^{-1}, displays a lower intensity in the spectra of *M. tuberculosis* cells from tissue due to the fixation and freezing procedure (Buijtels *et al.*, 2008, Galli *et al.*, 2014) (**Fig. 5.9 a** and **b**). The lipid band A and B are not impacted similarly by the procedure; when comparing LR, LP and tissue spectra using a ratio ($R_{\text{band B/Ref band}}$), we found that both phenotypes were present in tissue and that the population is skewed towards LR cells (**Fig. 5.9 c**). Similar results were found when using the lipid band A for the ratio (**Fig. 5.10**).

We observed that Nile red staining does not impact the Raman spectrum as no significant spectral differences could be found between *M. smegmatis* stained and unstained data sets (**Fig. 5.13**).

An initial experiment using both fluorescence and Raman spectroscopy showed that the fluorescence system could identify LR and LP cells (**Fig. 5.14 to Fig. 5.17**). The single cells were interrogated using standard Raman spectroscopy, and high background intensity was observed (**Fig. 5.18**).

Using WMR spectroscopy and fluorescence combined we achieved the discrimination between *M. tuberculosis* LR and LP cells with high sensitivity and specificity in *in-vitro* grown cells and in guinea pig infected lung tissue sections (**Fig. 5.22, Fig. 5.23** and **Fig. 5.24**). A good background subtraction was observed in the WMR spectra compared to the standard Raman spectra (**Fig. 5.18 and Fig. 5.22**).

Raman spectroscopy has been used to differentiate bacterial species and genus (Maquelin *et al.*, 2002b, Buijtels *et al.*, 2008). However, our study by genera *M. tuberculosis* phenotypes *in-vitro* and *ex-vivo* makes a major step forward. We are confident of this data as they come from multiple preparations interrogated over several days and combined at the end; removing, differences that could come from fluctuation in the laser power or different background signal from the preparation. Moreover, in all those *in-vitro* and *ex-vivo* experiments (**Fig. 5.19** to **Fig. 5.24**), both LR and LP cells were present on each slide (mixed population) compared to the previous experiments (**Chapter 4**) where LR and LP cells were located on separated preparation. Moreover, during the D_2O separation most of the cells are lost in the bottom of the cuvette (mainly clumps). Some of the population variability might be lost during the separation process. These last two points show some of the potential limitations of the initial experiments we designed in the **Chapter 4**. However, the

spectral differences between LR and LP cells observed after the separation are very comparable to the result observed after the combined and unbiased experiments shown in **Fig. 5.19** to **Fig. 5.22.**

LR spectra from *in-vitro* and *ex-vivo* cells are very comparable in peak intensity and cluster together in the PCA plot; the same is observed for the LP cells that show very comparable intensity between *in-vitro* and *ex-vivo* spectra and cluster together in the PCA plot (**Fig. 5.24 c** and **d**). LR cells from both *in-vitro* and *ex-vivo* experiments show wider cluster in the PCA plot compared to LP cells (**Fig. 5.22 b** and **Fig. 5.24 b**), suggesting more heterogeneity in the LR group. This could be explained by the fact that LR cells can present one to several intracellular lipid bodies and each lipid inclusion can vary in size (**Fig. 5.11** and **Fig. 5.12**). So there would be a continuum between LR cells that would have one small lipid bodies to LR cells that would have several large inclusions and all cases in between can be observed.

Being able to differentiate LR and LP cells is of high relevance as LR cells are associated with low metabolism (Garton *et al.*, 2008) and phenotypic tolerance to antibiotics (Gomez and McKinney, 2004, Deb *et al.*, 2009). LR cells can be up to 40 times more resistant to key components of the TB treatment regimen such as rifampicin (Hammond *et al.*, 2015). In this study, we showed that around 60% of the cells interrogated in tissue were LR and therefore may represent an antibiotic tolerant sub-population. This very important observation would suggest performing drug sensitivity testing (DST) on a population that presents a significant proportion of LR cells. Moreover, the bacteria responsible for relapse are thought to be dormant and LR (Phillips *et al.*, 2016). The tool developed in this study could be used to investigate the bacteria directly at the site of infection and start unravelling the phenomenon of relapse. The existence of LR cells in patient's sputum at a certain time in treatment is

correlated with a higher risk of poor outcome (Sloan *et al.*, 2015). Our results show that LR cells are present in infected lung tissue and suggest that LR cells could predominate (**Fig. 5.24 a** and **b**). The data were acquired from single bacilli in the alveoli and not in solid tissue. We do not know if the population observed in the alveoli is similar or different to the population present in the solid tissue.

The use of the combined methodology confirmed the results obtained from the previous experiments and that LR cells show a Raman spectrum with increased intensity mainly visible in the lipid bands A and B. WMR spectroscopy can be used on its own without any stain, similarly to what is shown in **Fig 5.8**. The lipid content can then be investigated by direct measurement of the intensity of the lipid band B or by using a ratio.

The Raman signal window used in this Chapter and **Chapter 4** is comprises between 1000 and 1800 cm^{-1}. This is where are located most of the Raman peaks related to the bacteria. Changing the size of this window only slightly impact the results. Sensitivity and specificity for the different window sizes tested vary a little; the maximum standard deviation observed was 0.044 (see in **Appendices section 4 Tab. 1 to 4** for more details). This shows that a similar discrimination of LR and LP cells could be achieved by using a reduced window (1400-1500 cm^{-1}). This corresponds mainly to the lipid band B. The fact that a reduced window could be used means that the system could use a specific wavelength selector (grating) for the range 1400-1500 cm^{-1}; this would increase the resolution and therefore allow a shorter acquisition time. Imaging tissue *in-vivo* using video-rate with a tuneable laser (either coherent anti-Stokes Raman scattering or stimulated Raman scattering) could be a potential approach for future experiments (Evans *et al.*, 2005, Saar *et al.*, 2010).

In order to understand better the pathology of the disease, it would be very useful if information in addition to the phenotype could be extracted from the tissue sample. The use of a non-destructive, label-free method such as WMR spectroscopy should permit to re-use the tissue sample for other techniques. Immunohistochemistry (IHC) staining to investigate immune cells surrounding the bacteria could be of high interest. To be able to perform both methods on the same tissue sample, the tissue has to be attached on quartz for Raman spectroscopy for optimal result and to a positively charged surface for IHC. We developed and validated a protocol to charge quartz slides and coverslips, which do not impact the Raman spectrum (**Fig. 5.25**). Optimal Raman spectroscopy results were obtained with tissue attached to quartz coverslips (**Fig 5.26**). WMR spectroscopy was found to be non-destructive and can be used before IHC (**Fig 5.27** and **Fig 5.28**). We also demonstrated that Nile red staining and IHC could not be combined as Nile red staining is a destructive method. Tissue samples investigated by Nile red staining cannot be used subsequently for further investigation by IHC. However, tissue samples investigated by WMR spectroscopy can be used subsequently for further investigation by IHC. (**Fig 5.28**). Immunostaining can be conducted on tissue sections attached to glass slides or quartz slides showing equivalent results (**Fig 5.29)**. This protocol could be used for any study that would aim at using both Raman spectroscopy and IHC.

In future experiments, WMR spectroscopy could be directly applied to tissue structures such as granuloma and in human tissue sections using the methodology validated in this Chapter. Following WMR spectroscopy IHC could be applied. Using this combined approach would first provide information about the bacteria, their phenotype and phenotypic resistance to antibiotics, and then information about the

surrounding immune cells. This approach could be conducted in human lung tissue section coming from different cohorts such as relapse, reinfection…

In summary, in this Chapter, we first validated a protocol to interrogate single bacteria in tissue section using WMR spectroscopy. We combined Raman spectroscopy and Nile red staining and discriminated both LR and LP cells *in-vitro* and *ex-vivo*. This experiment validated that LR cells present higher intensity bands mainly in lipid band A and B. We showed that both LR and LP cells are present in tissue and that the LR phenotype could predominate and also that *in-vitro* and *ex-vivo* spectra were comparable, even if some differences exist mainly due to the tissue section preparation process. In both *in-vitro* and *ex-vivo* samples, WMR spectroscopy can be used on its own to investigate the lipid content using the lipid band B intensity. The higher the intensity of the Raman peak is the more lipids are present in the single bacterium.

Finally, we developed a protocol to perform both WMR spectroscopy and IHC on the same tissue section; Nile red cannot be used for staining prior to IHC.

Chapter 6 Mycobacterial growth dynamics: lipid body formation and loss

6.1 Introduction

Bacteria can enter dormancy that is a reversible state by definition (Lipworth *et al.*, 2016). Dormancy is triggered when microorganisms are facing adverse environmental conditions (Lennon and Jones, 2011). As shown previously in **Chapter 1 section 1.4** many *in-vitro* models of dormancy exist in TB research. Dormancy in mycobacteria is associated with the accumulation of intracellular lipid bodies and also higher phenotypic antibiotic resistance (Lipworth *et al.*, 2016). This suggests that LP bacteria can become LR and vice-versa.

Mycobacteria entering stationary phase accumulate lipid bodies (Garton *et al.*, 2002, Shleeva *et al.*, 2002, Bowness *et al.*, 2015). It was also demonstrated that LP bacteria could rapidly, within 15 minutes, display lipid bodies when grown in medium supplemented with fatty acids (Garton *et al.*, 2002). Mycobacteria store lipids when facing adverse conditions as a dormancy phenomenon. Most bacteria in the environment can be found in a dormant state. However, as the environmental conditions start to improve the organisms can quit this dormant state and reactivate and start dividing (Lennon and Jones, 2011). Can LR bacteria convert to LP when facing favourable growth conditions and if yes, how quickly LR bacterium can become LP?

Investigating this conversion phenomenon is central in the field as LR cells are phenotypically resistant to antibiotics and LP cells are sensitive (Hammond *et al.*,

2015). Moreover, bacteria that survive treatment and are involved in relapse are thought to be dormant (Phillips *et al.*, 2016, Hammond *et al.*, 2015).

The conversion from LR to LP could be observed when growth conditions improve for bacteria. For example, in relapse or when a granuloma ruptures, in those cases the dormant, phenotypic antibiotic resistant cells, could reactivate and start replicating. Reduction of intracellular TAG level and increases of TAG lipase activity are observed in mycobacterial cells exiting dormancy. The assimilation of TAGs, and therefore the presence of TAG lipase activity, is necessary for mycobacterial regrowth and to exit dormancy (Low *et al.*, 2009).

In-silico models can be used to simplify very complex systems that are hard to study using *in-vitro* or *in-vivo* models. They can be used to combine knowledge from previous experiments, test hypotheses and make predictions. Those models are not expensive and use controlled parameters. However, *in-silico* models are limited by the knowledge given by *in-vitro* or *in-vivo* experiments. Mathematical models can be used to model TB infection, granuloma, relapse, ask questions through virtual experiments or to help to find new drug or regimens and test them in virtual clinical trials (Linderman and Kirschner, 2015). Many *in-silico* models have been designed to study TB infection and granulomatous structures (Segovia-Juarez *et al.*, 2004, Gammack *et al.*, 2005, Marino *et al.*, 2011, Fallahi-Sichani *et al.*, 2011).

Those models present many parameters about immune cells but not many about bacteria. The general structure and formation of granulomas have been proposed, however, the exact role that *M. tuberculosis* plays in this process is not well known. Recent studies have demonstrated the central role of the pathogen in the formation of

granulomatous structures and confirmed that is not only host-mediated (Guirado and Schlesinger, 2013, Davis and Ramakrishnan, 2009, Ehlers and Schaible, 2013).

Knowing more about the conversion rate from LR to LP would help to build more robust mathematical models of granuloma and relapse; it would also help to perform virtual experiments and virtual clinical trials. The aim of this chapter is to investigate the change in phenotypic proportions in culture over time and to try to understand if bacteria convert from LR to LP when re-cultured in nutrient rich medium. If this is the case, an additional aim would be to calculate this conversion rate. The findings of this study could be added to *in-silico* models.

6.2 Methods

6.2.1 Conversion rate

Eppendorf tubes (one per time point) were filled with 200 µL of a seven day old *M. smegmatis* culture (≈1.10^7 bacteria per ml). The bacteria were spun down for 3 minutes at 20,000 x g and the cell pellet washed with 200 µL of PBS. Bacteria were then spun down for 3 minutes at 20,000 x g and t=0 (first time point) was resuspended in 200 µL of PBS; all the other bacterial pellets were resuspended in 500 µL of fresh medium (7H9 broth with glycerol and tween 80) and incubated for a specific time at 37°C. After incubation bacteria were spun down for 3 minutes at 20,000 x g and resuspended in 200 µL of PBS. All time points were either investigated using Nile red (see **Chapter 2 General methods section 2.5**) and observed by fluorescence microscopy (see fluorescence microscopy in **Chapter 2 General methods section 2.6**) or interrogated using WMR spectroscopy (see **Chapter 2 General methods section 2.8**). From the 200 µL of bacterial suspension in PBS a fraction was used for either fluorescence microscopy (100 µL) or WMR spectroscopy (20 µL) and 20 µL was stored at -20°C for q-PCR analysis.

6.2.2 Slide preparation for WMR spectroscopy

For each time point (conversion rate experiment), from the 200 µL of bacterial suspension in PBS 20 µL were taken and diluted with 20 µL of PBS. Then, 10 µL were heat fixed on a quartz coverslip (01015T-AB, SPI Supplies, PA, USA). A thick quartz slide (01016-AB, SPI Supplies, PA, USA) with a spacer was used to trap the fixed bacteria between the two slides. The montage was then sealed using transparent

nail polish. The quartz coverslip was placed on the high NA microscope oil immersion objective of the Raman spectroscopy system and interrogated using WMR spectroscopy (see **Chapter 2 General methods section 2.8** for more details).

6.2.3 DNA quantification of the 16S rRNA gene by q-PCR

The tubes for q-PCR analysis were stored at -20°C, 80 µL of PBS were added to each tube. The tubes were then spun down for 3 minutes at 20,000 x g, the PBS was discarded and the bacterial pellet resuspended in 1X TE buffer. The tubes were well vortexed to re-suspend the cell pellet. The cell suspension was incubated at 95°C for 20 minutes under constant shaking at 1000 rpm (heat block with a shaking option), to lyse the bacteria. Only 2 µL of this suspension was used per q-PCR reaction. A pre-mix was prepared including 0.2 µL of sense primer (*M. tuberculosis* 16S 151F; CTGGGAAACTGGGTCTAA), 0.2 µL of antisense primer (*M. tuberculosis* 16S 256R; CACCAACAAGCTGATAGG) (200 nM final each), 5 µL of EvaGreen (BIO-RAD, UK), 2.6 µL of Milli-Q water. The pre-mix was added into 2 µL of DNA suspension to make a final volume of 10 µL per one PCR reaction. PCR cycles were performed using a Rotor-Gene machine (Rotor-Gene Q, QIAGEN). The temperature profiles consisted of 95°C for 2 minutes, 40 cycles of 95°C for 15 seconds, 60°C for 60 seconds and green fluorescence measurement and finally melting analysis (from 60°C to 99°C).

6.3 Results

6.3.1 LR and LP proportion over time

Stationary phase cultures of *M. smegmatis* (seven days old) were stained using Nile red and found to be predominantly LR (77.6% LR; STD ± 1.6% ; n=3). Stationary phase cultures (one week to two weeks old 100 µL in 10 mL) were re-cultured in fresh, nutrient rich, medium (at 37°C) and Nile red stained after 24 hours. The cultures after 24 hours in fresh medium were found predominantly LP (24% LR; STD ± 4.1% LR; n=3). The counts are presented in **Tab. 6.1** and **Fig. 6.1.** Fluorescent images from both conditions, stationary phase culture and 24 hour subculture, are shown in **Fig. 6.2.**

The changes in LR proportion are very important and occur in the first 24 hours after subculture. Is it due to conversion? If yes, how quickly those bacteria convert from LR to LP in nutrient rich conditions?

Table 6.1 LR and LP counts from seven day old cultures and 24 hour old cultures (started from stationary phase culture). Three distinct experiments (biological replicates) for each condition (n=3).

Time points	LR counts	LP counts	Total	% LR	Average %LR ± STD
7days 1	218	57	275	79.3	77.6 ± 1.6
7days 2	270	84	355	76.1	
7days 3	609	178	787	77.4	
24 hours 1	206	688	894	23	24 ± 4.1
24 hours 2	235	582	817	28.8	
24 hours 3	103	393	496	20.8	

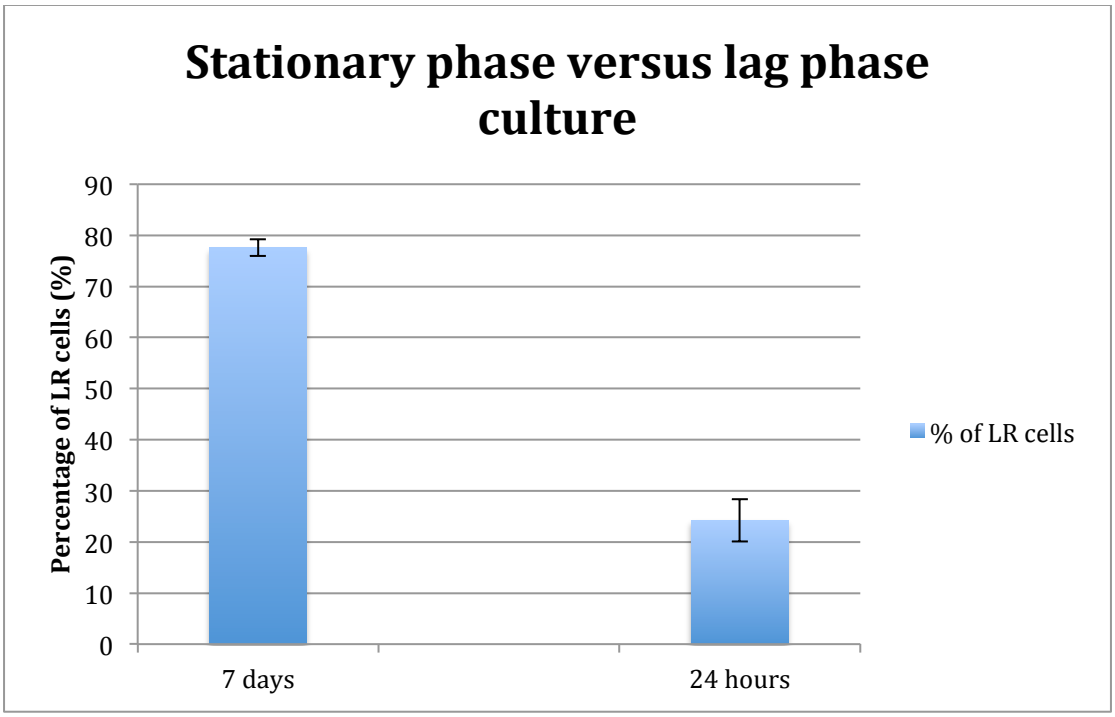

Figure 6.1 *LR percentages in M. smegmatis stationary phase cultures (seven days old) and 24 hour cultures (subcultured in fresh medium using ≥ 7 days old culture).*

(a)

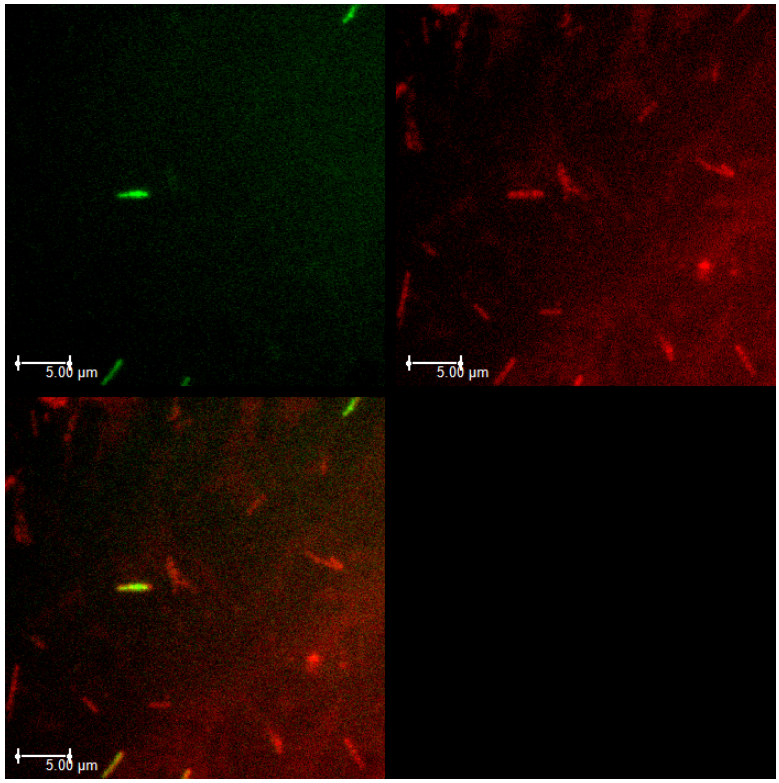

Nile red stained *M. smegmatis* cells 24 hours after subculture in fresh medium. The culture was inoculated from a stationary phase culture ≥ 7days old.

(b)

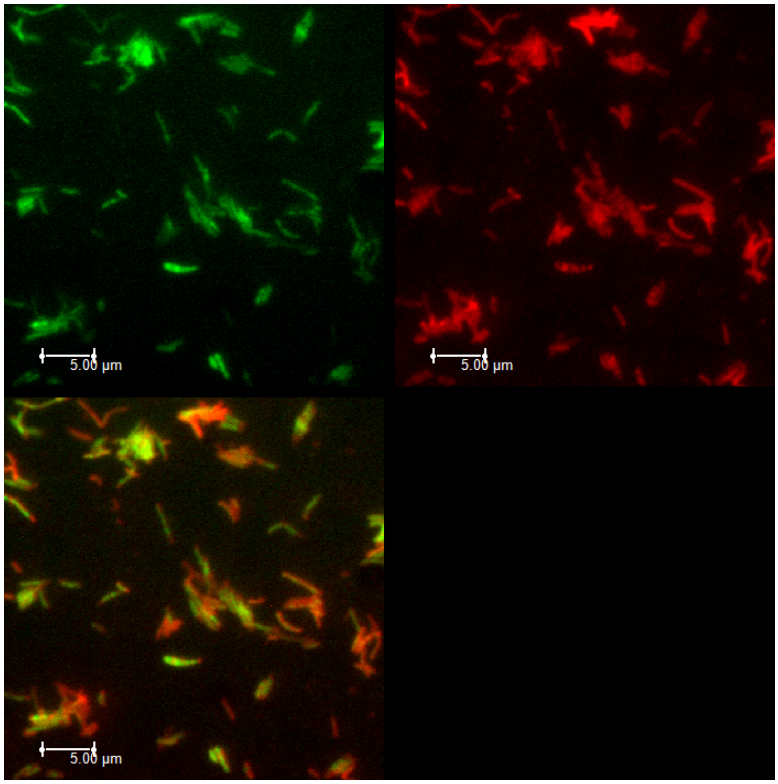

Nile red stained *M. smegmatis* stationary phase culture (7 days old).

(c)

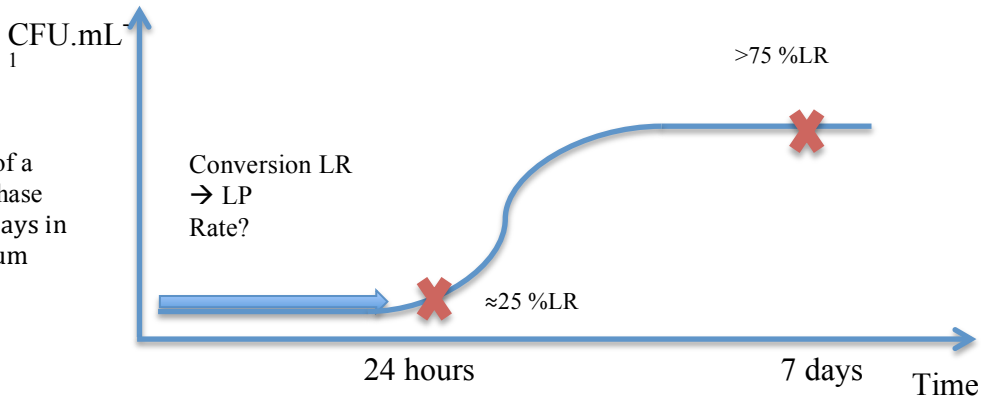

Subculture of a stationary phase culture ≥ 7days in fresh medium

Figure 6.2 *Do LR cells convert to LP cells in fresh, nutrient rich, medium?*

Fig. 6.2 a *shows an image of Nile red stained M. smegmatis cells 24 hours after subculture in fresh medium. The culture was from a stationary phase culture ≥ 7 days old.* ***Fig. 6.2 b*** *presents a picture of Nile red stained M. smegmatis stationary phase culture (7 days old).* ***Fig. 6.2 c*** *displays a growth curve showing the two time points: 24 hours predominantly LP and 7 days which is mostly LR. In* ***Fig. 6.2 a*** *and* ***b*** *the scale bars represent 5μm.*

6.3.2 Conversion rate experiment

In order to investigate the conversion from a predominantly LR population to a mostly LP population during the lag phase, a one week old *M. smegmatis* culture was placed into a fresh 7H9 medium for various durations. The bacteria were then observed under fluorescence microscopy after Nile red staining. In this initial experiment (representing the experimental set up that will be repeated in the future), eight time points were studied to understand the conversion: t=0 h, t=1 h, t=2 h, t=3 h, t=4 h, t=5 h, t=6 h and t=24 hours. Both LR and LP bacteria were counted by microscopic observation in all time points. The information regarding the number of bacteria counted and the proportion of LR and LP cells for each time point are shown in the **Tab. 6.2.**

Table 6.2 LR and LP count, using fluorescence microscopy, for each time point of the initial conversion rate experiment (n=1).

time points	LR count	LP count	total count	%of LR
t=0 h (7 days old)	218	57	275	79.27
t=1 h	210	56	266	78.95
t=2 h	293	268	561	52.23
t=3 h	329	234	563	58.44
t=4 h	125	293	418	29.90
t=5 h	203	482	685	29.64
t=6 h	134	408	542	24.72
t=24 h	206	688	894	23.04

The results are presented in **Fig. 6.3.** This shows the first conversion rate experiment. The one-week-old *M. smegmatis* culture was predominantly showing LR cells, over 75%, and after five hours in a fresh medium, the percentage of LR cells among the population dropped down to approximately 25%. Both LR and LP cells were observed at each time points in all fields of view. The rapid and very important changes in LR cell proportions could not be explained by the growth of LP cells. All the tubes initially received an equal inoculum volume from the one-week old culture (200 µL), and no increase in bacteria per mL is observed between 0 hours and 6 hours, as measured by q-PCR see **Fig. 6.4.**

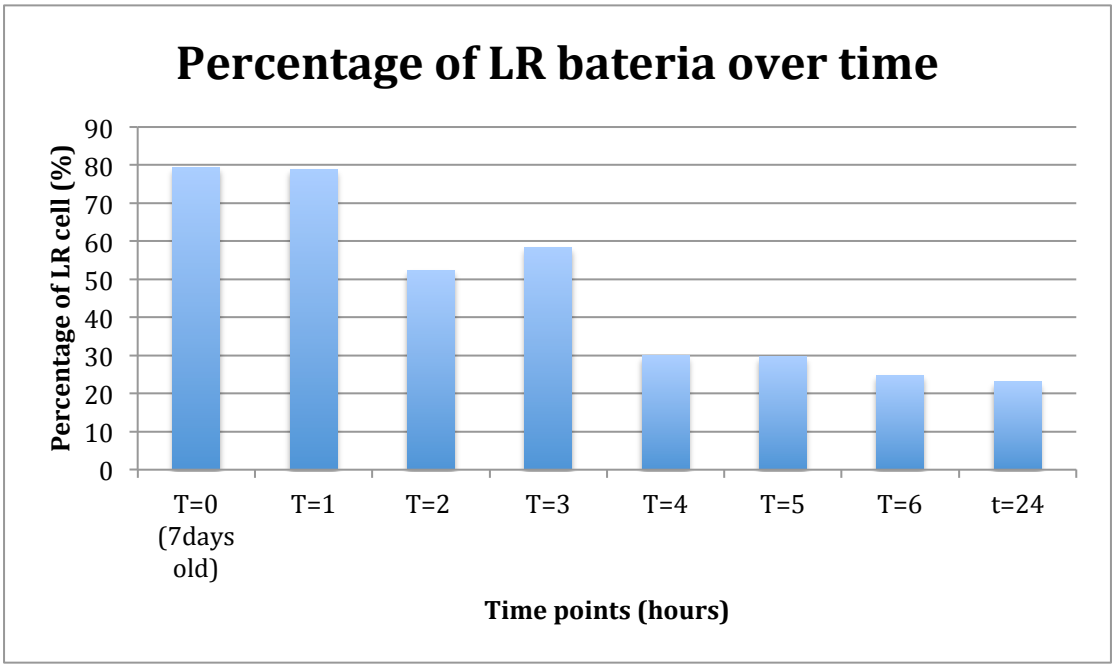

Figure 6.3 *Conversion of LR bacteria to LP when placed in fresh medium (n=1). The x-axis represents the time points in hours and the y-axis shows the percentage of LR bacteria in the population.*

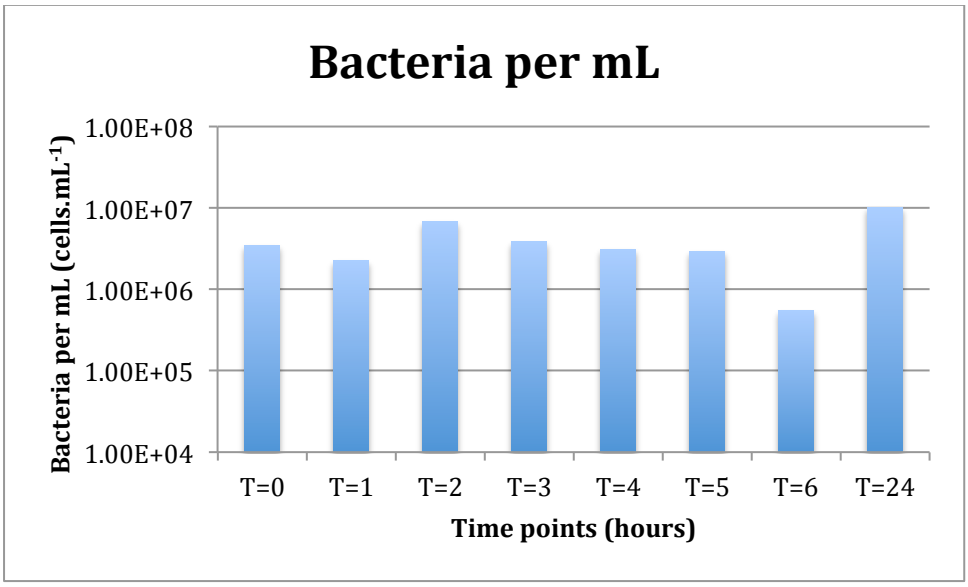

Figure 6.4 *DNA quantification of M. smegmatis 16S rRNA gene, converted to cells per mL, in all time points by q-PCR (n=1). The x-axis shows the time points in hours and the y-axis displays the bacterial concentration in cells per mL^{-1}. The 16S rRNA gene exists in two copies in M.smegmatis genome.*

The conversion from LR to LP in *M. smegmatis* has been further investigated using WMR spectroscopy. The conversion rate experiment was reproduced, but the changes in lipid content were followed by WMR spectroscopy instead of Nile red staining and fluorescence microscopy.

The one-week old bacteria were harvested and inoculated into fresh medium for 0, 2, 4 and 6 hours at 37°C. No significant changes in the number of cells were observed within the first 24 hours in this experiment, similarly to the previous experiment (quantification realised with q-PCR). The samples were interrogated by WMR spectroscopy, and 40 spectra of single bacteria were taken for each data point. WMR spectroscopy is a quantitative method that provides intensity values related to the lipid content of bacteria. Reduction in the main lipid bands can be related to a reduction in lipids. The WMR spectroscopy results from the conversion rate experiment are presented in **Fig. 6.5 a.** A decease in lipid band A and B intensity can be observed over time. This suggests that there is a reduction of lipid content in cells within the first two hours after being placed in a nutrient rich environment.

The **Fig. 6.5 b** shows the average WMR spectra of the times point t=0 h and t=4 h without the standard deviation to have a clear view of where the changes in intensity occur between the two time points. The **Fig. 6.5 c** displays the average WMR spectrum of total lipid extract from *M. tuberculosis*.

When comparing the **Fig. 6.5 b** and **c** it is apparent that the changes in Raman peak intensity that happen over time occur in bands that are also present in the spectrum of the total lipid extract.

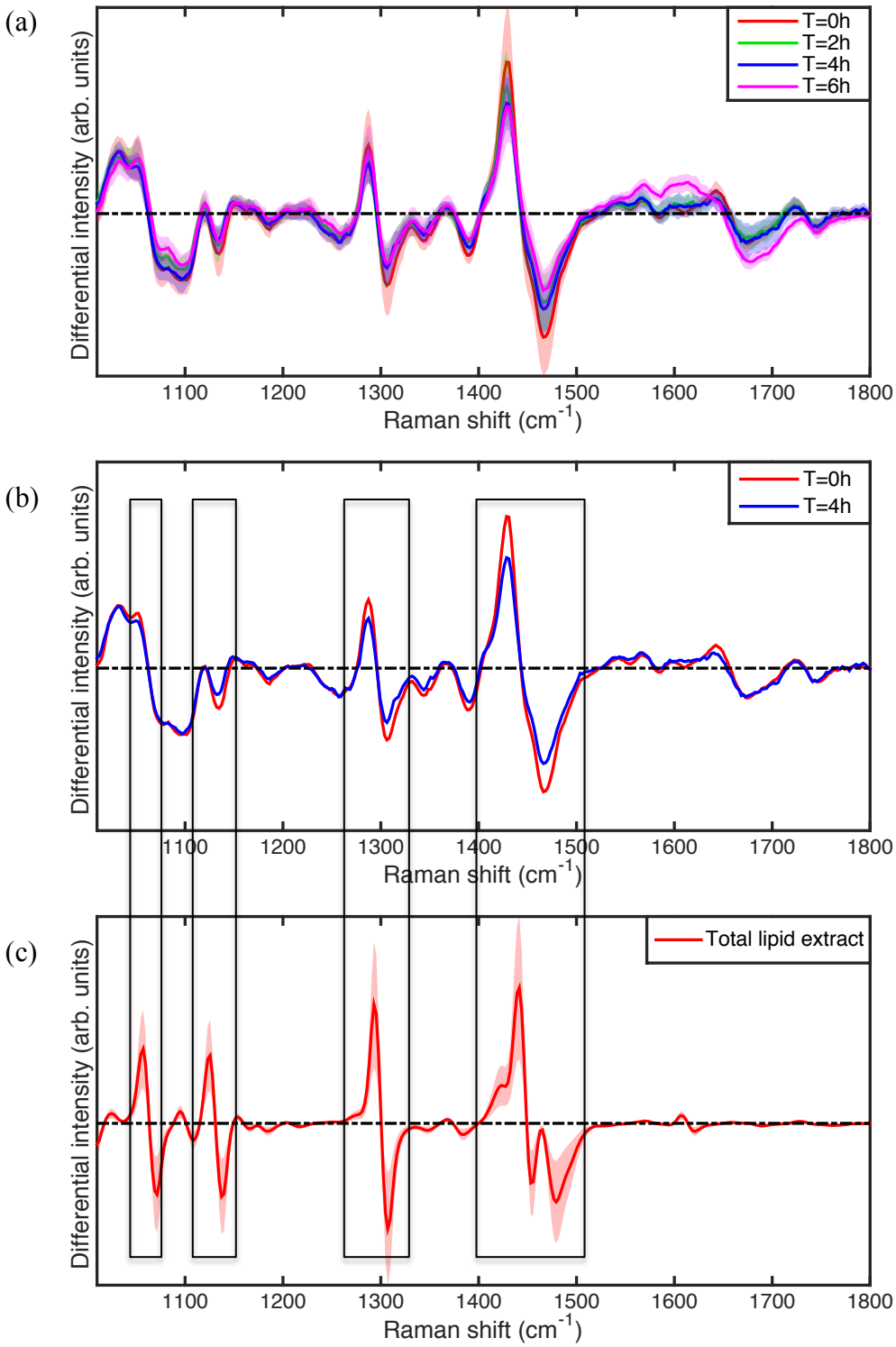
(a)
T=0h
T=2h
T=4h
T=6h
Differential intensity (arb. units)
1100
1200
1300
1400
1500
1600
1700
1800
Raman shift (cm-1)
(b)
T=0h
T=4h
Differential intensity (arb. units)
Raman shift (cm-1)
(c)
Total lipid extract
Differential intensity (arb. units)
Raman shift (cm-1)

Figure 6.5 *LR to LP conversion investigated by WMR spectroscopy (n=1).*

Fig. 6.5 a *shows the results of the conversion rate experiment, the coloured lines represent the average WMR spectrum (40 spectra of single bacterium) of the different time points t=0 h (red), t=2 h (green), t=4h (blue) and t=6 h (pink). The corresponding shaded coloured area displays the standard deviation. The x-axis represents the Raman shift (in wavenumber, cm^{-1}) and the y-axis shows the differential Raman intensity in arbitrary units. In a WMR spectrum, the Raman peaks correspond to the zero crossing point (the point where the curve cross the dash-dotted line); the Raman peak intensity is the peak-to-valley value around this zero crossing. The time point t=0 h corresponds to a one week old culture then t=2 h, t=4 h and t=6 h are coming from the same one week old culture that was subcultured for 2,4 and 6 hours into fresh medium at 37*°C. ***Fig. 6.5 b*** *displays the time points t=0 h and t=4 h without the standard deviation.* ***Fig. 6.5 c*** *shows the average WMR spectrum of total lipid extract (M. tuberculosis; 1 month old).*

In order to understand the reduction in lipid content over time in mycobacteria, when placed in nutrient rich conditions, we focused on the most intense lipid band of the fingerprint region: the lipid band B (1440-1450 cm^{-1}). The average lipid band B intensity for the different data points is shown in **Tab. 6.3**. A reduction in intensity can be observed from 525 at t=0 h to 352.8 at t=6 h; the standard deviation is also reducing over time suggesting that the bacteria interrogated at t=0 h were showing high variability in lipid content.

The results found previously (**Tab. 6.1**) suggest that over 75% of the bacteria are LR in a seven day old culture. In theory, LP bacteria are showing less intense lipid bands. The intensity values were classified in decreasing order, and the first 75% were found to be superior to 400 arbitrary Units. Applying this theoretical threshold between LR and LP to the other time points, it was found that at t=2 h, t=4 h and t=6 h; 55%, 47.5% and 22.5% of the bacteria were LR respectively (**Tab. 6.3; n=1**). The WMR spectra of the lipid band B, for all the time points, are shown in **Fig. 6.6 a**. All the lipid band B intensity values are plotted in **Fig 6.6 b** with the theoretical threshold at 400 arbitrary units.

Table 6.3 Lipid band B intensity during the conversion rate experiment (n=1).

Time points	Average intensity (Raman lipid band B)	Standard deviation	% of bacteria with a lipid band B intensity ≥ to 400 (arb. units)
t=0 (7 days old)	525	163.7	77.7
t=2h	416	109.4	55
t=4h	398	85.8	47.5
t=6h	352.8	82.7	22.5

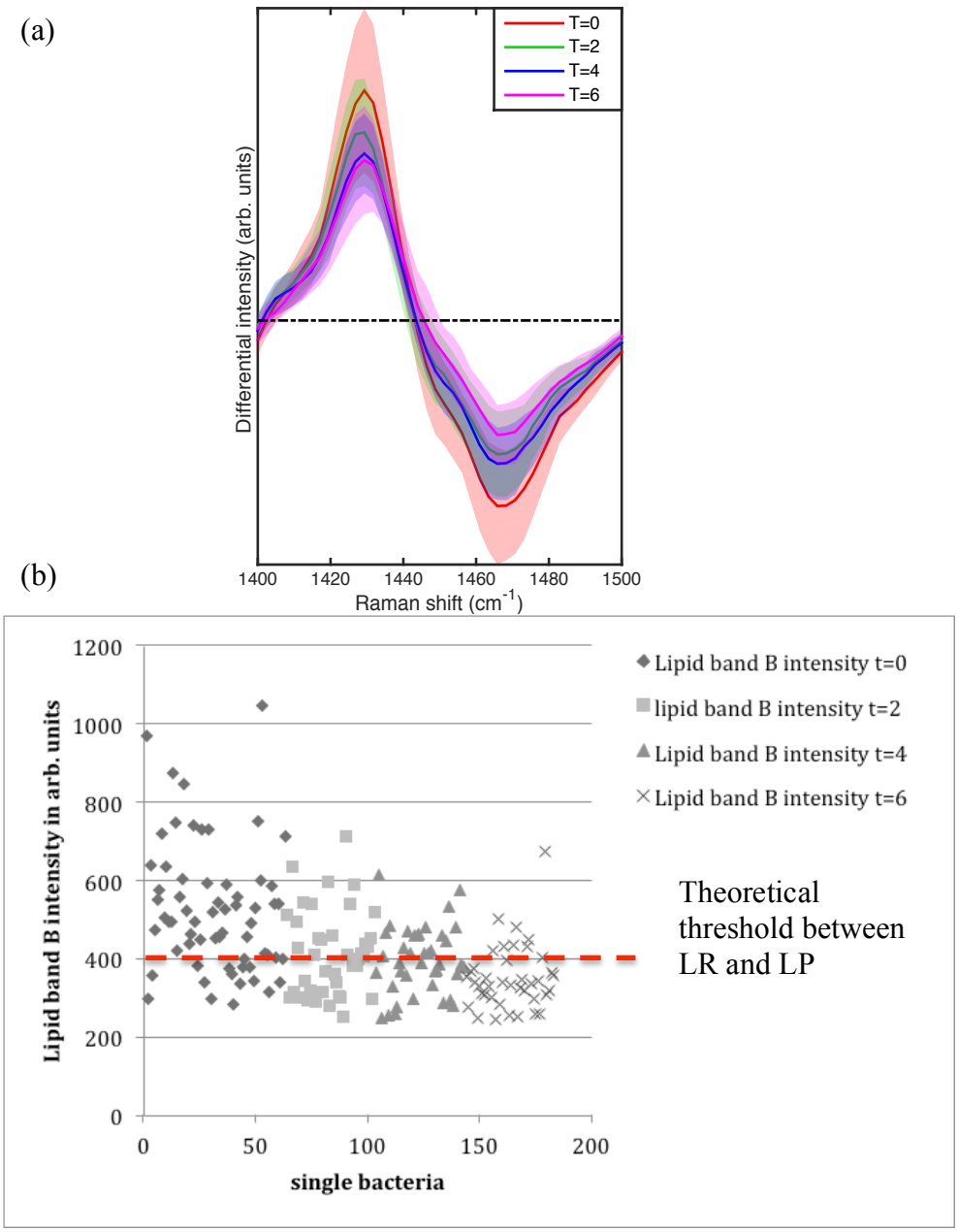

Figure 6.6 *Lipid band B intensity reduction during the conversion rate experiment (n=1).*

*The **Fig. 6.6 a** shows the results of the conversion rate experiment, the coloured lines represent the average WMR spectrum (40 spectra of single bacterium) of the different time points t=0 h (red), t=2 h (green), t=4 h (blue) and t=6 h (pink). The corresponding shaded coloured area displays the standard deviation. The x-axis represents the Raman shift (in wavenumber, cm^{-1}) and the y-axis shows the differential Raman intensity in arbitrary units. In a WMR spectrum, the Raman peaks correspond to the zero crossing point (the point where the curve cross the dash-dotted line); the Raman peak intensity is the peak-to-valley value around this zero crossing. The time point t=0 corresponds to a one week old culture then t=2 h, t=4 h and t=6 h are the same one week old culture that was subcultured for 2,4 and 6 hours in fresh medium at 37°C.* The ***Fig. 6.6 b*** *displays all the lipid band B intensity values of t=0 h (◆), t=2 h (■), t=4 h (Δ) and t=6 h (×). Each symbol represents a single bacterium.*

The reduction of the lipid band B over time was further investigated. The **Fig. 6.7 a** presents a boxplot of the lipid band B intensities of the different time points. The **Tab. 6.4** displays the result of a Tukey-test to compare the all the means pairwise. The time point t=0 h is found significantly different to the other time points. t=2 h, t=4 h and t=6 h are not significantly different to each other. All the statistical tests and corresponding figures were realised using the software R (R version 3.0.2 (2013-09-25) -- "Frisbee Sailing"; Copyright (C) 2013 The R Foundation for Statistical Computing). The full script, with the code and results, is presented in **Appendices section 5.**

Table 6.4 Tukey multiple comparisons of means (95% confidence level). (*) Infers that the means of the time points compared are significantly different (n=1).

Time points compared (pairwise)	p-value
2-0	1.08E-04 (*)
4-0	4.50E-06 (*)
6-0	0 (*)
4-2	9.13E-01
6-2	9.97E-02
6-4	3.53E-01

The **Fig. 6.7 b** presents all lipid band B intensity data, of all the time points, plotted with a regression line. The intercept (its starting point on the y-axis) of this regression line is 509.4 Lipid band B intensity in arbitrary units and the regression pace is -28.06 Lipid band B intensity in arbitrary units per hour.

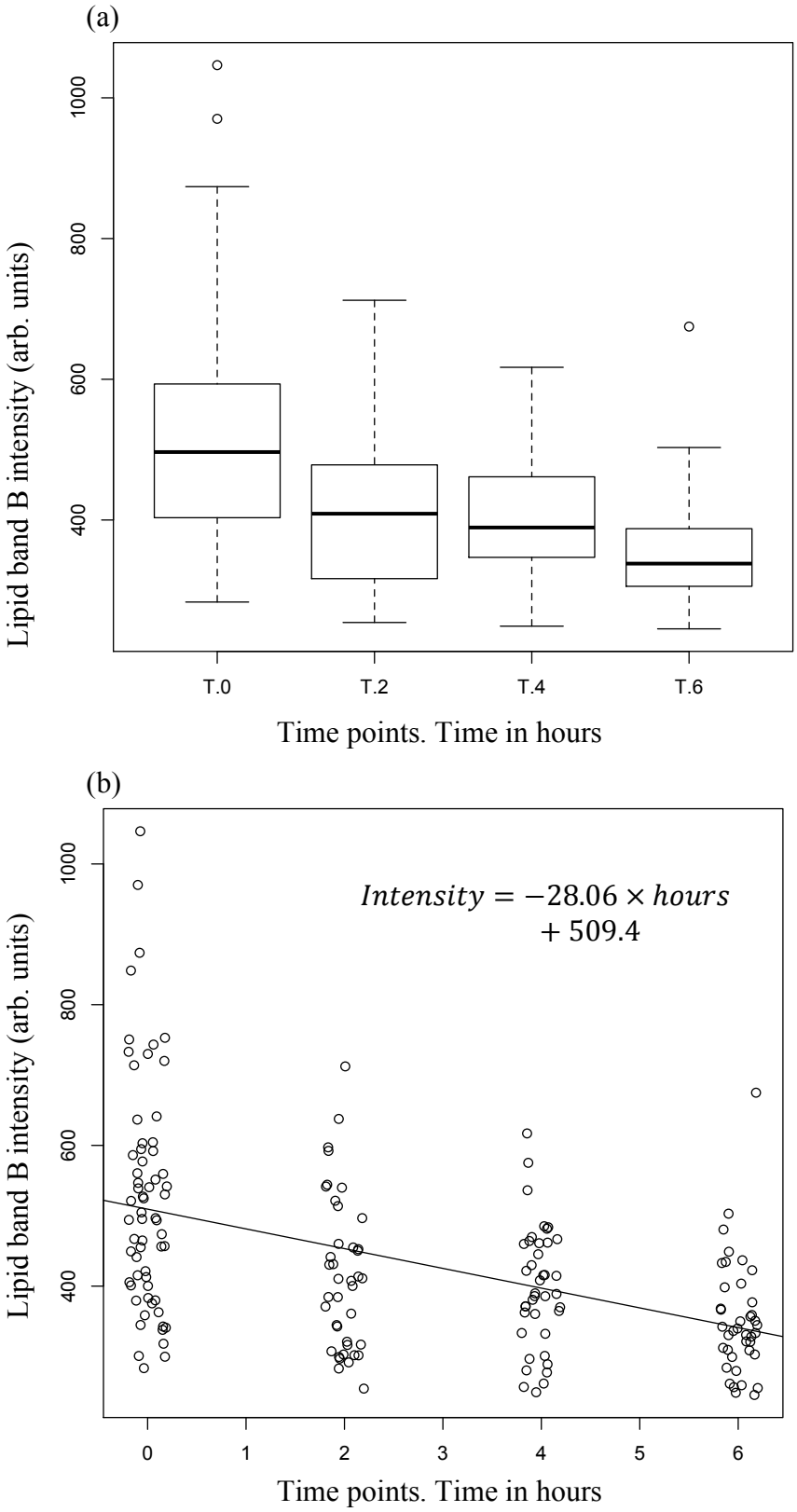

Figure 6.7 *Statistical analysis of the reduction of the lipid band B intensity over time (n=1).*

Fig 6.7 a *presents boxplots of the intensity values, of the lipid band B, for the t=0 h, t=2 h, t=4 h, t=6 h.* ***Fig 6.7 b*** *is a plot of the intensity values, of the lipid band B, for the t=0 h, t=2 h, t=4 h, t=6 h with the regression line that corresponds to the following equation:* $Intensity = -28.06 \times hours + 509.4$.

6.4 Discussion

Recent clinical trials, testing new regimens for four months therapy, did not succeed to show superiority compared to the current six month long regimen. Relapse due to bacteria that survive the antibiotic challenge is thought to be the main reason why the duration of treatment cannot be reduced (Gillespie *et al.*, 2014, Phillips *et al.*, 2016). Those bacteria are thought to be dormant (phenotypically antibiotic resistant and lipid rich cells) (Phillips *et al.*, 2016, Hammond *et al.*, 2015, Lipworth *et al.*, 2016). Investigating dormancy, phenotypic antibiotic resistance and lipid storage is central to the design of future TB treatments (Lipworth *et al.*, 2016).

A clinical trial is a long and very expensive process, and there are multiple drug regimens that could be tested. The use of mathematical model virtual experiments and virtual clinical trials could be a used to inform during the decision process and help to reduce the list of potential regimens before a new clinical trials are launch (Linderman and Kirschner, 2015).

In-silico models are inexpensive, and the parameters used are all controlled and known. These models miss any influence from unknown parameters (Guirado and Schlesinger, 2013). Moreover, to build accurate mathematical models more parameters need to be generated through experimentation to minimise the number of estimated values.

The capacity to convert between phenotypes (LR and LP) seems to be crucial as through this phenomenon bacteria can survive adverse conditions and reactivate later when conditions are favourable. It has been shown that bacteria grown in the presence of fatty acids can become LR (display intracellular lipid bodies) in only several minutes (Garton *et al.*, 2002).

In this Chapter, we investigated the conversion of LR cells to LP cells. It was observed in this study that *M. smegmatis* stationary phase cultures (seven days old) were predominantly LR (77.6% LR; STD ± 1.6% ; n=3). Seven day old or older cultures were subcultured in fresh, nutrient rich, medium. After 24 hours in those favourable growth conditions, the bacterial populations were found predominantly LP (24% LR; STD ± 4.1% LR; n=3; **Tab. 6.1**, **Fig. 6.1** and **Fig. 6.2**). This shows very important changes in phenotypic distribution in the first 24 hours of culture. Is this change is due to conversion from LR to LP and if so how quickly does it occur? Could this change in phenotypic distribution linked to replication of LP cells?

The first observation is that at these two time points both LR and LP cells are observed. Showing that not all cells become LR in nutrient poor conditions (stationary phase culture) and that not all cells are LP or convert rapidly to LP in a nutrient rich medium.

To try to answer those questions we designed a conversion rate experiment to investigate this window: the first 24 hours of culture. A seven day old culture was used to start this experiment, an equal volume of culture was re-cultured in fresh, nutrient rich, medium for 0, 1, 2, 3, 4, 5, 6 and 24 hours (t=0 hours is the seven days old culture). The proportion of LR and LP cells was followed by Nile red staining and fluorescence microscopy. The culture at t=0 h was highly LR (around 79%), and after 5, 6 hours in a nutrient rich medium the population was found predominantly LP with around 25% of LR cells. The proportion of LR cells was similar in t=24 h (around 25% LR), suggesting that most of the change in LR/LP proportion occurred within the first 6 hours (**Fig. 6.3** and **Tab. 6.2**). For all the conditions, *M. smegmatis* 16S rRNA gene copy number was measured by q-PCR and then converted to cells per mL, to observe a potential change over time due to cell division. The number of cells during

the first 6 hours seems unchanged, suggesting that no or very little cell division occurred during this lag phase period (**Fig. 6.4**). This observation suggests that the very important change in LR/LP proportion in the first 6 hours cannot be explained by replication of LP cells but can only come from the conversion of LR bacteria to LP bacteria. The hypothesis is that facing favourable growth conditions LR bacteria start to use their stored lipid before starting to actively replicate.

To investigate this conversion further and also to accurately calculate a conversion rate the experiment was repeated using WMR spectroscopy. This method can provide absolute quantification using the main lipid peak intensity values. A seven day old culture was used to start this experiment, an equal volume of culture was re-cultured in fresh, nutrient rich, medium for 0, 2, 4 and 6 hours (t=0 hours is the seven day old culture). Around 40 spectra of single cells were acquired for each time points. The main lipid peaks intensities reduce over time meaning that on average the bacteria interrogated were presenting less and less lipids (**Fig. 6.5 a** and **Tab 6.3**). The average WMR spectra of the time points t=0 h and t=4 h are directly compared in **Fig. 6.5 b,** showing that reduction in intensity over time is visible in peaks related to lipids. Those Raman peaks were also observed in the WMR spectrum of total lipid extract of *M. tuberculosis* **Fig. 6.5 c** (see **Chapter 3** for more details). The areas, of the WMR spectra of the two time points, not related to lipids remain very similar. The main lipid peak, the lipid band B, was then used to extract intensity values from all the WMR spectra (**Fig. 6.6**). The average lipid band B intensity at t=0 h is 525 ±163.7 arb.units and at t=6 h it is 352.8± 82.7 arb.units (**Tab. 6.3**). The intensity values of all the WMR spectra of the different time points are plotted in **Fig. 6.6 b** and **Fig. 6.7**. The time points were compared pairwise using the Tukey test (**Tab. 6.4**) t=0 h is found significantly different from the other time points. This suggests that an already

important change in lipid content occurred within the first two hours of incubation. The other three time points were not found significantly different even if t=2 h and t=6 h present a p-value between 0.05 and 0.1.

In order to calculate the conversion rate the intensity values were all plotted and a regression line was then calculated (**Fig. 6.7 b**) following the equation*:* $Intensity = -28.06 \times hours + 509.4$.

The conversion rate experiment using WMR spectroscopy needs to be repeated to obtain a more robust conversion rate. Another approach to calculate the conversion rate from LR to LP would be to use a methodology that permits the interrogation of living bacteria overtime. Trapping cells in a chamber using acoustic force combined with WMR spectroscopy could be an approach to investigate. This would allow following the spectra of a group of bacteria over time facing different conditions for example being re-cultured in fresh, nutrient rich, medium.

Understanding better the change in phenotypic proportions of cells in mycobacterial population would be of high relevance as LR cells are phenotypically resistant to antibiotics and an issue in TB treatment. In patients, a higher percentage of lipid body positive cells, at three and four weeks of treatment, is linked to an unfavourable outcome (Sloan *et al.*, 2015). Knowing the percentage of LR cells in patients' sputum represents therefore an interesting topic to investigate. Automated image analysis could represent a solution; initial tests were done using the data sets presented in **Fig. 6.1** and **Tab. 6.1** and comparable results were found compared to counting by eye with an average time to count each picture of only several seconds. An example is

shown in **Appendices section 6.** Automated image analysis could provide more objective, reliable and robust results than eye count.

In summary, this study showed that important change in LR/LP proportion occurs when a predominantly LR culture is re-cultured in a nutrient rich medium. The LR cells convert to LP cells very quickly within the first 6 hours of culture. This Chapter proposes an experiment and a methodology to calculate the conversion rate of LR cells to LP cells. This chapter also discusses further techniques that could help studying the proportion of LR and LP bacteria in various contexts.

Chapter 7 General discussion and future work

7.1 General discussion

The objective of the clinical trials was to shorten the duration of treatment from six months to four months. The regimens tested were not found superior to the current treatment and this mainly because of high relapse rates. The bacterial clearance was rapid in those clinical trials (Gillespie *et al.*, 2014, Jindani *et al.*, 2014, Merle *et al.*, 2014). This would suggest that a population of bacteria survive the treatment and is able, in the future, to induce relapse. Those bacteria are thought to be dormant and LR (Phillips *et al.*, 2016, Hammond *et al.*, 2015). Therefore, investigating dormancy and antibiotic resistance is central to propose new TB treatment regimens (Lipworth *et al.*, 2016). The presence of intracellular lipid bodies is associated with dormancy. Mycobacteria can be found in two phenotypes: LR (with intracellular lipid bodies) or LP (without intracellular lipid bodies). LR cells present a higher phenotypic resistance to antibiotics (Hammond *et al.*, 2015).

The bacteriology of relapse is still mostly unknown and studying dormancy could bring a better understanding of this phenomenon. The major goal of this thesis is to investigate the capacity of Raman spectroscopy, a label free and non-destructive methodology, to study and discriminate dormant (LR) cells and active (LP) cells in *in-vitro* and *ex-vivo* samples.

In **Chapter 3,** I interrogated total lipid extracts of *M. tuberculosis* with Raman spectroscopy to show the location of the main lipid peaks. Those Raman peaks were confirmed to be associated with lipids when compared to a Raman database

(Movasaghi *et al.*, 2007). This finding was central for the following experiments as it gave us a good understanding of the position of *M.tuberculosis* lipids Raman peaks and where to expect high intensity bands. Recently, a study using Raman spectroscopy to interrogate *M. tuberculosis* cells showed the association with lipids of some of the Raman peaks (Stockel *et al.*, 2016). However, our study presents the exact position of all the Raman peaks of *M. tuberculosis* lipids. This is the first study realised on total lipid extracts of *M. tuberculosis* using Raman spectroscopy providing new and key information central to our project.

In **chapter 4,** I demonstrated that it is possible to distinguish LR from LP cells, using Raman spectroscopy, for the first time. Until this work, only different mycobacterial species had been discriminated using Raman spectroscopy (Buijtels *et al.*, 2008, Stockel *et al.*, 2016). Being able to discriminate the two phenotypes (LR/LP) within the same mycobacterial species is very interesting as one of these phenotypes is associated with phenotypic antibiotic resistance and relapse. This represents a major advance, as it is the first time that mycobacterial cell states have been distinguished using Raman spectroscopy.

The work conducted in the **Chapter 3** and **4** confirmed some of the advantages of using WMR spectroscopy over standard Raman spectroscopy that were previously showed: higher signal to noise ratio (Mazilu *et al.*, 2010), easier to interpret the spectra (De Luca *et al.*, 2010), better discriminative power (Canetta *et al.*, 2011). WMR spectroscopy was then used for all the subsequent experiments in this thesis. This work demonstrates the advantages of using WMR spectroscopy to discriminate bacterial species or phenotypes.

I have identified two lipid peaks that permit the discrimination of LR and LP cells. This is the first study showing a marker to identify LR and LP cells in *Mycobacterium* species using Raman spectroscopy. This means that the window to study the phenotypes can be reduced to target specifically those two peaks. Reducing the window using a grating over a short range could permit high resolution spectral information to be obtained in a short acquisition time. Also, this is important for the use of other techniques of spectroscopy such as wide field video-rate acquisition using non-linear vibrational spectroscopy. This method uses a tuneable laser to perform either anti-Stokes Raman scattering or stimulated Raman scattering (Evans *et al.*, 2005, Saar *et al.*, 2010).

Applying this method to investigate TB infected tissue samples represents the following step. Previous studies interrogated sputum samples with fluorescence microscopy and showed that LR cells could be predominant *in-vivo* (Garton *et al.*, 2008). Patient sputum samples showed a population that was mainly Rpf dependent and showing a degree of phenotypic antibiotic resistance (Mukamolova *et al.*, 2010). However, the results observed in sputum samples may not entirely reflect the population present in the lungs. Therefore, to investigate and try to understand better the proportion of phenotypically antibiotic resistant cells, dormancy and the bacteriology of relapse it is central to interrogate *M. tuberculosis* directly in infected tissue.

In **Chapter 5**, I was able to take the results of **chapter 4** and translate them into an effective method for distinguishing the lipid status of bacteria in tissue. This chapter presents an innovative method that for the first time discriminated *M. tuberculosis* LR

and LP cells, directly at the site of the disease, in TB infected guinea pig lung tissue sections. I demonstrated, for the first time that LR cells could represent the predominant phenotype in TB infected tissue. Around 60% of the bacteria interrogated were identified as LR in the TB infected guinea pig lung tissue section. It has been shown that LR cells display a degree of phenotypic resistance toward antibiotics (Hammond *et al.*, 2015). The high proportion of LR cells in tissue suggests that DST should be performed on a sample that shows a high proportion of LR cells.

A significant number of patients relapse after a "successful" treatment and this could be due to dormant, LR cells that survive the treatment (Phillips *et al.*, 2016). The work of this thesis provides a tool that allows us to examine the phenotype (lipid content) of the bacteria directly at the site of the infection and obtain information regarding their phenotypic resistance. This could permit us to research the samples of patients with active disease and start to unravel the reasons for relapse.

Raman spectroscopy is label-free and non-destructive meaning that the tissue interrogated can be reused for additional analyses. For example, we can investigate the immune status around each individual cell giving us the opportunity to understand the relationship between Lipid status and immune response using IHC.

Clinical trials are very expensive and take a very long time to be conducted, and there are multiple drug regimens that could be tested. Using mathematical models, virtual experiments and also virtual clinical trials could help defining the regimen before starting a clinical trial (Linderman and Kirschner, 2015). Those *in-silico* models are not expensive, and the parameters they use are fully controlled. Their main drawback

is that they need good parameters coming from experiments. Moreover, an *in-silico* model cannot inform about the influence of unknown factors or parameters (Guirado and Schlesinger, 2013). There is, therefore, a great need for parameters defined experimentally to reduce the number of estimated values in *in-silico* models. Conversion between phenotypes (LR and LP) seems to be a central phenomenon to investigate as LR cells are showing higher phenotypic resistance to antibiotics. It has already been shown that in the presence of fatty acids a bacteria can become LR in just a few minutes (Garton *et al.*, 2002). In **Chapter 6,** I showed that in *M. smegmatis* stationary phase cultures LR cells are predominant. Stationary phase cultures of *Mycobacteria* are known to be associated with the development of intracellular lipid bodies (Garton *et al.*, 2002). Stationary phase cultures placed in favourable growth condition for 24 hours become predominantly LP. The proportion of LR/LP evolves rapidly when a predominantly LR culture is placed in a nutrient rich medium. I demonstrated that LR cells could convert quickly to LP cells within the first hours of culture. The results presented in **Chapter 6** also suggest that comparing stationary phase cultures (≈ 80% LR) and re-cultured cells 24 hours old (≈ 25% LR) or exponentially growing cultures could have been used as initial experiments to understand differences between Raman spectra of LR and LP cells. This would have been easier to perform and the whole bacterial population could have been interrogated.

To summarise this thesis, we demonstrated, for the first time, the ability of Raman spectroscopy to discriminate LR and LP cells (phenotype level) in both *in-vitro* samples and in TB infected tissue sections. The initial experiments (*in-vitro* n=1) to discriminate LR and LP cells shown in **Chapter 4** were confirmed and validated by

the combined approach of fluorescence imaging and WMR spectroscopy (*in-vitro* n=4; *ex-vivo* n=3), used in **Chapter 5**. This final experiment demonstrated, in an unbiased way, that the Raman lipid peak intensity increase observed in LR cells was due to the presence of intracellular lipids located in a non-polar environment (both *in-vitro* and in tissue). From this experiment, WMR spectroscopy can now be applied to samples on its own with the knowledge that the intensity of the lipid bands will reflect the lipid content of the single cells interrogated. This thesis also demonstrates that it is possible to combine WMR spectroscopy with another method, as this technology is label-free and non-destructive. In this thesis, we also began to study the conversion of LR cells to LP cells.

7.2 Future work

With the tools that I have created in this research, it now becomes possible to interrogate a single bacterium in TB infected lung tissue and infer the phenotypic antibiotic resistance of the cell based on its lipid content. This method can be used with another method, as it is label-free and non-destructive, to answer a large number of research questions and can interrogate both *in-vitro* or tissue samples. For example, IHC could be used. We developed a protocol that permits attachment of frozen tissue sections to positively charged quartz coverslips. Raman spectroscopy would first identify the phenotype, and therefore inference about the phenotypic antibiotic resistance of the bacteria could be made. Then IHC could inform on the surrounding immune cells. This approach could be conducted on human lung tissue sections and different conditions or cohorts could be compared regarding their proportion of LR cells and the immune cells present next to the bacteria. Such studies will bring a better

understanding of the bacteriology of relapse that remains largely unknown. This knowledge could then be used to feed *in-silico* models. This will contribute to the basic science that will underpin the design and evaluation of new and better treatments for tuberculosis.

In addition, the method and the protocols developed in this thesis can also be applied to other research areas that would be interested in multiple measurements in a tissue sample (Raman spectrum and IHC). This work provides a tool, to study bacterial phenotypes in various samples, to other researchers opening possibilities in numerous topics.

In this thesis, some of the experiments need to be confirmed or repeated. This is the case for the protocol developed to do a D_2O separation using centrifugation steps. The initial experiments showed promising results. This protocol could permit the separation of LR and LP cells quickly and minimise potential stress on living cells. The experiments proposed to calculate a conversion rate from LR to LP need to be repeated as well. Other methods could also be tested to answer this question such as combining acoustic trapping and Raman spectroscopy to interrogate living cells. Once calculated the conversion rate could then be added to *in-silico* models.

Understanding the proportion of LR cells is critical, as LR bacteria could be responsible for relapse (Phillips *et al.*, 2016), they are phenotypically resistant to antibiotics (Hammond *et al.*, 2015) and a higher percentage of LR cells, at three and four weeks of treatment, is associated with an unfavourable outcome (Sloan *et al.*, 2015). In the future, I would like to investigate the automated analysis of Nile red stained images. This could have potential application in diagnostics and also answer

research questions. An example of automated analysis of an image showing both LR and LP cells (Nile red stained) is shown in **Appendices section 6.**

References

ACKART, D. F., HASCALL-DOVE, L., CACERES, S. M., KIRK, N. M., PODELL, B. K., MELANDER, C., ORME, I. M., LEID, J. G., NICK, J. A. & BASARABA, R. J. 2014. Expression of antimicrobial drug tolerance by attached communities of *Mycobacterium tuberculosis*. *Pathog Dis,* 70**,** 359-69.

ADEREM, A. & UNDERHILL, D. M. 1999. Mechanisms of phagocytosis in macrophages. *Annu Rev Immunol,* 17**,** 593-623.

ALGOOD, H. M., CHAN, J. & FLYNN, J. L. 2003. Chemokines and tuberculosis. *Cytokine Growth Factor Rev,* 14**,** 467-77.

ALGOOD, H. M., LIN, P. L. & FLYNN, J. L. 2005. Tumor necrosis factor and chemokine interactions in the formation and maintenance of granulomas in tuberculosis. *Clin Infect Dis,* 41 Suppl 3**,** S189-93.

ALVAREZ, H. M. & STEINBÜCHEL, A. 2002. Triacylglycerols in prokaryotic microorganisms. *Appl Microbiol Biotechnol,* 60**,** 367-76.

ANDERSEN, P. & DOHERTY, T. M. 2005. The success and failure of BCG - implications for a novel tuberculosis vaccine. *Nat Rev Microbiol,* 3**,** 656-62.

BAEK, S. H., LI, A. H. & SASSETTI, C. M. 2011. Metabolic Regulation of Mycobacterial Growth and Antibiotic Sensitivity. *Plos Biology,* 9.

BESTE, D. J., ESPASA, M., BONDE, B., KIERZEK, A. M., STEWART, G. R. & MCFADDEN, J. 2009. The genetic requirements for fast and slow growth in mycobacteria. *PLoS One,* 4**,** e5349.

BETTS, J. C., LUKEY, P. T., ROBB, L. C., MCADAM, R. A. & DUNCAN, K. 2002. Evaluation of a nutrient starvation model of *Mycobacterium tuberculosis* persistence by gene and protein expression profiling. *Mol Microbiol,* 43**,** 717-31.

BLECK, C. K., MERZ, A., GUTIERREZ, M. G., WALTHER, P., DUBOCHET, J., ZUBER, B. & GRIFFITHS, G. 2010. Comparison of different methods for thin section EM analysis of *Mycobacterium smegmatis*. *J Microsc,* 237**,** 23-38.

BLIGH, E. G. & DYER, W. J. 1959. A rapid method of total lipid extraction and purification. *Can J Biochem Physiol,* 37**,** 911-7.

BOEHME, C. C., NABETA, P., HILLEMANN, D., NICOL, M. P., SHENAI, S., KRAPP, F., ALLEN, J., TAHIRLI, R., BLAKEMORE, R., RUSTOMJEE, R., MILOVIC, A., JONES, M., O'BRIEN, S. M., PERSING, D. H., RUESCH-GERDES, S., GOTUZZO, E., RODRIGUES, C., ALLAND, D. & PERKINS, M. D. 2010. Rapid molecular detection of tuberculosis and rifampin resistance. *N Engl J Med,* 363**,** 1005-15.

BOWNESS, R., BOEREE, M. J., AARNOUTSE, R., DAWSON, R., DIACON, A., MANGU, C., HEINRICH, N., NTINGINYA, N. E., KOHLENBERG, A., MTAFYA, B., PHILLIPS, P. P. J., RACHOW, A., VAN BALEN, G. P. & GILLESPIE, S. H. 2015. The relationship between *Mycobacterium tuberculosis* MGIT time to positivity and cfu in sputum samples demonstrates changing bacterial phenotypes potentially reflecting the impact of chemotherapy on critical sub-populations. *Journal of Antimicrobial Chemotherapy,* 70**,** 448-455.

BROWN, L., WOLF, J. M., PRADOS-ROSALES, R. & CASADEVALL, A. 2015. Through the wall: extracellular vesicles in Gram-positive bacteria, mycobacteria and fungi. *Nat Rev Microbiol,* 13**,** 620-30.

BUIJTELS, P. C. A. M., WILLEMSE-ERIX, H. F. M., PETIT, P. L. C., ENDTZ, H. P., PUPPELS, G. J., VERBRUGH, H. A., VAN BELKUM, A., VAN SOOLINGEN, D. & MAQUELIN, K. 2008. Rapid identification of mycobacteria by Raman spectroscopy. *J. Clin. Microbiol.,* 46**,** 961-965.

BURDON, K. L. 1946a. Disparity in Appearance of True Hansen Bacilli and Cultured Leprosy Bacilli When Stained for Fat. *Journal of Bacteriology,* 52**,** 679-680.

BURDON, K. L. 1946b. Fatty Material in Bacteria and Fungi Revealed by Staining Dried, Fixed Slide Preparations. *Journal of Bacteriology,* 52**,** 665-678.

BURKE, V., SPRAGUE, A. & BARNES, L. 1925. Dormancy in bacteria. *Journal of Infectious Diseases,* 36**,** 555-560.

CANDELORO, P., GRANDE, E., RAIMONDO, R., DI MASCOLO, D., GENTILE, F., COLUCCIO, M. L., PEROZZIELLO, G., MALARA, N., FRANCARDI, M. & DI FABRIZIO, E. 2013. Raman database of amino acids solutions: a critical study of Extended Multiplicative Signal Correction. *Analyst,* 138**,** 7331-7340.

CANETTA, E., MAZILU, M., DE LUCA, A. C., CARRUTHERS, A. E., DHOLAKIA, K., NEILSON, S., SARGEANT, H., BRISCOE, T., HERRINGTON, C. S. & RICHES, A. C. 2011. Modulated Raman spectroscopy for enhanced identification of bladder tumor cells in urine samples. *J Biomed Opt,* 16**,** 037002.

CHAN, J. W., TAYLOR, D. S., ZWERDLING, T., LANE, S. M., IHARA, K. & HUSER, T. 2006. Micro-Raman spectroscopy detects individual neoplastic and normal hematopoietic cells. *Biophysical Journal,* 90**,** 648-656.

CHANG, J. C., MINER, M. D., PANDEY, A. K., GILL, W. P., HARIK, N. S., SASSETTI, C. M. & SHERMAN, D. R. 2009. igr Genes and *Mycobacterium tuberculosis* cholesterol metabolism. *J Bacteriol,* 191**,** 5232-9.

CHAO, M. C. & RUBIN, E. J. 2010. Letting sleeping dos lie: does dormancy play a role in tuberculosis? *Annu Rev Microbiol,* 64**,** 293-311.

CHEN, M., MCREYNOLDS, N., CAMPBELL, E. C., MAZILU, M., BARBOSA, J., DHOLAKIA, K. & POWIS, S. J. 2015. The use of wavelength modulated Raman spectroscopy in label-free identification of T lymphocyte subsets, natural killer cells and dendritic cells. *PLoS One,* 10**,** e0125158.

CHENG, I. F., CHANG, H. C., CHEN, T. Y., HU, C. M. & YANG, F. L. 2013. Rapid (< 5 min) Identification of Pathogen in Human Blood by Electrokinetic Concentration and Surface-Enhanced Raman Spectroscopy. *Scientific Reports,* 3.

CHENG, W. T., LIU, M. T., LIU, H. N. & LIN, S. Y. 2005. Micro-Raman spectroscopy used to identify and grade human skin pilomatrixoma. *Microscopy Research and Technique,* 68**,** 75-79.

CHIRIBOGA, L., XIE, P., YEE, H., VIGORITA, V., ZAROU, D., ZAKIM, D. & DIEM, M. 1998. Infrared spectroscopy of human tissue. I. Differentiation and maturation of epithelial cells in the human cervix. *Biospectroscopy,* 4**,** 47-53.

CHOO-SMITH, L. P., EDWARDS, H. G. M., ENDTZ, H. P., KROS, J. M., HEULE, F., BARR, H., ROBINSON, J. S., BRUINING, H. A. & PUPPELS, G. J. 2002. Medical applications of Raman spectroscopy: From proof of principle to clinical implementation. *Biopolymers,* 67**,** 1-9.

CLARK, S., HALL, Y. & WILLIAMS, A. 2015. Animal models of tuberculosis: Guinea pigs. *Cold Spring Harb. Perspect. Med.,* 5**,** a018572.
CLARK, S. O., HALL, Y., KELLY, D. L. F., HATCH, G. J. & WILLIAMS, A. 2011. Survival of *Mycobacterium tuberculosis* during experimental aerosolization and implications for aerosol challenge models. *J. Appl. Microbiol.,* 111**,** 350-359.
COMBS, D. L., O'BRIEN, R. J. & GEITER, L. J. 1990. USPHS Tuberculosis Short-Course Chemotherapy Trial 21: effectiveness, toxicity, and acceptability. The report of final results. *Ann Intern Med,* 112**,** 397-406.
COOPER, A. M., DALTON, D. K., STEWART, T. A., GRIFFIN, J. P., RUSSELL, D. G. & ORME, I. M. 1993. Disseminated tuberculosis in interferon gamma gene-disrupted mice. *J Exp Med,* 178**,** 2243-7.
CULHA, M., KAHRAMAN, M., CAM, D., SAYIN, I. & KESEROGLU, K. 2010. Rapid identification of bacteria and yeast using surface-enhanced Raman scattering. *Surface and Interface Analysis,* 42**,** 462-465.
CUNNINGHAM, A. F. & SPREADBURY, C. L. 1998. Mycobacterial stationary phase induced by low oxygen tension: cell wall thickening and localization of the 16-kilodalton alpha-crystallin homolog. *J Bacteriol,* 180**,** 801-8.
CZAMARA, K., MAJZNER, K., PACIA, M. Z., KOCHAN, K., KACZOR, A. & BARANSKA, M. 2015. Raman spectroscopy of lipids: a review. *Journal of Raman Spectroscopy,* 46**,** 4-20.
DALTERIO, R. A., BAEK, M., NELSON, W. H., BRITT, D., SPERRY, J. F. & PURCELL, F. J. 1987. The Resonance Raman Microprobe Detection of Single Bacterial-Cells from a Chromobacterial Mixture. *Applied Spectroscopy,* 41**,** 241-244.
DALTERIO, R. A., NELSON, W. H., BRITT, D., SPERRY, J. & PURCELL, F. J. 1986. A Resonance Raman Microprobe Study of Chromobacteria in Water. *Applied Spectroscopy,* 40**,** 271-273.
DANIEL, J., DEB, C., DUBEY, V. S., SIRAKOVA, T. D., ABOMOELAK, B., MORBIDONI, H. R. & KOLATTUKUDY, P. E. 2004. Induction of a novel class of diacylglycerol acyltransferases and triacylglycerol accumulation in *Mycobacterium tuberculosis* as it goes into a dormancy-like state in culture. *J. Bacteriol.,* 186**,** 5017-5030.
DANIEL, J., KAPOOR, N., SIRAKOVA, T., SINHA, R. & KOLATTUKUDY, P. 2016. The perilipin-like PPE15 protein in *Mycobacterium tuberculosis* is required for triacylglycerol accumulation under dormancy-inducing conditions. *Molecular Microbiology,* 101**,** 784-794.
DANIEL, J., MAAMAR, H., DEB, C., SIRAKOVA, T. D. & KOLATTUKUDY, P. E. 2011. *Mycobacterium tuberculosis* uses host triacylglycerol to accumulate lipid droplets and acquires a dormancy-like phenotype in lipid-loaded macrophages. *PLoS Pathog,* 7**,** e1002093.
DANIEL, T. M. 2005a. Leon Charles Albert Calmette and BCG vaccine. *International Journal of Tuberculosis and Lung Disease,* 9**,** 944-945.
DANIEL, T. M. 2005b. Robert Koch and the pathogenesis of tuberculosis. *International Journal of Tuberculosis and Lung Disease,* 9**,** 1181-1182.
DANIEL, T. M. 2006. The history of tuberculosis. *Respiratory Medicine,* 100**,** 1862-1870.
DANIEL, T. M. & IVERSEN, P. A. 2015. Hippocrates and tuberculosis. *Int J Tuberc Lung Dis,* 19**,** 373-4.

DAVIS, J. M., CLAY, H., LEWIS, J. L., GHORI, N., HERBOMEL, P. & RAMAKRISHNAN, L. 2002. Real-time visualization of mycobacterium-macrophage interactions leading to initiation of granuloma formation in zebrafish embryos. *Immunity,* 17**,** 693-702.

DAVIS, J. M. & RAMAKRISHNAN, L. 2009. The Role of the Granuloma in Expansion and Dissemination of Early Tuberculous Infection. *Cell,* 136**,** 37-49.

DE GELDER, J., DE GUSSEM, K., VANDENABEELE, P. & MOENS, L. 2007a. Reference database of Raman spectra of biological molecules. *J. Raman Spectrosc.,* 38**,** 1133-1147.

DE GELDER, J., DE GUSSEM, K., VANDENABEELE, P., VANCANNEYT, M., DE VOS, P. & MOENS, L. 2007b. Methods for extracting biochemical information from bacterial Raman spectra: focus on a group of structurally similar biomolecules-fatty acids. *Anal. Chim. Acta,* 603**,** 167-75.

DE LUCA, A. C., MAZILU, M., RICHES, A., HERRINGTON, C. S. & DHOLAKIA, K. 2010. Online fluorescence suppression in modulated Raman spectroscopy. *Anal. Chem.,* 82**,** 738-45.

DEB, C., LEE, C. M., DUBEY, V. S., DANIEL, J., ABOMOELAK, B., SIRAKOVA, T. D., PAWAR, S., ROGERS, L. & KOLATTUKUDY, P. E. 2009. A novel in vitro multiple-stress dormancy model for *Mycobacterium tuberculosis* generates a lipid-loaded, drug-tolerant, dormant pathogen. *PLoS One,* 4**,** e6077.

DEN HERTOG, A. L., KLATSER, P. R. & ANTHONY, R. M. 2009. Buoyant density of *Mycobacterium tuberculosis*: implications for sputum processing. *International Journal of Tuberculosis and Lung Disease,* 13**,** 466-471.

DICK, T., LEE, B. H. & MURUGASU-OEI, B. 1998. Oxygen depletion induced dormancy in *Mycobacterium smegmatis*. *Fems Microbiology Letters,* 163**,** 159-164.

ECDC 2011. Use of interferon-gamma release assays in support of TB diagnosis. Stockholm: European Centre for Disease Prevention and Control, 2011 (http://ecdc.europa.eu/en/publications/Publications/1103_GUI_IGRA.pdf).

EHLERS, S. & SCHAIBLE, U. E. 2013. The granuloma in tuberculosis: dynamics of a host-pathogen collusion. *Frontiers in Immunology,* 3.

EPSTEIN, S. S. 2009. Microbial awakenings. *Nature,* 457**,** 1083.

ERNST, J. D. 1998. Macrophage receptors for *Mycobacterium tuberculosis*. *Infect Immun,* 66**,** 1277-81.

EVANS, C. L., POTMA, E. O., PUORIS'HAAG, M., COTE, D., LIN, C. P. & XIE, X. S. 2005. Chemical imaging of tissue in vivo with video-rate coherent anti-Stokes Raman scattering microscopy. *Proc. Natl. Acad. Sci. U.S.A.,* 102**,** 16807-16812.

FALLAHI-SICHANI, M., EL-KEBIR, M., MARINO, S., KIRSCHNER, D. E. & LINDERMAN, J. J. 2011. Multiscale Computational Modeling Reveals a Critical Role for TNF-alpha Receptor 1 Dynamics in Tuberculosis Granuloma Formation. *Journal of Immunology,* 186**,** 3472-3483.

FALZON, D., JARAMILLO, E., SCHUNEMANN, H. J., ARENTZ, M., BAUER, M., BAYONA, J., BLANC, L., CAMINERO, J. A., DALEY, C. L., DUNCOMBE, C., FITZPATRICK, C., GEBHARD, A., GETAHUN, H., HENKENS, M., HOLTZ, T. H., KERAVEC, J., KESHAVJEE, S., KHAN, A. J., KULIER, R., LEIMANE, V., LIENHARDT, C., LU, C., MARIANDYSHEV, A., MIGLIORI, G. B., MIRZAYEV, F., MITNICK, C.

D., NUNN, P., NWAGBONIWE, G., OXLADE, O., PALMERO, D., PAVLINAC, P., QUELAPIO, M. I., RAVIGLIONE, M. C., RICH, M. L., ROYCE, S., RUSCH-GERDES, S., SALAKAIA, A., SARIN, R., SCULIER, D., VARAINE, F., VITORIA, M., WALSON, J. L., WARES, F., WEYER, K., WHITE, R. A. & ZIGNOL, M. 2011. WHO guidelines for the programmatic management of drug-resistant tuberculosis: 2011 update. *Eur Respir J,* 38**,** 516-28.

FAN, C., HU, Z. Q., MUSTAPHA, A. & LIN, M. S. 2011. Rapid detection of food- and waterborne bacteria using surface-enhanced Raman spectroscopy coupled with silver nanosubstrates. *Applied Microbiology and Biotechnology,* 92**,** 1053-1061.

FAOLAIN, E. O., HUNTER, M. B., BYRNE, J. M., KELEHAN, P., LAMBKIN, H. A., BYRNE, H. J. & LYNG, F. M. 2005. Raman spectroscopic evaluation of efficacy of current paraffin wax section dewaxing agents. *Journal of Histochemistry & Cytochemistry,* 53**,** 121-129.

FILIPPINI, P., IONA, E., PICCARO, G., PEYRON, P., NEYROLLES, O. & FATTORINI, L. 2010. Activity of drug combinations against dormant *Mycobacterium tuberculosis*. *Antimicrob Agents Chemother,* 54**,** 2712-5.

FOX, W., ELLARD, G. A. & MITCHISON, D. A. 1999. Studies on the treatment of tuberculosis undertaken by the British Medical Research Council tuberculosis units, 1946-1986, with relevant subsequent publications. *Int J Tuberc Lung Dis,* 3**,** S231-79.

GALLI, R., UCKERMANN, O., KOCH, E., SCHACKERT, G., KIRSCH, M. & STEINER, G. 2014. Effects of tissue fixation on coherent anti-Stokes Raman scattering images of brain. *J. Biomed. Opt.,* 19**,** 071402.

GALLIER, S., GORDON, K. C., JIMENEZ-FLORES, R. & EVERETT, D. W. 2011. Composition of bovine milk fat globules by confocal Raman microscopy. *International Dairy Journal,* 21**,** 402-412.

GAMMACK, D., GANGULI, S., MARINO, S., SEGOVIA-JUAREZ, J. & KIRSCHNER, D. E. 2005. Understanding the immune response in tuberculosis using different mathematical models and biological scales. *Multiscale Modeling & Simulation,* 3**,** 312-345.

GARTON, N. J., CHRISTENSEN, H., MINNIKIN, D. E., ADEGBOLA, R. A. & BARER, M. R. 2002. Intracellular lipophilic inclusions of mycobacteria in vitro and in sputum. *Microbiology,* 148**,** 2951-8.

GARTON, N. J., WADDELL, S. J., SHERRATT, A. L., LEE, S. M., SMITH, R. J., SENNER, C., HINDS, J., RAJAKUMAR, K., ADEGBOLA, R. A., BESRA, G. S., BUTCHER, P. D. & BARER, M. R. 2008. Cytological and transcript analyses reveal fat and lazy persister-like bacilli in tuberculous sputum. *PLoS Med.,* 5**,** e75.

GENGENBACHER, M. & KAUFMANN, S. H. 2012. *Mycobacterium tuberculosis*: success through dormancy. *FEMS Microbiol Rev,* 36**,** 514-32.

GENGENBACHER, M., RAO, S. P., PETHE, K. & DICK, T. 2010. Nutrient-starved, non-replicating *Mycobacterium tuberculosis* requires respiration, ATP synthase and isocitrate lyase for maintenance of ATP homeostasis and viability. *Microbiology,* 156**,** 81-7.

GILLESPIE, S. H., CROOK, A. M., MCHUGH, T. D., MENDEL, C. M., MEREDITH, S. K., MURRAY, S. R., PAPPAS, F., PHILLIPS, P. P. J., NUNN, A. J. & CONSORTIUM, R. 2014. Four-month moxifloxacin-based regimens for drug-sensitive tuberculosis. *N. Engl. J. Med.,* 371**,** 1577-1587.

GLAZIOU, P., FLOYD, K., KORENROMP, E. L., SISMANIDIS, C., BIERRENBACH, A. L., WILLIAMS, B. G., ATUN, R. & RAVIGLIONE, M. 2011. Lives saved by tuberculosis control and prospects for achieving the 2015 global target for reducing tuberculosis mortality. *Bulletin of the World Health Organization,* 89**,** 573-582.

GOMEZ, J. E. & MCKINNEY, J. D. 2004. M. tuberculosis persistence, latency, and drug tolerance. *Tuberculosis (Edinb),* 84**,** 29-44.

GORELIK, V. S., KRYLOV, A. S. & SVERBIL, V. P. 2014. Local Raman spectroscopy of DNA. *Bulletin of the Lebedev Physics Institute,* 41**,** 310-315.

GREENSPAN, P. & FOWLER, S. D. 1985. Spectrofluorometric studies of the lipid probe, nile red. *J Lipid Res,* 26**,** 781-9.

GREENSPAN, P., MAYER, E. P. & FOWLER, S. D. 1985. Nile red: a selective fluorescent stain for intracellular lipid droplets. *J Cell Biol,* 100**,** 965-73.

GRIFFITHS, G., NYSTROEM, B., SABLE, S. B. & KHULLER, G. K. 2010. Nanobead-based interventions for the treatment and prevention of tuberculosis. *Nature Reviews Microbiology,* 8**,** 827-834.

GUIRADO, E. & SCHLESINGER, L. S. 2013. Modeling the *Mycobacterium tuberculosis* granuloma - the critical battlefield in host immunity and disease. *Frontiers in Immunology,* 4**,** 98.

GUMBO, T., LENAERTS, A. J., HANNA, D., ROMERO, K. & NUERMBERGER, E. 2015. Nonclinical Models for Antituberculosis Drug Development: A Landscape Analysis. *Journal of Infectious Diseases,* 211**,** S83-S95.

HAMMOND, R. J., BARON, V. O., ORAVCOVA, K., LIPWORTH, S. & GILLESPIE, S. H. 2015. Phenotypic resistance in mycobacteria: is it because I am old or fat that I resist you? *J. Antimicrob. Chemother.,* 70**,** 2823-7.

HANLON, E. B., MANOHARAN, R., KOO, T. W., SHAFER, K. E., MOTZ, J. T., FITZMAURICE, M., KRAMER, J. R., ITZKAN, I., DASARI, R. R. & FELD, M. S. 2000. Prospects for in vivo Raman spectroscopy. *Phys Med Biol,* 45**,** R1-59.

HARRIES, A. D. & DYE, C. 2006. Tuberculosis. *Annals of Tropical Medicine and Parasitology,* 100**,** 415-431.

HARZ, A., ROSCH, P. & POPP, J. 2009. Vibrational Spectroscopy-A Powerful Tool for the Rapid Identification of Microbial Cells at the Single-Cell Level. *Cytometry Part A,* 75A**,** 104-113.

HARZ, M., ROSCH, P., PESCHKE, K. D., RONNEBERGER, O., BURKHARDT, H. & POPP, J. 2005. Micro-Raman spectroscopic identification of bacterial cells of the genus Staphylococcus and dependence on their cultivation conditions. *Analyst,* 130**,** 1543-1550.

HERSHKOVITZ, I., DONOGHUE, H. D., MINNIKIN, D. E., BESRA, G. S., LEE, O. Y., GERNAEY, A. M., GALILI, E., ESHED, V., GREENBLATT, C. L., LEMMA, E., BAR-GAL, G. K. & SPIGELMAN, M. 2008. Detection and molecular characterization of 9,000-year-old *Mycobacterium tuberculosis* from a Neolithic settlement in the Eastern Mediterranean. *PLoS One,* 3**,** e3426.

HORSBURGH, C. R., JR. & RUBIN, E. J. 2011. Clinical practice. Latent tuberculosis infection in the United States. *N Engl J Med,* 364**,** 1441-8.

HUANG, W. E., GRIFFITHS, R. I., THOMPSON, I. P., BAILEY, M. J. & WHITELEY, A. S. 2004. Raman microscopic analysis of single microbial cells. *Analytical Chemistry,* 76**,** 4452-4458.

HUANG, Z. W., MCWILLIAMS, A., LUI, H., MCLEAN, D. I., LAM, S. & ZENG, H. S. 2003. Near-infrared Raman spectroscopy for optical diagnosis of lung cancer. *International Journal of Cancer,* 107**,** 1047-1052.

HUYNH, K. K. & GRINSTEIN, S. 2007. Regulation of vacuolar pH and its modulation by some microbial species. *Microbiol Mol Biol Rev,* 71**,** 452-62.

IBELINGS, M. S., MAQUELIN, K., ENDTZ, H. P., BRUINING, H. A. & PUPPELS, G. J. 2005. Rapid identification of Candida spp. in peritonitis patients by Raman spectroscopy. *Clinical Microbiology and Infection,* 11**,** 353-358.

JACKSON, M. 2014. The Mycobacterial Cell Envelope-Lipids. *Cold Spring Harbor Perspectives in Medicine,* 4**,** a021105 - a021105.

JAIN, M., PETZOLD, C. J., SCHELLE, M. W., LEAVELL, M. D., MOUGOUS, J. D., BERTOZZI, C. R., LEARY, J. A. & COX, J. S. 2007. Lipidomics reveals control of Mycobacterium tuberculosis virulence lipids via metabolic coupling. *Proc Natl Acad Sci U S A,* 104**,** 5133-8.

JARVIS, R. M. & GOODACRE, R. 2004. Ultra-violet resonance Raman spectroscopy for the rapid discrimination of urinary tract infection bacteria. *FEMS Microbiol Lett,* 232**,** 127-32.

JINDANI, A., HARRISON, T. S., NUNN, A. J., PHILLIPS, P. P. J., CHURCHYARD, G. J., CHARALAMBOUS, S., HATHERILL, M., GELDENHUYS, H., MCILLERON, H. M., ZVADA, S. P., MUNGOFA, S., SHAH, N. A., ZIZHOU, S., MAGWETA, L., SHEPHERD, J., NYIRENDA, S., VAN DIJK, J. H., CLOUTING, H. E., COLEMAN, D., BATESON, A. L. E., MCHUGH, T. D., BUTCHER, P. D., MITCHISON, D. A. & TEAM, R. T. 2014. High-dose rifapentine with moxifloxacin for pulmonary tuberculosis. *N. Engl. J. Med.,* 371**,** 1599-1608.

KAPOOR, N., PAWAR, S., SIRAKOVA, T. D., DEB, C., WARREN, W. L. & KOLATTUKUDY, P. E. 2013. Human granuloma in vitro model, for TB dormancy and resuscitation. *PLoS One,* 8**,** e53657.

KAPRELYANTS, A. S., GOTTSCHAL, J. C. & KELL, D. B. 1993. Dormancy in non-sporulating bacteria. *FEMS Microbiol Rev,* 10**,** 271-85.

KAPRELYANTS, A. S. & KELL, D. B. 1993. Dormancy in Stationary-Phase Cultures of Micrococcus luteus: Flow Cytometric Analysis of Starvation and Resuscitation. *Appl Environ Microbiol,* 59**,** 3187-96.

KATTI, M. K., DAI, G., ARMITIGE, L. Y., RIVERA MARRERO, C., DANIEL, S., SINGH, C. R., LINDSEY, D. R., DHANDAYUTHAPANI, S., HUNTER, R. L. & JAGANNATH, C. 2008. The Delta fbpA mutant derived from *Mycobacterium tuberculosis* H37Rv has an enhanced susceptibility to intracellular antimicrobial oxidative mechanisms, undergoes limited phagosome maturation and activates macrophages and dendritic cells. *Cell Microbiol,* 10**,** 1286-303.

KENDALL, C., HUTCHINGS, J., BARR, H., SHEPHERD, N. & STONE, N. 2011. Exploiting the diagnostic potential of biomolecular fingerprinting with vibrational spectroscopy. *Faraday Discussions,* 149**,** 279-290.

KLOSS, S., KAMPE, B., SACHSE, S., ROSCH, P., STRAUBE, E., PFISTER, W., KIEHNTOPF, M. & POPP, J. 2013. Culture Independent Raman Spectroscopic Identification of Urinary Tract Infection Pathogens: A Proof of Principle Study. *Analytical Chemistry,* 85**,** 9610-9616.

KLOSS, S., LORENZ, B., DEES, S., LABUGGER, I., ROSCH, P. & POPP, J. 2015. Destruction-free procedure for the isolation of bacteria from sputum samples for Raman spectroscopic analysis. *Anal. Bioanal. Chem.,* 407**,** 8333-8341.

KOCH, R. 1882. Die Aetiologie der Tuberkulose. *Berliner klinische Wochenschrift* 19**,** 221–230.

KUMAR, S., MATANGE, N., UMAPATHY, S. & VISWESWARIAH, S. S. 2015. Linking carbon metabolism to carotenoid production in mycobacteria using Raman spectroscopy. *FEMS Microbiol Lett,* 362**,** 1-6.

LAKSHMI, R. J., KARTHA, V. B., KRISHNA, C. M., SOLOMON, J. G. R., ULLAS, G. & DEVI, P. U. 2002. Tissue Raman spectroscopy for the study of radiation damage: Brain irradiation of mice. *Radiation Research,* 157**,** 175-182.

LAY, G., POQUET, Y., SALEK-PEYRON, P., PUISSEGUR, M. P., BOTANCH, C., BON, H., LEVILLAIN, F., DUTEYRAT, J. L., EMILE, J. F. & ALTARE, F. 2007. Langhans giant cells from M-tuberculosis-induced human granulomas cannot mediate mycobacterial uptake. *Journal of Pathology,* 211**,** 76-85.

LENNON, J. T. & JONES, S. E. 2011. Microbial seed banks: the ecological and evolutionary implications of dormancy. *Nat Rev Microbiol,* 9**,** 119-30.

LEVER, M. S., WILLIAMS, A. & BENNETT, A. M. 2000. Survival of mycobacterial species in aerosols generated from artificial saliva. *Lett. Appl. Microbiol.,* 31**,** 238-241.

LIM, A., ELEUTERIO, M., HUTTER, B., MURUGASU-OEI, B. & DICK, T. 1999. Oxygen depletion-induced dormancy in *Mycobacterium bovis* BCG. *J Bacteriol,* 181**,** 2252-6.

LINDERMAN, J. J. & KIRSCHNER, D. E. 2015. In silico models of M. tuberculosis infection provide a route to new therapies. *Drug Discov Today Dis Models,* 15**,** 37-41.

LIPWORTH, S., HAMMOND, R. J., BARON, V. O., HU, Y., COATES, A. & GILLESPIE, S. H. 2016. Defining dormancy in mycobacterial disease. *Tuberculosis (Edinb),* 99**,** 131-42.

LIU, P. T. & MODLIN, R. L. 2008. Human macrophage host defense against *Mycobacterium tuberculosis*. *Curr Opin Immunol,* 20**,** 371-6.

LOEBEL, R. O., SHORR, E. & RICHARDSON, H. B. 1933. The Influence of Adverse Conditions upon the Respiratory Metabolism and Growth of Human Tubercle Bacilli. *J Bacteriol,* 26**,** 167-200.

LOW, K. L., RAO, P. S., SHUI, G., BENDT, A. K., PETHE, K., DICK, T. & WENK, M. R. 2009. Triacylglycerol utilization is required for regrowth of in vitro hypoxic nonreplicating *Mycobacterium bovis* bacillus Calmette-Guerin. *J Bacteriol,* 191**,** 5037-43.

MACMICKING, J. D., TAYLOR, G. A. & MCKINNEY, J. D. 2003. Immune control of tuberculosis by IFN-gamma-inducible LRG-47. *Science,* 302**,** 654-9.

MAQUELIN, K., CHOO-SMITH, L. P., ENDTZ, H. P., BRUINING, H. A. & PUPPELS, G. J. 2002a. Rapid identification of Candida species by confocal Raman microspectroscopy. *J Clin Microbiol,* 40**,** 594-600.

MAQUELIN, K., CHOO-SMITH, L. P., VAN VREESWIJK, T., ENDTZ, H. P., SMITH, B., BENNETT, R., BRUINING, H. A. & PUPPELS, G. J. 2000. Raman spectroscopic method for identification of clinically relevant microorganisms growing on solid culture medium. *Analytical Chemistry,* 72**,** 12-19.

MAQUELIN, K., KIRSCHNER, C., CHOO-SMITH, L. P., VAN DEN BRAAK, N., ENDTZ, H. P., NAUMANN, D. & PUPPELS, G. J. 2002b. Identification of medically relevant microorganisms by vibrational spectroscopy. *J. Microbiol. Methods,* 51**,** 255-271.

MARINO, S., EL-KEBIR, M. & KIRSCHNER, D. 2011. A hybrid multi-compartment model of granuloma formation and T cell priming in Tuberculosis. *Journal of Theoretical Biology,* 280**,** 50-62.

MARIOTTI, S., PARDINI, M., GAGLIARDI, M. C., TELONI, R., GIANNONI, F., FRAZIANO, M., LOZUPONE, F., MESCHINI, S. & NISINI, R. 2013. Dormant Mycobacterium tuberculosis fails to block phagosome maturation and shows unexpected capacity to stimulate specific human T lymphocytes. *The Journal of Immunology,* 191**,** 274-282.

MARSHALL, G., J. W. S. BLACKLOCK, C. CAMERON, N. B. CAPON, R. CRUICKSHANK, J. H. GADDUM, F. R. G. HEAF, A. BRADFORD HILL, L. E. HOUGHTON, J. CLIFFORD HOYLE, H. RAISTRICK, J. G. SCADDING, W. H. TYTLER, G. S. WILSON & HART, P. D. A. 1948. STREPTOMYCIN treatment of pulmonary tuberculosis. *Br Med J,* 2**,** 769-82.

MAZILU, M., DE LUCA, A. C., RICHES, A., HERRINGTON, C. S. & DHOLAKIA, K. 2010. Optimal algorithm for fluorescence suppression of modulated Raman spectroscopy. *Opt. Express,* 18**,** 11382-95.

MCKINNEY, J. D., HONER ZU BENTRUP, K., MUNOZ-ELIAS, E. J., MICZAK, A., CHEN, B., CHAN, W. T., SWENSON, D., SACCHETTINI, J. C., JACOBS, W. R., JR. & RUSSELL, D. G. 2000. Persistence of *Mycobacterium tuberculosis* in macrophages and mice requires the glyoxylate shunt enzyme isocitrate lyase. *Nature,* 406**,** 735-8.

MCMURRAY, D. N. 1996. Mycobacteria and Nocardia. *In:* BARON, S. (ed.) *Medical Microbiology.* 4th ed. Galveston (TX).

MCNERNEY, R., MAEURER, M., ABUBAKAR, I., MARAIS, B., MCHUGH, T. D., FORD, N., WEYER, K., LAWN, S., GROBUSCH, M. P., MEMISH, Z., SQUIRE, S. B., PANTALEO, G., CHAKAYA, J., CASENGHI, M., MIGLIORI, G. B., MWABA, P., ZIJENAH, L., HOELSCHER, M., COX, H., SWAMINATHAN, S., KIM, P. S., SCHITO, M., HARARI, A., BATES, M., SCHWANK, S., O'GRADY, J., PLETSCHETTE, M., DITUI, L., ATUN, R. & ZUMLA, A. 2012. Tuberculosis diagnostics and biomarkers: needs, challenges, recent advances, and opportunities. *J Infect Dis,* 205 Suppl 2**,** S147-58.

MERLE, C. S., FIELDING, K., SOW, O. B., GNINAFON, M., LO, M. B., MTHIYANE, T., ODHIAMBO, J., AMUKOYE, E., BAH, B., KASSA, F., N'DIAYE, A., RUSTOMJEE, R., DE JONG, B. C., HORTON, J., PERRONNE, C., SISMANIDIS, C., LAPUJADE, O., OLLIARO, P. L., LIENHARDT, C. & PROJECT, O. G. T. 2014. A Four-month gatifloxacin-containing regimen for treating tuberculosis. *N. Engl. J. Med.,* 371**,** 1588-1598.

MIRANDA, M. S., BREIMAN, A., ALLAIN, S., DEKNUYDT, F. & ALTARE, F. 2012. The Tuberculous Granuloma: An Unsuccessful Host Defence Mechanism Providing a Safety Shelter for the Bacteria? *Clinical & Developmental Immunology*.

MOHN, W. W., VAN DER GEIZE, R., STEWART, G. R., OKAMOTO, S., LIU, J., DIJKHUIZEN, L. & ELTIS, L. D. 2008. The actinobacterial mce4 locus encodes a steroid transporter. *J Biol Chem,* 283**,** 35368-74.

MOVASAGHI, Z., REHMAN, S. & REHMAN, I. U. 2007. Raman spectroscopy of biological tissues. *Appl. Spectrosc. Rev.,* 42**,** 493-541.
MUKAMOLOVA, G. V., KAPRELYANTS, A. S., YOUNG, D. I., YOUNG, M. & KELL, D. B. 1998. A bacterial cytokine. *Proc Natl Acad Sci U S A,* 95**,** 8916-21.
MUKAMOLOVA, G. V., TURAPOV, O., MALKIN, J., WOLTMANN, G. & BARER, M. R. 2010. Resuscitation-promoting factors reveal an occult population of tubercle bacilli in sputum. *Am. J. Respir. Crit. Care Med.,* 181**,** 174-180.
NATHAN, C. & SHILOH, M. U. 2000. Reactive oxygen and nitrogen intermediates in the relationship between mammalian hosts and microbial pathogens. *Proc Natl Acad Sci U S A,* 97**,** 8841-8.
NESBITT, N. M., YANG, X., FONTAN, P., KOLESNIKOVA, I., SMITH, I., SAMPSON, N. S. & DUBNAU, E. 2010. A thiolase of *Mycobacterium tuberculosis* is required for virulence and production of androstenedione and androstadienedione from cholesterol. *Infect Immun,* 78**,** 275-82.
NICOLAOU, N., XU, Y. & GOODACRE, R. 2011. Fourier Transform Infrared and Raman Spectroscopies for the Rapid Detection, Enumeration, and Growth Interaction of the Bacteria Staphylococcus aureus and Lactococcus lactis ssp cremoris in Milk. *Analytical Chemistry,* 83**,** 5681-5687.
NOERTJOJO, K., TAM, C. M., CHAN, S. L. & CHAN-YEUNG, M. M. W. 2002. Extra-pulmonary and pulmonary tuberculosis in Hong Kong. *International Journal of Tuberculosis and Lung Disease,* 6**,** 879-886.
PAHLOW, S., MEISEL, S., CIALLA-MAY, D., WEBER, K., ROSCH, P. & POPP, J. 2015. Isolation and identification of bacteria by means of Raman spectroscopy. *Adv. Drug Deliv. Rev.,* 89**,** 105-120.
PANDEY, A. K. & SASSETTI, C. M. 2008. Mycobacterial persistence requires the utilization of host cholesterol. *Proc Natl Acad Sci U S A,* 105**,** 4376-80.
PHILLIPS, P. P., MENDEL, C. M., BURGER, D. A., CROOK, A. M., NUNN, A. J., DAWSON, R., DIACON, A. H. & GILLESPIE, S. H. 2016. Limited role of culture conversion for decision-making in individual patient care and for advancing novel regimens to confirmatory clinical trials. *BMC Med.,* 14**,** 19.
PILAT, Z., BERNATOVA, S., JEZEK, J., SERY, M., SAMEK, O., ZEMANEK, P., NEDBAL, L. & TRTILEK, M. 2012. Raman microspectroscopy of algal lipid bodies: beta-carotene quantification. *Journal of Applied Phycology,* 24**,** 541-546.
PUISSEGUR, M. P., BOTANCH, C., DUTEYRAT, J. L., DELSOL, G., CARATERO, C. & ALTARE, F. 2004. An in vitro dual model of mycobacterial granulomas to investigate the molecular interactions between mycobacteria and human host cells. *Cellular Microbiology,* 6**,** 423-433.
RAJNI, RAO, N. & MEENA, L. S. 2011. Biosynthesis and Virulent Behavior of Lipids Produced by *Mycobacterium tuberculosis*: LAM and Cord Factor: An Overview. *Biotechnol Res Int,* 2011**,** 274693.
RAMAN, C. V. & KRISHNAN, K. S. 1928. A new type of secondary radiation. *Nature,* 121**,** 501-502.
RAO, S. P. S., ALONSO, S., RAND, L., DICK, T. & PETHE, K. 2008. The protonmotive force is required for maintaining ATP homeostasis and viability of hypoxic, nonreplicating *Mycobacterium tuberculosis*. *Proceedings of the National Academy of Sciences of the United States of America,* 105**,** 11945-11950.

REECE, S. T. & KAUFMANN, S. H. 2012. Floating between the poles of pathology and protection: can we pin down the granuloma in tuberculosis? *Curr Opin Microbiol,* 15**,** 63-70.
REICHMAN, L. B. 1991. The U-Shaped Curve of Concern. *American Review of Respiratory Disease,* 144**,** 741-742.
RINGNER, M. 2008. What is principal component analysis? *Nat. Biotechnol.,* 26**,** 303-4.
RUBIN, E. J. 2009. The granuloma in tuberculosis--friend or foe? *N Engl J Med,* 360**,** 2471-3.
RUSCIANO, G., CAPRIGLIONE, P., PESCE, G., ABETE, P., CARNOVALE, V. & SASSO, A. 2013. Raman spectroscopy as a new tool for early detection of bacteria in patients with cystic fibrosis. *Laser Physics Letters,* 10**,** 075603.
RUSSELL, D. G. 2001. *Mycobacterium tuberculosis*: here today, and here tomorrow. *Nat Rev Mol Cell Biol,* 2**,** 569-77.
RUSSELL, D. G. 2007. Who puts the tubercle in tuberculosis? *Nat Rev Microbiol,* 5**,** 39-47.
RUSSELL, D. G., VANDERVEN, B. C., GLENNIE, S., MWANDUMBA, H. & HEYDERMAN, R. S. 2009. The macrophage marches on its phagosome: dynamic assays of phagosome function. *Nat Rev Immunol,* 9**,** 594-600.
SAAR, B. G., FREUDIGER, C. W., REICHMAN, J., STANLEY, C. M., HOLTOM, G. R. & XIE, X. S. 2010. Video-rate molecular imaging in vivo with stimulated Raman scattering. *Science,* 330**,** 1368-1370.
SARTAIN, M. J., DICK, D. L., RITHNER, C. D., CRICK, D. C. & BELISLE, J. T. 2011. Lipidomic analyses of *Mycobacterium tuberculosis* based on accurate mass measurements and the novel "Mtb LipidDB". *Journal of Lipid Research,* 52**,** 861-872.
SCHATZ, A., BUGIE, E. & WAKSMAN, S. A. 1944. Streptomycin, a substance exhibiting antibiotic activity against Gram positive and Gram-negative bacteria. *Proceedings of the Society for Experimental Biology and Medicine,* 55**,** 66-69.
SCHNAPPINGER, D., EHRT, S., VOSKUIL, M. I., LIU, Y., MANGAN, J. A., MONAHAN, I. M., DOLGANOV, G., EFRON, B., BUTCHER, P. D., NATHAN, C. & SCHOOLNIK, G. K. 2003. Transcriptional Adaptation of *Mycobacterium tuberculosis* within Macrophages: Insights into the Phagosomal Environment. *J Exp Med,* 198**,** 693-704.
SCHUSTER, K. C., URLAUB, E. & GAPES, J. R. 2000. Single-cell analysis of bacteria by Raman microscopy: spectral information on the chemical composition of cells and on the heterogeneity in a culture. *Journal of Microbiological Methods,* 42**,** 29-38.
SEGOVIA-JUAREZ, J. L., GANGULI, S. & KIRSCHNER, D. 2004. Identifying control mechanisms of granuloma formation during M-tuberculosis infection using an agent-based model. *Journal of Theoretical Biology,* 231**,** 357-376.
SENGUPTA, A., BRAR, N. & DAVIS, E. J. 2007. Bioaerosol detection and characterization by surface-enhanced Raman spectroscopy. *J Colloid Interface Sci,* 309**,** 36-43.
SETLOW, P. 2003. Spore germination. *Current Opinion in Microbiology,* 6**,** 550-556.
SHLEEVA, M., SALINA, E. & KAPRELYANTS, A. 2010. Dormant forms of mycobacteria. *Microbiology,* 79**,** 1-12.
SHLEEVA, M. O., BAGRAMYAN, K., TELKOV, M. V., MUKAMOLOVA, G. V., YOUNG, M., KELL, D. B. & KAPRELYANTS, A. S. 2002. Formation and

resuscitation of "non-culturable" cells of Rhodococcus rhodochrous and *Mycobacterium tuberculosis* in prolonged stationary phase. *Microbiology,* 148**,** 1581-91.

SHLEEVA, M. O., KUDYKINA, Y. K., VOSTROKNUTOVA, G. N., SUZINA, N. E., MULYUKIN, A. L. & KAPRELYANTS, A. S. 2011. Dormant ovoid cells of *Mycobacterium tuberculosis* are formed in response to gradual external acidification. *Tuberculosis,* 91**,** 146-154.

SILVEIRA, L., SATHAIAH, S., ZANGARO, R. A., PACHECO, M. T. T., CHAVANTES, M. C. & PASQUALUCCI, C. A. G. 2002. Correlation between near-infrared Raman spectroscopy and the histopathological analysis of atherosclerosis in human coronary arteries. *Lasers in Surgery and Medicine,* 30**,** 290-297.

SINGH, B. & MITCHISON, D. A. 1955. The bactericidal activities of combinations of streptomycin, isoniazid, p-aminosalicylic acid (PAS), oxytetracycline (terramycin) and viomycin against *Mycobacterium tuberculosis*. *J Gen Microbiol,* 13**,** 176-84.

SLOAN, D. J., MWANDUMBA, H. C., GARTON, N. J., KHOO, S. H., BUTTERWORTH, A. E., ALLAIN, T. J., HEYDERMAN, R. S., CORBETT, E. L., BARER, M. R. & DAVIES, G. R. 2015. Pharmacodynamic modeling of bacillary elimination rates and detection of bacterial lipid bodies in sputum to predict and understand outcomes in treatment of pulmonary tuberculosis. *Clin. Infect. Dis.,* 61**,** 1-8.

SMEKAL, A. 1923. Zur Quantentheorie der Dispersion. *Naturwissenschaften,* 11 873–875.

SMITH, E. & DENT, G. 2005. Modern Raman Spectroscopy: A Practical Approach. *Modern Raman Spectroscopy: A Practical Approach***,** 1-210.

STEVENSON, L. H. 1977. A case for bacterial dormancy in aquatic systems. *Microb Ecol,* 4**,** 127-33.

STOCKEL, S., MEISEL, S., LORENZ, B., KLOSS, S., HENK, S., DEES, S., RICHTER, E., ANDRES, S., MERKER, M., LABUGGER, I., ROSCH, P. & POPP, J. 2016. Raman spectroscopic identification of *Mycobacterium tuberculosis*. *J Biophotonics,* 10**,** 727-734.

STOCKEL, S., STANCA, A. S., HELBIG, J., ROSCH, P. & POPP, J. 2015. Raman spectroscopic monitoring of the growth of pigmented and non-pigmented mycobacteria. *Analytical and Bioanalytical Chemistry,* 407**,** 8919-8923.

STONE, N., KENDALL, C., SMITH, J., CROW, P. & BARR, H. 2004. Raman spectroscopy for identification of epithelial cancers. *Faraday Discuss,* 126**,** 141-57; discussion 169-83.

SWAMINATHAN, S., PADMAPRIYADARSINI, C., VENKATESAN, P., NARENDRAN, G., RAMESH KUMAR, S., ILIAYAS, S., MENON, P. A., SELVARAJU, S., POORANAGANGADEVI, N. P., BHAVANI, P. K., PONNURAJA, C., DILIP, M. & RAMACHANDRAN, R. 2011. Efficacy and safety of once-daily nevirapine- or efavirenz-based antiretroviral therapy in HIV-associated tuberculosis: a randomized clinical trial. *Clin Infect Dis,* 53**,** 716-24.

TU, Q. & CHANG, C. 2012. Diagnostic applications of Raman spectroscopy. *Nanomedicine-Nanotechnology Biology and Medicine,* 8**,** 545-558.

TUFARIELLO, J. M., JACOBS, W. R., JR. & CHAN, J. 2004. Individual *Mycobacterium tuberculosis* resuscitation-promoting factor homologues are dispensable for growth in vitro and in vivo. *Infect Immun,* 72**,** 515-26.

TUMA, R. 2005. Raman spectroscopy of proteins: from peptides to large assemblies. *Journal of Raman Spectroscopy,* 36**,** 307-319.
ULRICHS, T. & KAUFMANN, S. H. 2006. New insights into the function of granulomas in human tuberculosis. *J Pathol,* 208**,** 261-9.
VAN MANEN, H. J., KRAAN, Y. M., ROOS, D. & OTTO, C. 2005. Single-cell Raman and fluorescence microscopy reveal the association of lipid bodies with phagosomes in leukocytes. *Proc Natl Acad Sci U S A,* 102**,** 10159-64.
VOSKUIL, M. I., VISCONTI, K. & SCHOOLNIK, G. 2004a. Mycobacterium tuberculosis gene expression during adaptation to stationary phase and low-oxygen dormancy. *Tuberculosis,* 84**,** 218-227.
VOSKUIL, M. I., VISCONTI, K. C. & SCHOOLNIK, G. K. 2004b. *Mycobacterium tuberculosis* gene expression during adaptation to stationary phase and low-oxygen dormancy. *Tuberculosis (Edinb),* 84**,** 218-27.
WAGNER, M. 2009. Single-Cell Ecophysiology of Microbes as Revealed by Raman Microspectroscopy or Secondary Ion Mass Spectrometry Imaging. *Annual Review of Microbiology,* 63**,** 411-429.
WALTERMANN, M. & STEINBÜCHEL, A. 2005. Neutral lipid bodies in prokaryotes: Recent insights into structure, formation, and relationship to eukaryotic lipid depots. *Journal of Bacteriology,* 187**,** 3607-3619.
WANG, J. G. & BAKKEN, L. R. 1998. Screening of Soil Bacteria for Poly-beta-Hydroxybutyric Acid Production and Its Role in the Survival of Starvation. *Microb Ecol,* 35**,** 94-101.
WAYNE, L. G. & HAYES, L. G. 1996. An in vitro model for sequential study of shiftdown of *Mycobacterium tuberculosis* through two stages of nonreplicating persistence. *Infect Immun,* 64**,** 2062-9.
WAYNE, L. G. & LIN, K. Y. 1982. Glyoxylate metabolism and adaptation of *Mycobacterium tuberculosis* to survival under anaerobic conditions. *Infect Immun,* 37**,** 1042-9.
WAYNE, L. G. & SRAMEK, H. A. 1994. Metronidazole is bactericidal to dormant cells of *Mycobacterium tuberculosis*. *Antimicrob Agents Chemother,* 38**,** 2054-8.
WHITESIDES, M. D. & OLIVER, J. D. 1997. Resuscitation of Vibrio vulnificus from the viable but nonculturable state. *Applied and Environmental Microbiology,* 63**,** 1002-1005.
WHO 2010. *Treatment of Tuberculosis: Guidelines.* 4th ed. Geneva.
WHO 2011a. Rapid implementation of the Xpert MTB/RIF diagnostic test: technical and operational 'how-to': practical considerations.
.
WHO 2011b. Tuberculosis MDR-TB and XDR-TB.
WHO 2012. WHO policy on collaborative TB/HIV activities. Geneva: World Health Organization, 2012 (http://whqlibdoc.who.int/publications/2012/9789241503006_eng .pdf).
WHO 2016. Global Tuberculosis report 2016.
WINKLER, W., MUSSO, M. & KIRCHNER, E. C. 2003. Fourier transform Raman spectroscopic data on the fossil resin siegburgite. *Journal of Raman Spectroscopy,* 34**,** 157-162.
WU, H. W., VOLPONI, J. V., OLIVER, A. E., PARIKH, A. N., SIMMONS, B. A. & SINGH, S. 2011. In vivo lipidomics using single-cell Raman spectroscopy. *Proc. Natl. Acad. Sci. U.S.A.,* 108**,** 3809-3814.

XU, H. S., ROBERTS, N., SINGLETON, F. L., ATTWELL, R. W., GRIMES, D. J. & COLWELL, R. R. 1982. Survival and Viability of Nonculturable Escherichia-Coli and Vibrio-Cholerae in the Estuarine and Marine-Environment. *Microbial Ecology,* 8**,** 313-323.

YANG, H. & IRUDAYARAJ, J. 2003. Rapid detection of foodborne microorganisms on food surface using Fourier transform Raman spectroscopy. *Journal of Molecular Structure,* 646**,** 35-43.

YATES, R. M., HERMETTER, A. & RUSSELL, D. G. 2005. The kinetics of phagosome maturation as a function of phagosome/lysosome fusion and acquisition of hydrolytic activity. *Traffic,* 6**,** 413-20.

ZHANG, Y., YEW, W. W. & BARER, M. R. 2012. Targeting Persisters for Tuberculosis Control. *Antimicrobial Agents and Chemotherapy,* 56**,** 2223-2230.

ZIGNOL, M., VAN GEMERT, W., FALZON, D., SISMANIDIS, C., GLAZIOU, P., FLOYD, K. & RAVIGLIONE, M. 2012. Surveillance of anti-tuberculosis drug resistance in the world: an updated analysis, 2007-2010. *Bull World Health Organ,* 90**,** 111-119D.

ZINK, A., HAAS, C. J., REISCHL, U., SZEIMIES, U. & NERLICH, A. G. 2001. Molecular analysis of skeletal tuberculosis in an ancient Egyptian population. *Journal of Medical Microbiology,* 50**,** 355-366.

ZUMLA, A., RAVIGLIONE, M., HAFNER, R. & VON REYN, C. F. 2013. Tuberculosis. *N Engl J Med,* 368**,** 745-55.

Appendices

Section 1

Appendices table 1.1 Peak-to-peak ratios calculated using Raman spectra of *M. tuberculosis* lipid extraction at different culture age and corresponding standard deviation.

	1month		3 month		4 month	
Ratios	Average	Standard deviation	Average	Standard deviation	Average	Standard deviation
1060/1131	1.06	0.02	1.07	0.10	1.08	0.03
1060/1300	0.67	0.02	0.67	0.03	0.67	0.01
1060/1440	0.76	0.04	0.95	0.16	0.96	0.12
1060/1465	1.89	0.13	1.92	0.15	2.53	0.25
1060/2876	1.43	0.09	1.64	0.20	1.72	0.26
1060/2908	1.04	0.04	1.34	0.28	1.14	0.13
1131/1060	0.94	0.02	0.94	0.08	0.92	0.02
1131/1300	0.63	0.02	0.63	0.07	0.62	0.01
1131/1440	0.72	0.04	0.90	0.21	0.88	0.12
1131/1465	1.78	0.12	1.81	0.24	2.34	0.25
1131/2876	1.34	0.09	1.56	0.30	1.59	0.26
1131/2908	0.98	0.04	1.28	0.35	1.05	0.13
1300/1060	1.50	0.04	1.48	0.06	1.50	0.03
1300/1131	1.59	0.04	1.60	0.18	1.62	0.04
1300/1440	1.14	0.04	1.40	0.21	1.43	0.18
1300/1465	2.84	0.15	2.85	0.18	3.78	0.38
1300/2876	2.14	0.09	2.43	0.25	2.57	0.39

1300/2908	1.56	0.05	1.99	0.38	1.70	0.19
1440/1060	1.32	0.06	1.09	0.22	1.06	0.13
1440/1131	1.40	0.07	1.19	0.36	1.15	0.15
1440/1300	0.88	0.03	0.73	0.13	0.71	0.09
1440/1465	2.49	0.12	2.07	0.31	2.66	0.21
1440/2876	1.88	0.05	1.75	0.11	1.79	0.09
1440/2908	1.38	0.05	1.41	0.08	1.19	0.04
1465/1060	0.53	0.04	0.52	0.04	0.40	0.04
1465/1131	0.56	0.04	0.56	0.09	0.43	0.05
1465/1300	0.35	0.02	0.35	0.02	0.27	0.03
1465/1440	0.40	0.02	0.49	0.07	0.38	0.03
1465/2876	0.75	0.03	0.85	0.08	0.68	0.06
1465/2908	0.55	0.03	0.70	0.13	0.45	0.04
2876/1060	0.70	0.04	0.62	0.09	0.59	0.09
2876/1131	0.75	0.05	0.67	0.16	0.65	0.10
2876/1300	0.47	0.02	0.42	0.05	0.40	0.06
2876/1440	0.53	0.02	0.57	0.03	0.56	0.03
2876/1465	1.33	0.06	1.18	0.11	1.49	0.13
2876/2908	0.73	0.04	0.81	0.09	0.67	0.04
2908/1060	0.96	0.03	0.78	0.20	0.89	0.10
2908/1131	1.02	0.04	0.86	0.30	0.97	0.12
2908/1300	0.64	0.02	0.53	0.12	0.60	0.07
2908/1440	0.73	0.02	0.71	0.04	0.84	0.03
2908/1465	1.82	0.11	1.49	0.31	2.24	0.19
2908/2876	1.37	0.07	1.25	0.14	1.51	0.09

Section 2

D_2O Centrifugation protocol for LR/LP separation

The protocol explains how to get lipid rich (LR) and lipid poor (LP) cell from the same culture in two steps. The first step uses a lower density solution (1.04 $g.mL^{-1}$) and a higher centrifugation speed and harvest the top fraction (to obtain LR cells). The second step uses a higher density solution (1.08 $g.mL^{-1}$) and a lower centrifugation speed and harvest the bottom fraction (to obtain LP cells).

In order to generate the different density solutions the following formula was used:

$$Vy = Vi\ \frac{(pi - p)}{(p - py)}$$

Where:
Vy is the volume of D_2O in mL.
Vi is the volume of water in mL.
Pi is the density water in $g.mL^{-1}$ (1 $g.mL^{-1}$).
Py is the density of D_2O in $g.mL^{-1}$ (1.107 $g.mL^{-1}$).
P is the final density (1.04 $g.mL^{-1}$).

To do the separation you need a tube holder (**Appendices picture 2.1**) and a 50 mL falcon tube filled with tissue at the bottom (**Appendices picture 2.2**). A circular 2 mL eppendorf tube holder was designed. To draw the holder the software rihnocad was used and the item was printed in plastic using a 3D printer (PP3DPUP! printer). The diameter of the central hole is 10.9 mm, the holder diameter is 25.9 mm and the tube height is 50.3 mm.

***Appendices picture 2.1**: tube holder 3D printed*

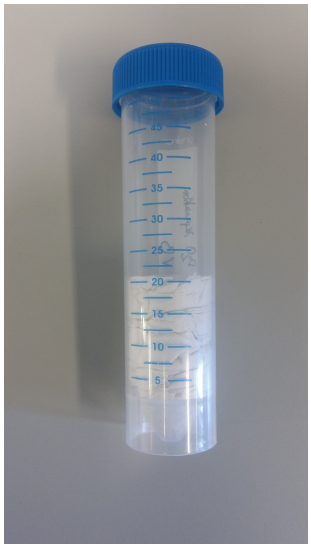

***Appendices Picture 2.2**: 50 mL falcon tube*

.

- Harvest one mL of cell culture that you grew in tween80 (0.05% final concentration) to avoid clumps.
- Wash the cells three times using PBS (spin down cells at 20,000 x g for three minutes, remove supernatant add PBS). Discard the supernatant.

To obtain LR cells from culture:

- Resuspend the cellular pellet in 755 µL of MiliQ H_2O, transfer this volume in a two mL eppendorf tube and add 450 µL of D_2O solution. This achieves a final density of 1.04 $g.mL^{-1}$.
- Mix the solution using your pipette to homogenise the solution.
- Place this tube in the tube holder (3D-printed, see **Appendices picture 1**), now insert the holder in a 50 mL falcon tube (see **Appendices picture 2**).
- Centrifuge the falcon tube at 500 x g (1500 rpm on the J6-M1 centrifuge) for 15 minutes.
- Harvest the top fraction (the first 100 µL) and place it in a 1.5 mL eppendorf tube (see **Appendices picture 3**, the red cross shows where to harvest the top fraction).

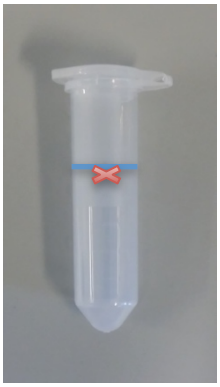

***Appendices picture 3**: harvest top fraction for LR cells (red cross).*

- You can stain the cells with Nile red or interrogate them with WMR spectroscopy or another methods understand the purity of the separation. If the purity is not high enough the centrifugation step can be repeated. Add one mL of 1.04 $g.mL^{-1}$ solution to your 80 to 100 µL of harvested cells that remain after the control and centrifuge again. Harvest the top fraction and perform your purity control again.

<u>To obtain LP cells from the culture</u>

- Resuspend the cellular pellet in 280 µL of MiliQ H_2O place this volume in a two mL eppendorf tube, add 830 µL of D_2O (1.08 $g.mL^{-1}$ final density).

- Place the two mL eppendorf tube the tube holder (3D-printed, see **Appendices picture 1**) insert the holder in a 50 mL falcon tube (**Appendices picture 2**).
- Centrifuge the tube at 35 x g (400 rpm on the J6-M1 centrifuge) for 15 minutes.
- Harvest the bottom fraction (100 µL. When harvesting the bottom fraction be careful to not take volume close to the pellet (see **Appendices picture 4**, red cross).

Appendices picture 4*: harvest bottom fraction for LP cells (red cross)*

- You can stain the cells with Nile red or interrogate them with WMR spectroscopy or another methods understand the purity of the separation. If the purity is not high enough the centrifugation step can be repeated. Add one mL of 1.08 $g.mL^{-1}$ solution to your 80 to 100 µL of harvested cells that remain after the control and centrifuge again. Harvest the top fraction and perform your purity control again.

Section 3

Animal infection

Work was conducted according to UK Home Office legislation for animal experimentation and was approved by the local ethical committee. Specific pathogen-free Dunkin Hartley guinea pigs were infected with *M. tuberculosis* H37Rv (NCTC cat. no. 7416) using a nose-only aerosol challenge exposure as described previously (Lever *et al.*, 2000) and (Clark *et al.*, 2011). All work with *M. tuberculosis* was conducted within an appropriate ACDP containment level 3 laboratory.

M. tuberculosis challenge inoculum at a titre of approximately 5.10^6 $CFU.mL^{-1}$ was prepared in a saline suspension. The inoculum was placed into the reservoir of the 3-jet Collison nebuliser and the Collison nebuliser was connected to the fully contained Henderson apparatus, the AeroMP control unit, laptop and air compressor pump. The 3-jet Collison nebuliser generates aerosol particles of *M. tuberculosis* with a mean diameter of 2 μm (diameter range of 0.5–7.0 μm).

The inoculum was aerosolised for 10 minutes, without animals present in the system, using the following parameter settings applied to the AeroMP software; relative humidity, RH (65 ± 1%), temperature (21 ± 1°C) and air flow rates (45 and 7.5 L mL^{-1}) 1 for circulating aerosol and Collison nebulizer, respectively), maintained at the same level throughout.

Following pre-aerosolisation of the *M. tuberculosis* suspension, the snout of each restrained guinea pig was presented to the nose only exposure system (sow) of the Henderson apparatus. The guinea pigs were exposed to aerosol particles using the same parameters as described in above for a total duration of 5 minutes (previously

shown to result in the delivery of approximately 50 surface lesions in the lungs of each animal).

Following aerosol challenge, animals were housed in appropriate ACDP level 3 facilities.

The relationship between the titre of inoculum in the aerosol nebulizer and the resulting CFU delivered to the lungs of each animal is specific for each nebuliser and apparatus type set-up. The parameters must be defined for each and the titre of inoculum adjusted as appropriate to obtain the required level of infection.

Section 4

Raman shift window

Raman spectra analysis of *M. tuberculosis* LR and LP single cells comparing different Raman shift window

Appendices Table. 4.1 *Sensitivity and specificity calculated using different Raman shift windows from standard Raman spectra for M. tuberculosis in-vitro (data shown in* ***Chapter 4, Fig 4.1****). Standard deviations are 0.034 and 0.022 for sensitivity and specificity respectively.*

Raman shift window	Variance from first 7 PCs	Sensitivity	Specificity
700~1800 cm^{-1}	81.2%	0.76	0.81
1000~1800 cm^{-1}	80.8%	0.82	0.80
1000~1500 cm^{-1}	86.3%	0.83	0.84
1250~1500 cm^{-1}	91.3%	0.83	0.82
1400~1500 cm^{-1}	95.4%	0.77	0.78

Appendices Table. 4.2 *Sensitivity and specificity calculated using different Raman shift windows from WMR spectra for M. tuberculosis in-vitro (data shown in* ***Chapter 4, Fig 4.3****). Standard deviations are 0.014 and 0.017 for sensitivity and specificity respectively.*

Raman shift window	Variance from first 7 PCs	Sensitivity	Specificity
700~1800 cm^{-1}	75.8%	0.96	0.91
1000~1800 cm^{-1}	78.1%	0.96	0.93
1000~1500 cm^{-1}	83.8%	0.98	0.93
1250~1500 cm^{-1}	89.8%	0.96	0.91
1400~1500 cm^{-1}	94.5%	0.94	0.89

Appendices Table. 4.3 *Sensitivity and specificity calculated using different Raman shift windows from WMR spectra for stained M. tuberculosis in-vitro (data shown in* ***Chapter 5 Fig. 5.22****). Standard deviations are 0.018 and 0.028 for sensitivity and specificity respectively.*

Raman shift window	Variance from first 7 PCs	Sensitivity	Specificity
700~1800 cm^{-1}	80.5%	0.86	0.82
1000~1800 cm^{-1}	79.2%	0.84	0.80
1000~1500 cm^{-1}	83.5%	0.86	0.79
1250~1500 cm^{-1}	88.9%	0.86	0.85
1400~1500 cm^{-1}	93.7%	0.89	0.85

Appendices Table. 4.4 *Sensitivity and specificity calculated using different Raman shift windows from WMR spectra for stained M. tuberculosis in tissue (data shown in* ***Chapter 5 Fig. 5.24 a****). Standard deviations are 0.022 and 0.044 for sensitivity and specificity respectively.*

Raman shift window	Variance from first 7 PCs	Sensitivity	Specificity
700~1800 cm^{-1}	78.9%	0.90	0.74
1000~1800 cm^{-1}	73.9%	0.93	0.85
1000~1500 cm^{-1}	79.4%	0.91	0.84
1250~1500 cm^{-1}	85.2%	0.87	0.79
1400~1500 cm^{-1}	92.9%	0.91	0.80

Section 5

Statistic on R software code and results.

```
R version 3.0.2 (2013-09-25) -- "Frisbee Sailing"
Copyright (C) 2013 The R Foundation for Statistical Computing
Platform: x86_64-apple-darwin10.8.0 (64-bit)

R is free software and comes with ABSOLUTELY NO WARRANTY.
You are welcome to redistribute it under certain conditions.
Type 'license()' or 'licence()' for distribution details.

  Natural language support but running in an English locale

R is a collaborative project with many contributors.
Type 'contributors()' for more information and
'citation()' on how to cite R or R packages in publications.

Type 'demo()' for some demos, 'help()' for on-line help, or
'help.start()' for an HTML browser interface to help.
Type 'q()' to quit R.

[R.app GUI 1.62 (6558) x86_64-apple-darwin10.8.0]

[Workspace restored from /Users/vincentbaron/.RData]
[History restored from /Users/vincentbaron/.Rapp.history]

> data1=read.csv("/Users/vincentbaron/Desktop/DATA.csv",h=T)
> boxplot(data1)
> data1
   seven.days two.hours four.hours six.hours
1      970.17    513.69     364.69    356.71
2      299.65    302.79     617.02    279.45
3      641.18    637.63     249.14    368.01
4      358.54    316.89     408.22    377.00
5      473.79    496.62     466.72    342.29
6      551.41    430.42     256.65    248.47
7      577.16    301.60     485.11    330.30
8      720.05    544.12     332.26    312.28
9      504.72    344.64     261.53    309.38
10     636.64    296.94     277.29    350.76
11     495.40    320.97     389.73    330.66
12     496.56    539.94     369.98    302.84
13     873.75    410.37     429.79    422.56
14     750.53    291.58     360.44    245.29
15     421.23    452.53     469.75    502.98
16     560.41    450.32     415.85    284.04
17     604.47    316.38     300.79    339.75
18     848.47    370.91     459.92    432.81
```

```
19    524.73   597.23   460.98   398.29
20    441.26   282.89   464.13   256.38
21    464.86   460.06   388.87   333.30
22    743.28   360.88   414.64   436.74
23    494.19   342.63   481.58   480.39
24    383.09   307.33   415.43   255.14
25    449.37   301.81   421.75   328.15
26    733.04   254.33   333.37   349.95
27    340.90   712.29   371.08   320.80
28    594.67   411.07   371.35   434.40
29    729.99   541.54   385.64   448.89
30    300.74   384.50   461.81   336.29
31    521.14   592.18   288.93   299.32
32    455.22   384.37   445.29   261.32
33    546.76   400.22   536.25   344.59
34    456.84   413.62   296.57   259.11
35    467.07   407.52   280.25   403.57
36    527.26   441.41   483.62   674.90
37    591.98   431.20   362.48   308.66
38    375.46   454.89   575.24   321.38
39    362.84   299.25   385.76   366.48
40    283.41   521.37   380.59   358.95
41    538.90       NA       NA       NA
42    559.48       NA       NA       NA
43    337.87       NA       NA       NA
44    379.42       NA       NA       NA
45    400.99       NA       NA       NA
46    456.29       NA       NA       NA
47    379.74       NA       NA       NA
48    493.59       NA       NA       NA
49    344.74       NA       NA       NA
50    530.34       NA       NA       NA
51    752.94       NA       NA       NA
52    603.07       NA       NA       NA
53   1046.47       NA       NA       NA
54    415.38       NA       NA       NA
55    412.81       NA       NA       NA
56    318.13       NA       NA       NA
57    586.19       NA       NA       NA
58    541.70       NA       NA       NA
59    405.52       NA       NA       NA
60    540.55       NA       NA       NA
61    342.57       NA       NA       NA
62    400.21       NA       NA       NA
63    713.84       NA       NA       NA
> data2=read.csv("/Users/vincentbaron/Desktop/DATA 2.csv",h=F)
> data2
   V1       V2
1   0  970.1682
2   0  299.6470
```

3 0 641.1773
4 0 358.5442
5 0 473.7915
6 0 551.4122
7 0 577.1578
8 0 720.0458
9 0 504.7231
10 0 636.6415
11 0 495.4011
12 0 496.5598
13 0 873.7460
14 0 750.5329
15 0 421.2295
16 0 560.4083
17 0 604.4728
18 0 848.4685
19 0 524.7292
20 0 441.2644
21 0 464.8579
22 0 743.2847
23 0 494.1931
24 0 383.0908
25 0 449.3667
26 0 733.0370
27 0 340.9044
28 0 594.6690
29 0 729.9924
30 0 300.7409
31 0 521.1425
32 0 455.2197
33 0 546.7627
34 0 456.8444
35 0 467.0652
36 0 527.2586
37 0 591.9849
38 0 375.4633
39 0 362.8421
40 0 283.4057
41 0 538.8952
42 0 559.4833
43 0 337.8735
44 0 379.4246
45 0 400.9935
46 0 456.2902
47 0 379.7440
48 0 493.5934
49 0 344.7438
50 0 530.3447
51 0 752.9377
52 0 603.0688

53 0 1046.4660
54 0 415.3847
55 0 412.8078
56 0 318.1340
57 0 586.1890
58 0 541.7040
59 0 405.5208
60 0 540.5470
61 0 342.5734
62 0 400.2095
63 0 713.8420
64 2 513.6892
65 2 302.7948
66 2 637.6294
67 2 316.8908
68 2 496.6226
69 2 430.4220
70 2 301.5972
71 2 544.1151
72 2 344.6396
73 2 296.9396
74 2 320.9727
75 2 539.9435
76 2 410.3705
77 2 291.5828
78 2 452.5343
79 2 450.3168
80 2 316.3850
81 2 370.9077
82 2 597.2334
83 2 282.8925
84 2 460.0623
85 2 360.8839
86 2 342.6260
87 2 307.3252
88 2 301.8118
89 2 254.3292
90 2 712.2870
91 2 411.0734
92 2 541.5449
93 2 384.4975
94 2 592.1793
95 2 384.3702
96 2 400.2192
97 2 413.6172
98 2 407.5156
99 2 441.4074
100 2 431.1964
101 2 454.8902
102 2 299.2491

103 2 521.3659
104 4 364.6897
105 4 617.0166
106 4 249.1387
107 4 408.2167
108 4 466.7179
109 4 256.6457
110 4 485.1123
111 4 332.2597
112 4 261.5285
113 4 277.2903
114 4 389.7332
115 4 369.9808
116 4 429.7885
117 4 360.4385
118 4 469.7470
119 4 415.8490
120 4 300.7862
121 4 459.9188
122 4 460.9774
123 4 464.1319
124 4 388.8653
125 4 414.6444
126 4 481.5850
127 4 415.4312
128 4 421.7547
129 4 333.3707
130 4 371.0782
131 4 371.3544
132 4 385.6427
133 4 461.8073
134 4 288.9343
135 4 445.2886
136 4 536.2483
137 4 296.5717
138 4 280.2547
139 4 483.6174
140 4 362.4844
141 4 575.2411
142 4 385.7603
143 4 380.5888
144 6 356.7140
145 6 279.4522
146 6 368.0119
147 6 376.9983
148 6 342.2893
149 6 248.4699
150 6 330.3042
151 6 312.2771
152 6 309.3832

```
153  6  350.7597
154  6  330.6567
155  6  302.8434
156  6  422.5643
157  6  245.2862
158  6  502.9833
159  6  284.0350
160  6  339.7541
161  6  432.8110
162  6  398.2851
163  6  256.3766
164  6  333.2959
165  6  436.7379
166  6  480.3897
167  6  255.1420
168  6  328.1468
169  6  349.9503
170  6  320.8040
171  6  434.4030
172  6  448.8908
173  6  336.2874
174  6  299.3153
175  6  261.3158
176  6  344.5874
177  6  259.1063
178  6  403.5717
179  6  674.9034
180  6  308.6613
181  6  321.3772
182  6  366.4823
183  6  358.9483
> h=data2[[2]]
> a1=aov(h~as.factor(data2[[1]]))
> summary(a1)
                  Df  Sum Sq Mean Sq F value   Pr(>F)
as.factor(data2[[1]])   3  849141  283047   18.89 1.09e-10 ***
Residuals             179 2682314   14985
---
Signif. codes:  0 ‘***’ 0.001 ‘**’ 0.01 ‘*’ 0.05 ‘.’ 0.1 ‘ ’ 1
> l1=lm(h~data2[[1]])
> summary(l1)

Call:
lm(formula = h ~ data2[[1]])

Residuals:
    Min      1Q  Median      3Q     Max
-225.99  -85.23  -11.48   63.32  537.07

Coefficients:
```

```
            Estimate Std. Error t value Pr(>|t|)
(Intercept)  509.394     13.790  36.938  < 2e-16 ***
data2[[1]]   -28.067      3.942  -7.121 2.44e-11 ***
---
Signif. codes:  0 ‘***’ 0.001 ‘**’ 0.01 ‘*’ 0.05 ‘.’ 0.1 ‘ ’ 1

Residual standard error: 123.5 on 181 degrees of freedom
Multiple R-squared:  0.2188,  Adjusted R-squared:  0.2145
F-statistic:  50.7 on 1 and 181 DF,  p-value: 2.444e-11

> TukeyHSD(x=a1)
  Tukey multiple comparisons of means
    95% family-wise confidence level

Fit: aov(formula = h ~ as.factor(data2[[1]]))

$`as.factor(data2[[1]])`
         diff       lwr        upr     p adj
2-0 -108.94525 -173.1259  -44.76460 0.0001077
4-0 -126.95626 -191.1369  -62.77561 0.0000045
6-0 -172.15423 -236.3349 -107.97358 0.0000000
4-2  -18.01101  -88.9967   52.97468 0.9126135
6-2  -63.20898 -134.1947    7.77671 0.0997463
6-4  -45.19797 -116.1837   25.78772 0.3527737

> plot (h~jitter(data2[[1]],+0.5))
> abline(509.394,-28.067)
```

Section 6
Image analysis using Definiens software

This section presents the image analysis of a picture showing a seven days old *M. smegmatis* culture stained with Nile red (see **Appendices figure 6.1)**.

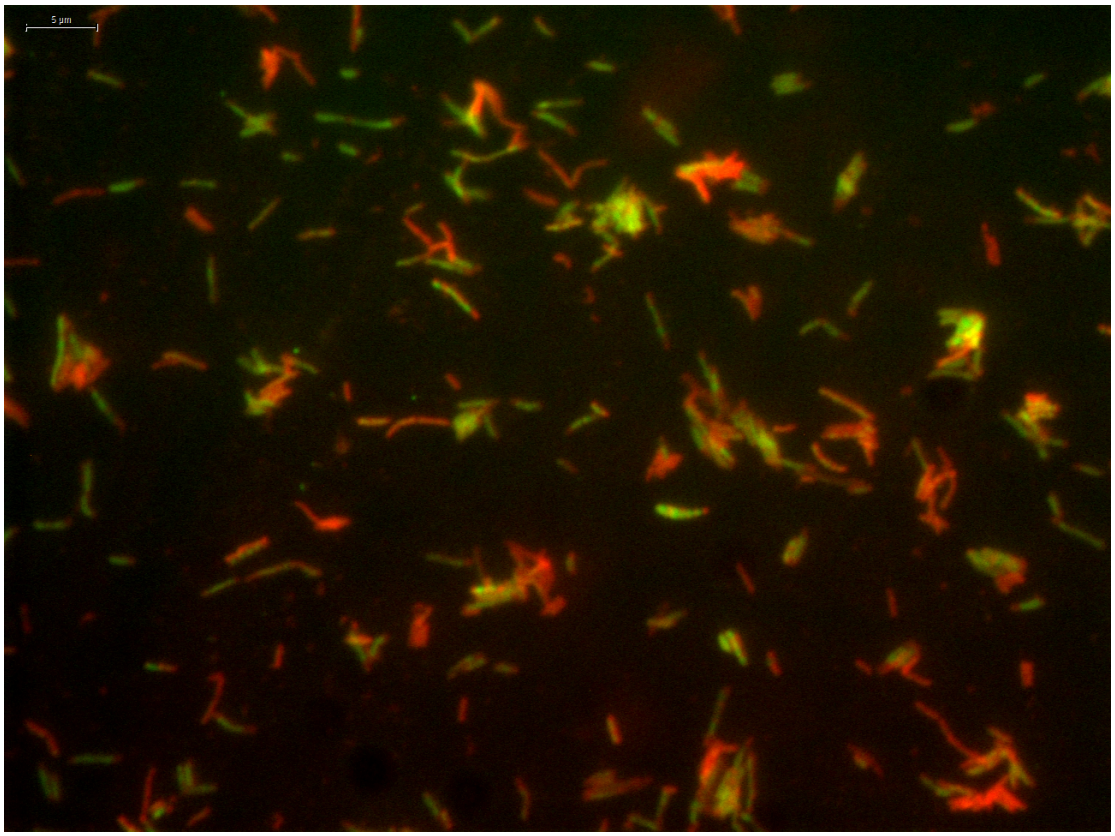

Appendices figure 6.1 *Combined red and green pictures of Nile red stained M. smegmatis cells. The red represents the polar lipids and the green the non-polar lipids. The scale bar represents 5 µm.*

Items showing a detectable intensity value (in the red channel) over a certain area, set at 6 μm^2, were defined as bacteria (see **Appendices Fig. 6.2**).

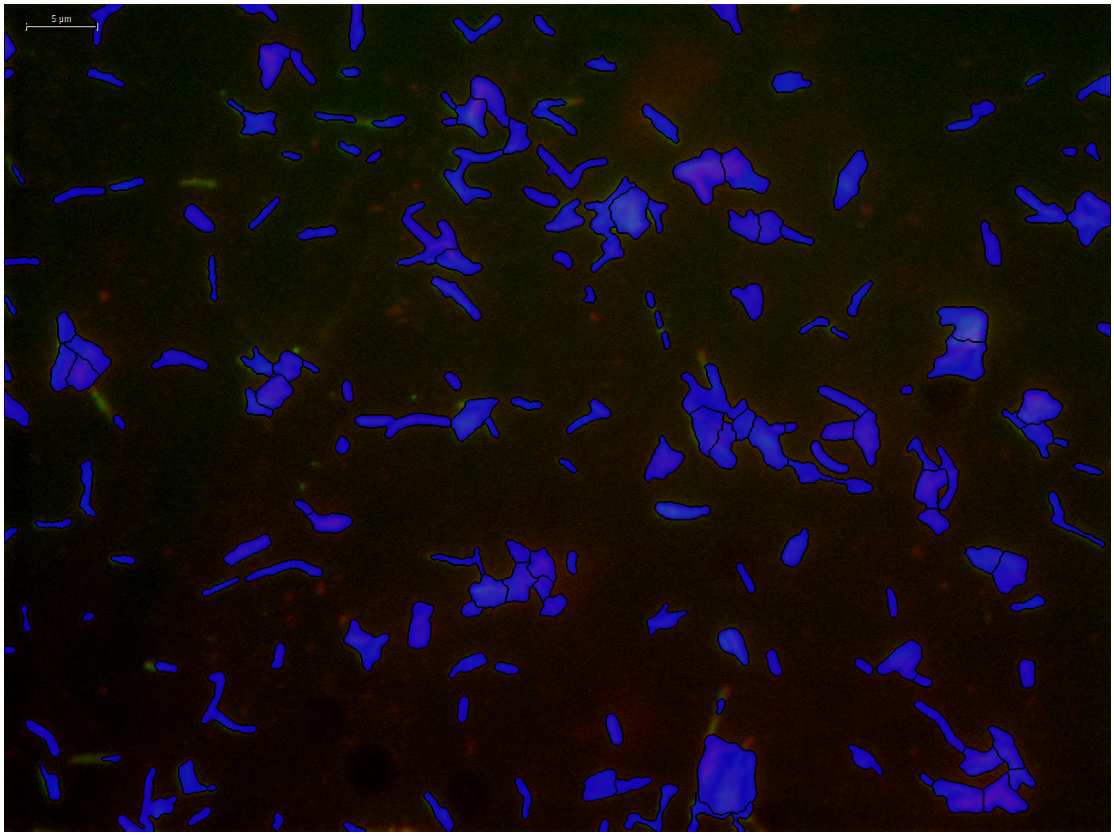

Appendices figure 6.2 *Items defined as bacteria before filters based on the red channel picture. The scale bar represents 5 µm.*

Some of the items selected are too small or too big and correspond to debris, clumps and aggregates of several cells. First we applied a filter to remove any items smaller or equal to 1 μm^2, see **Appendices Fig. 6.3.**

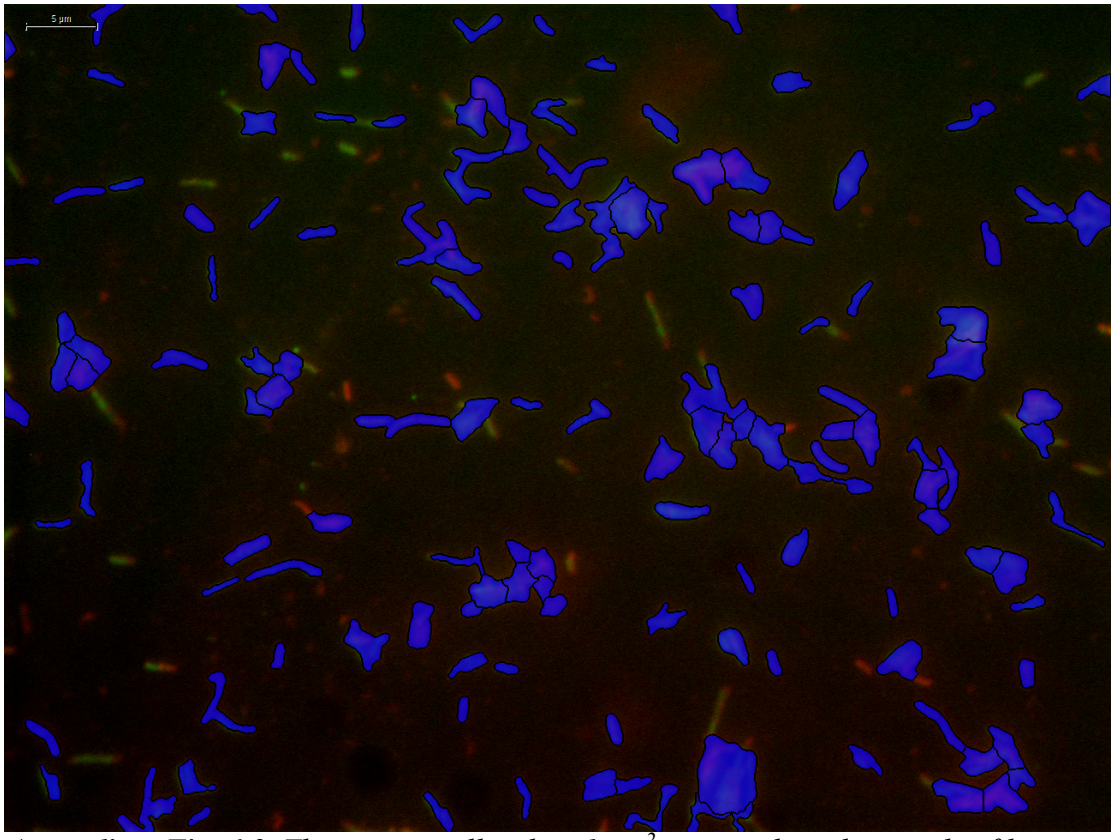

Appendices Fig. 6.3. *The items smaller than 1 μm^2 are unselected using this filter. They are now not in blue compared to the* ***Appendices Fig. 6.2****. The scale bar represents 5 µm.*

We applied a second filter to remove every item bigger than 7 μm^2. The idea is to try to remove the clump, aggregates or group of bacteria, see **Appendices Fig. 6.4.**

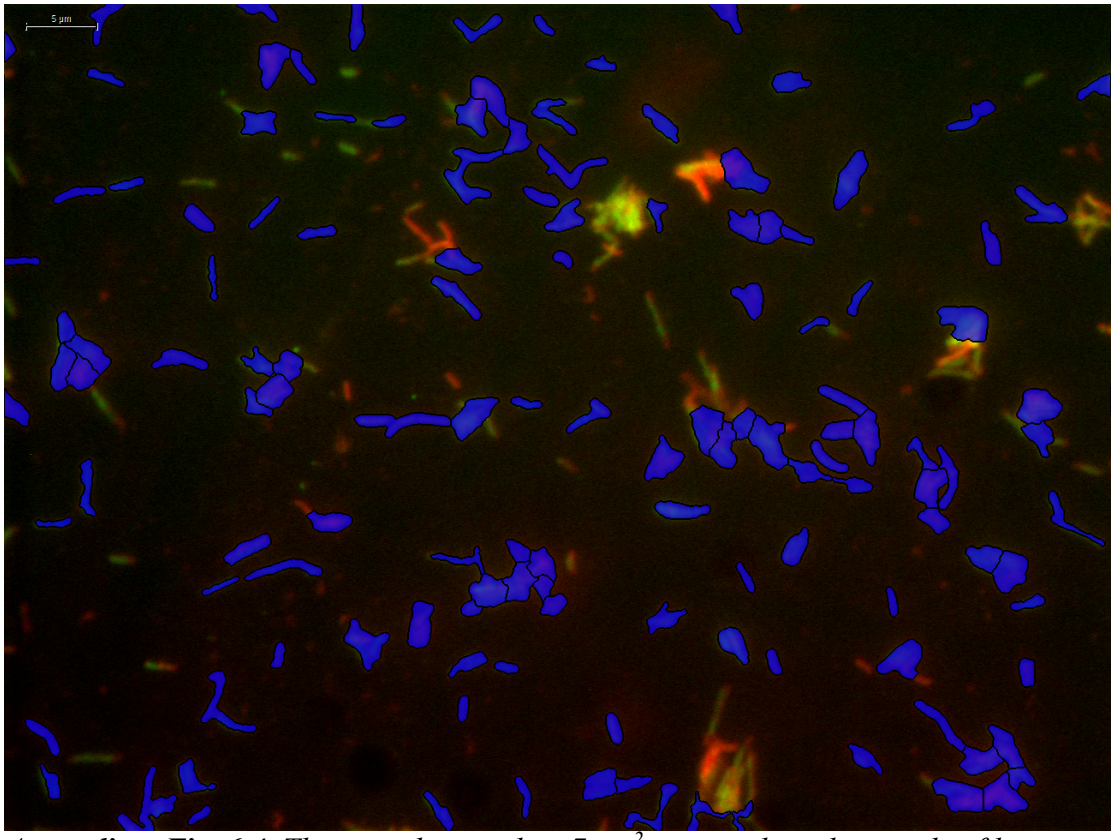

Appendices Fig. 6.4. *The items bigger than 7 μm^2 are unselected using this filter. They are now not in blue compared to the* ***Appendices Fig. 6.2****. The scale bar represents 5 µm.*

We applied a last filter to remove items that do not display a “bacillus shape”. The more an item is square the more likely this item will be removed by this filter, see **Appendices Fig. 6.5.**

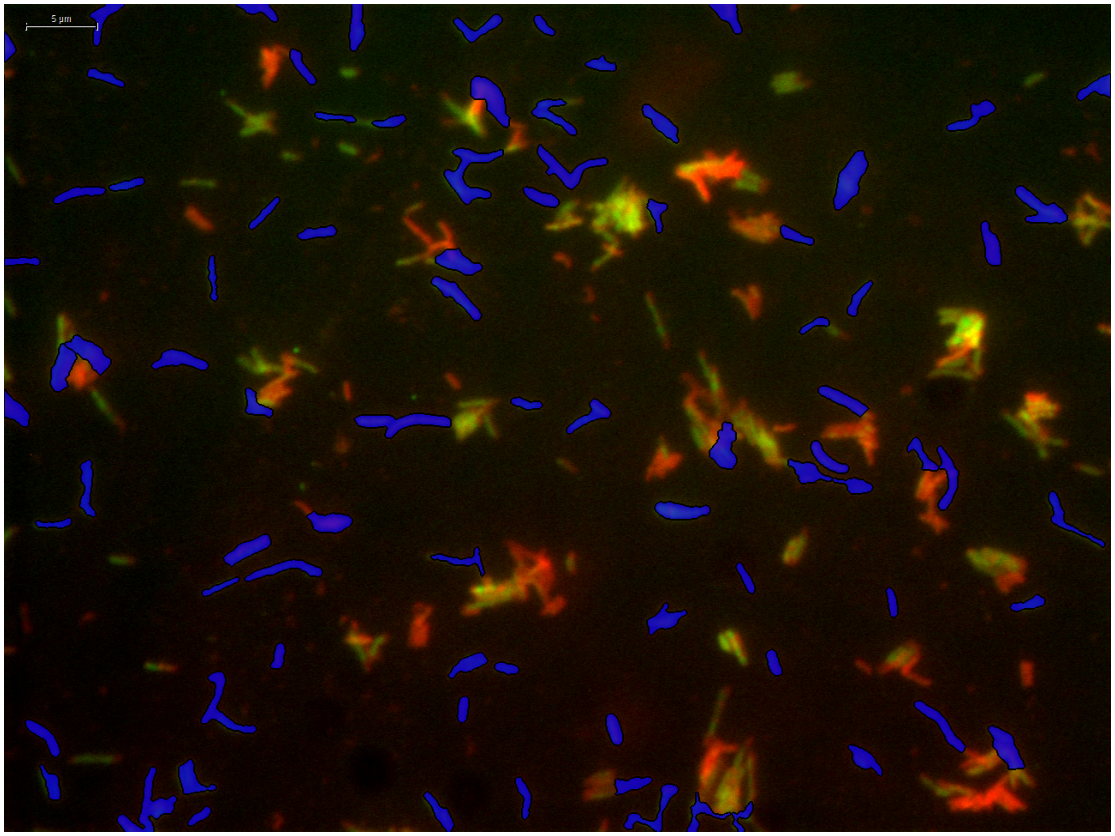

Appendices Fig. 6.5. *Using this filter the items are unselected based on their shape (if they are square). They are now not in blue compared to the* ***Appendices Fig. 6.2****. The scale bar represents 5 µm.*

Using the green picture (non-polar lipids) the software detects the lipid bodies based on their intensity over a certain surface. To be selected the green intensity has to be intracellular (overlap with the red). The **Appendices Fig. 6.6** shows the intracellular lipid bodies.

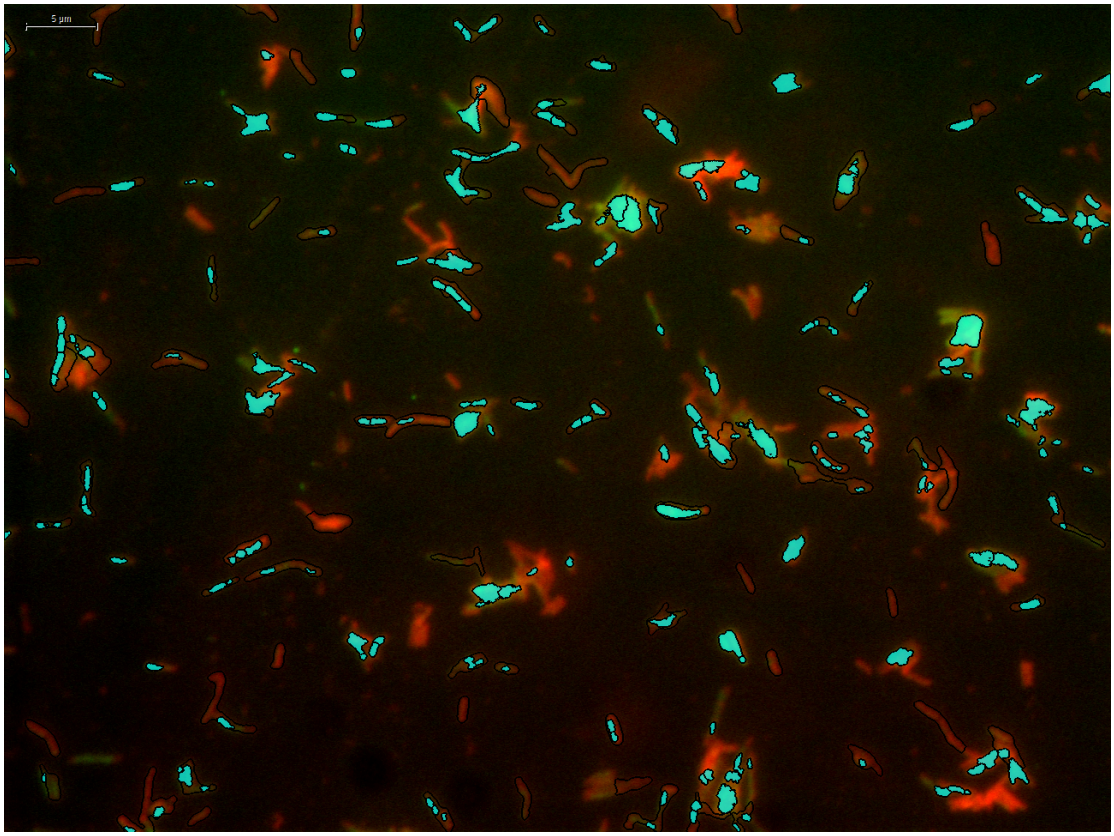

Appendices Fig. 6.6 *Detection of the intracellular lipid bodies using the green picture (non-polar lipids). The scale bar represents 5 µm.*

The lipid bodies are then ranked based on their size:
Small < 0.5 μm^2 (Yellow)
Medium 0.5-1μm^2 (Orange)
Large >1μm^2 (Red)

The **Appendices Fig. 6.7** shows the intracellular lipid bodies and their size.

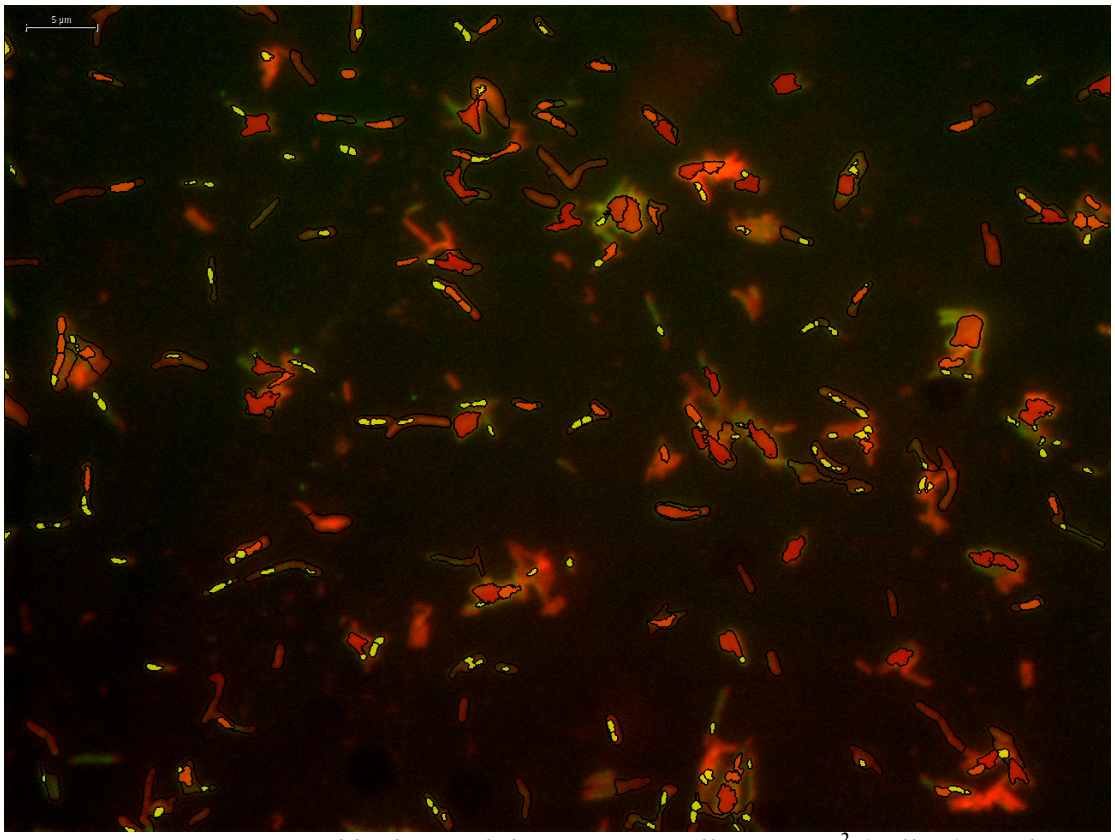

Appendices Fig. 6.7 *Lipid bodies and their sizes: small < 0.5 μm^2 (Yellow), medium 0.5-1 μm^2 (Orange) or large >1 μm^2 (Red). The scale bar represents 5 µm.*

Section 7
Impact of laser on single bacteria

To obtain a strong Raman signal from a single cell, a power of 150 mW was applied onto the sample plane. We designed an experiment to assess the impact of the laser to the bacteria. This experiment was carried out, using a stationary phase culture of *M. smegmatis,* on 3 individual bacteria (N=3). We took 10 spectra in a row on the same bacteria. This represents 1500 seconds of exposure to the laser. No spectral differences were observed between the first spectrum and the last one (same result for the 3 bacteria). The results for one bacterium are shown in the **Appendices Fig. 1 and Fig. 2.** The focused laser power we used in this thesis did not induce any damage to the cell during the acquisition of spectra.

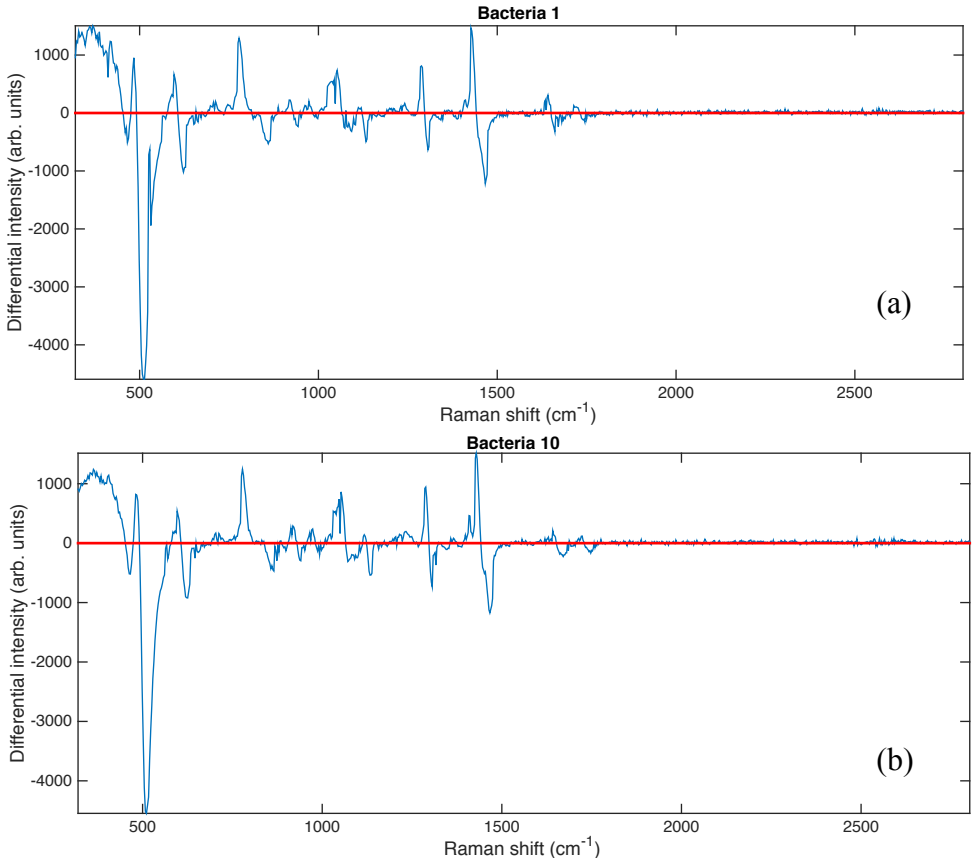

Appendices Fig. 7.1 *This figures shows the WMR spectra of a M. smegmatis bacterium (showed in* ***Appendices Fig. 7.2****). This cell was from a stationary phase culture. Ten WMR spectra in row were acquired from this cell to assess the impact that the laser has on the bacterium. The* ***Appendices Fig. 7.1 a*** *shows the first WMR spectrum taken and the* ***Appendices Fig. 7.1 b*** *shows the last WMR spectrum taken. No spectral differences could be observed between the two spectra. Ten spectra represent 1500 seconds of exposure. The laser power on the bacteria was 150 mW.*

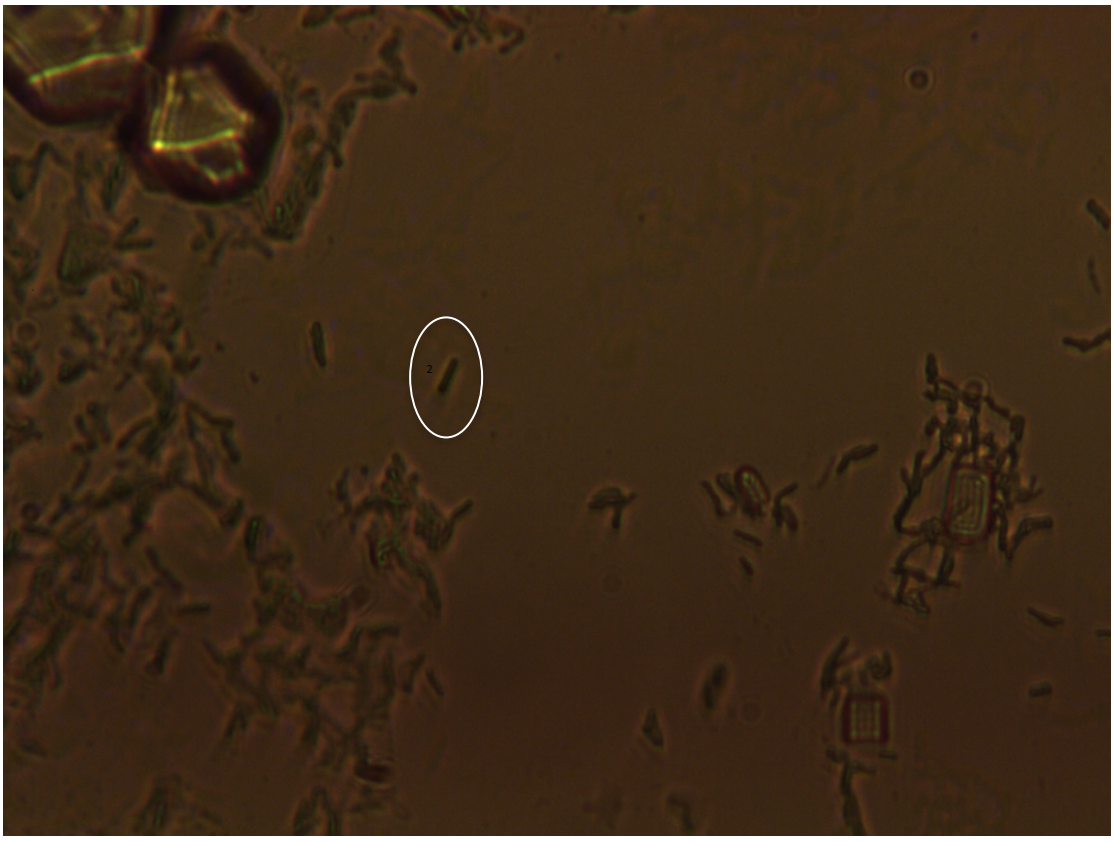

Appendices Fig. 7.2 *This figure shows one of the single bacterium targeted in the experiment to assess the impact that the laser has on bacterium (in the white circle). The corresponding WMR spectra are shown in the* ***Appendices Fig. 7.1****.*

Publications

Tuberculosis 99 (2016) 131–142

Contents lists available at ScienceDirect

Tuberculosis

journal homepage: http://intl.elsevierhealth.com/journals/tube

REVIEW

Defining dormancy in mycobacterial disease

S. Lipworth [a], R.J.H. Hammond [a], V.O. Baron [a], Yanmin. Hu [b], A. Coates [b], S.H. Gillespie [a, *]

[a] School of Medicine, University of St Andrews, Biomedical Science Building, North Haugh, St Andrews KY16 9TF, United Kingdom
[b] Institute for Infection and Immunity, St George's, University of London, London SW17 ORE, United Kingdom

ARTICLE INFO

Article history:
Received 16 February 2016
Received in revised form
6 May 2016
Accepted 23 May 2016

Keywords:
Mycobacterium tuberculosis
Dormancy
Latency
Persistence
Mycobacteria

SUMMARY

Tuberculosis remains a threat to global health and recent attempts to shorten therapy have not succeeded mainly due to cases of clinical relapse. This has focussed attention on the importance of "dormancy" in tuberculosis. There are a number of different definitions of the term and a similar multiplicity of different *in vitro* and *in vivo* models. The danger with this is the implicit assumption of equivalence between the terms and models, which will make even more difficult to unravel this complex conundrum. In this review we summarise the main models and definitions and their impact on susceptibility of *Mycobacterium tuberculosis*. We also suggest a potential nomenclature for debate. Dormancy researchers agree that factors underpinning this phenomenon are complex and nuanced. If we are to make progress we must agree the terms to be used and be consistent in using them.

Contents

* Corresponding author. Medical and Biological Sciences Building, University of St Andrews, North Haugh, St Andrews, Fife KY16 9TF, United Kingdom. Tel.: +44 1334 461871; fax: +44 1334 473482.
E-mail address: shg3@st-andrews.ac.uk (S.H. Gillespie).

http://dx.doi.org/10.1016/j.tube.2016.05.006
1472-9792/

1. Introduction

Improvement in tuberculosis treatment is seen widely as an important goal of research to reduce preventable deaths. One of the major barriers to progress is the prolonged duration of treatment, which has put an emphasis on the unusual nature of tuberculosis where the organism forms a life-long relationship with the host persisting in a low metabolic state in the tissues. Recent phase III clinical trials of shortened regimens have failed to show non-inferiority mainly due to higher relapse rates in the experimental arms despite more rapid clearance of bacteria [1–3]. This implies that hidden populations of bacteria may be important in defining outcome as has been implied by recent publications [4,5]. Unravelling the biology of the relationship between dormancy and response to antibiotics is critical for the development of better treatments for tuberculosis.

The diversity of terms used to describe the physiology of *Mycobacterium tuberculosis* and other mycobacterial cells in tissues creates a communication challenge. This has the effect that bacteriologists, immunologists, clinical trialists, clinicians and diagnosticians, are surrounded by a cloud of uncertain meaning. That the same words have different meanings to scientists blocks progress in this already difficult area. To address this issue we have reviewed and summarised the literature surrounding the term dormancy and its companion terms persistence and latency, whilst identifying some of the key biological questions that need to be addressed (Table 3). We believe that it is only by creating a common language to underpin the scientific conversation that efficient progress in scientific knowledge is possible and will allow a future consensus to emerge and this is what we attempt to do in this manuscript.

Text box 1
Assumptions around dormancy

The critical, implicit and as yet untested assumption is that

all dormancy phenotypes are equivalent
the phenotypes are predictive of a state found in the human host
bacteria in specimens and in tissue samples and animal models of disease share some phenotypic characteristics associated with dormancy
there is no unequivocal marker that identify mycobacterial cells in a dormant state

2. Dormant

It is important to distinguish the terms dormant and dormancy from others that are often erroneously used as synonyms: latent/latency and persistent and persistence (see below). A state of dormancy has been hypothesised for *M. tuberculosis* cells in human infection and it is a feature that has been recognised in a wide range of bacteria since 1944 [6]. At its simplest, the term dormant might be defined as “having normal physical functions suspended or slowed down for a period of time; in or as if in a deep sleep”, but how can this anthropomorphic concept be applied to bacteria in humans? The working definition of mycobacterial dormancy is complicated by the fact that it is usually described negatively: inability to grow on solid medium, the presence of low metabolic activity, alteration of gene regulation with the accumulation of triacylglycerides in intracellular lipid bodies, loss of acid fastness, tolerance to antibiotics, and the imputation that growth rate is slow. To explore this state a number of dormancy models have been developed and these are described in more detail in Table 1 and in the text below. The critical, implicit and as yet untested assumption is that they all result in a similar phenotype and that these phenotypes are predictive of a state found in the human host. Although there have been many descriptions of the histopathological changes found in human and animal models of disease none of these unequivocally identify mycobacterial cells in a dormant state [7,8].

Experimental data are starting to reveal the physiological state of organisms that might be candidates to be the elusive dormant cell, for example some organisms in human and animal specimens cannot be recovered on solid medium and can only be detected by growth in liquid culture broth or by the addition of resuscitation promotion factor (Rpf) [9–11]. Studies have shown that, after a course of chemotherapy, liquid culture and the tissues of mice contain un-culturable cells that transcribe messenger RNA [12]. Using a fluorescent marked reporter strain the lungs of chronically infected mice have been shown to harbour a subpopulation of non-growing but metabolically active bacteria. Such bacterial cells are notable in mice treated with the isoniazid, suggesting that they may have a role in post-chemotherapeutic relapses [13]. Reports also indicate that, as mycobacteria become increasingly difficult to resuscitate, they have less capacity to cause infection in mice [14].

The physiological conditions within a patient with tuberculosis are starting to be understood and research has been directed towards extending this knowledge and finding models that recreate these conditions. The caseous granuloma is thought to be an anaerobic environment providing circumstantial support for the importance of some *in vitro* models described in more detail below. A “dormancy” phenotype can be created in the laboratory by applying different forms of stress: oxygen or nutrient deficiency, hyper-acidity, antibiotics and multiple combinations of these. The published models include bacterial starvation [15], successive shift-down or anaerobiosis (the Wayne model) [16], external acidification [17], antibiotic survival [12,18], multiple stress [19–21] and these are reviewed in turn. For the moment we will call all of these “dormancy” models, recognising that, at present, we only have an atlas of phenomenology and there is a need to identify the characteristics of each model comprehensively.

Table 1
Summary of mycobacterial dormancy models with a description of methods of selecting cellular sub-types, and the phenotypic and metabolic characteristics.

Principle of model and organism	Morphology of cells	Buoyant density	Metabolism	Microscopic observations	Viability challenges	Lipids in resultant cells
Gradual acidification, *M. smegmatis* [17,86]	Three types of cells formed: ovoid, transitional, rod shaped – 60% ovoid after 30 days	Ovoid cells higher buoyant density 1.8 M zone in 1.4–2.2 M sucrose gradient	Post-stationary cultures exhibit low but non zero uptake of radioactive DNA/RNA precursors no detectable respiration	Thickened, multi-layered cell wall, electron dense cytoplasm	Ovoid forms more resistant to antibiotics and heat	Not reported
Growth in modified potassium free medium, *M. smegmatis* [87]	Spherical cells, condensation of cytoplasm		Decreased total metabolic activity and total respiratory activity	Increased number vacuoles, decreased ribosomes. Cells with "rarefied" cytoplasm non-viable		Total amount of lipid 2-fold lower than metabolically active cells.
Multiple-stress model on *M. tuberculosis* [16,20]		Buoyant density decreased with increasing time under multiple stress	- Enzymes of glyoxylate cycle are upregulated. Shutdown of ATP and NAD energy regeneration systems. - Overall slowdown of transcription/ translation apparatus	Loss of acid fatness – 30% after 30 days of multiple stress	Resistance to RIF and INH – at 18 days c. 12% survive 5 μg/mL RIF and c. 35% survive 0.8% μg/ mL INH	Increased lipid bodies (70% lipid bodies positive at 18 days). Accumulation of storage lipids (WE and TG) in anaerobic but not aerobic samples
Nutrient starvation *M. tuberculosis* [54]			Significantly decreased respiration rate		No loss of viability after 6 weeks. Starved cultures resistant to RIF and INH at 1 μg/ mL Sensitive to metronidazole	Down-regulation of genes involved in lipid biosynthesis (micro-array)
Low oxygen tension *M. bovis* and *M. tuberculosis* [88]	Cell diameter of anaerobically cultured cells significantly thinner than aerobic: *M. bovis* 255 vs 284 nm. *M. tb* 278 vs 338 nm			- *M. tuberculosis*, *M. bovis* – Markedly thickened (21.2 vs 16.1 nm) cell wall with rupturing and pealing after 6 months in anaerobic or micro-aerobic but not aerobic conditions. - No thickening in *M. smegmatis* – less than 1% of cells intact in 35 culture days.		Not reported
Long term anaerobic culture, *M. tuberculosis* [88]	No difference in cell length between anaerobic and aerobic cultures (1.14 vs 1.06 μm)			Thickened cell wall, dependent on anaerobiosis and not cell density. APP1 pigment produced, only significantly in anaerobic cultures		No qualitative difference in cell wall lipids
Plate based anaerobiosis *M. smegmatis* [89]					Sensitivity to MTZ in anaerobically grown cultures	Not reported
Oxygen depletion *M. smegmatis* [90]	Percentage of bacilli survival *M. smegmatis* CFU counting after 24 h exposure to the drug		Low level DNA and RNA synthesis		Anaerobic culture sensitive to MTZ but not OF	
Oxygen shift down *M. tuberculosis* [16]			DNA synthesis terminates with cell division but some low level RNA synthesis continues. Slight fall in ATP as cells enter stationary phase		Non-replicating persistent cells resistant to INH and CIP but not to MTZ	Not reported
						Nor reported

(*continued on next page*)

Table 1 (*continued*)

Principle of model and organism	Morphology of cells	Buoyant density	Metabolism	Microscopic observations	Viability challenges	Lipids in resultant cells
Wayne like oxygen depletion *M. tuberculosis* [91]			Specific glycine dehydrogenase activity increases sharply in NRP1 but declines in NRP2. Isocitrate lyase down-regulated in anaerobic cultures		Anaerobic cultures develop dose dependent Metronidazole susceptibility	
Culture in mHdeB* medium *M. smegmatis* [92]	Bacteria are Clumping and 2–3 times smaller		Low metabolism (rhodamine-123 staining) and negligible endogenous respiration			Not reported
Human granuloma *in vitro* model *M. tuberculosis* [93]					Significantly more cells resistant to rifampin after 8 days exposure to model	Loss of acid fastness and increase in Nile Red positive staining after 8 days of exposure to model

* Hartman's–de Bont medium.

3. Lipid body positive

Lipid bodies were first described in a range of bacteria among which was *M. tuberculosis* and other mycobacteria including *Mycobacterium leprae* where it was classified as "fatty material usually present but sometimes absent in common media [22,23]. These enigmatic bodies were little studied until the work of Garton and colleagues who showed that lipid bodies could be formed rapidly from uptake of fatty acids or from simple carbon sources in low-nitrogen conditions [24]. The lipid bodies contain poly-β-hydroxyalkanoates, tri-acylglycerides and wax esters [24]. Such lipid bodies are found more commonly as bacteria progress to stationary phase as illustrated in Figure 1. Lipid bodies are found more commonly in late stationary phase cultures of mycobacteria, which are known to be more resistant to drugs and the concentration of drug required to clear all bacteria (the MBC – minimum bactericidal concentration) rises significantly [25]. Older cells express lipid bodies [24,26,27] and it was assumed they are responsible for the phenotypic resistance found.

Lipid body positive bacteria have been found to predominate in human sputum and this was associated with transcriptional signatures similar to those found in non-replicating mycobacteria [9] The authors found that the lipid body count was highly correlated with time to positivity in diagnostic liquid cultures, which they concluded established a direct link between this cytological feature and the size of a potential non-replicating population. More recent work indicates that a range of growth-limiting stresses trigger a common signal transduction pathway slowing growth by redirecting carbon flux towards storage [7]. These data suggest that dormant bacteria survive chemotherapy both *in vitro* and in mice, and are metabolically active, although at a low level. Other studies show that there is a difference between number of organisms cultivated on solid medium and detected by use of MGIT [28]. In a study of sequential sputum samples from patients receiving standard chemotherapy between day 21 and 28 the change in the odds ratio of an unfavourable outcome for each percentage rise in percentage lipid body positive and the acid fast bacilli count was 1.21 (95% CI, .97–1.50; $P = .088$). Thus it appears that patients with a greater percentage of lipid body positive mycobacterial cells detected in their sputum smear at later time points are more likely to have an unfavourable outcome [29]. The importance of lipid body positive bacteria has been emphasised by an *in vitro* study that demonstrates lipid body positive cells can be purified from all mycobacterial cultures tested and are phenotypically resistant to antibiotics irrespective of whether they are derived from "old" or "young" cultures indicating that the presence of a lipid body is associated with phenotypic antibiotic resistance [30].

3.1. Hypoxia

To create an *in vitro* hypoxic model Wayne and colleagues uses a long term culture without agitation and oxygen excluded [16]. They demonstrated a fourfold increase in the isocitrate lyase activity and ten-fold increase in glycine dehydrogenase. In a later variant of the model where anaerobiosis was achieved sequentially, relative resistance to isoniazid rifampicin and ciprofloxacin was demonstrated [16] accompanied by a loss of glycine dehydrogenase activity. The Wayne model also includes an element of starvation (see below) through nutrient depletion [16]. The chaperonin alpha crystallin was found to be up-regulated in this model [31]and knockout of its gene led to an increased rate of growth in mice, suggesting that its function may be to slow growth in dormancy [32]. Many genes, including alpha crystallin alter their expression in response to hypoxia and are regulated by

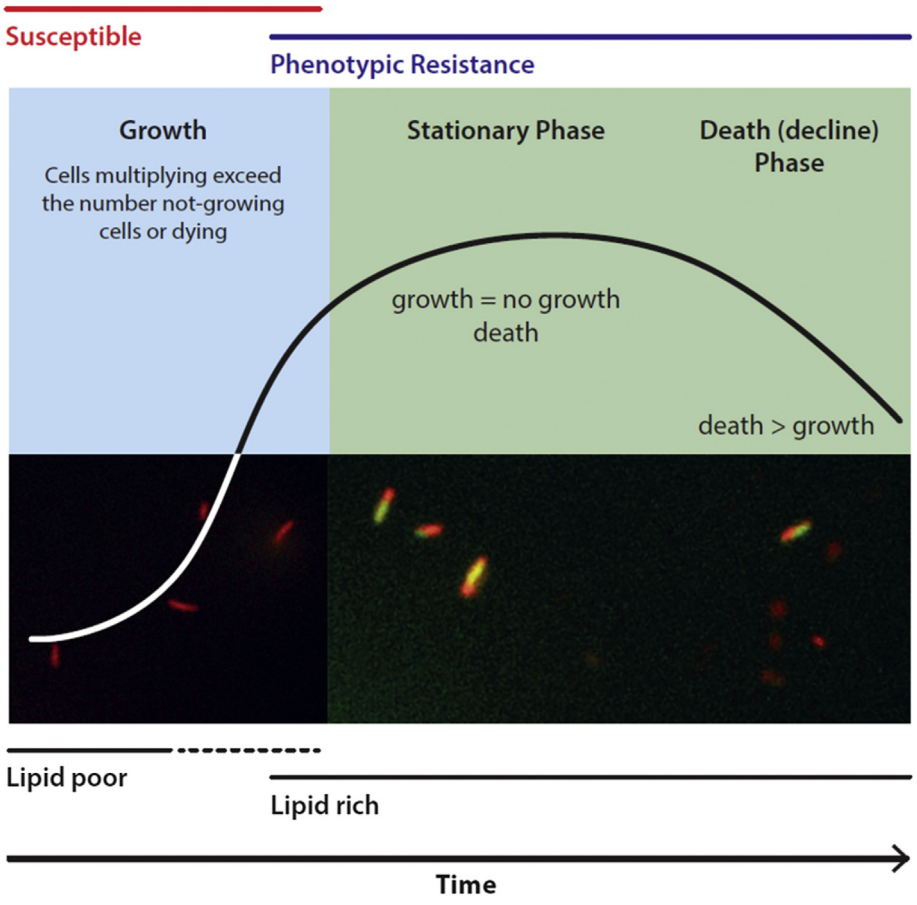

Figure 1. Mycobacterial cells stained with Nile Red and viewed by fluorescence microscopy at 100× (Leica DM5500) (excitation 480/40, 540/40. Emission 527/30, 645/75) showing lipid poor cells (red) and lipid rich cells (red with central green lipid body). This is set alongside a hypothetical mycobacterial growth curve and the change in the phenotypic susceptibility over time in a batch culture.

the DosR regulon. This two component regulator alters the expression of a series of genes in response to hypoxia and nitric oxide [33] and redox stress [34]. A total of 50 genes are up-regulated including tri-acylglyceride synthase [19,21]. Comparing cells in a Wayne model with SWATH mass spectrometry it was shown that the DosR regulon induced proteins make up 20% of hypoxic cells compared with 1% in exponentially growing cells. In comparison there was little change in ribosomal proteins. Many components of the electron transport chain and the energy generating machinery changed in abundance. Differential regulation of enzymes in the sub-networks of acetyl-CoA alanine/glutamate, and trehalose metabolism were found. Competing incorporation of acetyl-CoA either into TCA cycle or triacylglycerol biosynthesis was found consistently. Lipid pathways were significantly upregulated when absolute protein concentration and Vmax enzyme data were compared [35].

DosR is not an essential gene for survival in *M. tuberculosis* as knockout strains have only a modest decrease in viability in a hypoxic environment [36,37]. In a macaque model of infection, despite being able to replicate initially, animals infected with DosR regulon mutants failed to develop persistent infection or develop disease. This was associated with the appearance of a Th1 response and organization of hypoxic lesions where *M. tuberculosis* expressed *dosR* [38]. Interestingly, some Beijing lineage strains have been shown to express DosR constitutively as well as accumulating large quantities of lipid in lipid bodies [19]. A recent study where the DosR regulon was induced to wild type levels did not change *M. tuberculosis* replication kinetics and the authors concluded that DosR expression alone is insufficient to explain latency [39]. A recent hypothesis published by Orme suggests that the triggering of the DosR is an adaptation to these inimical conditions created by necrosis of tissue by host generated radicals. The necrotic centre created is hypoxic, but the dead neutrophils and other cells mean that the bacteria are not starved. His argument is that the DosR response readies the organism for transmission: survival as an extracellular state [40].

The importance of a hypoxia is supported by the accumulating evidence that anaerobic conditions are found in granulomas. A hypoxia marker EF5 demonstrated granulomas with necrotic centres in human tissue, which contrasts with mouse granulomatous lesions where hypoxia does not appear to occur [41]. Significantly it has been shown that metronidazole has no effect on the outcome from the Cornell model of tuberculosis treatment (see below) [42] whereas this drug has been shown to be bactericidal with dormant mycobacteria [43]. The probe pimonidazole (PIMO), which binds to thiol-containing peptides only at low partial pressures of oxygen, colocalised with areas of caseous necrosis in guinea pigs, rabbits, and cynomologous macaques [44, 45], but not with cellular granulomas in the standard mouse model [46]. However, metronidazole lacked activity in a murine hypoxic granuloma model and in guinea pigs [47,48].

In human lung tissue endothelial cells have been detected with an anti-CD31 immunohistochemistry probe in granulomas with necrotic centres; thought to represent mature lesions. These cells are not found in lesions without necrotic centres. This observation may support the idea that hypoxia is associated with granuloma maturity [41]. The importance of the nature of the animal model is confirmed by a study that compared the virulence of a strain of

M. tuberculosis with a *dosR–dosS* deletion mutant (*dosR–dosS* [*dosR-S*]), comparing it to complemented strain and wild-type H37Rv in rabbits, guinea pigs, and mice infected by the aerosol route as well as using a mouse hollow-fiber system. In the mouse and the guinea pig models, the *dosR-S* mutant exhibited a growth defect but did not replicate more than the wild type [49]. In another guinea pig model, bedaquiline failed to eradicate bacteria in residual primary lesion necrosis with incomplete dystrophic calcification that is hypoxic and morphologically similar to that described in human lung lesions. This suggests that this acellular rim may be a primary hypoxic location populated by bacilli phenotypically resistant to this drug [50].

These results contrast with those obtained when mycobacteria are exposed to a higher than atmospheric oxygen concentrations where there is increased multiplication by H37Ra and BCG strains [51].

3.2. Starvation

Loebel first demonstrated that starved cells had minimal evidence of respiration [9,15,52]. Gengenbacher also used the Loebel model and showed that depletion of oxygen killed starved bacilli but death was prevented by nitrate indicating that survival and respiration was possible in the presence of an alternative exogenous electron acceptor. Nutrient-starved bacilli lacking isocitrate lyase failed to reduce their intracellular ATP level and died, thus establishing a link between ATP control and intermediary metabolism. These data demonstrate a critical role for the glyoxylate shunt in survival in a nutrient limited environment [53].

Betts et al. developed this model further and demonstrated phenotypic resistance to rifampicin and isoniazid in starved cells that contrasted with full activity against exponentially growing cells. Importantly, metronidazole had no effect on starved bacteria [54] as would be expected as its mode of action depends on reducing conditions adding to the importance of recognising that not all dormant phenotypes are identical. Using this combined model they demonstrated differential up-regulation of proteins by micro-array [54,55]. They found evidence for slow-down of the transcription apparatus, energy metabolism, lipid biosynthesis and cell division in addition to induction of the stringent response and several other genes that may play a role in maintaining long-term survival within the host. Energy metabolism genes (15%), 16% of lipid metabolism genes 59% of the translation apparatus were down-regulated. Of the 12 *M. tuberculosis* sigma factors (*sigB*, *sigE*, *sigF* and *sigD*) four were up-regulated, but *sigA* expression did not change significantly. The majority of differentially expressed cell process genes belonged to the transport/binding protein subclass [54].

Another fermenter nutrient starvation model with controlled oxygen concentration, monitored nutrient depletion found up-regulation of genes in the glyoxylate shunt including isocitrate lyase, along with components of the TCA cycle. *SigB*, *sigE* and *sigH* were up-regulated and ATP synthase genes down-regulated. In contrast to the results obtained by Betts et al., *rpoA*, *B* and *rpoC* was up-regulated. All genes associated with the *mas* gene cluster were up-regulated throughout the period of stationary phase adaptation (*mas*, *fad*D26, *fad*D28, *mmp*L7, and *pps*A–E) and at day 75 there was a sharp rise in expression of *fad*D26. The enzyme Relmtb, which is required for survival of mycobacteria under long term *in vitro* starvation conditions was up-regulated by day 18 and then declined slowly [56].

Xie varied the PBS starvation model and added 16 different agents to cultures suspended only in PBS and incubated these for 6 weeks. Of these 16, only four (chlorpromazine, isoniazid, rifampin, trifluoperazine) were able to kill 99% of bacteria at concentrations less than 160 mg/L [57]. There was one log difference in rifampicin susceptibility between log phase and starved cells and this increased to 2 orders for isoniazid.

3.2.1. Nitrogen limitation

Anuchin and colleagues developed a nitrogen limitation model in which *M. tuberculosis* cells adopted an ovoid morphology that were more resistant to heat, hygromycin and doxycycline stresses compared to a 48 h culture [58]. In further studies, the authors found intra-species morphological heterogeneity of dormancy. They defined cyst-like, coccoid and poorly differentiated cells that all showed dormant-like properties and yet varied in their response to exogenous stress. Cyst-like cells were shown to contain electron transparent lipid bodies and were most resistant to heat stress and displayed the greatest difference (two orders of magnitude) between viable count measured by colony forming units (cfu) and most probably number methods (MPN).

3.2.2. Phosphate limitation

It has been hypothesised that *M. tuberculosis* encounter a phosphate limited environment in the macrophage and that its response mediated through pkk1 and RelA are important for establishing tolerance to antibiotics [59,60].

3.3. Acidification

M. tuberculosis is sensitive to low pH and survives in the phagolysosome by arresting acidification [61]. Pyrazinamide, a drug only active at low pH, can reduce treatment duration of tuberculosis chemotherapy from nine to six months, and it was postulated that this was due to its effect on cells in an acid environment [62]. When the pH was reduced, ovoid cells with thickened cell wall, a low metabolic activity and elevated resistance to antibiotics and heating developed and failed to form colonies on solid medium [17]. This phenomenon has been described in *M. tuberculosis* from sputum samples [9]. Acidification was also used as part of a multiple stress model in *M. tuberculosis* that included low oxygen (5%), high CO_2 (10%), low nutrient (10% Dubos medium) [20,63]. The cells stopped replicating, lost their acid-fastness, and had reduced susceptibility to isoniazid and rifampicin whilst accumulating triacylglycerols and wax esters (WE) and up-regulating putative neutral lipid biosynthetic genes [18,20,64].

3.4. Multiple stress

Since *M. tuberculosis* faces a range of stresses it is logical that a more pathophysiological model would be one with multiple stresses. Most models apply a single stress even though most impart additional unmeasured stresses on the culture (e.g. accumulation of metabolites, gradual acidification, nutrient depletion). Deb and colleagues created a 'multiple stress' model: low-nutrient (10% Dubos medium), acidic (pH 5.0), high CO_2 (10%) and low O_2 (5%) [20]. In these conditions the cells accumulated non-polar lipids as measured by TLC and [^{14}C]oelic acid incorporation, were resistant to isoniazid and rifampicin, lost acid fastness, increased Nile Red fluorescence and decreased in buoyant density. Genes involved in the glyoxylate cycle (*icl*, *gltA1*), carbon storage (*tgs*), stress response and hypoxia (*hspX*, *Rv2031c*, *dosR*) and anaerobic respiration (*frdA*, *narG/H/X*, *nirA*) were up-regulated. Genes coding for expression of ATP and NAD energy regeneration systems and the transcription/translation apparatus were down-regulated. The authors believe that this provides a model where cells display all of the proposed hallmarks of dormancy.

3.4.1. Stringent response

The stringent response, which utilizes hyperphosphorylated guanine [(p)ppGpp] as a signalling molecule, controls gene expression during starvation and is under the control of the RelA and SpoT proteins in other species and by Rel(Mtb) in *M. tuberculosis*. This response has been shown to be critical to establish persistent infection in mouse and guinea pig models of tuberculosis and is associated with shutdown of key metabolic pathways [65,66]. There is a link to differential antibiotic response as polyphosphate accumulation has been associated with tolerance to isoniazid in *M. tuberculosis* [67].

3.5. Resuscitation dependency

Bacterial cells with phenotypic similarities with dormant bacilli as measured by the presence of lipid bodies have been detected in human sputum specimens [9,27] and can be the dominant cell type making up to 99.9% of cells [12]. These cells may require the addition of a bacterial cytokine, resuscitation promotion factor (Rpf) to be detected by culture [9,68]. A study of smear-positive sputum samples from the UK and The Gambia revealed that up to 86% of those staining positively with Zhiel-Neelsen were also positive with Nile Red, a stain that preferentially binds lipid and showed these organisms had lipid bodies. The transcriptome of these cells is similar to slowly replicating or non-replicating mycobacteria. Since the lipid body count was correlated with time to positivity in diagnostic liquid cultures the authors concluded that the presence of lipid bodies was linked to the size of the non-replicating population [27]. It was notable that the characteristic of Rpf dependence was retained in long-term storage at 4 °C. There was a more rapid decline in the cfu count of non-Rpf dependent cells compared to the Rpf dependent count indicating that these latter cells are relatively resistant to rifampicin. This resuscitation index continued to increase among a small number of subjects who were monitored over an extended period. Direct treatment of sputum samples with rifampicin had less effect on Rpf cells supporting the idea that these cells were tolerant of this antibiotic at the low dose applied (1 mg/L) [9].

3.6. Antibiotic survival or persistence

The term “persistence” is often used to describe bacteria surviving after a period of treatment. The first description of rifampicin tolerant cultures in which no bacteria could be cultured but messenger RNA of specific *M. tuberculosis* genes could be detected and radioactive uracil was incorporated, was performed by Hu and colleagues [11]. These data suggest that dormant unculturable bacterial cells are metabolically active [69]. Further work led to the development of three separate models of antibiotic stress, namely 100 day microaerophilic cultures, pretreatment with rifampicin and the pulsed introduction of air [69–71]. These 100 day cultures contain 10–100 fold more unculturable cells which can be resuscitated with Rpf than culturable bacteria [11].

Clinical relapse was noted in the relapse of patients infected with resistant organisms in the first streptomycin trial [72] and it was McDermott who first suggested that the inability of drugs to kill all of the organisms was responsible for this phenomenon. It was recognised early that the organisms were not eliminated by treatment in the mouse model but could not be identified by any method that required their multiplication although small numbers of acid fast bacilli could be seen [73]. Following cortisol therapy or spontaneously the infection relapsed and mycobacteria became detectable again. It was in a subsequent paper that this group showed the importance of pyrazinamide in killing these “persisting” cells. A characteristic that the authors described as “sterilisation” [74]. These experiments were fundamental in developing what became known as the Cornell Model [75]. Further work with this model demonstrates that after the completion of chemotherapy, the tissues of the mice became “sterile”, no bacteria could be cultured from the tissues even in liquid cultures, yet messenger RNA of specific *M. tuberculosis* genes could be detected, suggesting that the bacteria, although dormant, were metabolically active [12]. The “sterile” phase of the Cornell model contains a high proportion of Rpf-dependent *M. tuberculosis* cells which can be killed by high but not low dose rifampicin [11]. A second “persistence” model is described where a relatively resistant mouse strain C57/BL6 is inoculated by the aerosol or parenteral route. The initial infection is controlled but the organism persists without causing overt disease [63].

Keren and colleagues have selected for antibiotic persister cells by treating an exponentially growing culture with cycloserine and performing an Afymetrix array. They found that 1408 genes were down regulated and 282 up-regulated with growth and energy related genes extensively down regulated. Of 65 Transcriptional activators listed in the *M. tuberculosis* genome 10 were overexpressed in persisters. One of these, Rv2866, is a *relE* homologue and was recently shown to increase drug tolerance when overexpressed in an *Escherichia coli* system. Key genes up-regulated included *sigF*, *dnaE2*, *acr2*, *lat* and *sigG*. They created a four-dimensional Venn diagram summarizing the differences and commonalities of four models: persisters, starvation, enduring hypoxic response (her), and non-replicating persistence. There are five genes that are common to all models and 55 genes that are common to persisters and at least 2 other models. Of special interest are the five genes that are overexpressed in all models. These genes are Rv0251c (acr2), encoding an alpha-crystallin, Rv1152, a transcriptional regulator of the gntR family, Rv2497c (pdhA), encoding a probable pyruvate dehydrogenase component, Rv2517c, encoding a hypothetical protein, and Rv3290c (lat), encoding an L-lysine-epsilon-aminotransferase [18,64].

3.6.1. Biofilm dormancy models

Ackart and colleagues showed that *M. tuberculosis* failed to form biofilms when cultured planktonically in the presence of Tween-80 and did not reach logarithmic phase growth and remained highly susceptible to antimicrobial drugs. In contrast when Tween is absent bacilli formed complex microbial communities attached to untreated well surfaces or to the extracellular matrix derived from lysed human leukocytes and tolerated drug treatment. This could be reversed by treatment of microbial communities with DNase I or Tween [76].

4. Implications of dormancy

4.1. Susceptibility

The importance of dormancy in *M. tuberculosis* is the repeated observation of phenotypic resistance to anti-tuberculosis agents although the degree is not fully delineated due to the different models of dormancy employed, the incomplete spectrum of agents tested and the diversity of susceptibility methods employed. Cell wall inhibitors are most affected but the action of the RNA polymerase inhibitor rifampicin and fluoroquinolones acting on DNA gyrase is also reduced [16]. This is not to say that testing susceptibility of “dormant” cells is easy since, *a priori*, they may not grow well on standard solid media making methodology problematic. In Table 2 we summarise the effect of different models on the susceptibility to antibiotics with the methods that were used.

Through *in vitro* dormancy models a range of susceptibility test are used (MIC, MBC and percentage of cell surviving after different exposure time using CFU or resazurin reduction). This results in

Table 2
Relative susceptibility of mycobacterial species to anti-tuberculosis agents in differing models of "dormancy".

Model	Methodologies	Susceptibilities				
	How was susceptibility measured?	Isoniazid	Rifampicin	Pyrazinamide	Ciprofloxacin	Metronidazole
Gradual acidification TB	MIC [92,94]	0.05 μg/mL	0.5 μg/mL	20 μg/mL		
Growth in modified potassium free medium	MIC [95]Plate counting methodology lowest viable number – TB	1.0 μg/mL	5.0 μg/mL			
Multiple-stress model TB	Cell survival after ≥96 h exposure to indicated levels of drug – CFU count [20]	0.8 μg/mL	5.0 μg/mL			12 μg/mL
Nutrient starvation TB	Cell survival after 168 h exposure to indicated levels of drug – CFU count [54]	10 μg/mL	10 μg/mL			
Low oxygen tension TB	MBC_{90} Wayne cidal concentration – the concentration of drug that reduced the CFU of the initial inoculum by 90% after 5 days exposure [96]	4.0 μg/mL				
Long term anaerobic culture TB	7, 14, 21 day exposures to drugs – CFU/MGIT (non-growth determined after negative for 100 days) [97]		8 μg/mL	100 μg/mL		8 μg/mL
Plate based anaerobiosis	*M. tuberculosis* number of viable cells determined by CFU on 7 h11 [98] *M. smegmatis* Solid media plating for CFU counting.	25 μM viable cell count is reduced by 50% compared to the control [98].				Wild type viable counts are reduced a 100 fold at 100 μg/mL [89].
Oxygen depletion	BCG Solid media plating for CFU counting [89,91].					BCG viable count are reduced a 1000 fold at 100 μg/mL and 3 fold at 10 μg/mL. There is a dose dependent effect using MTZ.
Oxygen shift down (Wayne model) TB	*M. tuberculosis* cells survival. Solid media plating for CFU counting.	0.4 μg/mL [16]	0.1 μg/mL [16]		1 μg/mL [16]	12 μg/mL in "non replicating stage 2" (Wayne & Hayes, 1996) 8 μg/mL (Wayne & Sramek, 1994)
Oxygen depletion	Percentage of bacilli survival *M. smegmatis* CFU counting after 24 h exposure to the drug [90]					120 μg/mL 20 ± 10 percent survival for persistent culture (240 h old sealed culture). 95 ± 9 percent survival for active culture (logarithmic aerobic culture).
Culture in mHdeB* medium	*M. smegmatis* percentage of resazurin (0 percent resazurin reduction) [99] Mtb h37rv MIC90 using resazurin microplate assay (REMA) [99]	10 μM	1 μM less than 0.19 μM MBC90: >100 μM		1 μM	
Human granuloma *in vitro* model [93]	*M. tb* MIC defined using Alamar blue reduction [76]	MIC: 1.25–2.5 μg/mL [76]	MIC: 0.47 –0.94 μg/mL [76]			

* Hartman's–de Bont medium.

different drug dose for the same species through different models. For example if we look at rifampicin in one species *M. tuberculosis*, in the Wayne model 0.1 μg/mL correspond to 4.2% of bacilli surviving after 192 h of drug exposure and for the *in vitro* granuloma model a MIC was found between 0.47 and 0.94 μg/mL, illustrating the difficulties in comparing susceptibility results from different models even if they are generating "dormancy" cells types. To some extent these observations have been clarified by the report that indicates that it is the presence of a lipid body irrespective of cell age that is associated with a significant increase in the minimal bactericidal concentration of any mycobacterial species suggesting that this is a phenomenon common to the genus [30].

5. Relationship to disease/pathology/treatment

A number of narratives have been created to link the concept of dormancy with clinical disease and chemotherapy.

5.1. Special populations hypothesis

The first "model" that attempted to this was the special populations hypothesis [62] based on clinical trial results with *in vitro* and mouse experiments. It has four cell "types": continuously growing cells, which isoniazid and rifampicin are said to act on, those in acid conditions, the target of pyrazinamide, intermittently metabolising cells against which rifampicin had its major activity and non-growing cells that are resistant to antibiotics [62]. This hypothesis has been influential in the design of clinical trials but there is limited direct bacterial or pathological evidence to support it.

5.2. Yin-yang hypothesis

Zhang and colleagues describe mixed growing and non-growing subpopulations that exist in a continuum of metabolic states.

Table 3
Summary of publications and their associated definitions of "dormancy".

Authors and reference	Definition
(Shleeva, Salina, & Kaprelyants, 2010) [100]	The dormant state is understood here as a *reversible* state of a bacterial cell, when the level of metabolic activity is decreased and the cell is able to survive for a long time without division
(Gengenbacher & Kaufmann, 2012) [53]	Non-replicating bacilli maintaining full viability at a very low metabolic rate; organisms show minor susceptibility or phenotypic drug resistance to antibiotics targeting functions required for growth.
(Voskuil, Visconti, & Schoolnik, 2004) [33]	Without replication or significant metabolism.
(Mariotti et al., 2013) [101]	Dormancy is defined as a stable but reversible non-replicating state of *Mycobacterium tuberculosis*.
(Kaprelyants, Gottschal, & Kell, 1993) [102]	A reversible state of low metabolic activity, in which cells can persist for extended periods without division.
(Karakousis et al., 2004) [103]	An altered physiologic state characterized by stationary-state colony-forming unit counts and decreased metabolic activity and greater susceptibility to rifampin than isoniazid.

Among the growing sub-population (yang), are a small non- or slow-growing population (yin). The evidence comes from batch culture growth curves and the authors describe that as bacteria enter stationary phase the yin increase and the yang decrease. This model, they postulate, explains why, after two months of treatment the persister cells revert to activity and can be killed by isoniazid and rifampicin and why isoniazid is effective in the treatment of latent disease [77]. This idea is supported by the observation that both lipid rich and lipid poor cells are found in cultures of all ages.

5.3. The scout hypothesis

Shleeva and colleagues created a three stage model that described the change in status from active growth, through a transition stage to "deep dormancy" [78] in which the cells were viable but not culturable. The authors postulate that cells can reverse the journey and become active again and contrast the results from the Wayne model where cells retain the ability to be cultured with their own model where cells do not grow on solid medium without the addition of Rpf or culture supernatant [16]. This apparent discrepancy is resolved by the description of a "Wayne zone" that arises because of the shorter time to achieve the state. They also describe a "Cornell zone" in which cells enter a non-culturable state that precedes cell death. These cells require external intervention before they can transition to the Wayne zone where resuscitation can occur if the correct conditions are encountered. Epstein built on this idea to postulate a dormant state from which microbial cells awake at random. The stochastic nature of this event could be precipitated by a change in a master regulatory gene. These newly activated cells become scouts that, if they survive in the environment go on to form new colonies and through quorum sensing link to the larger bacterial population [79]. Disease recurrence would occur when scouts encounter a favourable environment before the bacterial population is eradicated by the immune system or chemotherapy. Although this appears to be an anthropomorphic explanation of events, it remains a stochastic process because "scouts" are continually produced and reactivation only occurs when one survives to multiply and cause relapse. How dormancy might be linked with clinical models of latency is illustrated in Figure 2.

6. Disambiguation of dormancy

6.1. Latency

This term is an important concept in tuberculosis and the majority of those with primary infection are able to control the infection and may not show any clinical illness and some authors have suggested that latency and active disease are the extremes of a spectrum [80]. Epidemiological studies suggest that there is a 5–10% chance that the controlled, or latent infection will become patent to produce post primary disease. This is thought to be the most frequent route to pulmonary tuberculosis [81]. Our ability to study and manage the latent form of disease has been transformed by enhanced diagnostic methods depending on tuberculosis specific T cell response assays or Interferon gamma response assays (IGRAs) that are superior to tuberculosis skin tests [82].

The importance of latent infection in the natural history of tuberculosis has often led to a potentially false link with bacteriological considerations of dormancy. The assumption is that the mycobacterial cells in latent infection are dormant. Yet, there is little experimental evidence to support this hypothesis. Patients with latent infection can be treated successfully with isoniazid, a drug that inhibits cell wall synthesis. The observations of Rpf dependent cells that show reduced metabolic activity go some way to creating a bridge between the concepts of dormancy and latency [9,27]. PCR has detected *M. tuberculosis* in sections of adipose tissue samples from 39 subjects from Mexico and France who had died from causes other than TB. *M. tuberculosis* DNA could be detected fat tissue surrounding the kidneys, the stomach, the lymph nodes, the heart and the skin in 9/57 Mexican samples (6/19 individuals), and in 8/26 French samples (6/20 individuals) [83]. Other post mortem studies reported similar results [84]. A subsequent study identified viable bacilli in extrapulmonary sites, as evidenced by the detection of mycobacterial mRNA [85]. Further work is required using RNA based methods to confirm that activity level of bacterial cells in tissue. To avoid misunderstanding the authors believe that the term latency should only be used in relation to a clinical disease state and dormancy to the bacterial cell state.

7. A new nomenclature

Using the data set out in this review we propose that the term dormancy should only apply to bacterial cells and specifically those that are capable of regrowth: it should be a reversible phenomenon. Bacteria in a viable non-culturable state, for example, would have to be capable of resuscitation to qualify as "dormant" and to distinguish them from "dead".

Given the multiplicity and complexity of models described we propose here that a dormancy model should be sub-defined by additional terms. Thus, the Loebel model would be described as dormancy-starvation. Examples of how this approach could be notated are found in Text box 2 and applying this could do much to create clarity in this important area of mycobacterial research.

7.1. Future challenges and research

In this review we have described the range of models of "dormancy", yet, there are only a few reports of such cells from patient samples [9,27]. Further study of patient material is needed to understand the role of different dormancy phenotypes in human disease. This would test the relationship between *in vitro* and animal models and clinical disease. Descriptions of the cell state of *M. tuberculosis* in the tissues of patients with disease are handicapped by the absence of comprehensive specimen collections and methodologies to differentiate cells states reliably *in situ*. If we are to

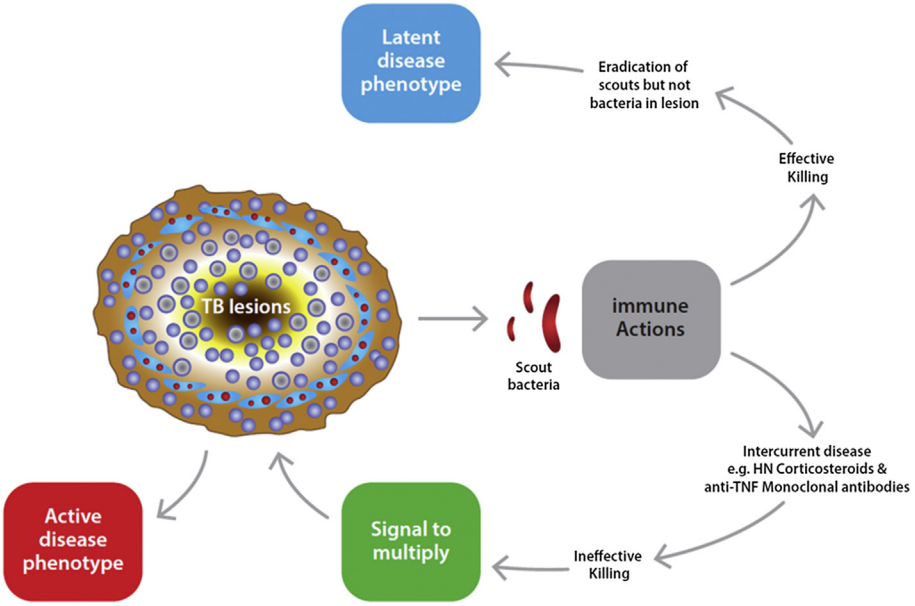

Figure 2. Illustration of how the "Scout" hypothesis might link to concepts of dormancy with dormant mycobacterial cells in the tuberculosis lesion "reactivating" and emerging. The fate of the lesion would depend on whether the re-activated or resuscitated scout to survive and give a signal.

understand the effect of these dormancy phenotypes on chemotherapy it is necessary to chart the number, occasion and cell state of *M. tuberculosis* in patients with disease, and to understand the rate that "dormant" cells transition to "active" states. The challenge for the future is to integrate these disparate models and data into a cohesive theory of pathology and its impact on the natural history of tuberculosis and the therapy of the disease. Dormancy researchers agree that the factors underpinning the phenomenon of dormancy are important, complex and nuanced. If we are to make progress we need to agree and use a consistent nomenclature. To support this approach we have proposed a candidate terminology for dormant TB, which should be updated regularly as new data become available. If we do not, progress will continue to stumble through mists of uncertain meaning.

Text box 2

Examples of nomenclature for different dormancy states and the application of the scheme to describe a cell or cells

A = Actively dividing cells
M = Multiplication rate high, medium, low, undetectable (h, m, l, u) qualified by medium used:
Growth medium S = solid, L = Liquid, A = animals (Mi = mice, R = rats, G = guinea-pigs, S = simian) e.g., $M^{u}S$
$Met^{h,m,l}$ = Metabolic rate high, medium, low. Addition of method used to detect growth could be: S35 = Methionine S35 uptake. U = Uridine Tritiated uptake. ATP = ATP production
Tol = Tolerant to antibiotics R = Rif, H = Isoniazid, E = ethambutol, Z = pyrazinamide
S = Sensitive to antibiotics R, H, E, Z
Rpf = Resuscitation Promoting Factor dependent
λ +/− = Lipid body present (+) or absent (−)

Thus, a cell or group of cells that was/were unculturable in solid and liquid but grow in mice, are tolerant of rifampicin, and resuscitated by the addition of Rpf would be represented by M^{u} $SLM^{h}MiAm$, TolR, Rpf.

Acknowledgements

The authors are grateful to members of the PreDiCT-TB consortium for their helpful comments on this manuscript.

Funding

This work was supported by the grant from the Innovative Medicines Initiative Joint Undertaking (www.imi.europa.eu) under grant agreement 115337.

Competing interests: None declared.

Ethical approval: Not required.

References

[1] Gillespie SH, Crook AM, McHugh TD, Mendel CM, Meredith SK, Murray SR, et al. Four-month moxifloxacin-based regimens for drug-sensitive tuberculosis. N Engl J Med 2014;371:1577–87. http://dx.doi.org/10.1056/NEJMoa1407426.

[2] Jindani A, Harrison TS, Nunn AJ, Phillips PPJ, Churchyard GJ, Charalambous S, et al. High-dose rifapentine with moxifloxacin for pulmonary tuberculosis. N Engl J Med 2014;371:1599–608. http://dx.doi.org/10.1056/NEJMoa1314210.

[3] Merle CS, Fielding K, Sow OB, Gninafon M, Lo MB, Mthiyane T, et al. A four-month gatifloxacin-containing regimen for treating tuberculosis. N Engl J Med 2014;371:1588–98. http://dx.doi.org/10.1056/NEJMoa1315817.

[4] Phillips PPJ, Mendel CM, Burger DA, Crook A, Nunn AJ, Dawson R, et al. Limited role of culture conversion for decision-making in individual patient care and for advancing novel regimens to confirmatory clinical trials. BMC Med 2016;14:19. http://dx.doi.org/10.1186/s12916-016-0565-y.

[5] Prideaux B, Via LE, Zimmerman MD, Eum S, Sarathy J, O'Brien P, et al. The association between sterilizing activity and drug distribution into tuberculosis lesions. Nat Med 2015. http://dx.doi.org/10.1038/nm.3937.

[6] Bigger J. Treatment of Staphylococcal infections with penicillin by intermittent sterilisation. Lancet nd;244:497–500.

[7] Baek S-H, Li AH, Sassetti CM. Metabolic regulation of mycobacterial growth and antibiotic sensitivity. PLoS Biol 2011;9. http://dx.doi.org/10.1371/journal.pbio.1001065. e1001065-5.

[8] Canetti G. The tubercle bacillus. 1955. New York.

[9] Mukamolova GV, Turapov O, Malkin J, Woltmann G, Barer MR. Resuscitation-promoting factors reveal an occult population of tubercle bacilli in sputum. Am J Respir Crit Care Med 2010;181:174–80. http://dx.doi.org/10.1164/rccm.200905-0661OC.

[10] Freeman R, Dunn J, Magee J, Barrett A. The enhancement of isolation of mycobacteria from a rapid liquid culture system by broth culture supernate of *Micrococcus luteus*. J Med Microbiol 2002;51:92–3.

[11] Hu Y, Liu A, Ortega-Muro F, Alameda-Martin L, Mitchison D, Coates A. High-dose rifampicin kills persisters, shortens treatment duration, and reduces relapse rate in vitro and in vivo. Front Microbiol 2015;6:641. http://dx.doi.org/10.3389/fmicb.2015.00641.

[12] Hu Y, Mangan JA, Dhillon J, Sole KM, Mitchison DA, Butcher PD, et al. Detection of mRNA transcripts and active transcription in persistent *Mycobacterium tuberculosis* induced by exposure to rifampin or pyrazinamide. J Bacteriol 2000;182:6358–65.

[13] Manina G, Dhar N, McKinney JD. Stress and host immunity amplify *Mycobacterium tuberculosis* phenotypic heterogeneity and induce nongrowing metabolically active forms. Cell Host Microbe 2015;17:32–46. http://dx.doi.org/10.1016/j.chom.2014.11.016.

[14] Shleeva M, Kondratieva T, Rubakova E, Vostroknutova G, Kaprelyants A, Apt A. Reactivation of dormant "non-culturable" *Mycobacterium tuberculosis* developed in vitro after injection in mice: both the dormancy depth and host genetics influence the outcome. Microb Pathog 2015;78:63–6. http://dx.doi.org/10.1016/j.micpath.2014.11.016.

[15] Loebel RO, Shorr E, Richardson HB. The influence of foodstuffs upon the respiratory metabolism and growth of human tubercle bacilli. J Bacteriol 1933;26:139–66.

[16] Wayne LG, Hayes LG. An in vitro model for sequential study of shiftdown of *Mycobacterium tuberculosis* through two stages of nonreplicating persistence. Infect Immun 1996;64:2062–9.

[17] Shleeva MO, Kudykina YK, Vostroknutova GN, Suzina NE, Mulyukin AL, Kaprelyants AS. Dormant ovoid cells of *Mycobacterium tuberculosis* are formed in response to gradual external acidification. Tuberculosis (Edinb) 2011;91:146–54. http://dx.doi.org/10.1016/j.tube.2010.12.006.

[18] Keren I, Minami S, Rubin E, Lewis K. Characterization and transcriptome analysis of *Mycobacterium tuberculosis* persisters. mBio 2011;2:e00100–11. http://dx.doi.org/10.1128/mBio.00100-11.

[19] Reed MB, Gagneux S, Deriemer K, Small PM, Barry CE. The W-Beijing lineage of *Mycobacterium tuberculosis* overproduces triglycerides and has the DosR dormancy regulon constitutively upregulated. J Bacteriol 2007;189:2583–9. http://dx.doi.org/10.1128/JB.01670-06.

[20] Deb C, Lee C-M, Dubey VS, Daniel J, Abomoelak B, Sirakova TD, et al. A novel in vitro multiple-stress dormancy model for *Mycobacterium tuberculosis* generates a lipid-loaded, drug-tolerant, dormant pathogen. PLoS ONE nd;4:15. http://dx.doi.org/10.1371/journal.pone.0006077.t003.

[21] Park H-D, Guinn KM, Harrell MI, Liao R, Voskuil MI, Tompa M, et al. Rv3133c/dosR is a transcription factor that mediates the hypoxic response of *Mycobacterium tuberculosis*. Mol Microbiol 2003;48:833–43.

[22] Burdon KL. Fatty material in bacteria and fungi revealed by staining dried, fixed slide preparations. J Bacteriol 1946;52:665–78.

[23] Burdon KL. Disparity in appearance of true Hansen's bacilli and cultured 'Leprosy bacilli' when stained for fat. J Bacteriol 1946;52:679–80.

[24] Garton NJ, Christensen H, Minnikin DE, Adegbola RA, Barer MR. Intracellular lipophilic inclusions of mycobacteria in vitro and in sputum. Microbiology (Reading, Engl) 2002;148:2951–8.

[25] Gomez JE, McKinney JD. *M. tuberculosis* persistence, latency, and drug tolerance. Tuberculosis (Edinb) 2004;84:29–44.

[26] D'Avila H, Melo RCN, Parreira GG, Werneck-Barroso E, Castro-Faria-Neto HC, Bozza PT. *Mycobacterium bovis* bacillus Calmette-Guérin induces TLR2-mediated formation of lipid bodies: intracellular domains for eicosanoid synthesis in vivo. J Immunol 2006;176:3087–97.

[27] Garton NJ, Waddell SJ, Sherratt AL, Lee S-M, Smith RJ, Senner C, et al. Cytological and transcript analyses reveal fat and lazy persister-like bacilli in tuberculous sputum. PLoS Med 2008;5:e75. http://dx.doi.org/10.1371/journal.pmed.0050075.st006.

[28] Bowness R, Boeree MJ, Aarnoutse R, Dawson R, Diacon A, Mangu C, et al. The relationship between *Mycobacterium tuberculosis* MGIT time to positivity and cfu in sputum samples demonstrates changing bacterial phenotypes potentially reflecting the impact of chemotherapy on critical sub-populations. J Antimicrob Chemother 2014. http://dx.doi.org/10.1093/jac/dku415. dku415.

[29] Sloan DJ, Mwandumba HC, Garton NJ, Khoo SH, Butterworth AE, Allain TJ, et al. Pharmacodynamic modeling of bacillary elimination rates and detection of bacterial lipid bodies in sputum to predict and understand outcomes in treatment of pulmonary tuberculosis. Clin Infect Dis 2015. http://dx.doi.org/10.1093/cid/civ195. civ195.

[30] Hammond RJH, Baron VO, Oravcova K, Lipworth S, Gillespie SH. Phenotypic resistance in mycobacteria: is it because I am old or fat that I resist you? J Antimicrob Chemother 2015;70:2823–7. http://dx.doi.org/10.1093/jac/dkv178.

[31] Hu Y, Coates AR. Transcription of the stationary-phase-associated hspX gene of *Mycobacterium tuberculosis* is inversely related to synthesis of the 16-kilodalton protein. J Bacteriol 1999;181:1380–7.

[32] Hu Y, Movahedzadeh F, Stoker NG, Coates ARM. Deletion of the *Mycobacterium tuberculosis* alpha-crystallin-like hspX gene causes increased bacterial growth in vivo. Infect Immun 2006;74:861–8. http://dx.doi.org/10.1128/IAI.74.2.861-868.2006.

[33] Voskuil MI, Visconti KC, Schoolnik GK. *Mycobacterium tuberculosis* gene expression during adaptation to stationary phase and low-oxygen dormancy. Tuberculosis (Edinb) 2004;84:218–27. http://dx.doi.org/10.1016/j.tube.2004.02.003.

[34] Kumar A, Toledo JC, Patel RP, Lancaster JR, Steyn AJC. *Mycobacterium tuberculosis* DosS is a redox sensor and DosT is a hypoxia sensor. Proc Natl Acad Sci U S A 2007;104:11568–73. http://dx.doi.org/10.1073/pnas.0705054104.

[35] Schubert OT, Ludwig C, Kogadeeva M, Zimmermann M, Rosenberger G, Gengenbacher M, et al. Absolute proteome composition and dynamics during dormancy and resuscitation of *Mycobacterium tuberculosis*. Cell Host Microbe 2015;18:96–108. http://dx.doi.org/10.1016/j.chom.2015.06.001.

[36] Rustad TR, Harrell MI, Liao R, Sherman DR. The enduring hypoxic response of *Mycobacterium tuberculosis*. PLoS ONE 2008;3:e1502. http://dx.doi.org/10.1371/journal.pone.0001502.

[37] Rustad TR, Sherrid AM, Minch KJ, Sherman DR. Hypoxia: a window into *Mycobacterium tuberculosis* latency. Cell Microbiol 2009;11:1151–9. http://dx.doi.org/10.1111/j.1462-5822.2009.01325.x.

[38] Mehra S, Foreman TW, Didier PJ, Ahsan MH, Hudock TA, Kissee R, et al. The DosR regulon modulates adaptive immunity and is essential for *Mycobacterium tuberculosis* persistence. Am J Respir Crit Care Med 2015;191:1185–96. http://dx.doi.org/10.1164/rccm.201408-1502OC.

[39] Minch K, Rustad T, Sherman DR. *Mycobacterium tuberculosis* growth following aerobic expression of the DosR regulon. PLoS ONE 2012;7:e35935. http://dx.doi.org/10.1371/journal.pone.0035935.

[40] Orme IM. A new unifying theory of the pathogenesis of tuberculosis. Tuberculosis (Edinb) 2014;94:8–14. http://dx.doi.org/10.1016/j.tube.2013.07.004.

[41] Tsai MC, Chakravarty S, Zhu G, Xu J, Tanaka K, Koch C, et al. Characterization of the tuberculous granuloma in murine and human lungs: cellular composition and relative tissue oxygen tension. Cell Microbiol 2006;8:218–32. http://dx.doi.org/10.1111/j.1462-5822.2005.00612.x.

[42] Dhillon J, Allen BW, Hu YM, Coates AR, Mitchison DA. Metronidazole has no antibacterial effect in Cornell model murine tuberculosis. Int J Tuberc Lung Dis 1998;2:736–42.

[43] Wayne LG, Sramek HA. Metronidazole is bactericidal to dormant cells of *Mycobacterium tuberculosis*. Antimicrob Agents Chemother 1994;38:2054–8.

[44] Garhyan J, Bhuyan S, Pulu I, Kalita D, Das B, Bhatnagar R. Preclinical and clinical evidence of *Mycobacterium tuberculosis* persistence in the hypoxic niche of bone marrow mesenchymal stem cells after therapy. Am J Pathol 2015;185:1924–34. http://dx.doi.org/10.1016/j.ajpath.2015.03.028.

[45] Via LE, Lin PL, Ray SM, Carrillo J, Allen SS, Eum SY, et al. Tuberculous granulomas are hypoxic in guinea pigs, rabbits, and nonhuman primates. Infect Immun 2008;76:2333–40. http://dx.doi.org/10.1128/IAI.01515-07.

[46] Aly S, Wagner K, Keller C, Malm S, Malzan A, Brandau S, et al. Oxygen status of lung granulomas in *Mycobacterium tuberculosis*-infected mice. J Pathol 2006;210:298–305. http://dx.doi.org/10.1002/path.2055.

[47] Klinkenberg LG, Sutherland LA, Bishai WR, Karakousis PC. Metronidazole lacks activity against *Mycobacterium tuberculosis* in an in vivo hypoxic granuloma model of latency. J Infect Dis 2008;198:275–83. http://dx.doi.org/10.1086/589515.

[48] Hoff DR, Caraway ML, Brooks EJ, Driver ER, Ryan GJ, Peloquin CA, et al. Metronidazole lacks antibacterial activity in guinea pigs infected with *Mycobacterium tuberculosis*. Antimicrob Agents Chemother 2008;52:4137–40. http://dx.doi.org/10.1128/AAC.00196-08.

[49] Converse PJ, Karakousis PC, Klinkenberg LG, Kesavan AK, Ly LH, Allen SS, et al. Role of the dosR–dosS two-component regulatory system in *Mycobacterium tuberculosis* virulence in three animal models. Infect Immun 2009;77:1230–7. http://dx.doi.org/10.1128/IAI.01117-08.

[50] Lenaerts AJ, Hoff D, Aly S, Ehlers S, Andries K, Cantarero L, et al. Location of persisting mycobacteria in a Guinea pig model of tuberculosis revealed by r207910. Antimicrob Agents Chemother 2007;51:3338–45. http://dx.doi.org/10.1128/AAC.00276-07.

[51] Sever JL, Youmans GP. The relation of oxygen tension to virulence of tubercle bacilli and to acquired resistance in tuberculosis. J Infect Dis 1957;101:193–202.

[52] Loebel RO, Shorr E, Richardson HB. The influence of adverse conditions upon the respiratory metabolism and growth of human tubercle bacilli. J Bacteriol 1933;26:167–200.

[53] Gengenbacher M, Kaufmann SHE. *Mycobacterium tuberculosis*: success through dormancy. FEMS Microbiol Rev 2012;36:514–32. http://dx.doi.org/10.1111/j.1574-6976.2012.00331.x.

[54] Betts JC, Lukey PT, Robb LC, McAdam RA, Duncan K. Evaluation of a nutrient starvation model of *Mycobacterium tuberculosis* persistence by gene and protein expression profiling. Mol Microbiol 2002;43:717–31.

[55] Betts JC, Dodson P, Quan S, Lewis AP, Thomas PJ, Duncan K, et al. Comparison of the proteome of *Mycobacterium tuberculosis* strain H37Rv with clinical isolate CDC 1551. Microbiology (Reading, Engl) 2000;146(Pt 12):3205–16.

[56] Hampshire T, Soneji S, Bacon J, James BW, Hinds J, Laing K, et al. Stationary phase gene expression of *Mycobacterium tuberculosis* following a progressive nutrient depletion: a model for persistent organisms? Tuberculosis (Edinb) 2004;84:228–38. http://dx.doi.org/10.1016/j.tube.2003.12.010.

[57] Xie Z, Siddiqi N, Rubin EJ. Differential antibiotic susceptibilities of starved *Mycobacterium tuberculosis* isolates. Antimicrob Agents Chemother 2005;49:4778–80. http://dx.doi.org/10.1128/AAC.49.11.4778-4780.2005.

[58] Anuchin AM, Mulyukin AL, Suzina NE, Duda VI, El-Registan GI, Kaprelyants AS. Dormant forms of *Mycobacterium smegmatis* with distinct morphology. Microbiology 2009;155:1071–9. http://dx.doi.org/10.1099/mic.0.023028-0.

[59] Rifat D, Bishai WR, Karakousis PC. Phosphate depletion: a novel trigger for *Mycobacterium tuberculosis* persistence. J Infect Dis 2009;200:1126–35. http://dx.doi.org/10.1086/605700.

[60] Rengarajan J, Bloom BR, Rubin EJ. Genome-wide requirements for *Mycobacterium tuberculosis* adaptation and survival in macrophages. Proc Natl Acad Sci U S A 2005;102:8327–32. http://dx.doi.org/10.1073/pnas.0503272102.

[61] Rohde KH, Veiga DFT, Caldwell S, Balázsi G, Russell DG. Linking the transcriptional profiles and the physiological states of *Mycobacterium tuberculosis* during an extended intracellular infection. PLoS Pathog 2012;8:e1002769. http://dx.doi.org/10.1371/journal.ppat.1002769.

[62] Mitchison DA. Basic mechanisms of chemotherapy. Chest 1979;76:771–81.

[63] Tufariello JM, Chan J, Flynn JL. Latent tuberculosis: mechanisms of host and bacillus that contribute to persistent infection. Lancet Infect Dis 2003;3:578–90.

[64] Keren I, Kaldalu N, Spoering A, Wang Y, Lewis K. Persister cells and tolerance to antimicrobials. FEMS Microbiol Lett 2004;230:13–8.

[65] Dahl JL, Kraus CN, Boshoff HIM, Doan B, Foley K, Avarbock D, et al. The role of RelMtb-mediated adaptation to stationary phase in long-term persistence of *Mycobacterium tuberculosis* in mice. Proc Natl Acad Sci U S A 2003;100:10026–31. http://dx.doi.org/10.1073/pnas.1631248100.

[66] Klinkenberg LG, Lee J-H, Bishai WR, Karakousis PC. The stringent response is required for full virulence of *Mycobacterium tuberculosis* in guinea pigs. J Infect Dis 2010;202:1397–404. http://dx.doi.org/10.1086/656524.

[67] Thayil SM, Morrison N, Schechter N, Rubin H, Karakousis PC. The role of the novel exopolyphosphatase MT0516 in *Mycobacterium tuberculosis* drug tolerance and persistence. PLoS ONE 2011;6:e28076. http://dx.doi.org/10.1371/journal.pone.0028076.

[68] Mukamolova GV, Kaprelyants AS, Young DI, Young M, Kell DB. A bacterial cytokine. Proc Natl Acad Sci U S A 1998;95:8916–21.

[69] Hu Y, Coates ARM, Mitchison DA. Comparison of the sterilising activities of the nitroimidazopyran PA-824 and moxifloxacin against persisting *Mycobacterium tuberculosis*. Int J Tuberc Lung Dis 2008;12:69–73.

[70] Hu Y, Coates AR, Mitchison DA. Sterilising action of pyrazinamide in models of dormant and rifampicin-tolerant *Mycobacterium tuberculosis*. Int J Tuberc Lung Dis 2006;10:317–22.

[71] Hu Y, Coates ARM, Mitchison DA. Sterilizing activities of fluoroquinolones against rifampin-tolerant populations of *Mycobacterium tuberculosis*. Antimicrob Agents Chemother 2003;47:653–7. http://dx.doi.org/10.1128/AAC.47.2.653-657.2003.

[72] Fox W, Sutherland I, Daniels M. A five-year assessment of patients in a controlled trial of streptomycin in pulmonary tuberculosis: report to the Tuberculosis Chemotherapy Trials Committee of the Medical Research Council. Q J Med 1954;23:347–66.

[73] Mccune RM, Feldmann FM, Lambert HP, Mcdermott W. Microbial persistence. I. The capacity of tubercle bacilli to survive sterilization in mouse tissues. J Exp Med 1966;123:445–68.

[74] Mccune RM, Feldmann FM, Mcdermott W. Microbial persistence. II. Characteristics of the sterile state of tubercle bacilli. J Exp Med 1966;123:469–86.

[75] Scanga CA, Mohan VP, Joseph H, Yu K, Chan J, Flynn JL. Reactivation of latent tuberculosis: variations on the Cornell murine model. Infect Immun 1999;67:4531–8.

[76] Ackart DF, Hascall-Dove L, Caceres SM, Kirk NM, Podell BK, Melander C, et al. Expression of antimicrobial drug tolerance by attached communities of *Mycobacterium tuberculosis*. Pathogens Dis 2014;70:359–69. http://dx.doi.org/10.1111/2049-632X.12144.

[77] Zhang Y, Yew WW, Barer MR. Targeting persisters for tuberculosis control. Antimicrob Agents Chemother 2012;56:2223–30. http://dx.doi.org/10.1128/AAC.06288-11.

[78] Shleeva MO, Bagramyan K, Telkov MV, Mukamolova GV, Young M, Kell DB, et al. Formation and resuscitation of "non-culturable" cells of *Rhodococcus rhodochrous* and *Mycobacterium tuberculosis* in prolonged stationary phase. Microbiology (Reading, Engl) 2002;148:1581–91.

[79] Epstein SS. Microbial awakenings. Nature 2009;457:1083. http://dx.doi.org/10.1038/4571083a.

[80] Barry CE, Boshoff HI, Dartois V, Dick T, Ehrt S, Flynn J, et al. The spectrum of latent tuberculosis: rethinking the biology and intervention strategies. Nat Rev Microbiol 2009;7:845–55. http://dx.doi.org/10.1038/nrmicro2236.

[81] Harries AD, Dye C. Tuberculosis. Ann Trop Med Parasitol 2006;100:415–31. http://dx.doi.org/10.1179/136485906X91477.

[82] Diel R, Loddenkemper R, Nienhaus A. Predictive value of interferon-γ release assays and tuberculin skin testing for progression from latent TB infection to disease state: a meta-analysis. Chest 2012;142:63–75. http://dx.doi.org/10.1378/chest.11-3157.

[83] Neyrolles O, Hernández-Pando R, Pietri-Rouxel F, Fornès P, Tailleux L, Barrios Payán JA, et al. Is adipose tissue a place for *Mycobacterium tuberculosis* persistence? PLoS ONE 2006;1:e43. http://dx.doi.org/10.1371/journal.pone.0000043.

[84] Hernandez-Pando R, Jeyanathan M, Mengistu G, Aguilar D, Orozco H, Harboe M, et al. Persistence of DNA from *Mycobacterium tuberculosis* in superficially normal lung tissue during latent infection. Lancet 2000;356:2133–8.

[85] Barrios-Payán J, Saqui-Salces M, Jeyanathan M, Alcántara-Vazquez A, Castañon-Arreola M, Rook G, et al. Extrapulmonary locations of *Mycobacterium tuberculosis* DNA during latent infection. J Infect Dis 2012;206:1194–205. http://dx.doi.org/10.1093/infdis/jis381.

[86] Kudykina YK, Shleeva MO, Artsabanov VY, Suzina NE, Kaprel'iants AS. Generation of dormant forms by *Mycobacterium smegmatis* in the poststationary phase during gradual acidification of the medium. Mikrobiologiia 2011;80:625–36.

[87] Salina EG, Zhogina YA, Shleeva MO, Sorokoumova GM, Selishcheva AA, Kaprelyants AS. Biochemical and morphological changes in dormant ("Nonculturable") *Mycobacterium smegmatis* cells. Biochemistry (Mosc) 2010;75:72–80.

[88] Cunningham AF, Ashton PR, Spreadbury CL, Lammas DA, Craddock R, Wharton CW, et al. Tubercle bacilli generate a novel cell wall-associated pigment after long-term anaerobic culture. FEMS Microbiol Lett 2004;235:191–8. http://dx.doi.org/10.1016/j.femsle.2004.04.036.

[89] Lim A, Dick T. Plate-based dormancy culture system for *Mycobacterium smegmatis* and isolation of metronidazole-resistant mutants. FEMS Microbiol Lett 2001;200:215–9.

[90] Dick T, Lee BH, Murugasu-Oei B. Oxygen depletion induced dormancy in *Mycobacterium smegmatis*. FEMS Microbiol Lett 1998;163:159–64.

[91] Lim A, Eleuterio M, Hutter B, Murugasu-Oei B, Dick T. Oxygen depletion-induced dormancy in *Mycobacterium bovis* BCG. J Bacteriol 1999;181:2252–6.

[92] Shleeva M, Mukamolova GV, Young M, Williams HD, Kaprelyants AS. Formation of "non-culturable" cells of *Mycobacterium smegmatis* in stationary phase in response to growth under suboptimal conditions and their Rpf-mediated resuscitation. Microbiology (Reading, Engl) 2004;150:1687–97. http://dx.doi.org/10.1099/mic.0.26893-0.

[93] Kapoor N, Pawar S, Sirakova TD, Deb C, Warren WL, Kolattukudy PE. Human granuloma in vitro model, for TB dormancy and resuscitation. PLoS ONE 2013;8:e53657. http://dx.doi.org/10.1371/journal.pone.0053657.

[94] Wayne LG, Lin KY. Glyoxylate metabolism and adaptation of *Mycobacterium tuberculosis* to survival under anaerobic conditions. Infect Immun 1982;37:1042–9.

[95] Salina EG, Waddell SJ, Hoffmann N, Rosenkrands I, Butcher PD, Kaprelyants AS. Potassium availability triggers *Mycobacterium tuberculosis* transition to, and resuscitation from, non-culturable (dormant) states. Open Biol 2014;4:140106. http://dx.doi.org/10.1098/rsob.140106.

[96] Daniel J, Deb C, Dubey VS, Sirakova TD, Abomoelak B, Morbidoni HR, et al. Induction of a novel class of diacylglycerol acyltransferases and triacylglycerol accumulation in *Mycobacterium tuberculosis* as it goes into a dormancy-like state in culture. J Bacteriol 2004;186:5017–30. http://dx.doi.org/10.1128/JB.186.15.5017-5030.2004.

[97] Filippini P, Iona E, Piccaro G, Peyron P, Neyrolles O, Fattorini L. Activity of drug combinations against dormant *Mycobacterium tuberculosis*. Antimicrob Agents Chemother 2010;54:2712–5. http://dx.doi.org/10.1128/AAC.01736-09.

[98] Mak PA, Rao SPS, Ping Tan M, Lin X, Chyba J, Tay J, et al. A high-throughput screen to identify inhibitors of ATP homeostasis in non-replicating *Mycobacterium tuberculosis*. ACS Chem Biol 2012;7:1190–7. http://dx.doi.org/10.1021/cb2004884.

[99] Bassett IM, Lun S, Bishai WR, Guo H, Kirman JR, Altaf M, et al. Detection of inhibitors of phenotypically drug-tolerant *Mycobacterium tuberculosis* using an in vitro bactericidal screen. J Microbiol 2013;51:651–8. http://dx.doi.org/10.1007/s12275-013-3099-4.

[100] Shleeva MO, Salina EG, Kaprelyants AS. Dormant forms of mycobacteria. Microbiology 2010;79:1–12. http://dx.doi.org/10.1134/S0026261710010017.

[101] Mariotti S, Pardini M, Gagliardi MC, Teloni R, Giannoni F, Fraziano M, et al. Dormant *Mycobacterium tuberculosis* fails to block phagosome maturation and shows unexpected capacity to stimulate specific human T lymphocytes. J Immunol 2013;191:274–82. http://dx.doi.org/10.4049/jimmunol.1202900.

[102] Kaprelyants AS, Gottschal JC, Kell DB. Dormancy in non-sporulating bacteria. FEMS Microbiol Rev 1993;10:271–85. http://dx.doi.org/10.1111/j.1574-6968.1993.tb05871.x.

[103] Karakousis PC, Yoshimatsu T, Lamichhane G, Woolwine SC, Nuermberger EL, Grosset J, Bishae WR. Dormancy phenotype displayed by extracellular *Mycobacterium tuberculosis* within artificial granulmoas in mice. J Exp Med 2004;200:647–57. http://dx.doi.org/10.1084/jem.20040646.

SCIENTIFIC REPORTS

OPEN

Label-free optical vibrational spectroscopy to detect the metabolic state of *M. tuberculosis* cells at the site of disease

Received: 27 February 2017
Accepted: 7 August 2017
Published online: 29 August 2017

Vincent O. Baron[1], Mingzhou Chen[2], Simon O. Clark[3], Ann Williams[3], Robert J. H. Hammond[1], Kishan Dholakia[2] & Stephen H. Gillespie[1]

Tuberculosis relapse is a barrier to shorter treatment. It is thought that lipid rich cells, phenotypically resistant to antibiotics, may play a major role. Most studies investigating relapse use sputum samples although tissue bacteria may play an important role. We developed a non-destructive, label-free technique combining wavelength modulated Raman (WMR) spectroscopy and fluorescence detection (Nile Red staining) to interrogate *Mycobacterium tuberculosis* cell state. This approach could differentiate single "dormant" (lipid rich, LR) and "non-dormant" (lipid poor, LP) cells with high sensitivity and specificity. We applied this to experimentally infected guinea pig lung sections and were able to distinguish both cell types showing that the LR phenotype dominates in infected tissue. Both *in-vitro* and *ex-vivo* spectra correlated well, showing for the first time that *Mycobacterium tuberculosis*, likely to be phenotypically resistant to antibiotics, are present in large numbers in tissue. This is an important step in understanding the pathology of relapse supporting the idea that they may be caused by *M. tuberculosis* cells with lipid inclusions.

Tuberculosis is now established as the most important cause of death due to infectious disease, yet treatment has not improved in fifty years. Relapse after successful treatment is the major barrier to shorter therapy for tuberculosis as has been confirmed by recent tuberculosis clinical trials where more bactericidal regimens have failed due to higher relapse rate[1–3]. Despite its importance, we know very little about the bacteriology of relapse even though this outcome is possible with patients who clear their sputum rapidly[4]. We need improved and non-destructive methods to study mycobacteria at the site of the disease.

It is often speculated that relapse is linked to bacteria that survive treatment. Several studies demonstrate the accumulation of lipids in intracellular bodies that are associated with a lower metabolic rate[5–8]. It has been shown recently that these lipid body positive cells are up to 40 times more resistant to key components of the treatment regimen such as isoniazid[9].

An attractive approach to investigate the lipid content of *Mycobacterium tuberculosis* would be to use an all-optical label-free method to examine bacterial cells in tissue in a way that would, for example, allow additional immunology studies. Optical interrogation can lead to inelastic scattering of light and distinct vibrational bands in subsequent spectra that can be used to distinguish the molecular content of the bacteria under investigation. In particular, Raman spectroscopy has been used previously as a means of identifying bacterial taxonomy at a single cell level in a range of species including mycobacteria[10,11]. These studies, however, have only previously been performed on isolated cultured cells[12] and isolated cells from sputum[13].

This letter reports, for the first time, the metabolic cell state of mycobacteria by exploring the lipid content of individual cells in tissue using wavelength modulated Raman (WMR) spectroscopy. WMR analysis uses a scan of the laser wavelengths, rather than a single wavelength, for Raman excitation combined with subsequent multivariate statistical analysis that removes all background fluorescence[14,15]. WMR spectroscopy shows an increase in

[1]School of Medicine, University of St Andrews, St Andrews, KY16 9TF, UK. [2]SUPA, School of Physics and Astronomy, University of St Andrews, KY16 9SS, St Andrews, UK. [3]Public Health England, Porton Down, Salisbury, Wiltshire, SP4 0JG, UK. Vincent O. Baron and Mingzhou Chen contributed equally to this work. Correspondence and requests for materials should be addressed to M.C. (email: mingzhou.chen@st-andrews.ac.uk) or S.H.G. (email: shg3@st-andrews.ac.uk)

signal-to-noise ratio compared to other methods including standard Raman spectroscopy[16]. Using this approach, we were able to detect LR *M. tuberculosis* cells in infected tissue with very high sensitivity and specificity. This is a major step towards understanding the pathogenesis of tuberculosis at the infection site and provides a paradigm for its application to a broad range of infectious diseases.

Results

Single cell discrimination between lipid rich and lipid poor bacteria. We separated mixed cultures of *M. smegmatis, M. bovis* (Bacillus Calmette-Guérin, BCG) and *M. tuberculosis* into lipid rich (LR) and lipid poor (LP) fractions with greater than 90% purity using our previously published method[9], and performed WMR spectroscopy on the separated cells.

We recorded Raman spectra from ~60 individual lipid rich (LR) and lipid poor (LP) mycobacteria cells (*M. smegmatis*, BCG and *M. tuberculosis*) *in-vitro*. The spectra from the mycobacterial species are illustrated in the Supplementary Section 1. In wavelength modulated Raman spectra (WMR spectra) zero-crossings are equivalent to peak positions in standard Raman spectra and the peak-to-valley corresponds to the peak intensity in standard Raman spectra. The two phenotypes mainly differ in two lipid peaks at 1300 cm^{-1} (designated lipid band A) and at 1440–1450 cm^{-1} (designated lipid band B), see Supplementary Fig. 1 (see Supplementary Section 4 for the peak assignment). LR cells showed higher Raman peak intensity in both lipid bands (A and B) compared to LP cells. The two phenotypes are distinguished with high specificity and sensitivity, *M. smegmatis* (93.8%/96.8%), *BCG* (100%/96.8%) and *M. tuberculosis* (92.6%/96.1%) (see Supplementary Fig. 1).

Identification of *M. tuberculosis* in unstained infected lung tissue sections. Having created a tool to determine the lipid status of mycobacterial cells non-destructively we applied the technique to unstained, formaldehyde-fixed guinea pig lung tissue infected by *M. tuberculosis* to understand the cell state of the bacteria at the site of disease (see Methods section for more details). Guinea pig tissue was used in the analyses because the lesions which develop during pulmonary tuberculosis in guinea pigs are histologically similar to the disease seen in humans[17]. In total, 107 single *M. tuberculosis* cells were interrogated by WMR spectroscopy from the lung alveoli (Figs 1c and 2b). An example of a single bacillus in an alveoli is shown in Fig. 1a. The tissue section is attached to a quartz coverslip. The background of the lung alveoli was compared to the signal from a clean quartz slide. The two signals were found very comparable and no significant signal is attributed to the lung alveoli itself (Fig. 1b). The Fig. 1c shows the average WMR spectrum of the bacteria acquired in the alveoli with the two background signals.

It was not possible to relate our *in-vitro* and *ex-vivo* data directly as it was noted that lipid bands A and B were impacted differently by formalin fixation and freezing[11,18] (Fig. 2a and b). In *M. tuberculosis* lipid band A, intensity is much lower when acquired in tissue as compared to *in-vitro*. In contrast, there is less variation in lipid band B intensity between *in-vitro* and *ex-vivo* samples. Lipid band B was therefore used in subsequent examinations (Fig. 2c). To compare *in-vitro* with *ex-vivo* data we needed to establish a ratio between a band that varies and one that varies very little. Moreover, when *in-vitro* data are compared (Fig. 2a) similar peak intensities are found in the band between 1050 cm^{-1} and 1070 cm^{-1} (see Supplementary Section 4, peak assignments) for both *M. tuberculosis* LR and LP phenotypes. This was also true for *M. tuberculosis* in *ex-vivo* samples. Thus, this band is ideal as an internal reference. We, therefore calculated the peak-to-peak ratio ($R_{\text{band B/Ref band}}$) between the maximum peak intensity of lipid band B and the maximum peak intensity in the internal reference band (1050 cm^{-1} and 1070 cm^{-1}) for each WMR spectrum acquired from *M. tuberculosis* in lung tissue (Fig. 2b) and also for each WMR spectrum acquired from *M. tuberculosis in-vitro* (Fig. 2a). A higher ratio indicates a higher lipid concentration in the cell.

Using this technique it is notable that the distribution of values for LR and LP cells *in-vitro* overlaps, but the peak of the distributions are clearly separated (Fig. 2c). We are able to observe a lipid ratio value $R_{\text{band B/Ref band}}$ analogous to both LP and LR among cells in tissue. The $R_{\text{band B/Ref band}}$ obtained from WMR spectra of cells in infected lung tissue shows a wide distribution confirming the presence of both LR and LP phenotypes. It is notable that the distribution of cell state in tissue is skewed towards LR phenotype (Fig. 2c). A similar result was obtained when ($R_{\text{band A/Ref band}}$), with band A adjusted for the losses associated with fixation and freezing was used (see Supplementary Section 3).

Identification of LR and LP single bacterium in the *M. tuberculosis* infected tissue. To ensure that the match between *in-vitro* and *ex-vivo* cells that we demonstrate is not an *in-vitro* artefact, we obtained an alternative measure of lipid cell state from tissue in parallel with WMR spectroscopy. To do this we used our previously published staining method[9]. As shown in Fig. 3, all LP cells appear only red caused by excitation from cell wall polar lipids. LR bacteria are red from polar cell wall lipids and are distinguished from LP by green fluorescence emission caused by the non-polar lipid body. We studied *in-vitro* stained cells and stained cells in guinea pig infected lung. Nile red staining does not impact significantly the WMR spectrum of bacteria as shown in Supplementary Section 6. We scored the Nile Red stained bacilli as either LR or LP as previously described and recorded the Raman spectrum from these defined cells (Fig. 4). This showed that, for both *in-vitro* cells and cells in tissue that the main source of variability is found in bands A and B. We also showed that *in-vitro* LR and LP cells could be discriminated by WMR spectroscopy (sensitivity (84.0%) and specificity (80.2%)) (Fig. 4a and b). LP cells cluster closely but LR are more dispersed. The presence of green fluorescence emission coming from intracellular lipid bodies correlates with higher Raman lipid peaks (in both lipid band A and B).

We then applied this method to *M. tuberculosis* cells (93 in total) in infected lung tissue sections. 56 cells were classified LR by Nile Red staining and 37 as LP (Fig. 3e–l). Using PCA LR and LP cells clustered together although there is a wider distribution for the LR cells as had been noted *in-vitro* (Fig. 4d). As in the case of our *in-vitro* data, green fluorescence correlates with higher lipid peaks in lipid bands A and B. A broader cluster in LR group

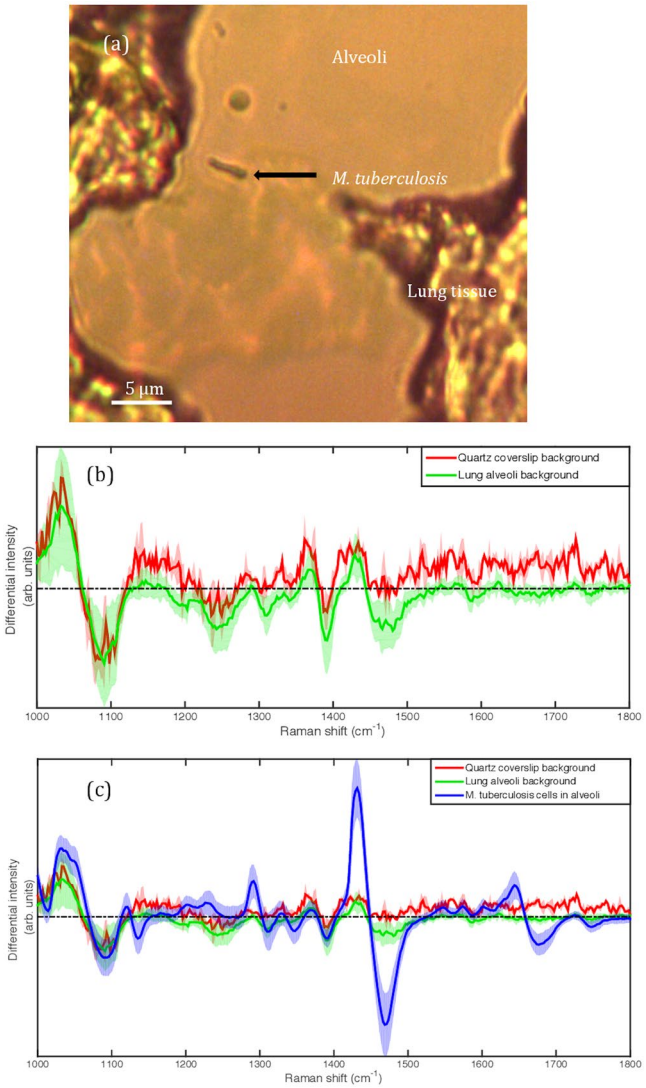

Figure 1. Investigation of the impact of the lung alveoli to the bacterial Raman spectrum. (**a**) shows an example of single bacillus in a lung alveoli interrogated by WMR spectroscopy. The scale bar corresponds to 5 µm. (**b**) presents the average Raman spectrum of the quartz slide surface (red line) and the average Raman spectrum of the lung alveoli (background)(green line). The tissue section like any other preparation interrogated with WMR spectroscopy is on a quartz coverslip. (**c**) the average spectrum of *M. tuberculosis* cells acquired in tissue are added (blue line) and compared with the lung alveoli and the quartz slide background. In both Fig. 1b and c the shaded coloured areas represent the standard deviation. In Fig. 1b and c the x-axis is in wavenumbers. The y-axis represents the differential intensity in arbitrary units.

observed in Fig. 4d also shows higher variability among the LR population than the LP population in tissue. Thus, it was possible to discriminate between LR and LP cells with high sensitivity (92.6%) and specificity (84.6%) (Fig. 4c and d). This is illustrated by combining the figures to demonstrate the overlap between the differing cell types *in-vitro* and *ex-vivo* which cluster together (Fig. 4e and f). Using this measure, we are able to demonstrate that *M. tuberculosis* cells in the lung are predominately LR (60%).

Discussion

Preventing relapse is the main reason for prolonged treatment in tuberculosis, yet the causes are still not fully understood[1,4]. In particular we have shown that some patients who become sputum culture negative rapidly still go on to relapse[4]. Our research provides a new tool to unravel this problem. This is the first time the label-free vibrational spectroscopy has been used to study the pathogenesis of tuberculosis *in situ*. Whilst Raman has been used previously to distinguish bacterial genus and species[10,11], our work makes a major leap forward giving us the ability to distinguish bacterial cell state at the site of disease. Reducing the Raman signal window size may affect the results slightly but does so within a small standard deviation of 0.044 in the obtained sensitivity and specificity (see in Supplementary Section 2 for more details). The possibility of this window reduction with a similar performance actually gives us a way to make our system more compact and to have higher resolution, i.e. using a grating

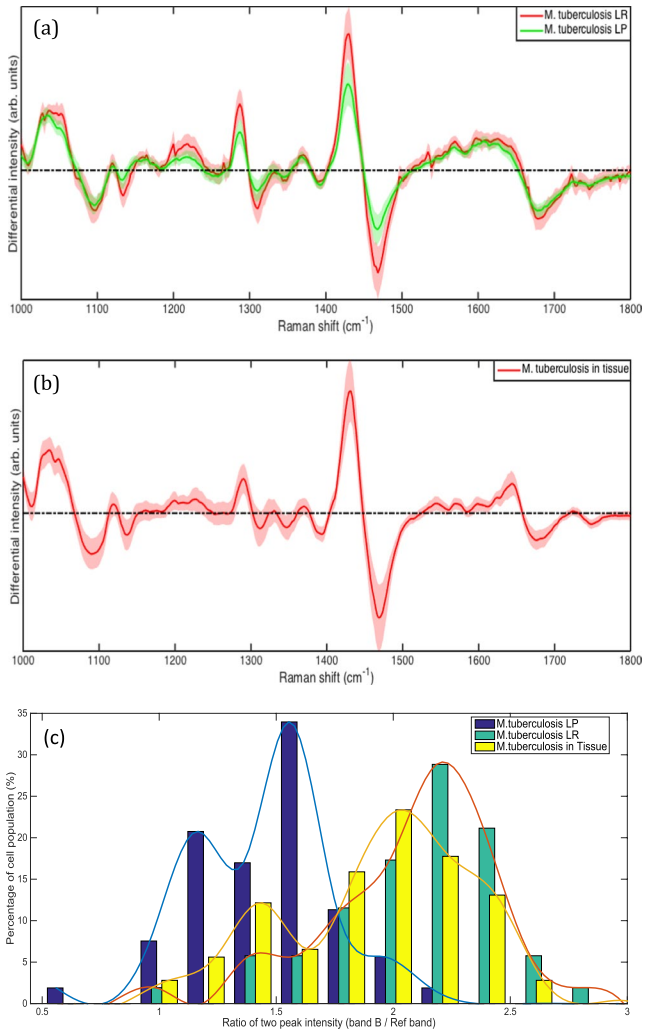

Figure 2. (**a**) WMR spectra of LR and LP *M. tuberculosis* cells. Mean spectra of both LR (red curves) and LP (green curves) cells are calculated from ~60 WMR spectra are taken from single bacteria cells. The shaded area represents one standard deviation. The x-coordinate corresponds to the Raman shift (in wavenumber, cm^{-1}) and the y-coordinate the differential Raman intensity in arbitrary units. (**b**) WMR spectra from *M. tuberculosis* cells in the infected lung tissue. The solid red line shows the mean WMR spectrum averaged over from all spectra of 107 cells taken at the single bacterium cell level. The colour-shaded area represents the associated single standard deviation. The acquisition time for each single bacterium was 150 seconds in total (see **Methods section** for more details). (**c**) Percentage of *M. tuberculosis in-vitro* LR, LP and form tissue with a given peak-to-peak ratio ($R_{band\ B/Ref\ band}$) calculated by dividing the lipid band B intensity value by an internal reference band (Ref band: 1050 cm^{-1} to 1070 cm^{-1}) peak intensity for each *in-vitro M. tuberculosis* WMR spectra (Fig. 2a) and each *M. tuberculosis* acquired in the lung tissue (Fig. 2b). The x-coordinate corresponds to $R_{band\ B/Ref\ band}$ between 0.5 and 3 and the y-coordinates represent the percentage of the bacterial population for each specific lipid ratio value. The blue, green and yellow bars correspond to the *in-vitro* LP, the *in-vitro* LR and the *ex-vivo* populations respectively. The lines in Fig. 2c are included to illustrate the shape of the distribution.

only over a range of 1400–1500 cm^{-1} and a shorter acquisition time. Future developments of our work therefore could lead to wide field video-rate acquisition *in-vivo* with non-linear vibrational spectroscopy approaches using suitable tuneable lasers for coherent anti-Stokes Raman scattering or stimulated Raman scattering[19,20]. This confirms that vibrational spectroscopy can be a powerful methodology that can be applied to pathogenesis and pharmacodynamics studies.

The study of the physiological status of *M. tuberculosis* bacteria has been limited to the sputum while may not fully represent the cells responsible for relapse. The physiological state of the bacteria that never get into the sputum are missed by such approaches[21]. Using WMRS we have been able to differentiate lipid rich from lipid poor mycobacteria in tissue and consequently our data bridges the gap between tissue and sputum. Importantly, current methods, for example Nile Red staining (see in Supplementary Section 5 for more details), require destructive techniques, which means that no additional studies can be performed[22]. The preparations that we have used could be re-examined with, for example, immunohistochemical methods to differentiate macrophage activation

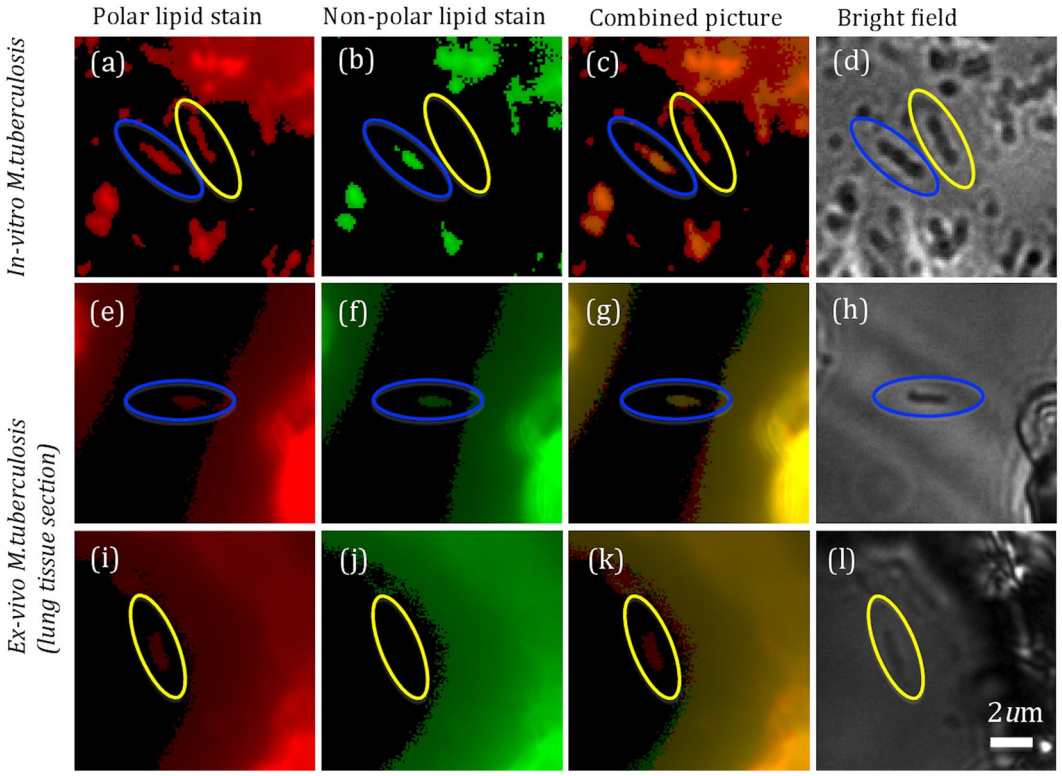

Figure 3. *M. tuberculosis in-vitro* and from frozen lung tissue section stained with Nile red and observed on the fluorescence-Raman combined system (more details in the method section). (**a–d**) show *in-vitro M. tuberculosis* and (**e–l**) show *M. tuberculosis* in lung tissue. (**a**,**e**,**i**) show the red fluorescence (polar lipids) and (**b**,**f**,**j**) show the green fluorescence emission (non-polar lipids). (**c**,**g**,**k**) represent the pseudo images made by combining red and green fluorescence emissions images. Bright field images (White light) are shown in (**d**,**h** and **l**). Both red and green fluorescence emissions can be observed in LR cells encircled in blue,while only red fluorescence emission is presented in LP cells encircled in yellow. The size of bacteria can be calculated from the scale bar shown in **l** (typically between 0.5–1 μm in width and 2–4 μm in length).

near to *M. tuberculosis* for which the metabolic state is now known. This opens up a wide range of new research possibilities that we will explore in future experiments.

The distinction between LR and LP is important as the LR phenotype has been associated with a reduced metabolic activity and down regulation of a series of enzymes[6]. More importantly, such LR cells have been shown to be phenotypically resistant to anti-tuberculosis antibiotics[7,23]. Antibiotic susceptibility testing of purified populations of LR and LP cells suggest that the resistance can increase from between 3–5 times (ciprofloxacin) to more than 20 times for isoniazid and rifampicin[9]. We have now shown that in tissue the majority of the cells that we examined had a LR phenotype that implies a significant degree of phenotypic resistance. Our confidence in this result is increased by the concordance of *in-vitro* and *ex-vivo* clustering as demonstrated in Fig. 4f; confirming as well that no significant signal from the lung is participating to the WMR spectra (Fig. 1). Thus, our observation may throw some light on the mismatch between standard anti-tuberculosis susceptibility testing and the outcome of treatment in patients and the overall result of clinical trials. Many patients relapse after apparently successful treatment and this is thought to be due to dormant bacteria able to survive treatment and regrow[4]. The presence of lipid bodies positive bacteria in TB infected patients' sputum has been linked to a higher risk of poor outcome[24]. However sputum data might not be representative of the bacterial population living in patient lungs. Our data derived from lung tissue supports the idea that relapses may be caused by LR *M. tuberculosis* with phenotypic resistance to the prescribed treatment. It should be noted, however, that we characterised bacteria in the alveoli and not in the complex structure within solid tissue. Future developments will enable us to achieve this. Thus, using Raman spectroscopy we have shown that lipid rich bacteria are present in the lung at the site of disease and are the predominant cell type (Figs 2c and 4c and d). This observation suggests that this characteristic may allow LR cells to survive antibiotic chemotherapy.

Methods

Bacterial culture conditions. *M. bovis* (BCG, NCTC 5692), *M. smegmatis* (NCTC 8159), *M. tuberculosis* (NCTC7416) were grown at 37 °C in Middlebrook 7H9 medium (Sigma-Aldrich) supplemented with 4 ml of 50% glycerol (for 450 ml) (Sigma-Aldrich) and 0.05% tween80 (Fisher BioReagents). BCG and *M. tuberculosis* culture medium were also supplemented with 1 vial of Middlebrook ADC enrichment (Sigma-Aldrich).

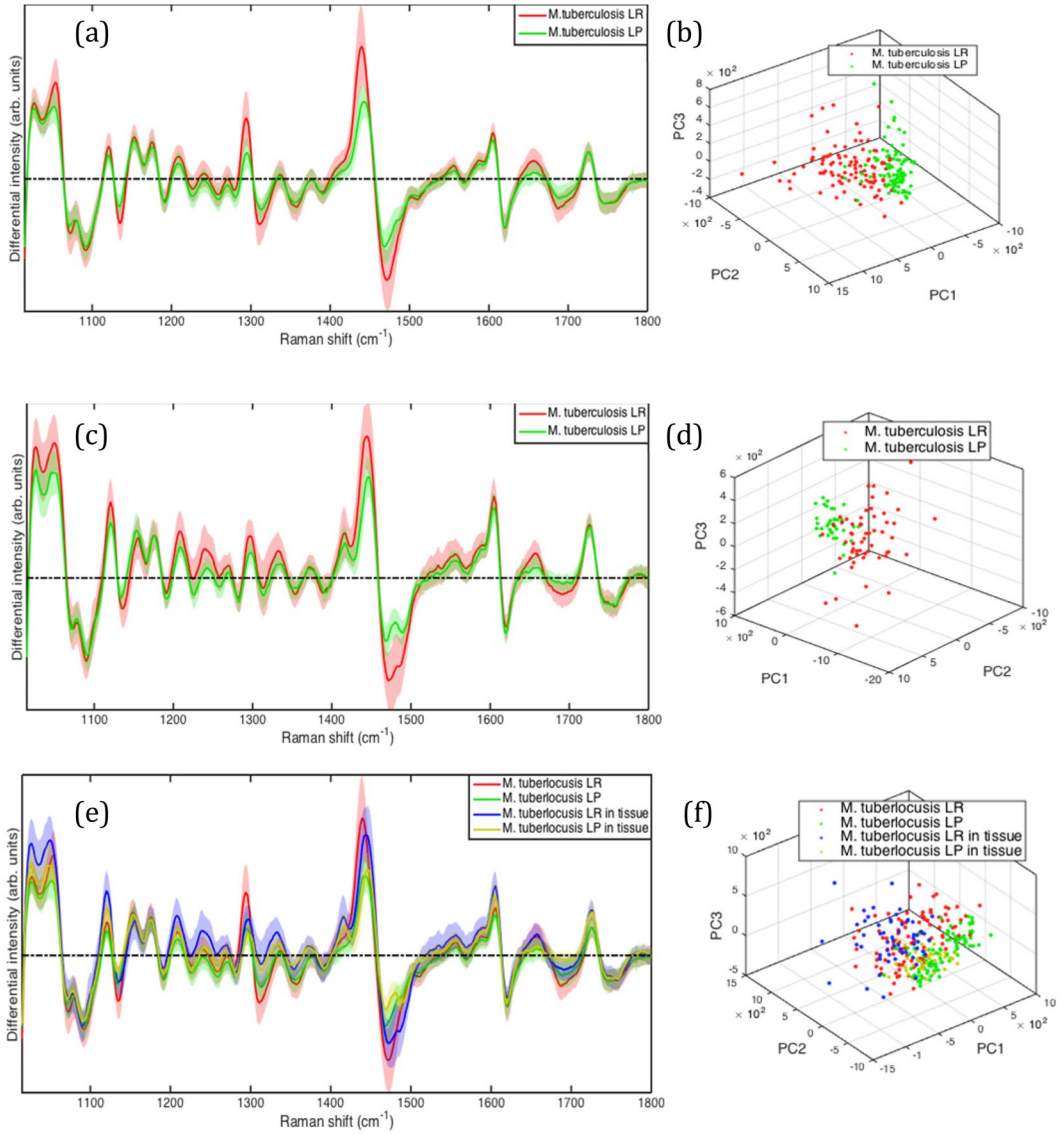

Figure 4. *M. tuberculosis in-vitro* and from infected lung tissue WMR spectra and PCA clusters. LR and LP bacteria are pre-assigned by fluorescence signals from Nile red stained bacteria. (**a**) Mean spectra of both LR (red curve) and LP (green curve) cells averaged over 100 WMR spectra taken *in-vitro*. The light coloured area represents the associated single standard deviation. The first three PCs for both LR and LP cells form two 3D clusters in (**b**). The LR cluster shows a broader cluster compared to LP group. (**c**,**d**) *M. tuberculosis* from lung tissue WMR spectra and PCA clusters. (**c**) Mean spectra of both LR (red curve) and LP (green curve) cells. The first three PCs for both LR and LP cells form two 3D clusters in (**d**). The LR cluster shows a broader cluster compared to LP group similarly than *in-vitro*. (**e**) Comparison of *in-vitro* and lung tissue *M. tuberculosis* LR and LP cells. *In-vitro* LR (red) and *in-vitro* LP (green) were compared to the *ex-vivo* LR (blue) and *ex-vivo* LP (yellow) bacilli acquired in infected lung tissue. (**e**) Mean spectra of both lipid rich and lipid poor cells acquired with WMR spectroscopy. (**f**) 3D clusters are plotted with the first three PCs for LR and LP *in-vitro* cells and the cells from infected tissue.

Animal infection. The lung sample analysed in these studies were from specific pathogen-free guinea pigs infected with an aerosol dose of 10–50 CFU (retained dose in the lung) of *M. tuberculosis* H37Rv (NCTC cat. no. 7416)[25]. Nose-only aerosol challenge was performed using a fully contained Henderson apparatus as previously described[26] and[27] in conjunction with the AeroMP (Biaera) control unit[28].

Guinea pig experimental work was conducted according to UK Home Office legislation for animal experimentation and was approved by the UK Home Office. All animals were weighed weekly and observed daily in order to monitor any adverse effects.

Four weeks post-challenge, animals were killed by an overdose of sodium pentobarbital. At necropsy, the lung was immediately excised and sections of the left and right cranial lobes and right caudal lobes were fixed in 10% neutral buffered formalin for up to 18 months.

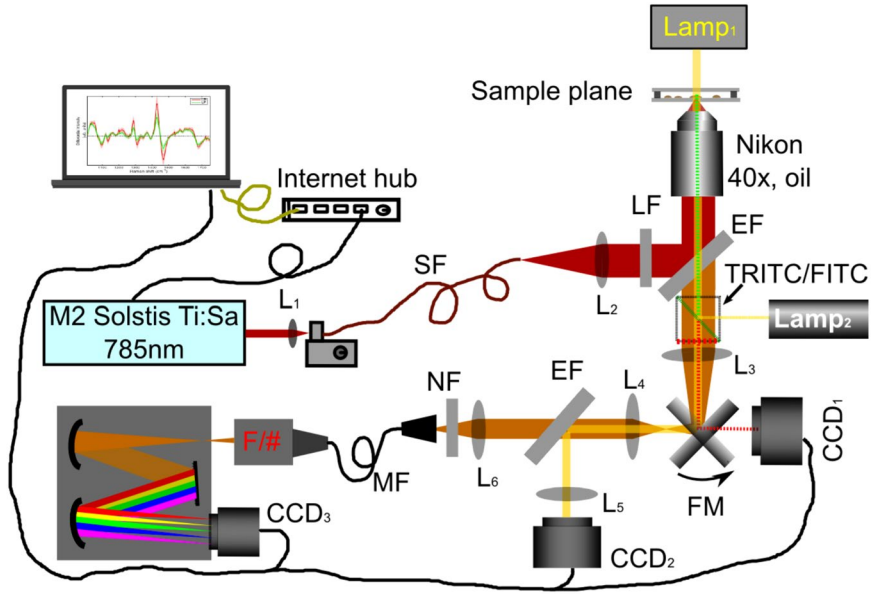

Figure 5. System setup for a combined Raman-fluorescence microscope**: SF**: single-mode fibre; **MF**: multi-mode fibre (200um core diameter); **LF**: Laser line filter (Semrock LL01-785); **EF**: Edge filter (Semrock LPD02-785RU); **NF**: Notch filter (Semrock NF03-785E); **TRITC/FITC**: Fluorescence Filter cubes (FITC: excitation 475–490 nm/emission 500–540 nm, TRITC: excitation 545–565 nm/emission 580–620 nm); **FM**: flip mirror; **CCD_1**: Hamamatsu ORCA_ER; **CCD_2**:Imaging Source USB camera (DFK 42AUC03); **CCD_3**:Andor Newton Camera (cooled to −70 °C); **L1~L6**: lenses; **F/#**: F number matcher.

Frozen section. Following fixation, the lung tissue was placed into OCT (optimal cutting temperature) solution (30% sucrose in PBS) to embed and freeze the tissue on dry ice. The fixed and frozen tissue was sectioned into 5 μm slices using a cryostat by Amsbio Ltd, UK (AMS Biotechnology (Europe) Limited/Registered office: 184 Park Drive, Milton Park, Abingdon OX14 4SE/Registered in England & Wales: Company number 2117791/ISO 9001:2008 registered firm). In this study three serial lung sections coming from one guinea pig were interrogated.

Nile Red staining of Bacterial culture. The bacteria were stained using a Nile Red stock solution at 250 μg/ml diluted in DMSO (Sigma-Aldrich) and a 1 μl aliquot added to 100 μl of bacterial suspension, vortexed and left for ten minutes in the dark at room temperature. The tubes were spun down at 20,000 g for 3 minutes the supernatant was discarded. The bacteria were washed twice using PBS. The bacterial pellet was resuspended in 20 μl of PBS and 10 μl heat fixed on a glass slide for light microscope or a quartz slide for Raman spectroscopy.

Nile Red staining of guinea pig lung tissue section. A 5 μm thick guinea pig frozen lung section mounted on quartz coverslip (SPI Supplies, 01015T-AB) was stained using 2 μl of Nile red diluted in PBS, 25 μg/ml final concentration. The 2 μl were placed on the tissue section and the coverslip was then placed on top of a thick quartz slide (SPI Supplies, 01016-AB). The mount was sealed as noted previously. The sample was then interrogated by WMR spectroscopy.

Combined Raman-fluorescence spectroscopy setup. WMR spectra were recorded by a combined confocal Raman-fluorescence imaging system based on a Nikon microscope (Nikon TE2000-E). A tunable Ti:Sa laser (M^2 SolsTis lasers, 1 W@785 nm) was focused by a microscope objective (Nikon Plano, 40x, oil) onto a single cell using the arrangement illustrated in Fig. 5. Excited Raman photons were then collected by a spectrometer formed with a monochromator (Andor Shamrock SR303i, 400 lines/mm grating @850 nm) and a cooled CCD camera (Andor Newton, CCD_3). With this configuration, the confocal diameter and depth of the system are 5 μm and 4.68 μm respectively. In order to obtain a sufficient Raman signal from a single cell, we apply a laser dosage of 150 mW at the sample plane. Over a long period of exposure time, this focused laser power didn't show any damage to the cells.

The system is able to switch from Raman spectroscopy to fluorescence imaging by placing FITC/TRITC cubes into the microscope and flipping the flip mirror (FM) to CCD_1 (Hamamatsu ORCA-ER). Fluorescence images were taken via standard Nikon fluorescence cubes (FITC and TRITC) using a Nikon fluorescence white light source ($Lamp_2$). Red fluorescence emission (580~620 nm) of Nile red stained samples excited by a green wavelength (545~565 nm) light shows the signals from the polar lipids whereas green fluorescence emission (500~540 nm) excited by a blue wavelength (475~490 nm) light shows the signals from the non-polar lipids (lipid bodies).

WMR spectra. In order to obtain the WMR spectrum from a single cell, five spectra were recorded continuously over 2.5 minutes with a 30 seconds integration time for each spectrum. During acquisition, the laser line was tuned continuously over a total modulation range of $\Delta\lambda = 1$ nm. A single WMR spectrum can be produced

from these five spectra with all background fluorescence being removed essentially. In the WMR spectrum, all Raman peaks will locate at the zero crossings while their peak intensity will be reflected by the peak-to-valley value around the zero crossing.

Raman calibration and spectra processing. Raman spectra were taken from polystyrene beads (1μm in diameter) as a control to calibrate the laser line and the drift in the system. The known Raman peak position (1001.4 cm^{-1}) of polystyrene bead was used for calculate the laser line. In this way, the drift in the laser line can be monitored during the whole data acquisition procedure. Suppose the drift is very slow (typically <0.2 nm over a day), we can calibrate the laser line used for each Raman spectrum from cells through an interpolation. Each Raman spectrum was also normalized by its total intensity (i.e. the integration over the area covered by the spectrum) in order to avoid any fluctuation in the laser power during wavelength modulation. The spectral region between 1000 cm^{-1} and 1800 cm^{-1} was used for the data analysis.

Principal component analysis (PCA). WMR spectra were collected from 60~100 cells from each cell phenotype. PCA was then applied to these training dataset in order to reduce the dimensionality. To distinguish between each two different cell phenotypes, the first seven principal components were taken into account, as they accounted for more than 70% of variances in these training dataset. This algorithm was written in Matlab codes.

Leave-one-out cross validation (LOOCV). The ability of distinguishing between each two different cell subsets was estimated by the method of leave-one-out cross validation. A multiple-dimensional space was defined by the principle components from the training dataset without one Raman spectrum. This leave-out spectrum was then classified in this space with the nearest neighbor algorithm. With this LOOCV method, correct or incorrect predictions for lipid rich and lipid poor cells in the training dataset were then used to estimate the specificity and sensitivity. Confusion matrix can also be estimated from correct and incorrect predictions for more than three cell subsets in the training dataset. This algorithm was written in Matlab codes.

Data Availability. Part of experimental datasets are available at http://dx.doi.org/10.17630/4be70c0f-7f62-45e5-9b94-a717c2b6e061.

References

1. Gillespie, S. H. *et al*. Four-month moxifloxacin-based regimens for drug-sensitive tuberculosis. *N. Engl. J. Med.* **371**, 1577–1587, doi:10.1056/Nejmoa1407426 (2014).
2. Merle, C. S. *et al*. A Four-month gatifloxacin-containing regimen for treating tuberculosis. *N. Engl. J. Med.* **371**, 1588–1598, doi:10.1056/NEJMoa1315817 (2014).
3. Jindani, A. *et al*. High-dose rifapentine with moxifloxacin for pulmonary tuberculosis. *N. Engl. J. Med.* **371**, 1599–1608, doi:10.1056/NEJMoa1314210 (2014).
4. Phillips, P. P. *et al*. Limited role of culture conversion for decision-making in individual patient care and for advancing novel regimens to confirmatory clinical trials. *BMC Med.* **14**, 19, doi:10.1186/s12916-016-0565-y (2016).
5. Daniel, J. *et al*. Induction of a novel class of diacylglycerol acyltransferases and triacylglycerol accumulation in *Mycobacterium tuberculosis* as it goes into a dormancy-like state in culture. *J. Bacteriol.* **186**, 5017–5030, doi:10.1128/Jb.186.15.5017-5030.2004 (2004).
6. Garton, N. J. *et al*. Cytological and transcript analyses reveal fat and lazy persister-like bacilli in tuberculous sputum. *PLoS Med.* **5**, e75, doi:10.1371/journal.pmed.0050075 (2008).
7. Deb, C. *et al*. A novel *in vitro* multiple-stress dormancy model for *Mycobacterium tuberculosis* generates a lipid-loaded, drug-tolerant, dormant pathogen. *PLoS One* **4**, e6077, doi:10.1371/journal.pone.0006077 (2009).
8. Baek, S. H., Li, A. H. & Sassetti, C. M. Metabolic regulation of mycobacterial growth and antibiotic sensitivity. *PLoS Biol.* **9**, e1001065, doi:10.1371/journal.pbio.1001065 (2011).
9. Hammond, R. J., Baron, V. O., Oravcova, K., Lipworth, S. & Gillespie, S. H. Phenotypic resistance in mycobacteria: is it because I am old or fat that I resist you? *J. Antimicrob. Chemother.* **70**, 2823–2827, doi:10.1093/jac/dkv178 (2015).
10. Maquelin, K. *et al*. Identification of medically relevant microorganisms by vibrational spectroscopy. *J. Microbiol. Methods* **51**, 255–271, doi:10.1016/S0167-7012(02)00127-6 (2002).
11. Buijtels, P. C. A. M. *et al*. Rapid identification of mycobacteria by Raman spectroscopy. *J. Clin. Microbiol.* **46**, 961–965, doi:10.1128/Jcm.01763-07 (2008).
12. Pahlow, S. *et al*. Isolation and identification of bacteria by means of Raman spectroscopy. *Adv. Drug Deliv. Rev.* **89**, 105–120, doi:10.1016/j.addr.2015.04.006 (2015).
13. Kloss, S. *et al*. Destruction-free procedure for the isolation of bacteria from sputum samples for Raman spectroscopic analysis. *Anal. Bioanal. Chem.* **407**, 8333–8341, doi:10.1007/s00216-015-8743-x (2015).
14. De Luca, A. C., Mazilu, M., Riches, A., Herrington, C. S. & Dholakia, K. Online fluorescence suppression in modulated Raman spectroscopy. *Anal. Chem.* **82**, 738–745, doi:10.1021/ac9026737 (2010).
15. Chen, M. *et al*. The use of wavelength modulated Raman spectroscopy in label-free identification of T lymphocyte subsets, natural killer cells and dendritic cells. *PLoS One* **10**, e0125158, doi:10.1371/journal.pone.0125158 (2015).
16. Mazilu, M., De Luca, A. C., Riches, A., Herrington, C. S. & Dholakia, K. Optimal algorithm for fluorescence suppression of modulated Raman spectroscopy. *Opt. Express* **18**, 11382–11395, doi:10.1364/OE.18.011382 (2010).
17. Clark, S., Hall, Y. & Williams, A. Animal models of tuberculosis: Guinea pigs. *Cold Spring Harb. Perspect. Med.* **5**, a018572, doi:10.1101/cshperspect.a018572 (2015).
18. Galli, R. *et al*. Effects of tissue fixation on coherent anti-Stokes Raman scattering images of brain. *J. Biomed. Opt.* **19**, 071402, doi:10.1117/1.JBO.19.7.071402 (2014).
19. Evans, C. L. *et al*. Chemical imaging of tissue *in vivo* with video-rate coherent anti-Stokes Raman scattering microscopy. *Proc. Natl. Acad. Sci. USA* **102**, 16807–16812, doi:10.1073/pnas.0508282102 (2005).
20. Saar, B. G. *et al*. Video-rate molecular imaging *in vivo* with stimulated Raman scattering. *Science* **330**, 1368–1370, doi:10.1126/science.1197236 (2010).
21. Mukamolova, G. V., Turapov, O., Malkin, J., Woltmann, G. & Barer, M. R. Resuscitation-promoting factors reveal an occult population of tubercle bacilli in sputum. *Am. J. Respir. Crit. Care Med.* **181**, 174–180, doi:10.1164/Rccm.200905-0661oc (2010).
22. Davies, A. P. *et al*. Resuscitation-promoting factors are expressed in Mycobacterium tuberculosis-infected human tissue. *Tuberculosis* **88**, 462–468, doi:10.1016/j.tube.2008.01.007 (2008).

23. Gomez, J. E. & McKinney, J. D. M. tuberculosis persistence, latency, and drug tolerance. *Tuberculosis* **84**, 29-44, doi:10.0.3.248/j.tube.2003.08.003 (2004).
24. Sloan, D. J. *et al*. Pharmacodynamic modeling of bacillary elimination rates and detection of bacterial lipid bodies in sputum to predict and understand outcomes in treatment of pulmonary tuberculosis. *Clin. Infect. Dis.* **61**, 1–8, doi:10.1093/cid/civ195 (2015).
25. James, B. W., Williams, A. & Marsh, P. D. The physiology and pathogenicity of Mycobacterium tuberculosis grown under controlled conditions in a defined medium. *J. Appl. Microbiol.* **88**, 669–677, doi:10.1046/J.1365-2672.2000.01020.X (2000).
26. Lever, M. S., Williams, A. & Bennett, A. M. Survival of mycobacterial species in aerosols generated from artificial saliva. *Lett. Appl. Microbiol.* **31**, 238–241, doi:10.1046/J.1365-2672.2000.00807.X (2000).
27. Clark, S. O., Hall, Y., Kelly, D. L. F., Hatch, G. J. & Williams, A. Survival of Mycobacterium tuberculosis during experimental aerosolization and implications for aerosol challenge models. *J. Appl. Microbiol.* **111**, 350–359, doi:10.1111/j.1365-2672.2011.05069.x (2011).
28. Hartings, J. M. & Roy, C. J. The automated bioaerosol exposure system: preclinical platform development and a respiratory dosimetry application with nonhuman primates. *J. Pharmacol. Toxicol. Methods* **49**, 39–55, doi:10.1016/j.vascn.2003.07.001 (2004).

Acknowledgements

This work was supported by the PreDiCT-TB consortium [IMI Joint undertaking grant agreement number 115337, resources of which are composed of financial contribution from the European Union's Seventh Framework Programme (FP7/2007–2013) and EFPIA companies' in kind contribution (www.imi.europa.eu)]. M.C. and K.D. thank the UK Engineering and Physical Sciences Research Council (Grant code EP/J01771X/1) and a European Union FAMOS project (FP7 ICT, 317744) for funding. K.D. acknowledges support from a Royal Society Leverhulme Trust Senior Fellowship and the loan of a laser from M Squared Lasers. This work was supported by the Department of Health, UK. The views expressed in this publication are those of the authors and not necessarily those of the Department of Health. We thank the staff of the Biological Investigations Group at PHE Porton for assistance in conducting the study and thank Dr. Peter Caie and Mrs In Hwa Um from School of Medicine in University of St Andrews for their help with the immunostaining.

Author Contributions

V.O.B. and M.C. contributed equally to this work. M.C. designed the optical system. V.O.B. prepared the samples. V.O.B. and M.C. performed the experiments and data analysis. V.O.B., M.C., K.D. and S.H.G. contributed to the development and planning of the project, interpretation and discussion of the data and the writing of the manuscript. S.O.C. and A.W. provided TB *in-vivo* modelling expertise and *in-vivo* samples and contributed to the writing of the manuscript. R.J.H.H. provided the mouse tissue infected with BCG and characterized the LP/LR cells using Nile red staining and helped with tissue sectioning and contributed to the writing of methods.

Additional Information

Supplementary information accompanies this paper at doi:10.1038/s41598-017-10234-z

Competing Interests: The authors declare that they have no competing interests.

Publisher's note: Springer Nature remains neutral with regard to jurisdictional claims in published maps and institutional affiliations.

Detecting Phenotypically Resistant *Mycobacterium tuberculosis* Using Wavelength-Modulated Raman Spectroscopy

Vincent O. Baron [1]✉

Email vb25@st-andrews.ac.uk

Mingzhou Chen [2]

Simon O. Clark [3]

Ann Williams [3]

Kishan Dholakia [2]

Stephen H. Gillespie [1]

[1] School of Medicine, University of St Andrews, St Andrews, UK

[2] SUPA, School of Physics and Astronomy, University of St Andrews, St Andrews, UK

[3] National Infectious Service, Public Health England, Salisbury, Wiltshire, UK

Abstract

Raman spectroscopy is a non-destructive and label-free technique. Wavelength-modulated Raman (WMR) spectroscopy was applied to investigate *Mycobacterium tuberculosis* cell state, lipid rich (LR) and lipid poor (LP). Compared to LP cells, LR cells can be up to 40 times more resistant to key antibiotic regimens. Using this methodology single lipid rich (LR) from lipid poor (LP) bacteria can be differentiated with both high sensitivity and specificity. It can also be used to investigate experimentally infected frozen tissue sections where both cell types can be differentiated. This methodology could be utilized to study the phenotype of mycobacterial cells in other tissues.

AQ1

Keywords

Raman spectroscopy
Mycobacteria
Phenotypic resistance
Lipids

1. Introduction

Tuberculosis is a major health issue worldwide and a major cause of death due to infectious disease. Treatment of tuberculosis has not improved in the past 50 years. Shortening therapy would make an

important step forward to reducing the global burden of tuberculosis. Recent clinical trials using more bactericidal regimens to shorten TB therapy to 4 months failed to do so due to higher relapse rate after successful treatment [1, 2, 3]. Those observations confirmed that relapse is the main barrier to shorter tuberculosis treatment. The bacteriology of relapse remains largely unknown and due to its importance represents a key research area in tuberculosis. Patients that clear *Mycobacterium tuberculosis* from their sputum rapidly during treatment can still undergo relapse [4]. In order to improve our knowledge of relapse and its bacteriology, we need nondestructive methods to study bacteria directly at the site of the disease. Relapse could be linked to bacteria that survive therapy, and several studies have shown that mycobacteria accumulate lipid in intracellular bodies and these cells exhibit a lower metabolic rate [5, 6, 7, 8]. Recently lipid body positive mycobacteria were shown to be much more resistant to key components of the tuberculosis therapy, up to 40 times more resistant to rifampicin [9]. Both phenotypes, lipid rich (LR) and lipid poor (LP), can be observed in any mycobacterial population in a range of species. To study the lipid content of *Mycobacterium tuberculosis,* we describe a novel method consisting of an all-optical label-free Raman spectroscopy based system that can be applied to bacteria directly in tissue.

Raman spectroscopy has been applied previously to discriminate cultured bacteria and mycobacteria species but never discriminate between two phenotypes or target mycobacteria in tissue [10, 11, 12]. We use wavelength modulated Raman (WMR) spectroscopy to improve both sensitivity and specificity. Rather than using a single excitation wavelength, WMR spectroscopy scans over a small range of the laser wavelengths. Combined with subsequent multivariate statistical analysis, all background fluorescence from biological samples can be removed. Importantly, WMR spectroscopy is a label-free technology and can be therefore combined with other techniques such as immunostaining.

2. Materials

2.1. In-Vitro Investigation

1. Test organism in this case: *Mycobacterium tuberculosis* (NCTC7416).
2. Growth medium: Middlebrook 7H9 medium (Sigma-Aldrich, UK).
3. Glycerol (Sigma-Aldrich, UK).
4. Tween 80 (Fisher BioReagents, UK).
5. Middlebrook ADC enrichment (Sigma-Aldrich, UK).
6. Bacterial culture tube.
7. Incubator set at 37 °C.
8. Phosphate-buffered saline (PBS)~~PBS~~.
9. Quartz coverslip (01015T-AB, SPI Supplies, PA, USA).
10. Quartz slide (01016-AB, SPI Supplies, PA, USA).
11. Transparent nail polish.

2.2. Tissue Investigation

1. Frozen infected tissue to investigate: in this example infected guinea pig (Specific pathogen-free Dunkin Hartley strain guinea pigs) lung sections.
2. Cryostat to produce 3–5 μm thick frozen tissue sections (*see* **Note 1**).
3. Formalin solution.
4. Sucrose.
5. PBS.
6. Quartz coverslip (01015T-AB, SPI Supplies, PA, USA).
7. Quartz slide (01016-AB, SPI Supplies, PA, USA).
8. Transparent nail polish.

2.3. Raman System

An example of the Raman system design is presented in Fig. 1.

1. Tunable laser that can generate light at 785 nm (*see* **Note 2**).
2. Microscope objective (Nikon, 50×, oil immersion).
3. Spectrometer: formed with a monochromator (Andor Shamrock SR303i, 400 lines/mm grating at 850 nm) and a cooled CCD camera (Newton 920, Andor Technology, UK).
4. A computer linked to the Ramen system and connected to the Internet.
5. Software list: Matlab, Andor Solis.

Fig. 1

Schematic diagram of the ~~first~~ experimental setup. The system is using a tunable Ti:Sapphire laser (Spectra-Physics 3900 s, 785 nm, 1 W) pumped by a green laser (Verdi V6, 532 nm, 5 W). L_1, L_2, and L_3 are lens. LF denotes line filter. EF denotes edge filter and NF denotes notch filter. The laser is focused on the sample using a microscope objective (Nikon, 50×, oil). The spectrometer is composed of a monochromator (Andor Shamrock SR303i, 400 lines/mm grating at 850 nm) and a cooled CCD camera (Andor Newton).

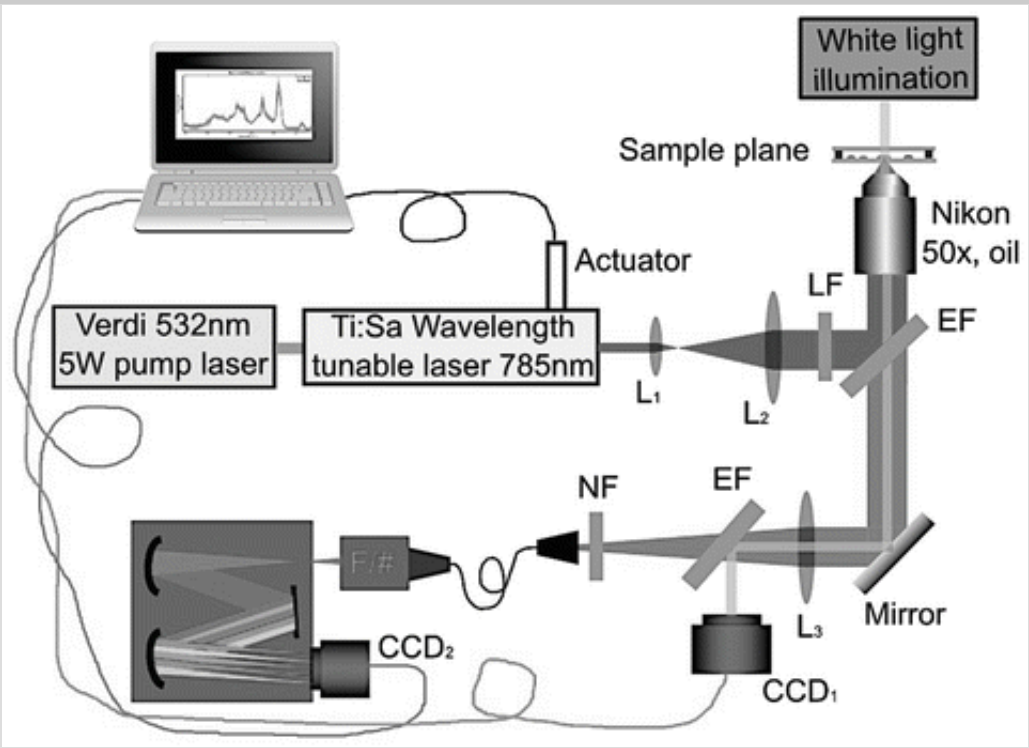

List of optics:

6. **LF**: Laser line filter (LL01-785, Semrock, USA).
7. **EF**: Edge filter (LPD02-785RU, Semrock, USA).
8. **NF**: Notch filter (NF03-785E, Semrock, USA).
9. **FM**: flip mirror.
10. **CCD_1**: Imaging Source USB camera (DFK 42AUC03, Imaging Source, Germany).
11. **CCD_2**: Andor Newton Camera (cooled at −70 °C).
12. **L1–L36**: lenses; **F/#**: F number matcher.

3. Methods

3.1. Bacteria from Culture

3.1.1. Culture

Perform all steps before the heat killing of bacilli in a level 3 laboratory facility (or equivalent). Grow *M. tuberculosis* (NCTC7416) at 37 °C in Middlebrook 7H9 medium supplemented with 0.05% (v/v) tween 80 and 24 mL of ~~50%~~ glycerol (for 450 mL of medium). Add one vial of Middlebrook ADC supplement (M0678, FLUKA) to the 450 mL.

3.1.2. Heat Killing of Bacilli

Harvest 1 mL of *M. tuberculosis* culture and place it at 80 °C for 20 min to heat inactivate the bacteria. Take the inactivated bacteria out of the Cat3 facility (*see* **Note 3**).

3.1.3. Wash

Take 100 μL of bacterial suspension and spin it at 20,000 × *g* for 3 min at room temperature. Discard the supernatant. Wash the cells twice with 100 μL of PBS.

3.1.4. Raman Slide Preparation from In-Vitro Cell

Resuspend the bacteria in 20 μL of PBS, take 10 μL out and heat fix onto a quartz coverslip (SPI Supplies). Mount the fixed bacteria that are on the coverslip, on top of a quartz slide (SPI Supplies). The cells end up between the quartz slides and coverslip. Seal mount using a transparent nail polish (leave to air-dry for an hour before use). Interrogate the sample with WMR spectroscopy.

3.2. Tissue Sample Preparation

3.2.1. Tissue Sectioning

AQ2

Treat the tissue to investigate with 10% neutral buffered formalin for an appropriate amount of time if it is infected with *M. tuberculosis* (or another pathogen). Remove the tissue from the formalin solution and freeze the tissue sample on a bed of dry ice in OCT (optimal cutting temperature) solution (30% sucrose in PBS) for future Raman investigation. From the OCT block cut 3–5 μm sections using a cryostat. Place the tissue section on the quartz coverslip.

3.2.2. Tissue Section Mounting

Mount the frozen tissue section that is on the quartz coverslip (SPI Supplies, 01015T-AB), directly on top of a quartz slide (SPI Supplies, 01016-AB). Seal the mount with transparent nail polish (leave to air-dry for an hour before use). Interrogate the tissue sample with WMR spectroscopy. An example of single *M. tuberculosis* bacillus in guinea pig lung tissue section observed under the Raman system is shown in Fig. 2 (*see* **Note 4**).

Fig. 2

M. tuberculosis in infected guinea pig lung tissue section observed under the Raman system (bright field). A single bacillus can be observed (black arrow) in alveoli. The scale bar represents 5 μm

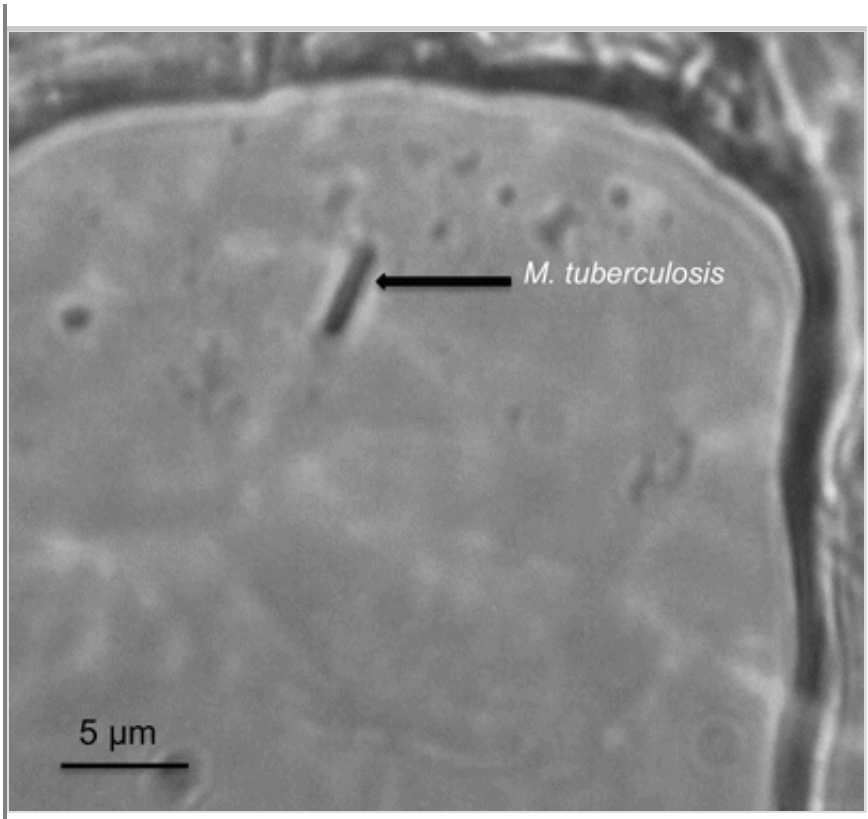

3.3. Raman Microscopy Methods

3.3.1. Raman System

Use your Raman system to acquire the spectra, an example of a confocal Raman system shown in Fig. 1. This system uses a green laser (Verdi V6, 532 nm, 5 W) to pump a tunable Ti:Sapphire laser (Spectra-Physics 3900 s, 785 nm, 1 W). To focus the laser on the bacteria use an oil immersion objective a Nikon, 50×, oil for example. A spectrometer with a monochromator (Andor Shamrock SR303i, 400 lines/mm grating at 850 nm) with a cooled CCD camera (Andor Newton) is used to collect the Raman photons. Determine the laser power to use according to the sample type being investigated (*see* **Note 5**).

3.3.2. Acquisition

3.3.2.1. Standard Raman Spectra

Use for each single bacteria a 30 s integration time with a stable excitation laser wavelength at 784.6 nm. Record a separate background Raman spectrum with the same condition from a (bacteria-free position) position near the bacteria. Use it to subtract the background signals afterward. Determine the integration time you need to obtain an optimal signal-to-noise ratio; this could vary depending on your system, the organism under investigation and the power on the sample plane (*see* **Note 6**).

3.3.2.2. WMR Spectra

Record five spectra continuously, with 30 s of integration each, while the laser is tuning over a small range of 1 nm. From these five original spectra calculate a single WMR spectrum with the autofluorescence background removed. Compare to the standard Raman spectrum; all Raman peaks will locate at the zero crossings while their peak intensity corresponds to the peak-to-valley value (*see* **Note 7**).

3.3.3. Raman Calibration and Spectra Processing

Use control Raman spectra from polystyrene beads (1 μm in diameter) to monitor any possible drift in the laser wavelength or the optical system. Acquire the Raman spectra of the polystyrene beads with the same integration time as the experimental conditions.

The laser wavelength may vary during the experiments. We use a standard chemical, polystyrene, to monitor this variation. As the known largest peak position of polystyrene is at 1001.4 cm^{-1}, the actual laser wavelength can be calculated (*see* **Note 8**).

If the drift in laser wavelength is very small (typically <0.2 nm over a day) and slow, the actual laser line used to acquire each Raman spectrum can be calculated using an interpolation.

To avoid any influence from laser power fluctuation during wavelength tuning, normalize each Raman spectrum by its total intensity (i.e., the integration over the area covered by the spectrum). To compare your data sets and do the data processing use mainly the fingerprint region from 1000 cm^{-1} to 1800 cm^{-1} (*see* **Note 9**).

After Raman investigation, the tissue sample can be used for another method (*see* **Note 10**).

3.3.4. Principal Component Analysis

To distinguish between two different cell phenotypes or species, apply principal component analysis (PCA) to each training dataset containing standard Raman spectra or WMR spectra. Use approximately 60–80 cells for each phenotype or specie.

Use a number of principal components (PCs) that corresponds to more than 70% of variances in the training dataset. In this example, the first seven principal components (PCs) have been used (*see* **Note 11**).

3.3.5. Leave-One-Out Cross Validation

Use the method of leave-one-out cross validation (LOOCV) to estimate the ability of classification for the different cell phenotypes or species. Without considering one Raman spectrum, a multiple-dimensional space is defined by all the PCs in the training data set. This leave-out spectrum is then classified to be a spectrum taken from either of your cell types based on its position in the multiple-dimensional space. With this LOOCV for each spectrum in the data set, the specificity and sensitivity for a data set containing two cell types are calculated (*see* **Note 11**).

4. Notes

1. Frozen tissue slicing

   We have used 5 μm thick formalin-fixed, frozen tissue sections successfully. However, the tissue thickness can be adjusted according to the experiment. Commercial companies can slice fixed, frozen tissue and mount onto quartz slides if cryostat equipment is not available.

2. Laser

A laser that can generate light at 785 nm and its wavelength can be tuned over 1 nm. For example, a tunable Ti:Sapphire laser (Spectra-Physics 3900 s, 1 W at 785 nm) pumped by a green laser (Coherent Verdi V6, 532 nm, 5 W) or a tunable Ti:Sa laser system (SolsTis M Squared lasers, 1 W at 785 nm).

3. Heat killing

   To heat kill mycobacteria prior to the transfer of material from level 3 containment to a lower level for analysis, 1 mL of cell culture (up to 10^8 cfu.mL^{-1}) is placed in a heat block for 20 min at 80 °C. This protocol was validated as follows:

   After heat killing, *M. tuberculosis* was plated onto 7H10 (Sigma-Aldrich, UK) supplemented with 0.05% glycerol (Sigma-Aldrich, UK) and 10% OADC (Sigma-Aldrich, UK) and no growth was observed after 4 weeks. Completion of this protocol allows transfer of fixed *M. tuberculosis* out of the containment level 3 (CL3) laboratory to be analyzed at a lower containment level.

4. Preparation storage

   Store tissue sections at –80 °C before use. Once sliced and mounted onto quartz slides store the frozen tissue section preparation at –20 °C between two experimental days.

5. Laser power adjustment

   Adjust the power on the sample plane to obtain an optimal signal-to-noise ratio. The power used will depend on the sample being targeted. In the case of single mycobacterial cells, you can use 150 mW on the sample plane. This condition does not produce any damage to the cells during the acquisition of the spectra. However, the integration time and laser power can be adjusted depending on the cell size, specie or if a group of bacteria is targeted instead of a single cell. It is important to optimize these parameters on the different organisms in advance.

6. Standard Raman acquisition

   The acquisition time set to obtain a standard Raman spectrum is 30 s, 6 s five times accumulated. The laser wavelength is constant through the measure and set at 784.6 nm. To produce a final spectrum, a background Raman spectrum is first acquired next to a single bacterium. Once the background is taken the signal from the single cell is recorded, and the background signal is subtracted afterward. It takes 30 s to have the background signal and 30 s of acquisition to obtain the bacterial spectrum. So, in this case, it takes around 1 min in total per single bacterium standard Raman spectrum.

7. WMR spectroscopy acquisition

   During acquiring WMR spectra, each spectrum was taken at an integration time of 30 s that accumulates 6 s for five times. Five spectra were acquired continuously over 150 s when the laser was tuning over a range of 1 nm around 785 nm. So, in this case, it takes around two and a half minutes in total per single bacterium to acquire a WMR spectrum.

8. Laser wavelength calibration

To calculate the laser wavelength using the known position of the main polystyrene peak ($\Delta\omega = 1001.4\ cm^{-1}$) use the following equation:

$$\Delta\omega\left(cm^{-1}\right) = \left(\frac{1}{\lambda_0(nm)} - \frac{1}{\lambda_1(nm)}\right) \times \frac{(10^7 nm)}{(cm)}$$

where $\Delta\omega$ corresponds to the Raman shift, λ_0 (nm) is the laser wavelength to calculate and λ_1 (nm) the measured wavelength of the main polystyrene peak in the Raman spectrum.

9. Raman spectra analysis

   We observed that both standard and WMR spectroscopy could discriminate LR and LP cells. However, WMR spectroscopy brings both higher sensitivity and specificity [13]. The autofluorescence background is completely removed by the use of the modulation method showing the spectrum with only the Raman peaks and with the accurate ratio between peaks [14, 15]. LR mycobacteria display higher intensity in the Raman bands associated with lipids mainly at 1300 cm^{-1} and around 1440–1450 cm^{-1}. [16]~~(Paper title: "Label-free optical vibrational spectroscopy to detect the metabolic state of M. tuberculosis cells at the site of disease" submitted)~~.

10. Raman spectroscopy a label-free and non-destructive methodology

    Raman spectroscopy is label-free and non-destructive; therefore the tissue sample investigated can be used again to perform another test such as immunostaining [16]~~(cite our paper here)~~. If the tissue is studied with a staining method, the sample can be damaged meaning that it cannot be reused. However, Raman spectroscopy is an interesting method to study single bacteria both in vitro and in tissue especially if the sample is to be analyzed further using another method.

11. PCA LOOCV and Matlab

    Additional information on PCA can be found in this article [~~16~~17]. We used Matlab to run the PCA and the LOOCV analysis (MathWorks, UK, version R2014b).

Acknowledgment

This work was supported by the PreDiCT-TB consortium [IMI Joint undertaking grant agreement number 115337, resources of which are composed of financial contribution from the European Union's Seventh Framework Programme (FP7/2007-2013) and EFPIA companies' in kind contribution (www.imi.europa.eu). This work was supported by the Department of Health, UK. The views expressed in this chapter are those of the authors and not necessarily those of the Department of Health. This work was supported by the UK Engineering and Physical Sciences Research Council (Grant code EP/J01771X/1) and a European Union FAMOS project (FP7 ICT, 317744). Authors acknowledge the loan of a laser from M Squared Lasers.

References

1. Gillespie SH, Crook AM, McHugh TD et al (2014) Four-month moxifloxacin-based regimens for drug-sensitive tuberculosis. N Engl J Med 371(17):1577–1587

2. Merle CS, Fielding K, Sow OB et al (2014) A four-month gatifloxacin-containing regimen for treating tuberculosis. N Engl J Med 371(17):1588–1598

3. Jindani A, Harrison TS, Nunn AJ et al (2014) High-dose rifapentine with moxifloxacin for pulmonary tuberculosis. N Engl J Med 371(17):1599–1608

4. Phillips PP, Mendel CM, Burger DA et al (2016) Limited role of culture conversion for decision-making in individual patient care and for advancing novel regimens to confirmatory clinical trials. BMC Med 14:19

5. Daniel J, Deb C, Dubey VS et al (2004) Induction of a novel class of diacylglycerol acyltransferases and triacylglycerol accumulation in *Mycobacterium tuberculosis* as it goes into a dormancy-like state in culture. J Bacteriol 186(15):5017–5030

6. Garton NJ, Waddell SJ, Sherratt AL et al (2008) Cytological and transcript analyses reveal fat and lazy persister-like bacilli in tuberculous sputum. PLoS Med 5(4):e75

7. Deb C, Lee CM, Dubey VS et al (2009) A novel in vitro multiple-stress dormancy model for *Mycobacterium tuberculosis* generates a lipid-loaded, drug-tolerant, dormant pathogen. PLoS One 4(6):e6077

8. Baek SH, Li AH, Sassetti CM (2011) Metabolic regulation of mycobacterial growth and antibiotic sensitivity. PLoS Biol 9(5):e1001065

9. Hammond RJ, Baron VO, Oravcova K et al (2015) Phenotypic resistance in mycobacteria: is it because I am old or fat that I resist you? J Antimicrob Chemother 70(10):2823–2827

10. Maquelin K, Kirschner C, Choo-Smith LP et al (2002) Identification of medically relevant microorganisms by vibrational spectroscopy. J Microbiol Methods 51(3):255–271

11. Buijtels PCAM, Willemse-Erix HFM, Petit PLC et al (2008) Rapid identification of mycobacteria by Raman spectroscopy. J Clin Microbiol 46(3):961–965

12. Pahlow S, Meisel S, Cialla-May D et al (2015) Isolation and identification of bacteria by means of Raman spectroscopy. Adv Drug Deliv Rev 89:105–120

13. Canetta E, Mazilu M, De Luca AC et al (2011) Modulated Raman spectroscopy for enhanced identification of bladder tumor cells in urine samples. J Biomed Opt 16(3):037002

14. De Luca AC, Mazilu M, Riches A et al (2010) Online fluorescence suppression in modulated Raman spectroscopy. Anal Chem 82(2):738–745

15. Mazilu M, De Luca AC, Riches A et al (2010) Optimal algorithm for fluorescence suppression of modulated Raman spectroscopy. Opt Express 18(11):11382–11395

~~16. Ringner M (2008) What is principal component analysis? Nat Biotechnol 26(3):303–304~~

16 Baron VO, Chen M, Clark SO et al (2017) Label-free optical vibrational spectroscopy to detect the

metabolic state of M. tuberculosis cells at the site of disease. Sci Rep 7(1):9844

17 Ringnér M (2008) What is principal component analysis? Nat Biotechnol 26 (3):303-304